Hall C Proposal to PAC34

The Neutron Electric Form Factor at Q^2 up to 7 (GeV/c)^2 from the Reaction $^2H(\vec{e}, e'\vec{n})^1H$ via Recoil Polarimetry

Spokepersons:

B. D. Anderson (Kent State University), J. Arrington (Argonne National Lab.), S. Kowalski (MIT), R. Madey (Kent State University), B. Plaster (University of Kentucky), A.Yu. Semenov (University of Regina)

Abstract

We propose to extend our previous measurements of G_E^n from deuterium to $Q^2 = 6.88$ (GeV/c)^2. Additional measurements at 5.22, 3.95, and 2.18 (GeV/c)^2 will provide continuity with our prior measurements up to $Q^2 = 1.45$ (GeV/c)^2, and overlap with recent (unpublished) measurements from a polarized ^3He target.

The JLab E93-038 collaboration measured G_E^n from the $d(\vec{e}, e'\vec{n})p$ reaction on a liquid deuterium target at Q^2 values of 0.45, 1.13, and 1.45 (GeV/c)^2. The experiment used a high-luminosity neutron polarimeter and the dipole neutron-spin-precession magnet [Charybdis] to measure the ratio of two scattering asymmetries associated with positive and negative precessions of the neutron polarization vector. In this ratio technique, systematic uncertainties are extremely small because the analyzing power of the polarimeter cancels in the ratio, and sensitivity to the beam polarization is reduced because it depends only on the small drift in polarization between sequential measurements. In addition, the reaction mechanism and nuclear physics corrections [for FSI, MEC, and IC] are best understood and most reliable for the deuteron.

The primary motivation for this proposed experiment is the ability to measure a fundamental quantity of the neutron – one of the basic building blocks of matter. A successful model of confinement must be able to predict both neutron and proton electromagnetic form factors simultaneously. The neutron electric form factor is especially sensitive to the nucleon wave function, and differences between model predictions for G_E^n tend to increase rapidly with Q^2. Calculations and fits to the data up to 1.45 (GeV/c)^2 show significant quantitative differences in the few (GeV/c)^2 range, and make qualitatively different predictions for the behavior of G_E^n at higher Q^2 values, with some showing G_E^n falling off more slowly than G_M^n, and others showing G_E^n falling rapidly to zero and becoming negative. The proposed measurements of G_E^n will be able to challenge theoretical calculations, including both models and new rigorous lattice QCD calculations, with a focus on the high Q^2 range where the models of the nucleon are generally meant to be more complete. Finally, these measurements of G_E^n are also needed to understand electron scattering experiments that probe electric structure functions at high Q^2, and will be important for the analysis of precision few-body data from measurements at Jefferson Lab.

List of Participants

R. Madey (Spokesman), B.D. Anderson (Co-Spokesman and Institutional Representative), A.R. Baldwin, D.M. Manley, J.W. Watson, W.-M. Zhang, Graduate Student

Kent State University

R. Carlini (Institutional Representative), R. Ent, H. Fenker, D. Gaskell, M. Jones, D. Higinbotham, A. Lung, D. Mack, G. Smith, S. Taylor, W. Vulcan, B. Wojtsekhowski, S. Wood, C. Yan

Thomas Jefferson National Accelerator Facility

S. Kowalski (Co-Spokesman and Institutional Representative), W. Deconinck, Graduate Student

Massachusetts Institute of Technology

B. Plaster (Co-Spokesman and Institutional Representative), W. Korsch, Graduate Student

University of Kentucky

A.Yu. Semenov (Co-Spokesman and Institutional Representative), G.J. Lolos, Z. Papandreou, I.A. Semenova, Graduate Student

University of Regina

C. Howell (Institutional Representative), Postdoc

Duke University

J. Arrington (Co-Spokesman and Institutional Representative), K. Hafidi, R. Holt, P. Reimer, P. Solvignon

Argonne National Laboratory

J.M. Finn (Institutional Representative), C. Perdrisat

The College of William and Mary

C. Keppel (Institutional Representative), L. Tang, I. Albayrak, O. Ates, C. Chen, M.E. Christy, M. Kohl, Y. Li, A. Liyanage, Z. Ye, T. Walton, L. Yuan, L. Zhu

Hampton University

A. Ahmidouch (Institutional Representative), S. Danagoulian, A. Gasparian

North Carolina A&T State University

List of Participants (continued)

M. Elaasar

Southern University at New Orleans

H. Arenhovel

University of Mainz

H.G. Mkrtchyan (Institutional Representative), A. Asaturyan, A. Mkrtchyan, V. Tadevosyan

Yerevan Physics Institute

A. Opper

George Washington University

S. Wells (Institutional Representative), N. Simicevic

Louisiana Tech

P. Markowitz (Institutional Representative), B. Raue, J. Reinhold

Florida International University

D. Day (Institutional Representative), P. McKee

University of Virginia

W. Tireman

Northern Michigan University

S. Tajima

Los Alamos National Laboratory

M. Khandaker (Institutional Representative), V. Punjabi

Norfolk State University

R.E. Segel

Northwestern University

R. Wilson

Harvard University

List of Participants (continued)

A.I. Malakhov (Institutional Representative), A.K. Kurilkin, P.K. Kurilkin, V.P. Ladygin, S.M. Piyadin.

Joint Institute for Nuclear Research (Dubna)

J. Martin

University of Winnipeg

S. Jin, W.-Y. Kim (Institutional Representative), S. Stepanyan, S. Yang, Graduate Student

Kyungpook National University

H. Breuer

University of Maryland

T. Reichelt

University of Bonn

L. Gan

University of North Carolina at Wilmington

I. Sick

University of Basel

F. Wesselmann

Xavier University of Louisiana

K. McCormick

Pacific Northwest National Laboratory

CONTENTS

List of Figures

List of Tables

1 Introduction

PAC 26 approved E04-110 to measure the electric form factor of the neutron, G_E^n, at a squared four-momentum transfer, Q^2, of 4.3 (GeV/c)^2 via recoil polarimetry with a liquid deuterium target. The jeopardy resubmission to PAC 33 was deferred with regret because it could not be fit into the schedule with the 6 GeV beam. Here we propose to extend measurements of G_E^n to a Q^2 value of 6.88 (GeV/c)^2 with additional measurements at lower Q^2 values to provide continuity with the previous measurements on deuterium and to provide overlap with the polarized ^3He data that is currently being analyzed. Measurements at $Q^2 = 2.18$, 3.95, 5.22, and 6.88 (GeV/c)^2 can be made in a time of 5, 10, 15, and 30 days, respectively. The projected uncertainties in G_E^n are about 0.002, comparable or slightly smaller than those projected in the E02-013 (^3He) proposal at $Q^2 = 2.4$ and 3.4 (GeV/c)^2. The systematic errors from the recoil polarimetry measurements with a liquid deuterium target are estimated to be small, and the total error would be completely statistics dominated.

The previously-approved experiment E02-013 used a polarized ^3He target to measure G_E^n at Q^2=1.3, 2.4, and 3.4 (GeV/c)^2. The E02-013 proposal projected systematic uncertainties of 10.4%, with statistical uncertainties ranging from 8.7% at 1.3 (GeV/c)^2 to 13.8% at 3.4 (GeV/c)^2. The total systematic uncertainty in the neutron polarimeter measurements is typically 2.5% [as documented in detail in Appendix B]. At higher Q^2 values, high rates and larger backgrounds become more important issues. Much of the background is associated with scattering from the protons, which is minimized by making measurements on deuterium. For the proposed measurement, background and DAQ rates can be handled and clean identification of the quasielastic neutron events can be performed using well established techniques; we do not rely on any improvements over what has been demonstrated.

Recent studies indicate that the total errors in E02-013 will be larger than projected in that proposal for the following reasons: (1) The veto detectors are too small to fully cover the scintillators of the Neutron Detector [NDet]; (2) there is no magnetic field in front of NDet [to deflect away the flux of quasi-elastic protons, which is a few times higher than the flux of quasi-elastic neutrons]; and (3) there is no shielding to prevent proton scattering and proton inelastic reactions in the dense material around the NDet scintillators, which produce false "neutron" events in NDet. These deficiencies lead to a proton contamination of E02-013 "neutron" data of about 50%. To address this problem, a detailed GEANT or FLUKA simulation is needed, and a large beam-energy-dependent correction of about a factor of two must be applied that introduces a significant additional systematic uncertainty in the final G_E^n results from E02-013.

Our proposed measurements are in a most interesting region. Until the results of the polarized ^3He measurement are published, the world's data are limited to Q^2 values below 1.5 (GeV/c)^2. Extrapolations of the world's data suggest that G_E^n may exceed G_E^p somewhere in the range of 4–5 (GeV/c)^2 and consequently, the isovector electric form factor [$G_E^v \equiv G_E^p - G_E^n$] would become negative. This idea is also supported by calculations, e.g. [Miller (2002)], which predict that the ratio G_E^n/G_M^n will continue to increase with increasing Q^2. Other calculations, e.g. [Lomon (2002)], suggest that the ratio G_E^n/G_M^n will level off somewhere above 2–3 (GeV/c)^2 or even decrease with G_E^n becoming negative somewhere above 4–5 (GeV/c)^2, as in the calculation of [Cloet et al. (2008)] or the duality-constrained fit of [Bodek et al. (2008)]. While calculations and fits show some differences in the 2–3 (GeV/c)^2 range, they predict *qualitatively different behavior* at even higher Q^2 values. Clearly, providing precise measurements of G_E^n in this range will strongly challenge the assumptions that go into these models. There is an added benefit to testing these models at high Q^2, as the low Q^2 behavior is believed to have large contributions from pion cloud effects, and as such cannot directly evaluate models which do not include pion cloud effects or which make only estimates of these effects. At high Q^2, inconsistencies between the calculations and G_E^n measurements should directly test modeling of the the quark core, which is the focus of many of these calculations.

In summary, we are extending G_E^n measurements to $Q^2 = 6.9$ (GeV/c)^2 with smaller systematic uncertainties and the same total uncertainty [$\Delta G_E^n = 0.002$] as projected for the ^3He measurement [E02-013] at 3.4 (GeV/c)^2 in a comparable beam time [30 days vs. 22 days], and we are requesting an additional 5, 10, and 15 days of beam time to obtain three other points at $Q^2 = 2.18$, 3.95, and 5.22 (GeV/c)^2. The measurements have small and well understood systematics, and requires the SHMS and an expanded recoil polarimeter, but do not rely on any R&D for new equipment or any special techniques to deal with rates or backgrounds.

2 Scientific Motivation and Background

2.1 Extension of E93-038 to Measure G_E^n up to $Q^2 = 7$ (GeV/c)^2

The electric form factor of the neutron, G_E^n, is a fundamental quantity needed for the understanding of both nucleon and nuclear structure. The dependence of G_E^n on Q^2 reflects the distribution of charge in the neutron. The E93-038 collaboration carried out measurements of G_E^n from September 8, 2000 to April 26, 2001 at three values of Q^2 [viz., 0.45, 1.13, and 1.45 (GeV/c)^2]. Results were reported in Physical Review Letters [Madey et al. (2003)], and in Physical Review C [Plaster et al. (2006)]. Data from E93-038 are plotted (as filled squares) in Fig. 1 together with the current world data extracted from polarization measurements [Eden et al. (1994), Herberg et al. (1999), Bermuth et al. (2003), Golak et al. (2001), Passchier et al. (1999), Zhu et al. (2001), Warren et al. (2004), Glazier et al. (2005)] and from an analysis of the deuteron quadrupole form factor [Schiavilla and Sick (2001)]. We fitted these data and the G_E^n slope at the origin as measured via low-energy neutron scattering from electrons in heavy atoms [Kopecky et al. (1997)] to a Galster et al. (1971) parameterization:

$$G_E^n = -a\mu_n \tau G_D/(1 + b\tau), \tag{1}$$

where $\tau = Q^2/4M_n^2$, $G_D = (1 + Q^2/\Lambda^2)^{-2}$, and $\Lambda^2 = 0.71$ (GeV/c)^2. Our best-fit parameters are a = 0.886±0.023 and b = 3.29±0.31 [Kelly (2003)].

The reported values of the ratio of the neutron electric to magnetic form factor ratio, G_E^n/G_M^n, represent both the highest Q^2 extraction and most precise published determinations of G_E^n. Even after the results from the polarized ^3He target measurements are published, extending the Q^2 range to 3.4 (GeV/c)^2, the measurements from deuterium will represent the highest precision extractions, with relative statistical uncertainties of 8.4% and 9.5% at the two highest Q^2 points and relative systematic uncertainties of 2-3%. The small systematic uncertainties occur because a measurement from deuterium has a theoretical advantage, and the use of a neutron polarimeter provides an experimental advantage. Theoretically, the quasielastic $^2\mathrm{H}(\vec{e}, e'\vec{n})^1\mathrm{H}$ reaction is insensitive to FSI, MEC, IC, and the choice of the NN potential for the deuteron wavefunction. Experimentally, the polarimeter permits measurement of scattering asymmetries by the cross-ratio technique. In the cross-ratio technique, the asymmetry is calculated as the ratio of geometric means of the up and down scattering yields in the polarimeter for the two beam helicity states. The advantage of this technique is that the resulting value for the asymmetry is independent of the luminosities for the two electron beam helicity states and independent of the efficiencies and acceptances of the top and bottom halves of the polarimeter. Also contributing to the small systematic uncertainties in our technique is the fact that the analyzing power

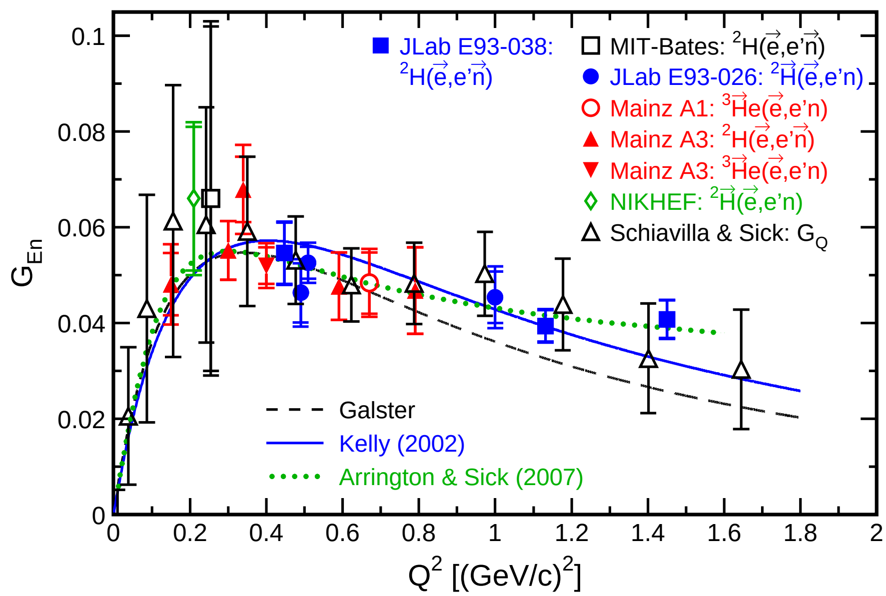

Figure 1: G_E^n versus Q^2. Data from E93-038 and world data. The black dashed line reflects the Galster parameterization; the blue solid line is our modified Galster fit (Kelly 2002); the green dotted line reflects the Arrington and Sick (2007) fit.

of the polarimeter and the polarization of the electron beam cancel in the form factor ratio. Other sources of uncertainty, such as radiative corrections and neutron depolarization by the lead shielding, are small also because they nearly cancel in the ratio. (See Section 4.1 for more details.)

Figure 2 shows the projected uncertainties for the proposed measurements, arbitrarily placed at zero, along with the published G_E^n measurement from previous JLab experiment, and the projected uncertainties for the completed ^3He measurement (open black triangles).

2.2 Better Understanding of Nucleon Structure

Measurements of G_E^n at high Q^2 will help us to understand the symmetry structure of nucleon electromagnetic form factors. Two symmetries play a crucial role: (1) relativistic invariance, which fixes the form of the nucleon current and hence the form of the form factors; and (2) isospin invariance, which gives relations between neutron and proton form factors. While relativistic invariance is expected to be exact, isospin invariance is not exact; however, it is expected to be only slightly broken in a realistic theory of the strong interaction. Isospin invariance leads to the introduction of isoscalar, F_{1S} and F_{2S}, and isovector, F_{1V} and F_{2V}, form factors, and hence to relations among proton and neutron form factors. The observed Sachs form factors, G_E^p and G_E^n, can be obtained from the relations:

$$G_E^p = F_1^p - \tau F_2^p = (F_{1S} + F_{1V}) - \tau (F_{2S} + F_{2V}) \quad (2)$$

$$G_E^n = F_1^n - \tau F_2^n = (F_{1S} - F_{1V}) - \tau (F_{2S} - F_{2V}) \quad (3)$$

where F_1 and F_2 are the Dirac and Pauli form factors. As a consequence of the two-term structure of Eqs. (2,3), with the second term being multiplied by $-Q^2/4M^2$, G_E^p and G_E^n may have zeros at some value of Q^2, depending on the relative sign of the two terms.

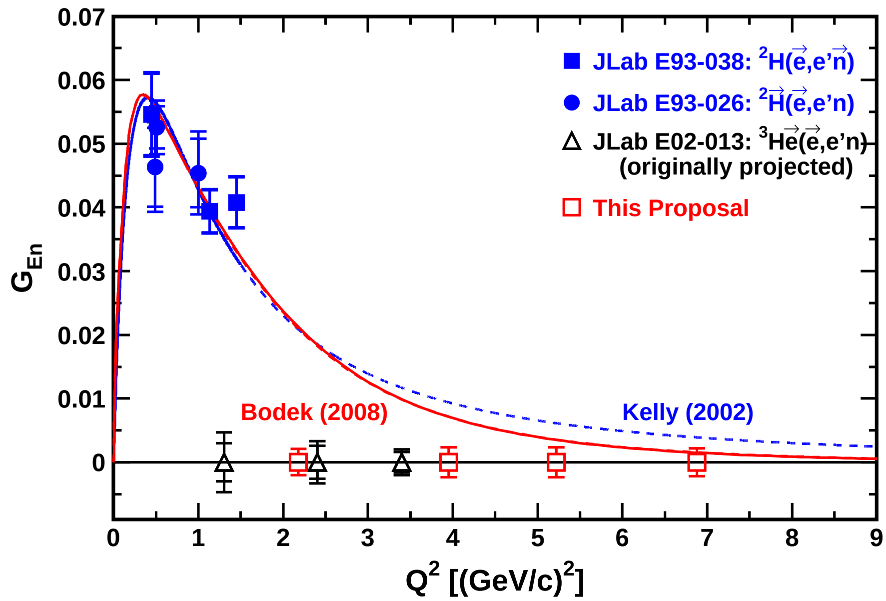

Figure 2: G_E^n versus Q^2. Data from JLab, original projections from E02-013 proposal, and projections from this proposal. The red line reflects the Bodek (2008) fit; the blue line is our modified Galster fit (Kelly 2002).

Different models of the nucleon correspond to different assumptions for the Dirac and Pauli form factors. Models with a two-term structure produce results in qualitative agreement with data; for example, a soliton model [Holzwarth (2002)], two relativistic constituent quark models [Miller (2002) and Cardarelli and Simula (2002)], and a model [Lomon (2002)] that couples vector meson dominance with the predictions of pQCD all have this structure and produce results in qualitative agreement with data. Predictions of these models are compared with data in Fig. 3. The chiral soliton model [Holzwarth (2002)] reproduces the dramatic linear decrease observed in $\mu_p G_E^p/G_M^p$ for $1 < Q^2 < 6$ (GeV/c)^2; however, this model fails to reproduce the neutron data at large Q^2. A light-front calculation using point-like constituent quarks surrounded by a cloud of pions [Miller (2002)], denoted "LFCBM", describes the neutron data, but falls below the proton data at high Q^2. A one-gluon exchange light-front calculation, denoted "OGE CQM", using constituent quark form factors fitted to $Q^2 < 1$ (GeV/c)^2 data [Cardarelli and Simula (2000)] agrees with the neutron data, but deviates from the proton data above $Q^2 \sim 3.0$ (GeV/c)^2. The Lomon model, denoted "VMD + pQCD", agrees with the proton data but falls below the neutron data above $Q^2 \sim 1.2$ (GeV/c)^2.

In 1973, Iachello, Jackson, and Lande [1973] suggested that the structure of the nucleon consists of two components: (1) an intrinsic structure (presumably three valence quarks), and (2) a meson cloud parameterized in terms of vector mesons (ρ, ω, ϕ). In this 1973 model of the nucleon, the external photon couples to both the intrinsic structure and the meson cloud. Iachello [2003] showed that the 1973 model agrees well with the new Hall A data on the proton form factor ratio $\mu_p G_E^p/G_M^p$; however, this 1973 model disagrees with the JLab E93-038 data on the neutron form factor ratio $\mu_n G_E^n/G_M^n$. Recently, Bijker and Iachello [2004] carried out a new isospin-invariant calculation that yielded agreement with the E93-038 neutron data. This 2004 calculation allows an intrinsic spin-flip amplitude, in addition to the spin-flip amplitude coming from the vector mesons. The results from both the 1973 and 2004 calculations are shown in Fig. 4 as a function of Q^2; the ratio for protons (neutrons) is shown in the top (bottom) panel.

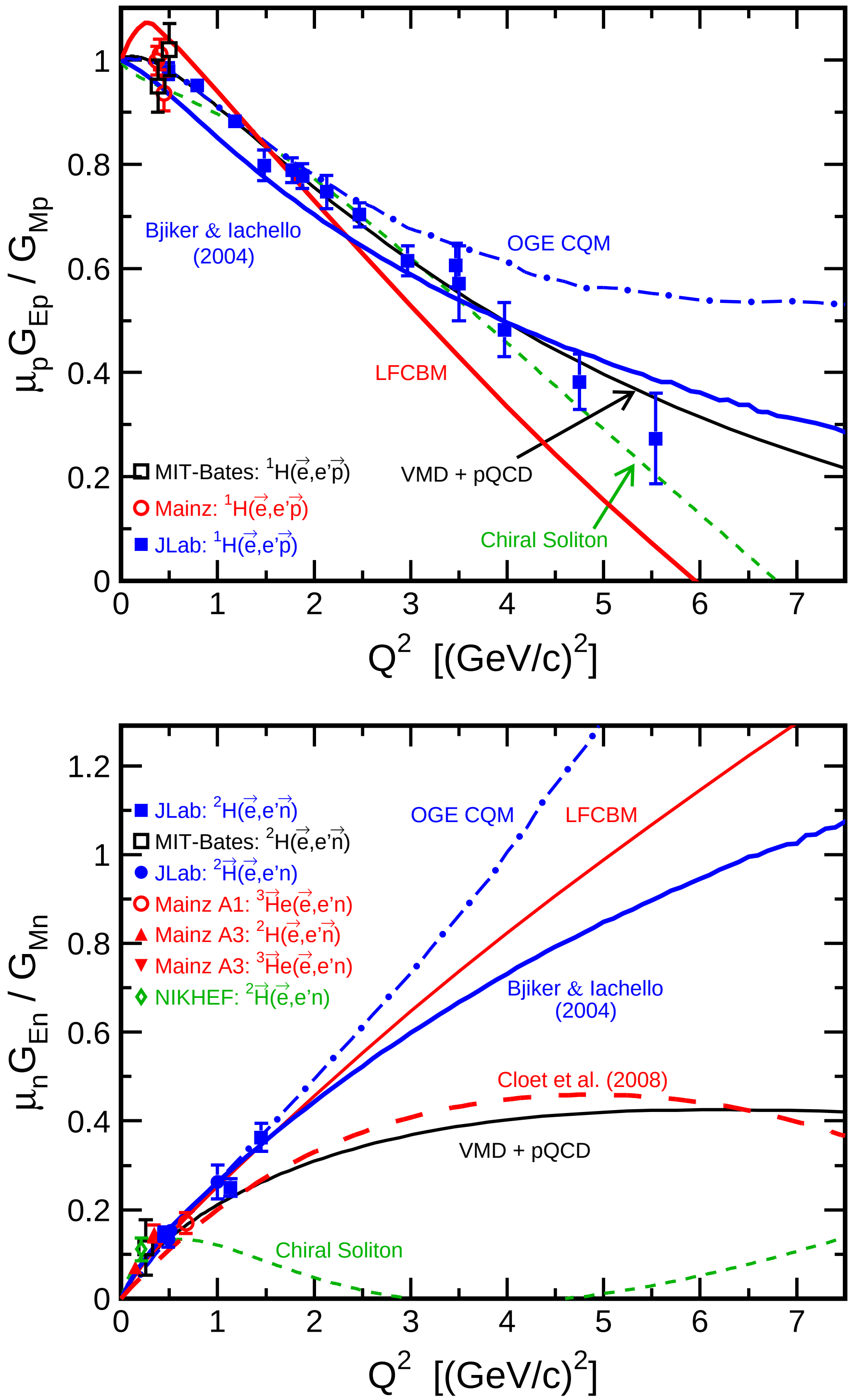

Figure 3: Predictions of selected models (see text for descriptions and the legend) for $\mu_p G_E^p/G_M^p$ and $\mu_n G_E^n/G_M^n$ compared with proton and neutron data. The neutron data symbols are the same as in Fig. 1.

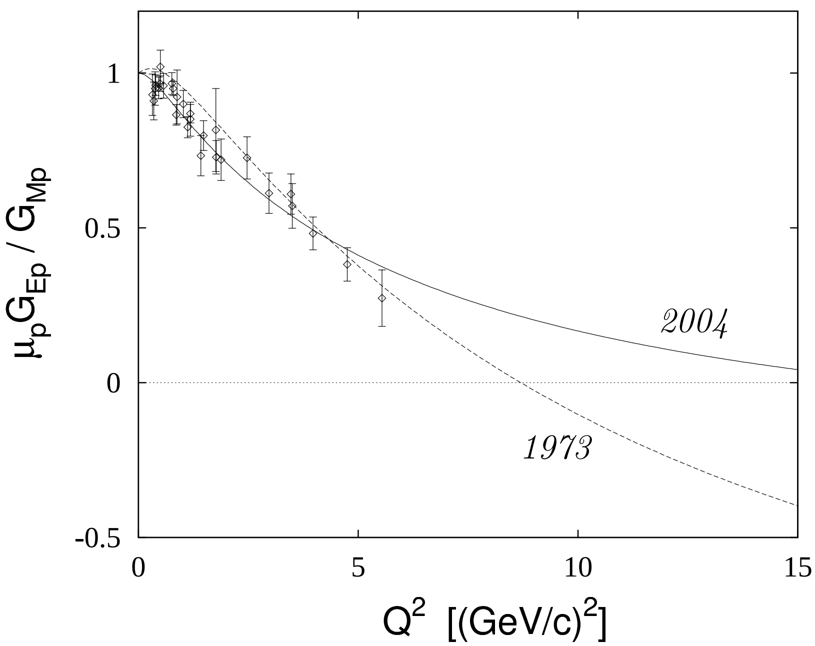

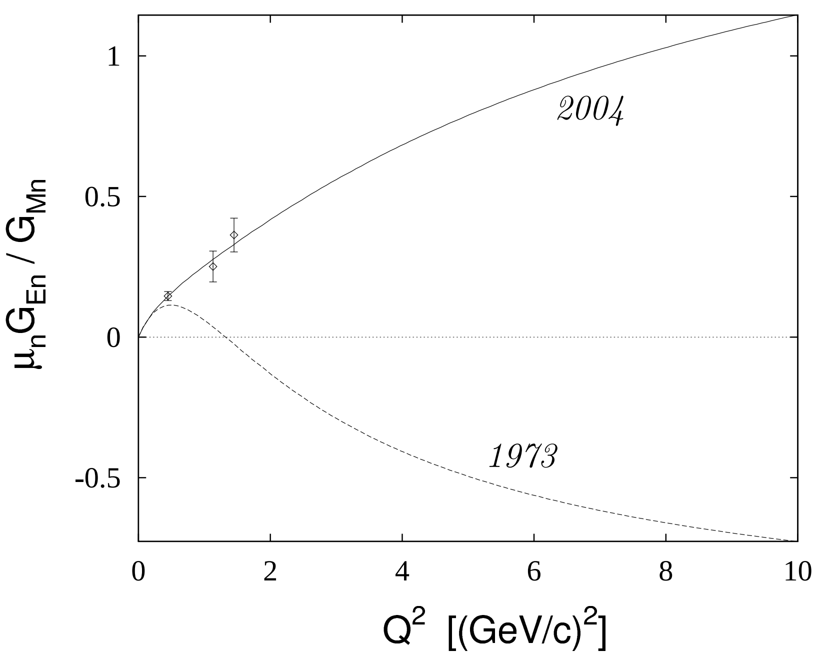

Figure 4: Predictions of the 1973 model (dashed) by Iachello, Jackson, and Lande, and the 2004 model (solid) by Bijker and Iachello for $\mu_p G_E^p / G_M^p$ (top panel) and $\mu_n G_E^n / G_M^n$ (bottom panel) compared with proton and neutron data.

For G_E^p, the 1973 calculation predicts a zero at about 8 (GeV/c)^2, whereas the 2004 calculation pushes this zero to about 15 (GeV/c)^2; for G_E^n, the 2004 calculation predicts a zero at a Q^2 in excess of 20 (GeV/c)^2. To discriminate between various models, it is necessary to determine the Q^2 values where the zero crossings occur.

The two calculations shown in Fig. 4 represent two limiting cases:

(1) 1973 calculation: Helicity here is strictly conserved in the intrinsic part and the Pauli form factor F_2 comes entirely from coupling to the vector mesons.

(2) 2004 calculation: Helicity flip is allowed in the intrinsic part (as in the light front calculations). The anomalous part of the form factor, F_2, comes almost entirely from intrinsic spin-flip components (not from vector mesons).

The 2004 calculation is consistently better for the proton data except at the highest Q^2 point. The neutron data need the 2004 calculation; the 1973 calculation deviates markedly from the E93-038 neutron data. Measurements of the sign of G_E^p and G_E^n are crucial for disentangling the structure of the nucleon.

Models of the nucleon structure make a wide range of predictions for G_E^n at high Q^2, from cases where $G_E^n/\mu_n G_M^n$ continues to grow almost linearly to well above 5 (GeV/c)^2, to those that show the ratio flattening or even turning over and changing sign. A very recent Fadeev calculation [Cloet et al. (2008)] predicts that the increase in G_E^n/G_M^n only extends to $\sim$4 (GeV/c)^2, and that the ratio begins to decrease around 5–6 (GeV/c)^2, with a predicted zero crossing near 11 (GeV/c)^2. Similarly, various parameterization of the form factors, e.g. the Galster form or the parameterization by Kelly, have $\mu_n G_E^n/G_M^n$ increasing with Q^2 but leveling off at high Q^2 values, while the recent BBBA08 parameterization [Bodek et al. (2008)] uses constraints for the high Q^2 limit and predicts, based on duality arguments, that $G_E^n/\mu_n G_M^n$ will level off near 3–4 (GeV/c)^2, and then will cross zero and change sign somewhere near 10 (GeV/c)^2.

Because the calculations and fits yield such a wide range of results, it is important to go to high Q^2 to evaluate these models. Preliminary results from the ^3He measurement (up to 3.4 (GeV/c)^2) have been shown, but are not yet released. The preliminary results suggest that between 1.5 and 3.5 (GeV/c)^2, G_E^n falls more rapidly than the Galster-like fits based on a modified dipole form. This could indicate that G_E^n is beginning to fall more rapidly than G_M^n, similar to what has been observed in the falloff of the proton electric form factor; however, the uncertainties and the preliminary status of the results makes it difficult to reach a clear conclusion on this point. Even with final results from the ^3He measurement, it will be critical to extend the measurements to higher Q^2 values where the models and parameterizations begin to show qualitatively different predictions. At 3.4 (GeV/c)^2, the difference between the Kelly parameterization and the BBBA08 is only 10–20%, while at 7 (GeV/c)^2, they differ by nearly a factor of two.

2.3 Better Understanding of Effects of Relativistic Quarks

Another motivation for measuring G_E^n at higher Q^2 is to obtain a better understanding of effects of relativistic quarks. In the Light Front Cloudy Bag Model (LFCBM) of Miller (2002), the nucleon is modeled as a relativistic system of three bound constituent quarks immersed in a cloud of pions. The pionic cloud is important for understanding low-momentum transfer physics, whereas the quarks dominate at high values of Q^2. The LFCBM predicts that the contribution to G_E^n from the relativistic quarks exceeds the Galster parameterization, as shown in Fig. 5 (top

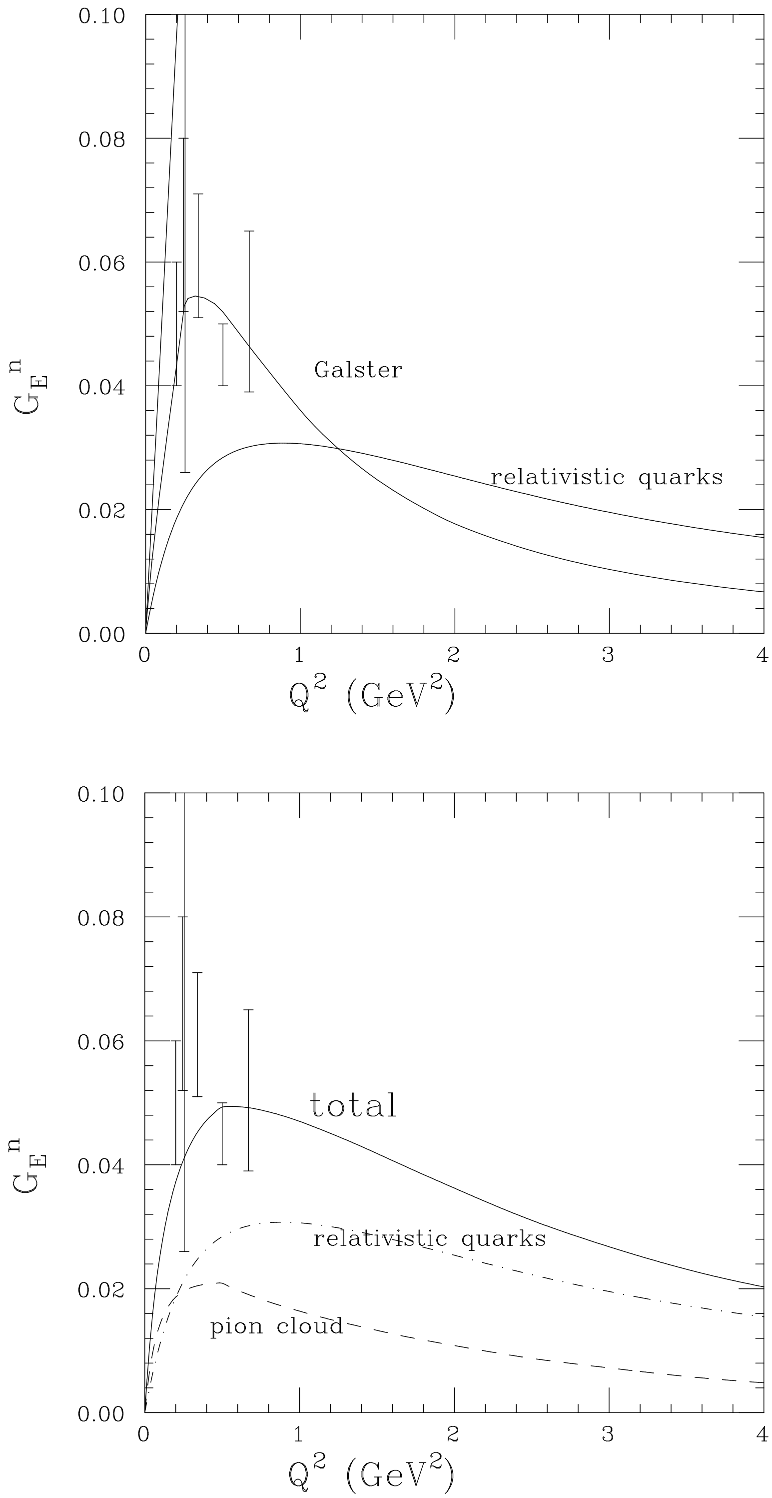

Figure 5: Calculation of G_E^n by Miller (2002): relativistic quarks contribution (top panel) and total LFCBM calculation (bottom panel). [Figure taken from Miller (2002).]

panel); and that the relativistic quarks make the main contribution to G_E^n at high Q^2, as shown in Fig. 5 (bottom panel).

It is not just the improved lever arm that makes high Q^2 measurement highly desirable. Many models treat only the three constituent quarks, and thus do not expect to do a good job of reproducing the data in the lower Q^2 region where pion cloud effects are important. At low Q^2, this makes G_E^n a unique way to examine the pion cloud effects, but it cannot provide strong tests of the models of nucleon structure that do not explicitly include these effects. At high Q^2 values, the proposed measurements of G_E^n will provide a complete set of elastic form factor measurements in the high Q^2 region where pion cloud effects are expected to be small, and where models that can provide reasonable results for the other form factors make wildly varying predictions for G_E^n. In this region, G_E^n takes on another important role, as it is sensitive to the difference in the spatial distribution of positive and negative charge in the neutron, and thus uniquely probes the difference between the up and down quark distributions in the quark core of the nucleon.

2.4 Comparisons to Lattice QCD

J. Negele at MIT has been leading a major effort to use lattice QCD to understand the structure and interaction of hadrons. Fundamental lattice calculations are becoming available to solve QCD, the field theory of quarks and gluons. Currently, lattice calculations are limited by computer power; however, increased computing power is becoming available. Lattice QCD calculations are fundamental, whereas various model calculations are not. Lattice QCD has made impressive strides recently, with rigorous methods for separating hard and soft contributions and recent methods for extrapolation to the chiral limit for light quarks using explicit representations of nonanalytic contributions. In recent years, lattice calculations have entered the regime of precision calculations of selected properties. Computer resources and theoretical developments now permit calculations at light enough quark masses that many quantities can be extrapolated to the physical quark mass using chiral perturbation theory. Edwards et al. (2006) calculated the nucleon axial charge from first principles with 6.8% errors and in agreement with experiment. Recently, Hagler et al. (2007) calculated a range of generalized form factors related to generalized parton distributions. One particularly nice result is the contribution of the quark spin and of the quark orbital angular momentum to the total spin of the nucleon. The chiral extrapolations agree well with the recent Hermes analysis. Alexandrou et al. (2006) published results on the isovector electromagnetic form factors, obtained in quenched and unquenched lattice QCD studies, out to Q^2 values of ~ 2 (GeV/c)^2. The unquenched (quenched) calculations employed lattice spacings of 0.08 fm (0.09 fm), and quark masses corresponding to pion masses down to about 380 MeV (410 MeV). An interesting finding reported here (subject to the numerous caveats concerning extrapolations to the continuum limit, and the chiral extrapolation) was that both the unquenched and quenched results were higher than the experimentally extracted isovector form factors, with the deviations largest for the electric isovector form factor. The authors noted that this disagreement was puzzling and warranted further studies with finer lattice spacings.

The present state of the art of lattice calculations has some caveats: (1) Currently, a class of Feynman diagrams, called "disconnected diagrams" are ignored. They are believed to be small, but are roughly two orders of magnitude more expensive to calculate than the connected diagrams that are included at present. These diagrams cancel out of isovector quantities, which therefore are the most reliable quantities to calculate at present. Negele et al. [private communication (2007)] hope to publish their first results of disconnected diagrams soon. (2)

Because current lattice spacings of ~ 0.1 fm make it unrealistic to calculate form factors at $Q^2 = 4$ (GeV/c)^2, the calculations generally go only up to $Q^2 = 2$ (GeV/c)^2. The next round will treat finer lattice spacings, which should permit reaching $Q^2 = 4$ (GeV/c)^2.

2.5 Better Understanding of Electron Scattering Data From Nuclei

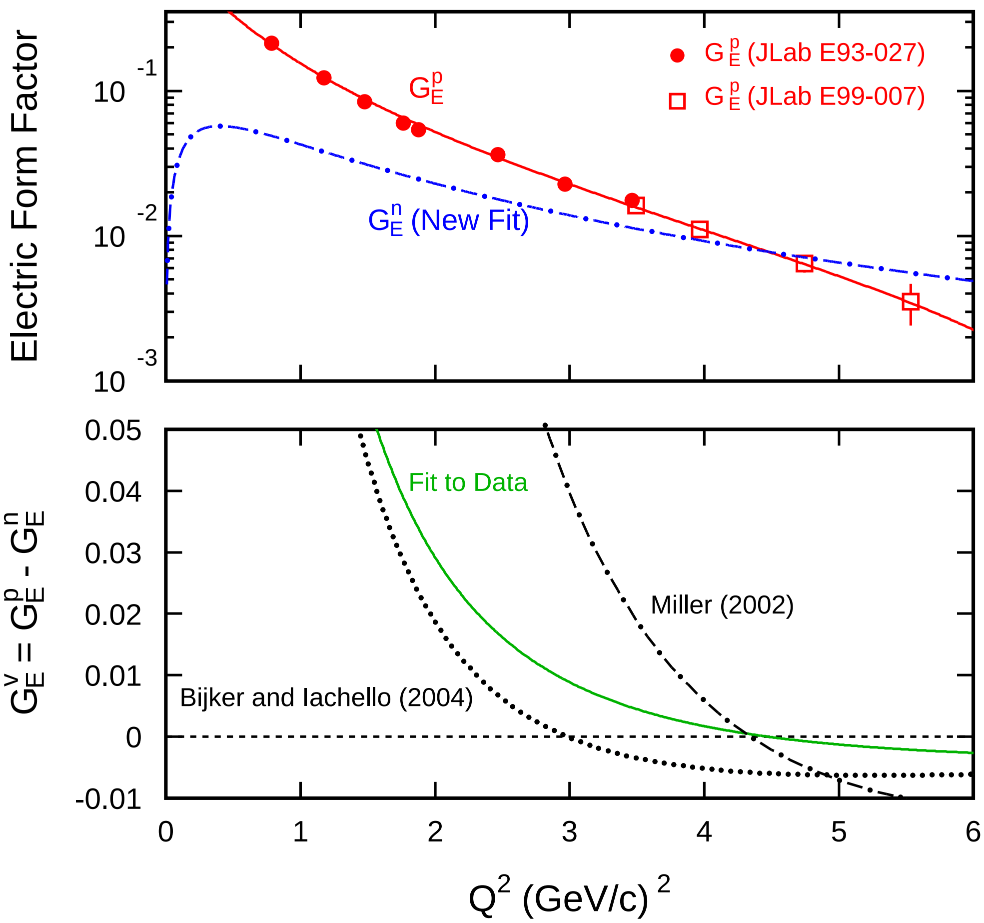

Figure 6: Proton, neutron, and isovector form factors as a function of Q^2. The solid line through the G_E^p points in the top panel is a parameterization from Eq. (4) for G_E^p. Bottom panel: the solid line is a difference of the G_E^p and G_E^n parameterizations from the top panel, the dotted line is a calculation by Bijker and Iachello (2004), and the dash-dotted line is a calculation by Miller et al. (2002).

In their paper on electron scattering from nuclei, Drechsel and Giannini (1989) state (on page 1109) that *"All calculations of nuclear electromagnetic properties suffer from the poor knowledge of G_E^n."* As Q^2 increases, the values of G_E^p, the electric form factor of the proton, approach the values of G_E^n, represented by the modified Galster parameterization. Plotted in Fig. 6 (top panel) as a function of Q^2 are the neutron electric form factor for the modified Galster parameterization, and the proton electric form factor points measured in JLab E93-027 and E99-007. The measured G_E^p points have been fitted with the following parameterization:

$$G_E^p = G_D\,[1 - 0.14(Q^2 - 0.30)] \qquad (\mathit{Fit\ to\ Hall\ A\ FPP\ Measurements}) \tag{4}$$

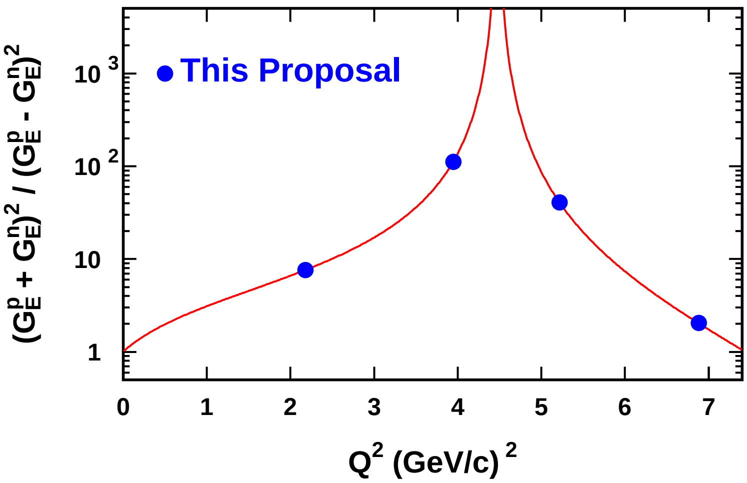

Figure 7: The ratio of isoscalar and isovector cross-sections [Eq. (6)] as a function of Q^2. We assume the modified Galster parameterization (New Fit from E93-038) for G_E^n and the parameterization from Eq. (4) for G_E^p.

with

$$G_D \equiv (1+Q^2/0.71)^{-2} \qquad (Dipole) \tag{5}$$

The magnitude of G_E^n is not insignificant compared to G_E^p in the Q^2 region above about 2 (GeV/c)^2. The value of G_E^n from the modified Galster fit exceeds the value of G_E^p above $Q^2 \sim$ 4.4 (GeV/c)^2; accordingly, the isovector electric form factor would become negative in this Q^2 region. As shown in Fig. 6, the most recent model of Bijker and Iachello (2004) predicts that the isovector electric form factor becomes negative at a Q^2 of about 3 (GeV/c)^2; whereas the model of Miller et al. (2002) predicts a crossover at $\sim$4.3 (GeV/c)^2. The isovector form factor [i.e., a difference between G_E^p (E93-027/E99-007) and G_E^n (New Fit from E93-038)] is plotted in the bottom panel of Fig. 6. The G_E^p data measured in E93-027 turned out to be a surprise — falling faster with Q^2 than expected from the global analysis of earlier SLAC data. The nature of the decrease of G_E^n with Q^2 may be a surprise also.

Because the isovector electric form factors of nuclei are proportional to the difference $G_E^p - G_E^n$ (and the isoscalar electric form factors are proportional to the sum $G_E^p + G_E^n$), the value of G_E^n is needed for the understanding of electron scattering experiments that probe electric structure functions at high momentum transfer. The ratio of the isoscalar cross section to the isovector cross section depends sensitively on the value of G_E^n:

$$\frac{\sigma_{isoscalar}}{\sigma_{isovector}} = \left(\frac{G_E^p + G_E^n}{G_E^p - G_E^n}\right)^2 \tag{6}$$

This ratio is plotted in Fig. 7 as a function of Q^2. This ratio is unity if $G_E^n = 0$; however, this ratio is about 8 at $Q^2 = 2.2$ (GeV/c)^2 and about 100 at $Q^2 = 4.0$ (GeV/c)^2 if G_E^n continues to follow the modified Galster parameterization and if G_E^p follows Eq. (4). A better knowledge of G_E^n is needed for the interpretation of electron scattering from nuclei at high momentum transfer. This knowledge is needed for the analysis of few-body data from measurements at Jefferson Lab, which are in the Q^2 range above the existing G_E^n data. With the projected uncertainty $\Delta G_E^n \approx$ 0.002 at $Q^2 = 2.2$ and 4.0 (GeV/c)^2, we will be able to distinguish easily between $G_E^n = 0$ and the modified Galster parameterization at the Q^2 values proposed herein.

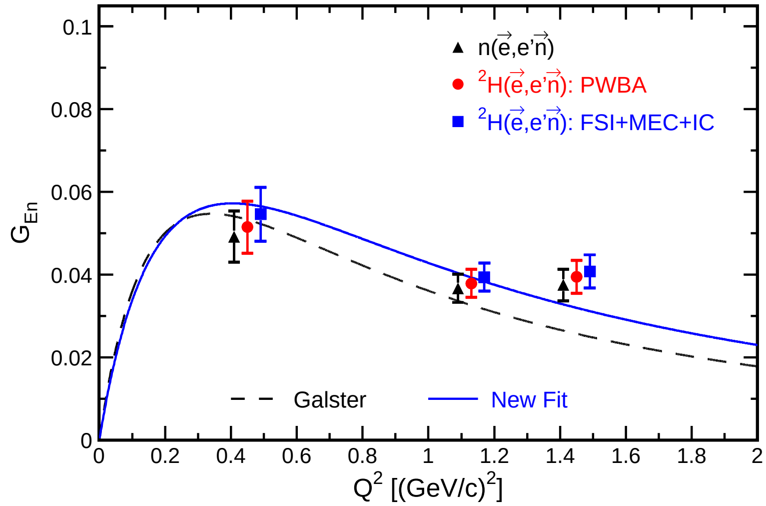

Figure 8: Comparison of the final results for G_E^n extracted from analyses assuming $n(\vec{e}, e'\vec{n})$ elastic scattering and a point acceptance (triangles), the acceptance-averaged $^2\mathrm{H}(\vec{e}, e'\vec{n})^1\mathrm{H}$ Arenhövel PWBA model (circles), and the acceptance-averaged $^2\mathrm{H}(\vec{e}, e'\vec{n})^1\mathrm{H}$ Arenhövel FSI+MEC+IC model (squares). The error bars shown are the quadrature sum of the statistical and systematic errors.

2.6 Nuclear Physics Corrections and Reaction Mechanism Questions

Figure 8 shows the results from E93-038 for three cases: (1) The triangles are for a point acceptance; (2) the circles are acceptance-averaged PWBA values; and (3) the squares are the acceptance-averaged values based on Arenhoevel's full calculation [including FSI, MEC, and IC]. In E93-038, the nuclear physics corrections [for FSI, MEC, and IC] increased G_E^n over the values obtained with the PWBA model by 5.6, 4.0, and 3.3 percent at $Q^2 = 0.45$, 1.13, and 1.45 (GeV/c)^2, respectively. While the magnitude of the nuclear corrections are expected to continue to decrease with increasing Q^2, the nuclear corrections are more reliable [and most likely smaller] for deuterium than for helium. Arenhoevel [2003] carried out calculations for deuterium for the previously proposed kinematics at $Q^2 = 4.3$ (GeV/c)^2; his results are shown in Fig. 9.

Also, the reaction mechanism is expected to be simpler in deuterium than in helium. In the case of the proton form factor ratio, comparisons of results obtained via the recoil polarization technique with results obtained via the Rosenbluth separation technique have provided strong evidence that two-photon exchange physics can significantly impact elastic electron-proton scattering observables. Thus, measurements of the neutron form factor ratio via different techniques (i.e., recoil polarization from unpolarized deuterium, or asymmetry from polarized ^3He) may reveal (or alleviate) similar questions about the reaction mechanisms employed for extractions of G_E^n/G_M^n from quasielastic scattering from different nuclei.

3 Theoretical Background: Extraction of G_E^n

For the proton, the form factors have typically been performed by measuring the elastic electron–proton cross section over a range of angles, i.e., performing a Rosenbluth separation. The fundamental limitation of the Rosenbluth separation technique is that is it sensitive to a combination of the electric and magnetic form factors, $\tau(G_M^n)^2 + \varepsilon(G_E^n)^2$, where $\tau = Q^2/4M^2$, and ε is the

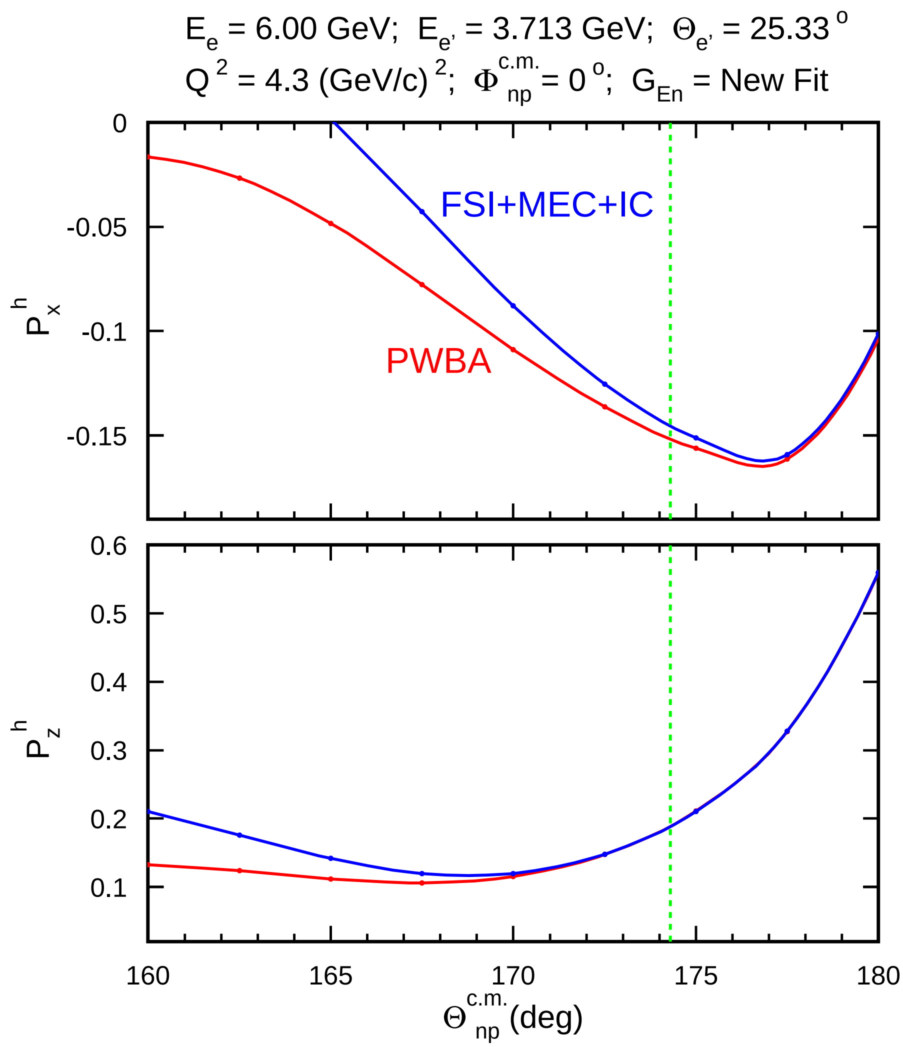

Figure 9: Comparison of Arenhoevel's PWBA and FSI+MEC+IC calculations of P_x^h and P_z^h at the previously proposed kinematics of $Q^2 = 4.3$ (GeV/c)^2.

virtual photon polarization parameter, which is sensitive to the electron scattering angle. At fixed Q^2, G_E^n is determined by measuring the variation of the cross section with scattering angle (ε). For the neutron, $(G_E^n)^2 \ll (G_M^n)^2$, and so the cross section has little sensitivity to G_E^n, and measurements would be difficult even if a free neutron target were available.

The lack of free neutron targets meant that the electron–neutron cross section had to be determined from quasielastic scattering on a deuteron target. Subtraction of the contribution from the proton in the deuteron introduced large uncertainties. In addition, there are large model-dependent corrections and uncertainties due to uncertainties in the theoretical description of the deuteron, mostly from final-state interactions (FSI) and meson-exchange currents (MEC). In the Q^2 region from 1.75 to 4.00 (GeV/c)^2, Lung et al. (1993) reported measurements from SLAC-NE11 of quasielastic $e-d$ cross sections at forward and backward angles which permit a Rosenbluth separation of G_E^n and G_M^n at $Q^2 = 1.75$, 2.50, 3.25, and 4.00 (GeV/c)^2. Although Lung et al. (1993) stated that their data from SLAC-NE11 were consistent with $(G_E^n)^2 = 0$ for $1.75 < Q^2$ (GeV/c)$^2 < 4.00$, these data appear consistent also with the modified Galster parameterization. The NE11 error bars do not permit distinguishing between $G_E^n = 0$ and the

Galster parameterization.

In contrast to the Rosenbluth separation method, measurements utilizing polarization observables are sensitive to the ratio G_E^n/G_M^n; therefore, knowledge of G_M^n taken from cross section measurements can be combined with polarization measurements to make precise extractions of both G_E^n and G_M^n. In addition, this technique allows an experimental determination of the sign of G_E^n, which is impossible in the Rosenbluth separation (as only $(G_E^n)^2$ appears). This is another nice feature of the polarization transfer technique - especially in view of the fact that nothing is known about the sign of G_E^n at high Q^2.

The measurements still require scattering from a neutron in a nucleus, but the corrections due to nuclear effects are much smaller than for the case of unpolarized scattering. Arenhoevel (1987) calculated the effect of the electric form factor of the neutron on the polarization transfer in the $d(\vec{e}, e'\vec{n})p$ reaction in the quasifree region, where the deuteron serves as a neutron target while the proton acts mainly as a spectator. Using a nonrelativistic theory and a realistic nucleon-nucleon potential, Arenhoevel found that the sideways polarization of the recoil neutron $P_{S'}$, which vanishes for coplanar kinematics and unpolarized electrons, is most sensitive to G_E^n for neutron emission along the momentum-transfer direction in the quasifree case. Using the parameterization of Galster et al. (1971) for G_E^n, Arenhoevel's calculation indicates that even away from the forward-emission direction (with respect to the direction of the momentum transfer $\vec{q}$), the increase in the sideways polarization of the neutron $P_{S'}$ is small for $G_E^n = 0$, but increases when G_E^n is switched on, and that this increase prevails up to a neutron angle of nearly 30^o measured with respect to $\vec{q}^{\,c.m.}$ in the center-of-mass system. In the forward direction with respect to $\vec{q}^{\,c.m.}$, Arenhoevel found also that the neutron polarization $P_{S'}$ is insensitive to the influence of final-state interactions (FSI), meson-exchange currents (MEC), and isobar configurations (IC), and that this lack of sensitivity holds again up to an angle of nearly 20^o away from the forward direction with respect to $\vec{q}^{\,c.m.}$, which corresponds to a laboratory angle of about a few degrees away from the forward direction with respect to the $\vec{q}^{\,lab}$. Arenhoevel also studied the influence of different deuteron wave functions on the sideways neutron polarization $P_{S'}$. His results for quasifree kinematics (i.e., for neutron emission along $\vec{q}$) show almost no dependence on the deuteron model. The Arenhoevel calculation shows that dynamical uncertainties are very small. Finally, Beck and Arenhoevel (1992) investigated the role of relativistic effects in the electrodisintegration of the deuteron for quasifree kinematics. They found that the dependence on the parameterization of the nucleon current in terms of Dirac-Pauli or Sachs form factors is reduced considerably by inclusion of the relativistic contributions. Also, for quasifree emission, Arenhoevel (2002) demonstrated that $P_{L'}$ is insensitive to FSI, MEC, IC, and to theoretical models of deuteron structure.

Rekalo, Gakh, and Rekalo (1989) used the relativistic impulse approximation to describe the polarization effects sensitive to G_E^n in deuteron electrodisintegration. In the deuteron quasielastic peak, the neutron polarizations calculated in the relativistic approach agree with the results of Arenhoevel (1987). A later study by Mosconi, Pauschenwein, and Ricci (1991) of nucleonic and pionic relativistic corrections in deuteron electrodisintegration does not change the results of Arenhoevel. Laget (1990) investigated the effects of nucleon rescatterings and meson-exchange currents on the determination of the neutron electric form factor in the $d(\vec{e}, e'\vec{n})p$ reaction. He concluded that a measurement of the sideways polarization of the neutron appears to be the most direct way to determine the neutron electric form factor. He concluded also that in quasifree (colinear) kinematics, the neutron polarization in the exclusive reaction is equal to the value expected in the elementary reaction $n(\vec{e}, e'\vec{n})$ and that corrections from final-state interactions and meson-exchange currents are negligible above $Q^2 = 0.30$ (GeV/c)^2, but that these corrections become sizeable below this momentum transfer; however, Herberg et al. (1999)

found that (even in the quasifree peak) corrections for FSI in $d(\vec{e}, e'\vec{n})p$ measurements at Mainz amounted to (8±3)% for $Q^2 = 0.34$ (GeV/c)^2 and (65±3)% for $Q^2 = 0.15$ (GeV/c)^2 of the value unperturbed by FSI. In E93-038, we found that the nuclear physics [FSI+MEC+IC] corrections were small and decreased with increasing Q^2. The nuclear physics corrections increased G_E^n over the value obtained with the PWBA by only 5.6, 4.0, and 3.3 percent at $Q^2 = 0.45$, 1.13, and 1.45 (GeV/c)^2, respectively. These corrections were based on the model of Arenhoevel et al. (1988).

4 Description of the Experiment

4.1 Experimental Arrangement

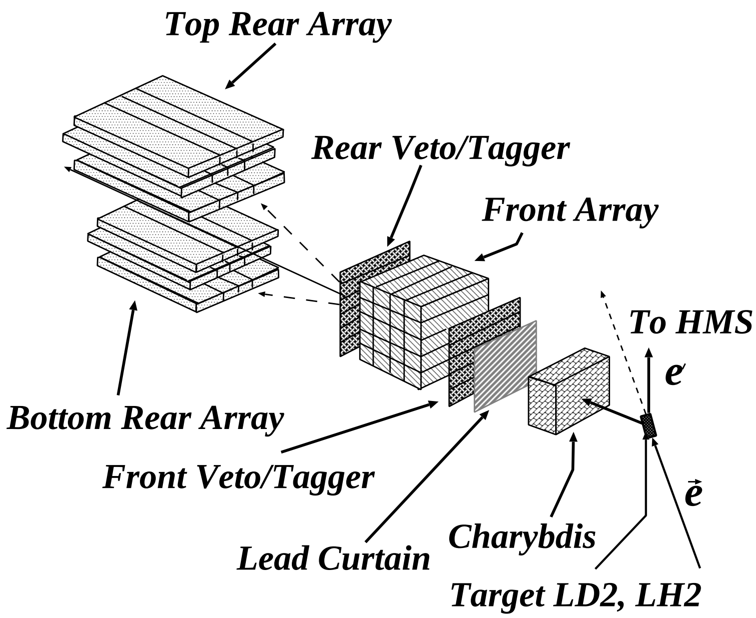

Figure 10: Schematic diagram of the experimental arrangement in E93-038.

The experimental arrangement is similar in principle to the one used in E93-038 (shown in Fig. 10). A polarimeter detects the recoil neutron from the quasielastic d($\vec{e}$,e'$\vec{n}$)p reaction and measures the up-down scattering asymmetry from the projection of the polarization vector on the transverse axis. A dipole magnet in front of the polarimeter precesses the neutron polarization vector through an angle χ to permit measuring the scattering asymmetry ξ_+ from the polarization vector component on the transverse (or sideways) direction. With another measurement of the scattering asymmetry ξ_- for a precession through an angle $-\chi$, the ratio of G_E and G_M is given by

$$g \equiv \left(\frac{G_E}{G_M}\right) = K_R \, tan(\chi) \, \frac{(\eta+1)}{(\eta-1)} \tag{7}$$

where the asymmetry ratio

$$\eta \equiv \frac{\xi_-}{\xi_+} = \frac{P_-^x}{P_+^x} \tag{8}$$

and K_R is a kinematic function that is determined by the electron scattering angle θ_e and four-momentum transfer Q^2 in the d($\vec{e}$,e'$\vec{n}$)p reaction. For a total data-acquisition time T, the time fractions for measuring ξ_+ and ξ_- are optimized to minimize the statistical uncertainty in g. The scattered electron from the d($\vec{e}$,e'$\vec{n}$)p reaction is detected with the Super High Momentum Spectrometer (SHMS) in coincidence with the recoil neutron.

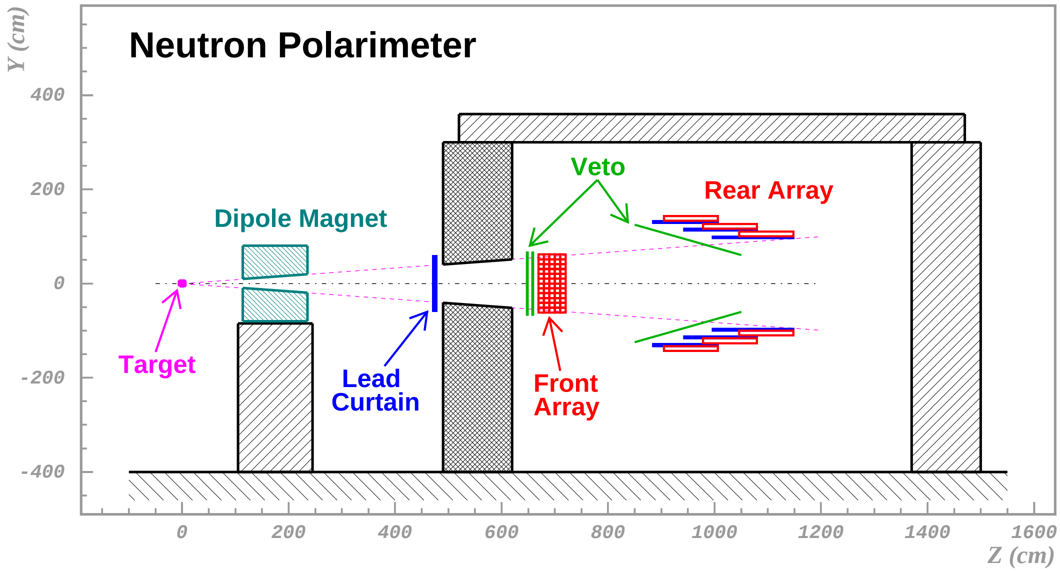

Figure 11: Neutron polarimeter to be used in the measurements.

Source	$\langle Q^2 \rangle$ [(GeV/c)^2] $0.447^{(a)}$	$1.132^{(a)}$	$1.132^{(b)}$	$1.450^{(a)}$	$1.45^{(b)}$
Beam Polarization	1.6	0.7	0.4	1.2	0.3
Charge-Exchange	<0.1	<0.1	0.1	<0.01	0.2
Depolarization	<0.1	0.1	<0.1	<0.1	0.6
Positioning/Traceback	0.2	0.3	0.3	0.4	0.4
Precession Angle	1.1	0.3	0.1	0.5	0.1
Radiative Corrections	0.7	0.1	0.1	0.1	0.1
Timing Calibration	2.0	2.0	2.0	2.0	2.0
Total of Above Sources	2.9	2.2	2.1	2.4	2.2

(a) $\chi = \pm 40^\circ$ precession.
(b) $\chi = 0^\circ$, $\pm 90^\circ$ precession.

Table 1: Systematic and scale uncertainties in G_E^n/G_M^n [%] achieved in E93-038.

The polarimeter to be used for these measurements (see Fig. 11) is an enhanced version of the one used for E93-038. In order to increase the vertical acceptance of the front array, we plan to increase the number of detectors in each layer from 5 to 12. In order to increase the efficiency, we are increasing the number of detector layers in the front array to five layers [from the four used in E93-038], and we are inserting 3-cm steel converters ahead of each layer in the rear detector arrays. The thickness of the converters was optimized to maximize the gain (~1.6) in the detection efficiency for neutrons [Semenova et al. (2002)]. Another advantage of using the converters is that the converters ahead of each detector in the rear array will prevent the detection of gammas from π^0 decays in the front array. Examination of the geometry of the enhanced polarimeter in Fig. 11 reveals that the mean photon path length through the center of the middle-layer converter is 10.6 cm [= ∼6.0 radiation lengths]; similarly, the mean path length is 6.5 [∼5.5] radiation lengths for the outer [inner] converter. Note that a thickness of 5.5 radiation lengths reduces the energy of the incident photon to ∼0.40% of its initial value. The polarimeter now consists of 60 detectors in the front array and 18 detectors in each of two rear arrays for a total of 96 detectors. A double layer of veto/tagger detectors is located ahead of the front array, and a tagger detector is located in front of the upper and lower rear arrays. The proposed configuration of the rear tagger is mostly out of the direct path of particles from the target so that it decreases the singles rate in the tagger from the charged background and simplifies the identification of neutrons in the rear array (compared with E93-038). To permit high luminosity, the dimensions of each of the 36 detectors in the front three layers of the front array are 10 cm×10 cm×100 cm; the dimensions of the 24 detectors in the rear two layers are 10 cm×12.5 cm×100 cm. The 18 [10 in×40 in×4 in] detectors in each rear array are shielded from the direct path of neutrons from the target.

A significant advantage of this technique for measuring the ratio of the two scattering asymmetries is that the scale and systematic uncertainties are minimal because the relative uncertainty in the analyzing power of the polarimeter does not enter in the ratio. The same is true for the beam polarization P_L because, as demonstrated in E93-038, P_L does not change much during sequential measurements of ξ_+ and ξ_-.

In the cross-ratio method of analysis of the scattering asymmetries measured in the polarimeter, Ohlsen and Keaton (1973) showed that false asymmetries cancel to all orders from helicity-dependent errors in charge integration or system dead-times, or from errors in detection efficiency and acceptances; and that false asymmetries cancel to first order from misalignments with respect to $\vec{q}$, or from a difference in the beam polarization for the two helicity states. The cross ratio is the ratio of two geometric means $(N_U^+ N_D^-)^{1/2}$ and $(N_U^- N_D^+)^{1/2}$, where $N_U^+(N_D^-)$ is the yield in the peak for scattering neutrons up (down) when the helicity is positive (negative).

The systematic and scale uncertainties achieved in E93-038 are listed in Table 1, which is Table VIII of our archival Physical Review paper [B. Plaster et al., Phys. Rev. C73, 025205 (2006)]. The overall systematic uncertainties are of the order of 2.5% in Δg, where $g = G_E^n/G_M^n$, and are discussed in detail in this paper.

In E93-038, we used the CHARYBDIS dipole magnet with an 8.25-inch gap and 2-inch field clamps. The 8.25-inch gap was large enough to illuminate fully the 0.5-m high by 1-m wide front array of the E93-038 polarimeter. To illuminate fully the increased front array of the proposed polarimeter, we plan to use the dipole magnet with the tapered gap between the magnet poles (see Fig. 12). Such a configuration of the gap permits minimizing the current in the magnet that is needed to reach the desired field integral. Other advantages of such a gap are:

1. The magnetic field in the gap is almost perpendicular to the momentum of all neutrons emitted from the target in to the front array;

2. The dipole magnet poles provide additional collimation to protect the polarimeter rear array from the direct particles from the target.

The precession angle χ is the angle of rotation of the polarization vector after traversing the magnetic field. The neutron spin precession angle χ is given by

$$\chi \;=\; -\frac{ge}{2M_p c\beta_n}\int B\Delta l \;=\; \frac{1.913e}{M_p c\beta_n}\int B\Delta l \tag{9}$$

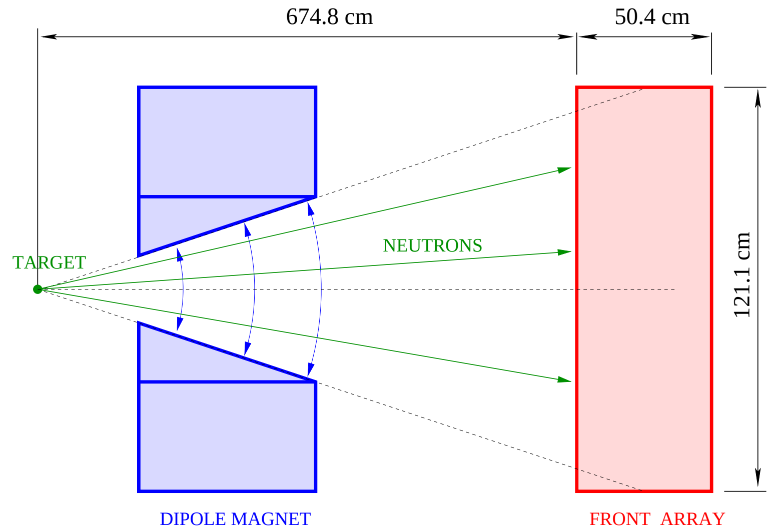

Figure 12: Tapered poles of Dipole Magnet (side view). [Drawing is not to scale to emphasize the vertical dimension.]

Four-Momentum Transfer, Q^2 (GeV/c)^2	2.18	3.95	5.22	6.88
Beam Energy, E_0 (GeV)	2.2	4.4	6.6	11.0
Electron Scattering Angle, θ_e (deg)	58.60	36.53	26.31	16.79
Scattered Electron Momentum, $P_e^{;}$ (GeV/c)	1.035	2.288	3.815	7.330
Neutron Scattering Angle, θ_n (deg)	28.0	28.0	28.0	28.0
Neutron Momentum, P_n (GeV/c)	1.881	2.901	3.602	4.511
Neutron Kinetic Energy, T_n (GeV)	1.163	2.110	2.783	3.668
Flight Path, x (m)	7.0	7.0	7.0	7.0
Precession Angle, χ (deg)	155	155	155	155
Field Integral to Precess Neutron Spin through χ Degree, $B\Delta l$ (Tm)	4.333	4.282	4.210	3.959

Table 2: Kinematic conditions at a neutron scattering angle of 28.0^o. Also listed is the dipole magnet field integral $B\Delta l$ required to precess the neutron polarization vector.

where $g/2$ = -1.913.

The 15-cm lead curtain ahead of the polarimeter is required to attenuate electromagnetic radiation and also to reduce the flux of charged particles incident on the polarimeter. The curtain thickness is chosen to maintain an acceptable singles rate at a beam current of 80 μA (see description of the simulation in Section 4.4). *If we find during the experiment that the singles rates in the front array are too high, we will increase the thickness of the lead curtain; the loss in the neutron rate will be compensated partly with a smaller fraction of corrupted events.* In E93-038, the singles counting rate in one of the detectors decreased markedly when the thickness of the Pb was increased from 5 cm to 10 cm; for example, the singles rates in one of the veto detectors (160 cm wide $\times$ 11 cm high $\times$ 0.64 cm thick) at a distance of about 6.7 m from a 15-cm LD_2 target are plotted in Fig. 13 as a function of the electron beam current at an energy of 884 MeV. For all beam currents, the singles rate is about five times higher with a 5-cm Pb curtain. E93-038 used a 10-cm lead curtain in order to run at higher beam currents. We do not have data with a 5-cm lead curtain at higher beam energies. E93-038 ran with a 10-cm Pb

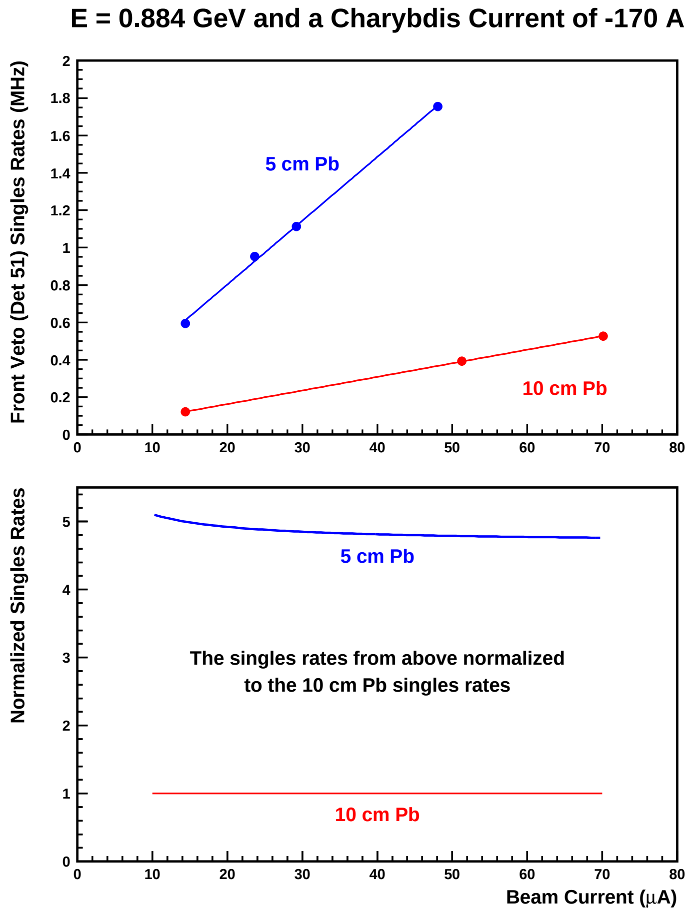

Figure 13: Singles rates for beam energy of 884 MeV and a CHARYBDIS current of -170 A.

curtain for all these energies.

To measure the false asymmetry or the dilution of the asymmetry from the two-step process $d(\vec{e}, e'\vec{p})n + Pb(\vec{p}, \vec{n})$, we will take data with an LH_2 target. In the second charge-exchange step, the sign of the polarization transferred to the neutron will be opposite to that from the primary $d(\vec{e}, e'\vec{n})p$ process because the sign of the magnetic moment of the proton is opposite to that of the neutron.

4.2 Kinematics

Table 2 lists the kinematic conditions and the $B\Delta l$ required to precess the neutron polarization vector through χ degrees. The accelerator should be able to deliver a beam polarization of 80% at any energy (see Fig. 31). The range of reasonable angles of neutron spin precession is limited on the small-angle side by the requirement to have the magnetic field in the dipole magnet strong enough to deflect a significant part of the quasielastic protons away from the front array of the polarimeter, and on the large-angle side by the fact that the statistical uncertainty increases with precession angle χ, as shown in Fig. 24. A precession angle χ of 155 deg. was chosen.

4.3 Count Rates

The rate of electron-neutron coincidence events, which comes from quasielastic scattering of electrons on the 40-cm LD_2 target, was projected at Q^2 = 2.2, 4.0, 5.2, and 6.9 $(\mathrm{GeV/c})^2$ for a

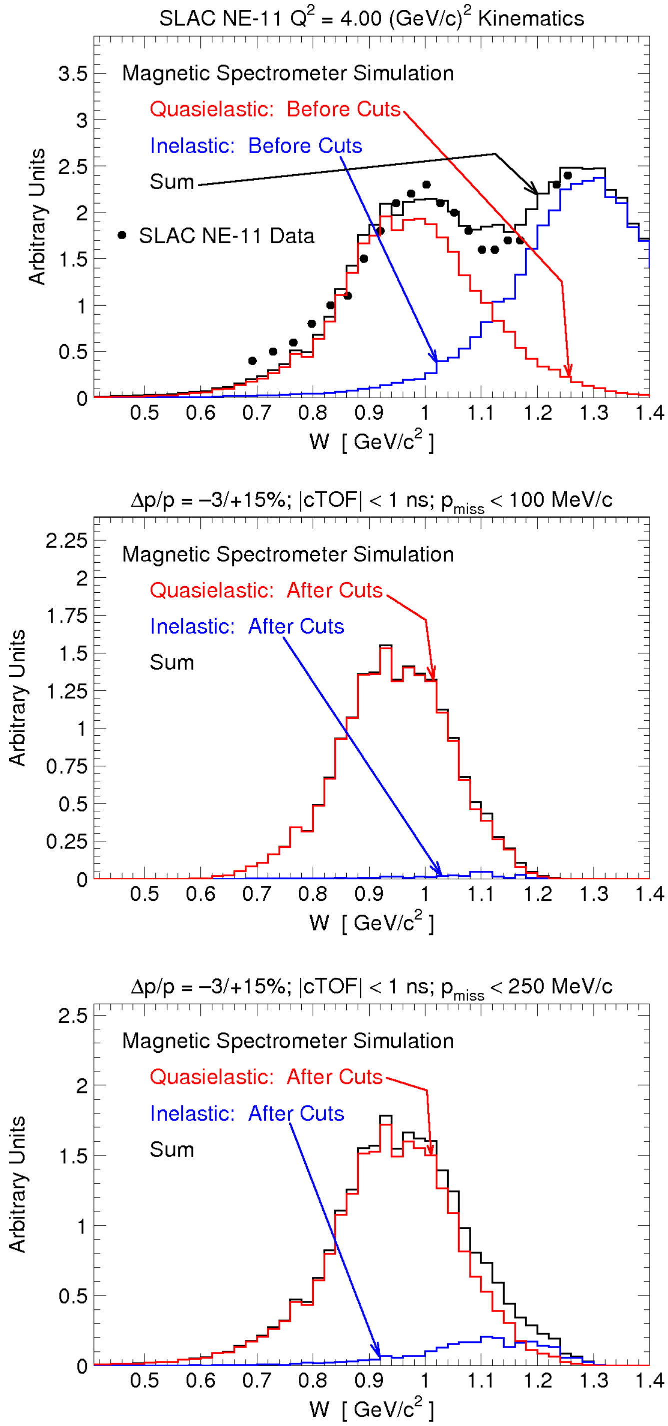

Figure 14: Invariant mass spectra at $Q^2 = 4.0$ (GeV/c)^2 before (top panel) and after (middle and bottom panels) cuts on the scattered electron momentum, the missing momentum, and an SHMS-NPOL coincidence time-of-flight. Quasielastic and pion-production spectra are simulated separately with GENGEN 2.9 code [Kelly (2000)] and normalized on the invariant mass spectrum at similar kinematics from SLAC NE-11 (Lung et al. (1993)]. Details of the sumulation are in the Appendix A. The inelastic contamination for $W < 1.1$ GeV/c^2 is estimated to be $\sim 1\%$ for $p_{miss} < 100$ MeV/c cut (middle panel) and $\sim 6\%$ for $p_{miss} < 250$ MeV/c cut (bottom panel).

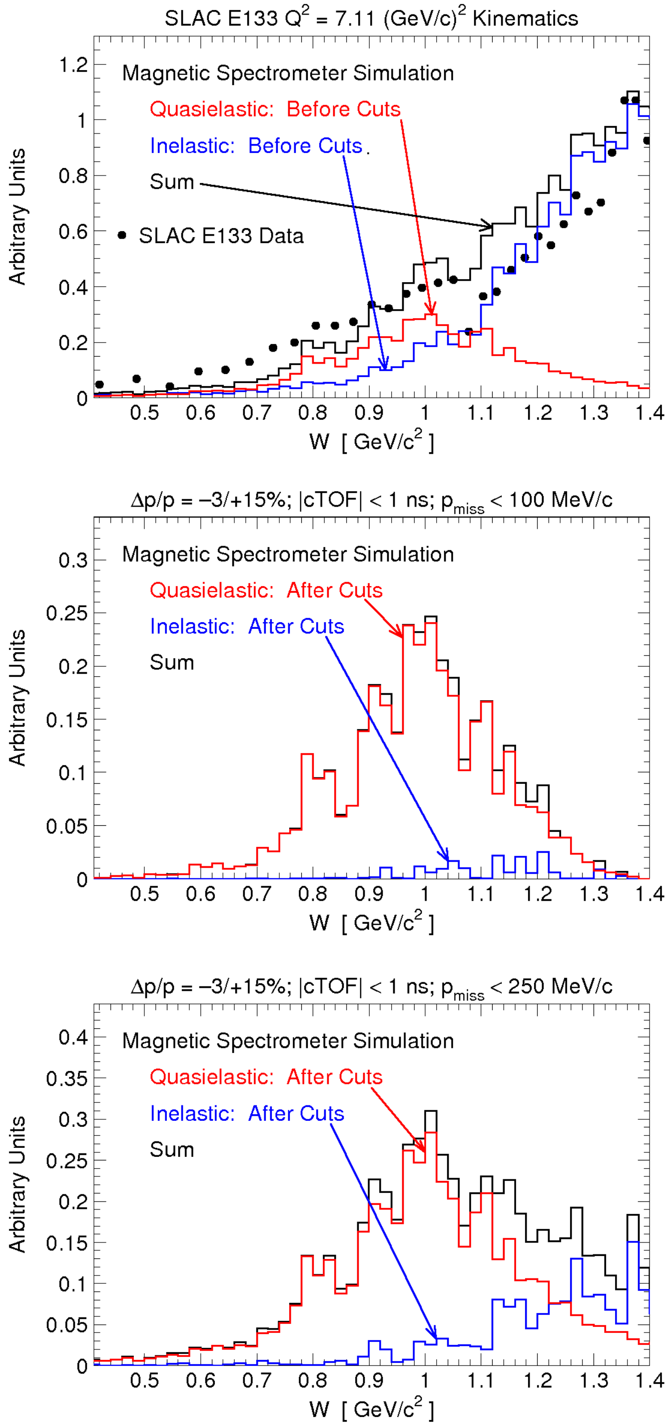

Figure 15: Invariant mass spectra at $Q^2 = 7.1$ (GeV/c)^2 before (top panel) and after (middle and bottom panels) cuts on the scattered electron momentum, the missing momentum, and an SHMS-NPOL coincidence time-of-flight. Quasielastic and pion-production spectra are simulated separately with GENGEN 2.9 code [Kelly (2000)] and normalized on the invariant mass spectrum at similar kinematics from SLAC E-133 (Rock et al. (1992)]. Details of the sumulation are in the Appendix A. The inelastic contamination for $W < 1.1$ GeV/c^2 is estimated to be $\sim 3\%$ for $p_{miss} < 100$ MeV/c cut (middle panel) and $\sim 8\%$ for $p_{miss} < 250$ MeV/c cut (bottom panel).

Four-Momentum Transfer, Q^2 $(\mathrm{GeV}/c)^2$	2.2	4.0	5.2	6.9
SHMS Angular Acceptance:				
$\Delta\theta_e$ (mrad)	$\pm$ 24	$\pm$ 24	$\pm$ 24	$\pm$ 24
$\Delta\phi_e$ (mrad)	$\pm$ 55	$\pm$ 55	$\pm$ 55	$\pm$ 55
SHMS Efficiency, ϵ_e (%)	92	92	92	92
SHMS Momentum Bite, $\Delta p_e/p_e$ (%)	-3/+15	-3/+15	-3/+15	-3/+15
Neutron Polarimeter Angular Acceptance:				
$\Delta\theta_n$ (mrad)	$\pm$ 71.4	$\pm$ 71.4	$\pm$ 71.4	$\pm$ 71.4
$\Delta\phi_n$ (mrad)	$\pm$ 85.5	$\pm$ 85.5	$\pm$ 85.5	$\pm$ 85.5
Neutron Polarimeter Efficiency, ϵ_n (%)	1.0	1.0	1.0	1.0
Beam Current, I_{beam} (μA)	80	80	80	80
MCEEP Rate, $< R_{MCEEP} >$ (Hz)	85.8	30.0	23.1	20.9
Real-Event Rate, R_{real} (Hz)	1.55	0.49	0.35	0.29
Neutron Polarimeter Analyzing Power, A_Y	11.1	7.2	5.8	4.6
Precession Angle, χ (deg)	155	155	155	155
Expected Asymmetries:				
for -χ Precession (%)	-4.45	-2.39	-1.61	-0.95
for +χ Precession (%)	1.90	1.06	0.74	0.46

Table 3: The neutron polarimeter and SHMS acceptances, estimated neutron polarimeter parameters, and calculated real event rate at $Q^2 = 2.2$, 4.0, 5.2, and 6.9 (GeV/c)^2 for a beam current of 80 μA incident on a 40-cm LD_2 target in JLab Hall C. Also listed are the simulated NPOL efficiency and estimated analyzing power (see Section 5 and Fig. 30 for details), and expected asymmetries for -χ and +χ precession of the neutron polarization vector.

beam current of 80 μA (which corresponds to a beam luminosity $L = 1.02 \times 10^{39}$ cm^{-2}s^{-1}). The calculation was done for a momentum bite $\Delta p/p$ of $-3/+15\%$ for the scattered electron. This SHMS momentum bite (combined with the cuts on the missing momentum and SHMS-NPOL coincidence time) helps to suppress the neutrons associated with pion production (see Figs. 14, 15, 25 and Appendix A).

We used the kinematic conditions from Table 2 for $Q^2 = 2.2$, 4.0, 5.2, and 6.9 (GeV/c)^2. Based on the acceptance-averaged SHMS-NPOL coincidence rate of quasielastic events, $< R_{MCEEP} >$, from MCEEP [Ulmer (1991) version 3.8 includes radiative corrections], we estimated the real-event rate R_{real} for an assumed SHMS efficiency $\epsilon_{HMS} = 0.92$, the SHMS momentum bite of -3/+15%, and the SHMS-NPOL coincidence time-of-flight ($cTOF$) window of $\pm$1 ns. For this estimation, we simulated the neutron polarimeter efficiency, ϵ_n, (including neutron transmission through 15-cm lead curtain and loss of events due to analysis cuts) with the FLUKA 2002 code (see also Section 5). To estimate the NPOL analyzing power, A_Y, we used the analyzing power $A_Y = 14.4\pm1.3\%$ measured in E93-038 at neutron momentum $P_n = 1.45$ MeV/c (see Plaster et al. (2006)) as well as an assumption that the analyzing power for the neutron scales the same way as the analyzing power for protons (see Azhgirei et al.(2005) and Fig. 16):

$$A_Y \sim 1\,/\,P_{nucleon} \qquad or \qquad A_Y \cdot P_{nucleon} \;=\; const \tag{10}$$

Listed in Table 3 are neutron polarimeter and SHMS acceptances, estimated neutron polarimeter parameters (viz., A_Y and ϵ_n), and the calculated real event rates in Hall C.

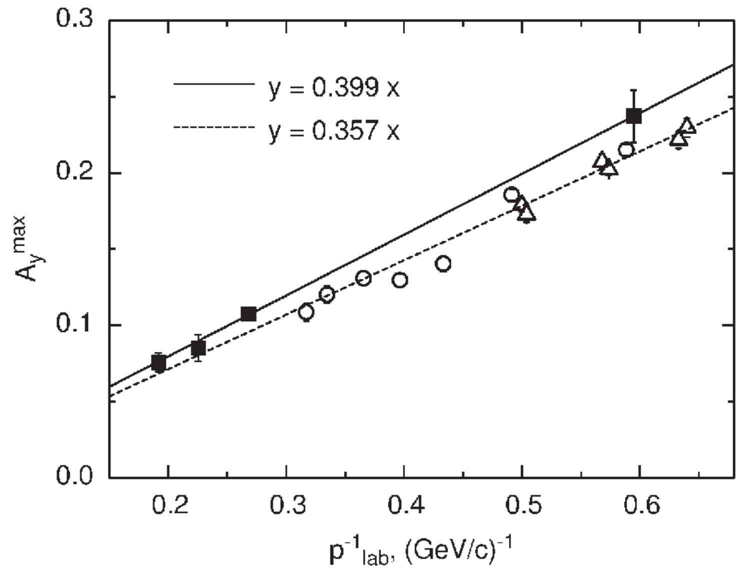

Figure 16: Momentum dependence of an analyzing power measured for protons on CH_2 and C (Azhgirei et al.(2005)). Solid line – fit of CH_2-data, dashed line – fit of C-data.

4.4 Projected Uncertainties

To estimate statistical uncertainties, we use the simple pairwise analysis here, but the actual analysis in the experiment will include acceptance averaging using methods similar to E93-038.

The up-down asymmetry, measured in JLab E93-038, is proportional to the projection of the neutron polarization vector on the axis that is perpendicular to the neutron momentum direction. Thus, the ratio of asymmetries for neutron spin precession through $\pm\chi$ degrees is given by:

$$\eta \equiv \frac{\xi_-}{\xi_+} = \frac{P^x_-}{P^x_+} = \frac{P_{S'} cos(-\chi) + P_{L'} sin(-\chi)}{P_{S'}\ cos(\chi) + P_{L'}\ sin(\chi)} = \frac{(P_{S'}/P_{L'})\ cos(\chi) - sin(\chi)}{(P_{S'}/P_{L'})\ cos(\chi) + sin(\chi)} \tag{11}$$

$$(P_{S'}/P_{L'}) = \frac{-sin(\chi)\ (\eta+1)}{cos(\chi)\ (\eta-1)} = -tan(\chi)\ \frac{(\eta+1)}{(\eta-1)} \tag{12}$$

where $P_{S'}$ and $P_{L'}$ are transverse and longitudinal projections of the neutron polarization vector:

$$P_{S'} = -h\ P_e\ \frac{K_S\ g}{K_0\ (1\ +\ g^2/K_0)} \tag{13}$$

$$P_{L'} = h\ P_e\ \frac{K_L}{K_0\ (1\ +\ g^2/K_0)} \tag{14}$$

Here h is the beam helicity, P_e is the beam polarization, and $g \equiv (G_E/G_M)$.

$$(P_{S'}/P_{L'}) = -g\ (K_S/K_L) \tag{15}$$

From (15) and (12) :

$$g = -\left(\frac{K_L}{K_S}\right)\ \left(\frac{P_{S'}}{P_{L'}}\right) = \left(\frac{K_L}{K_S}\right)\ tan(\chi)\ \frac{(\eta+1)}{(\eta-1)} \tag{16}$$

The statistical uncertainty in the g value is:

$$(\delta g)_{stat} \;=\; \left(\frac{K_L}{K_S}\right)\; tan(\chi)\; \frac{2}{(\eta-1)^2}\; \delta\eta \tag{17}$$

The relative statistical uncertainty $(\delta g/g)_{stat}$ is:

$$\left(\frac{\delta g}{g}\right)_{stat} \;=\; \frac{2}{(\eta+1)(\eta-1)}\; \delta\eta \tag{18}$$

Here $\delta\eta$ is the statistical error in the asymmetry ratio:

$$\left(\frac{\delta\eta}{\eta}\right)^2 \;=\; \left(\frac{\delta\xi_-}{\xi_-}\right)^2 \;+\; \left(\frac{\delta\xi_+}{\xi_+}\right)^2 \tag{19}$$

or

$$(\delta\eta)^2 \;=\; \left(\frac{\delta\xi_-}{\xi_+}\right)^2 \;+\; \xi_-^2\left(\frac{\delta\xi_+}{\xi_+^2}\right)^2 \tag{20}$$

To project the statistical uncertainties, we used the statistical errors for asymmetries which come from Poisson statistics:

$$\left(\frac{\delta\xi_\pm}{\xi_\pm}\right)^2 \;=\; \frac{1}{\xi_\pm^2}\;\left(\frac{1+2/r}{N_\pm}\right) \;=\; \frac{1}{(A_Y P_\pm^x)^2}\;\left(\frac{1+2/r}{N_\pm}\right) \tag{21}$$

Here $N_\pm$ is the number of events taken during $\pm\chi$ precession angle runs, A_Y is the polarimeter analyzing power, and r is the ratio of real-to-accidental coincidences. For these projections, we used the value r = 35.0, 13.3, 8.1, and 4.5 from the simulation for an 80 μA beam at Q^2 = 2.2, 4.0, 5.2, and 6.9 (GeV/c)^2, respectively. To estimate accidental coincidence rates (∼0.044, 0.037, 0.043, and 0.065 Hz), the electron single rates in the SHMS (∼1.56, 0.52, 0.41, and 0.47 kHz) were calculated with the MONQEE code (Dytman 1987), and the rates of coincidences in the front and the rear arrays of the polarimeter from inclusive neutrons (∼18.9, 47.0, 70.0, 92.7 kHz) were simulated with the program of P. Degtyarenko. This program, based on GEANT 3.21 (Brun 1993), uses the GCALOR (Zeitnitz 1994) program package in order to simulate hadronic interactions down to 1 MeV for nucleons and charged pions and into the thermal region for neutrons, and uses DINREG (Degtyarenko 1992, 2000) – Deep Inelastic Nuclear Reaction Exclusive Generator with a model for hadronic interactions of electrons and photons. Values of r achieved in E93-038 are compared with the results of the simulation in Fig. 29. Using the single rates of neutral and charged particles in the front array of the polarimeter from the simulation with the program of P. Degtyarenko for E = 2.2, 4.4, 6.6, and 11.0 GeV (see Figs. 17, 18, 19, 20, respectively), we calculated fractions of electron-neutron coincidence events corrupted from background particles. We consider a "good" neutron scattering event to be "corrupted" if the background particle (charged or neutral) appears near to the "good" neutron hit (ΔY = ±25 cm) during a coincidence time window of 20 ns. For an 80 μA beam, 40-cm LD_2 target, and 15-cm Pb curtain, the corrupted fractions are calculated to be about 18, 26, 31, and 36% at Q^2 = 2.2, 4.0, 5.2, and 6.9 (GeV/c)^2 (see Fig. 21).

The projected uncertainties $\Delta g_n/g_n$ and ΔG_E^n are plotted in Fig. 22 as a function of the data acquisition time for a luminosity of 1.02 × 10^{39} cm^{-2}s^{-1}, which is achievable with a beam current of 80 μA on a 40-cm liquid deuterium target. The DAQ time that is designated by the dotted line in Fig. 22 was chosen to target an uncertainty [ΔG_E^n] in the vicinity of 0.0020.

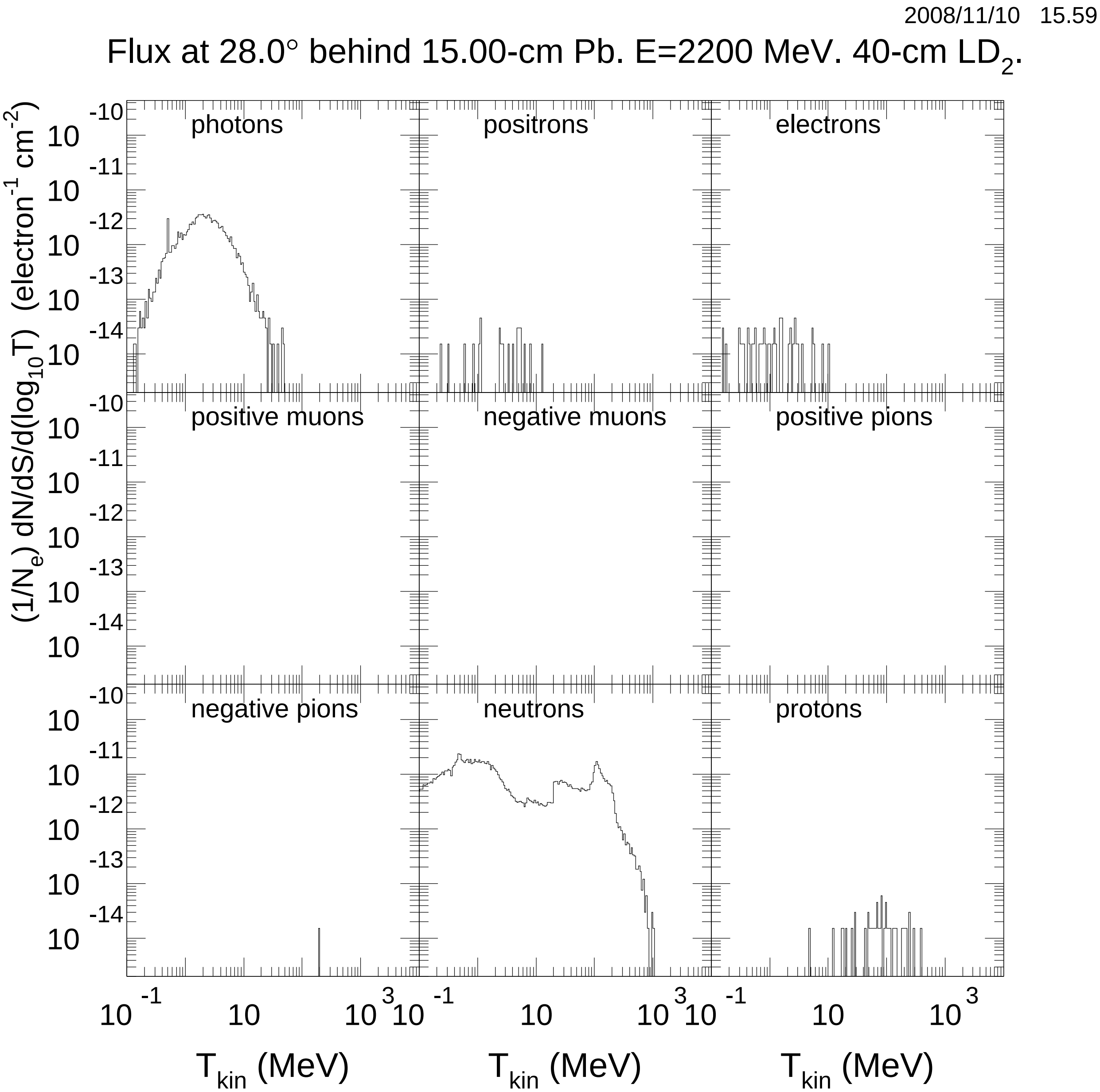

Figure 17: Simulated spectra of the particles at 28^o behind 15-cm Pb curtain from 2.2 GeV electron beam incident on a 40-cm LD_2 target.

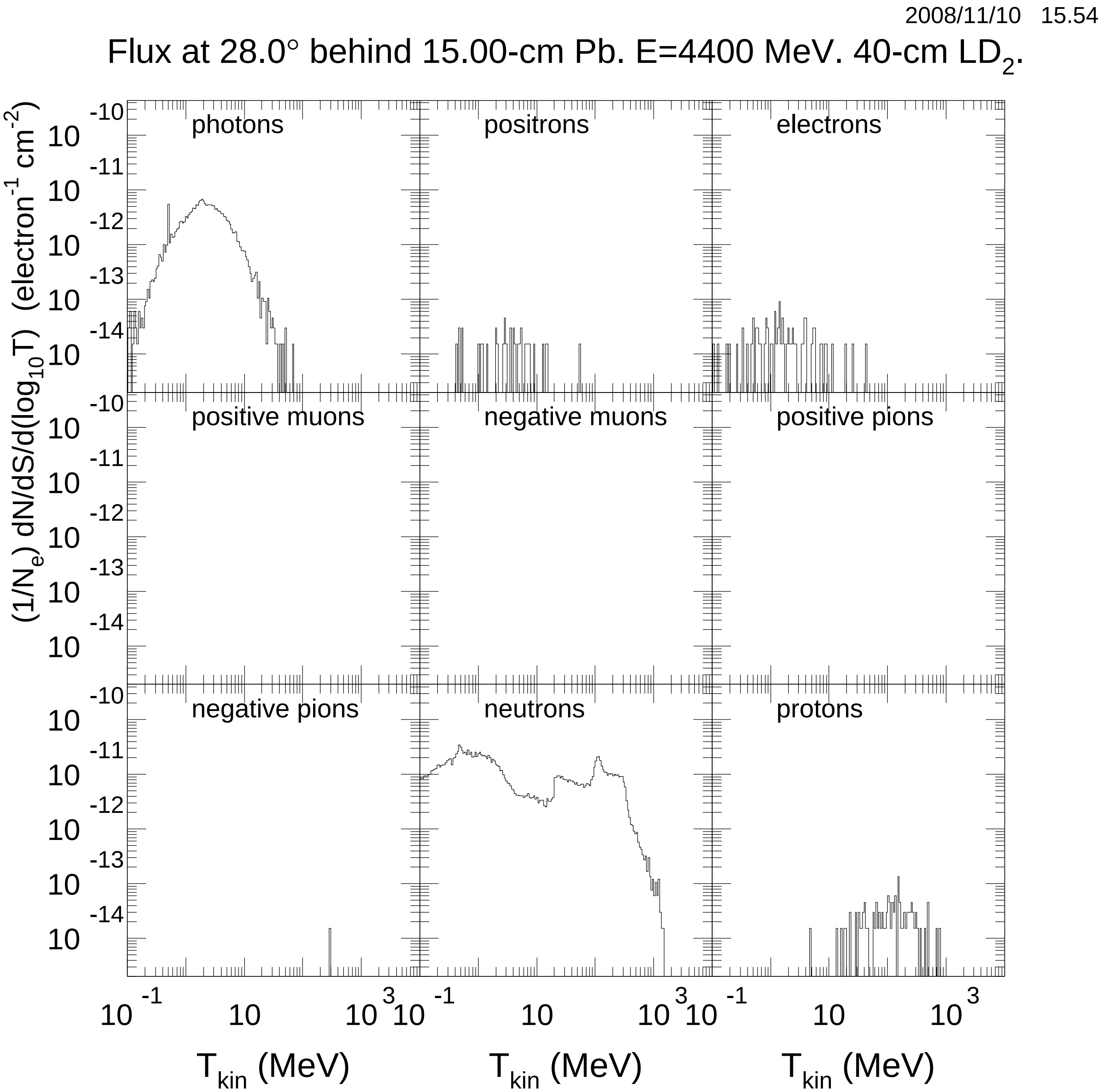

Figure 18: Simulated spectra of the particles at 28^o behind 15-cm Pb curtain from 4.4 GeV electron beam incident on a 40-cm LD_2 target.

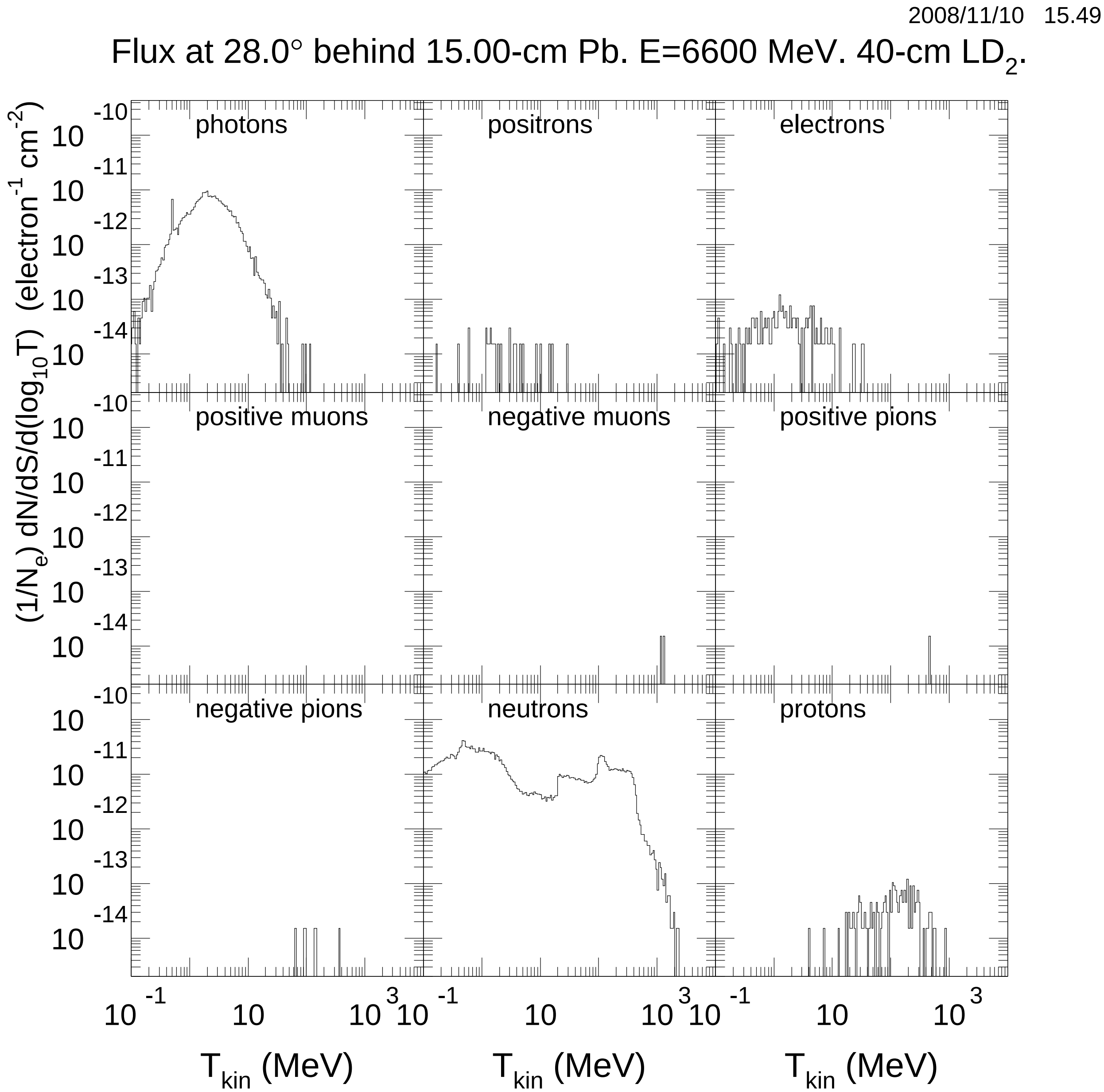

Figure 19: Simulated spectra of the particles at 28^o behind 15-cm Pb curtain from 6.6 GeV electron beam incident on a 40-cm LD_2 target.

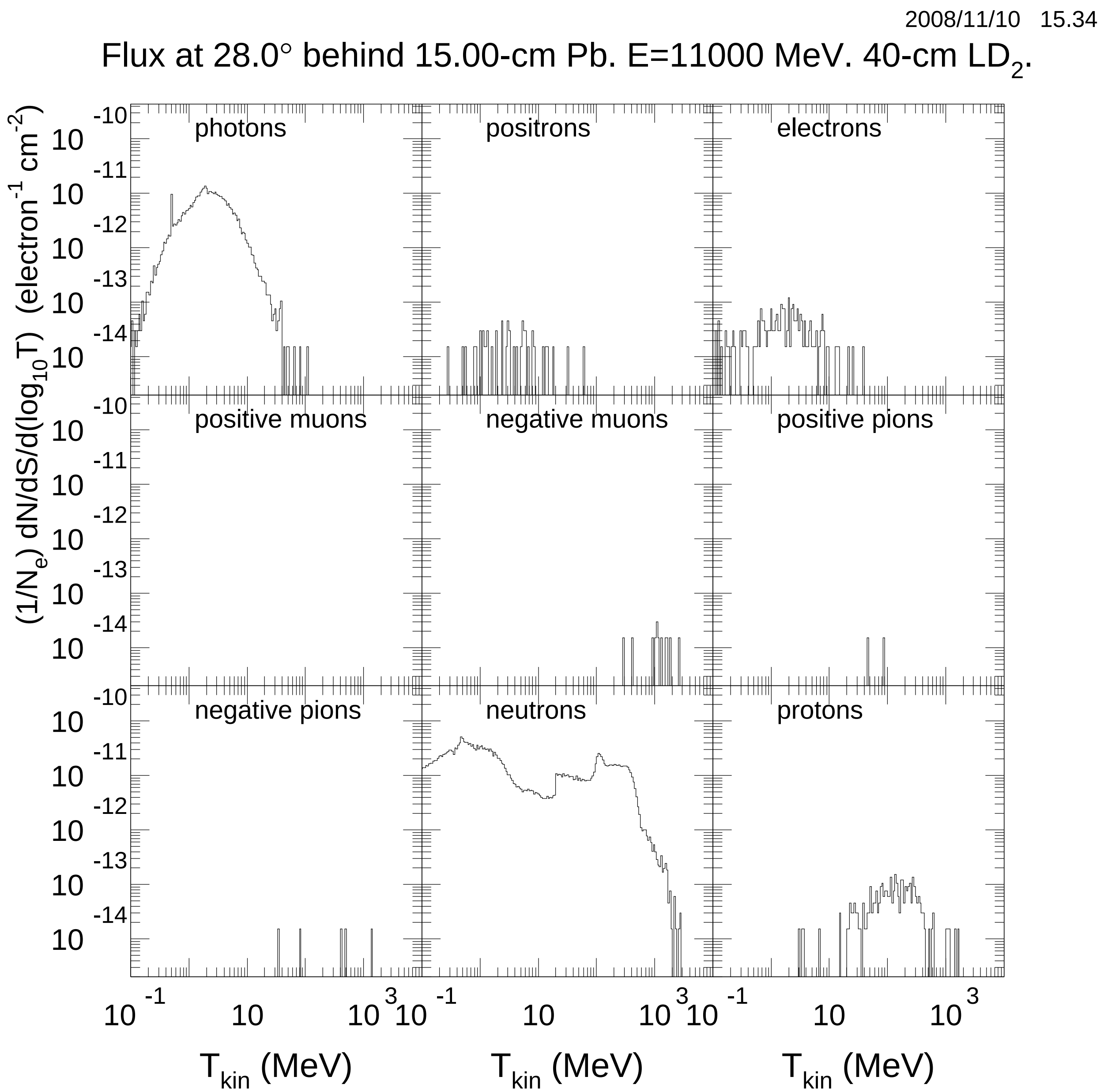

Figure 20: Simulated spectra of the particles at 28^o behind 15-cm Pb curtain from 11.0 GeV electron beam incident on a 40-cm LD_2 target.

Figure 24 shows the statistical uncertainties $\Delta g/g$, projected at $Q^2 = 2.2$, 4.0, 5.2, and 6.9 $(\mathrm{GeV/c})^2$ for the DAQ time of 120, 240, 260, and 720 hours (respectively) as a function of precession angle χ.

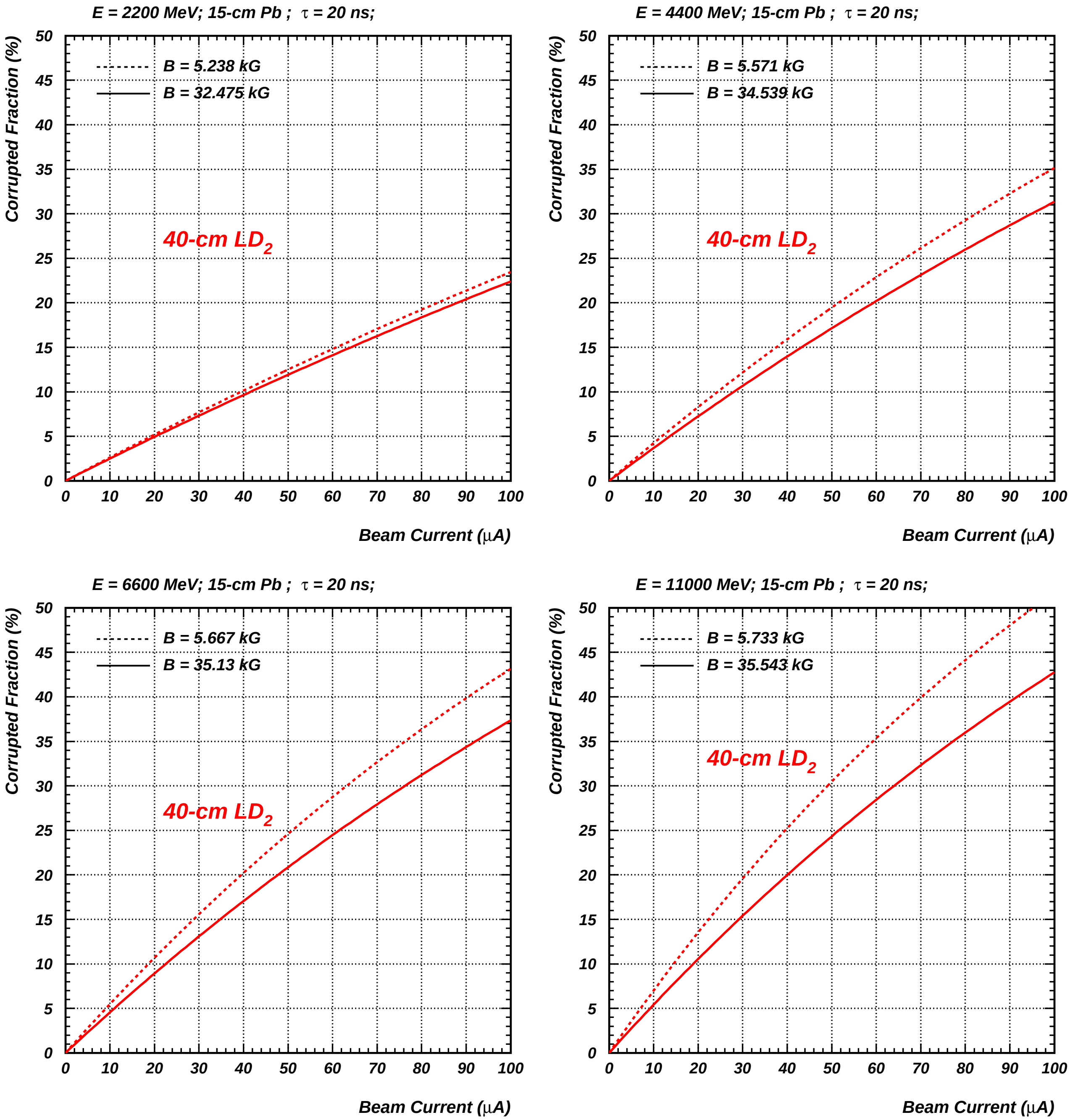

Figure 21: Calculated fraction of electron-neutron coincidence events corrupted from a background particle (charged or neutral) that appears during the coincidence time window of 20 ns as a function of the beam current. The thickness of the Pb curtain is 15 cm. Solid lines correspond to the dipole magnet field needed to precess a neutron polarization vector for 155 degrees (viz., chosen precession); dashed lines correspond to the precession of 25 degrees.

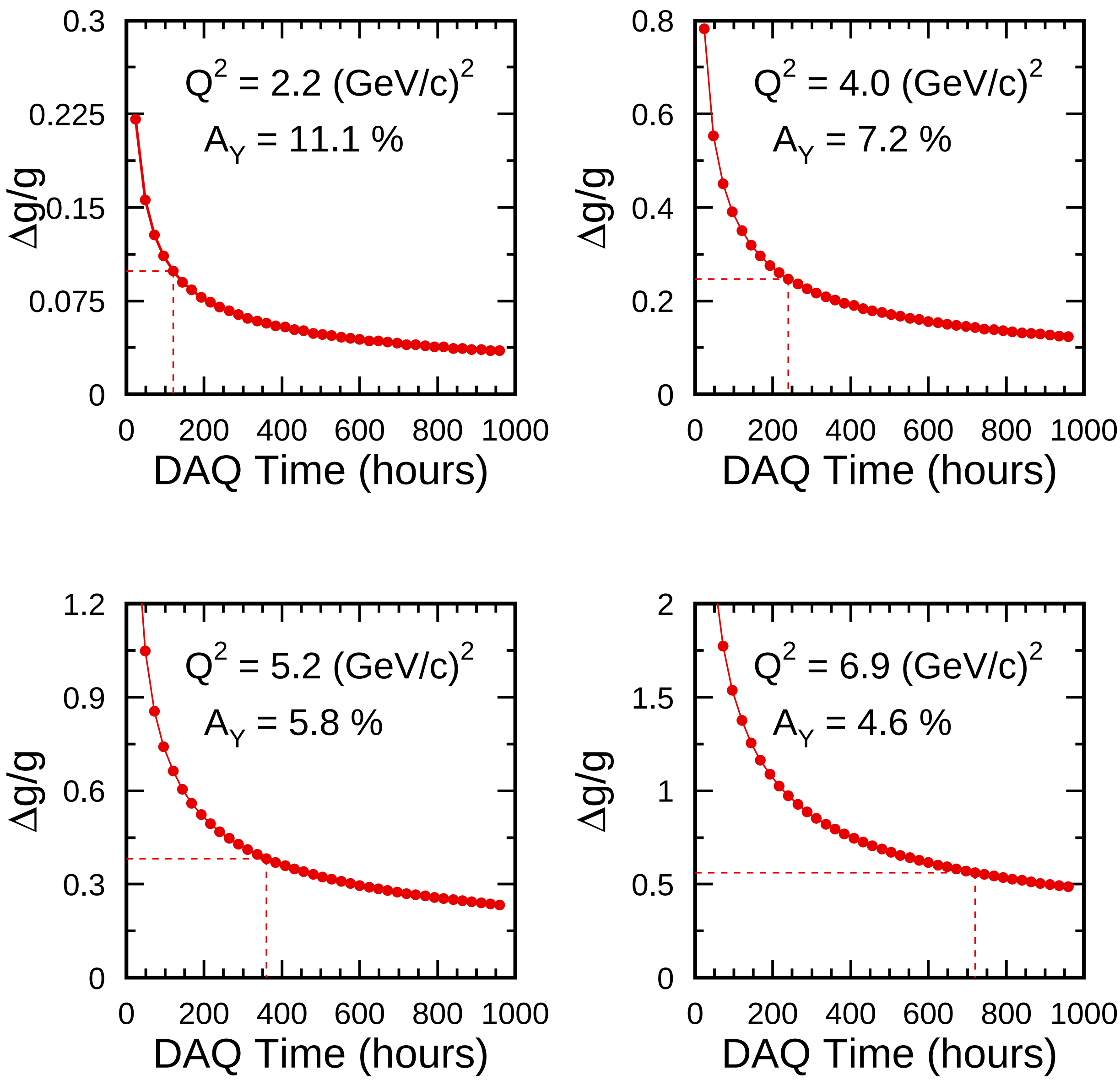

Figure 22: Projected uncertainties $\Delta g_n/g_n$ at Q^2 = 2.2, 4.0, 5.2, and 6.9 $(\mathrm{GeV/c})^2$ for a beam current of 80 μA as a function of the DAQ time in Hall C.

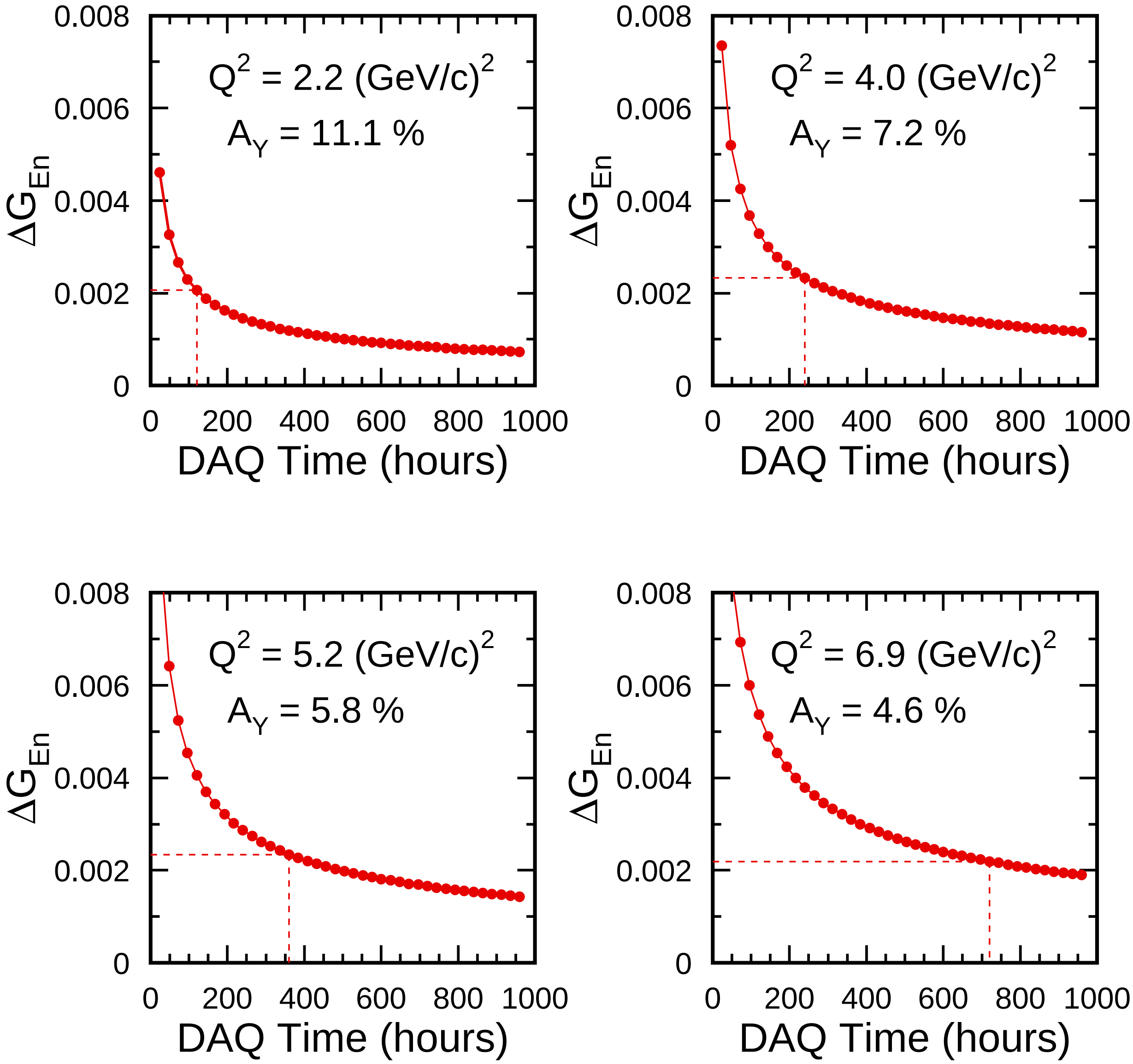

Figure 23: Projected uncertainties ΔG_E^n at $Q^2 = 2.2$, 4.0, 5.2, and 6.9 (GeV/c)^2 for a beam current of 80 μA as a function of the DAQ time in Hall C. Galster parameterization for G_E^n is assumed.

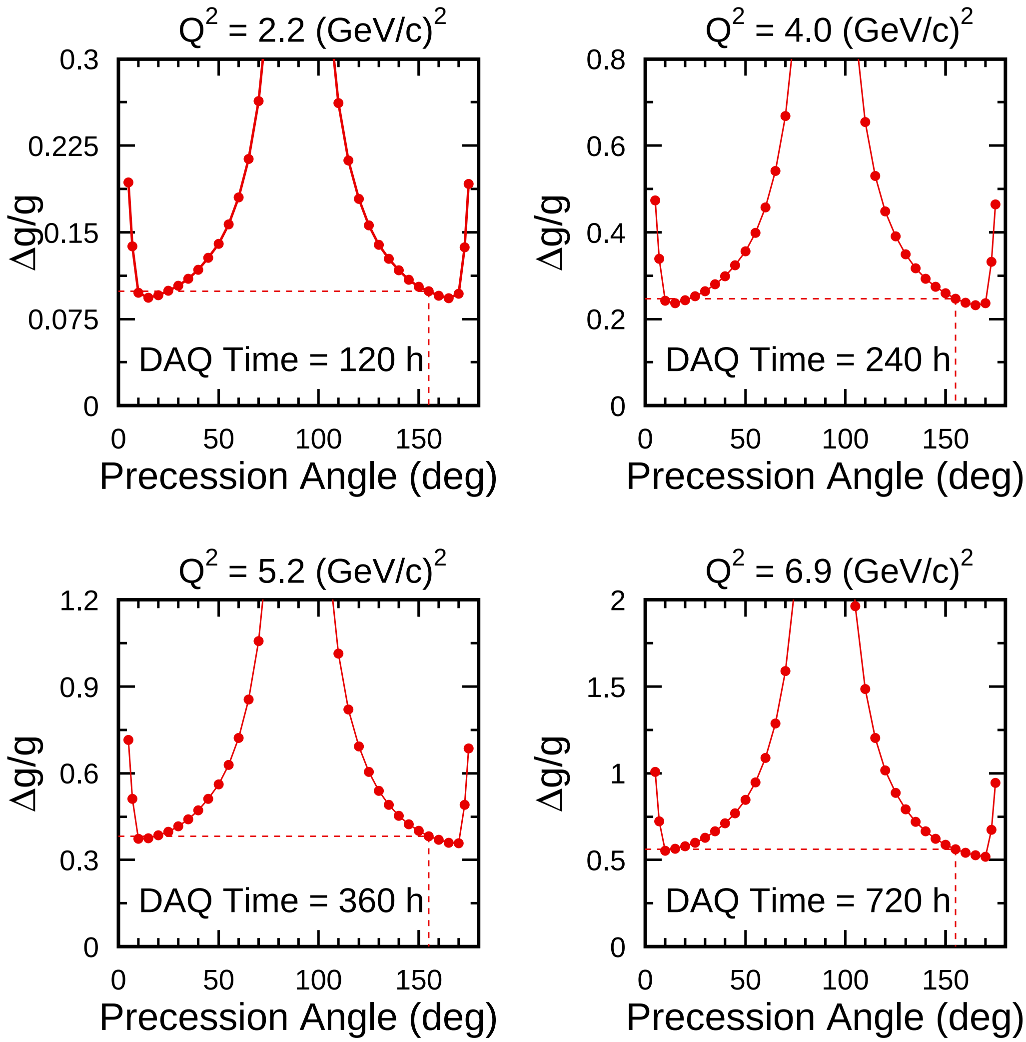

Figure 24: Statistical uncertainties $\Delta g/g$, projected at $Q^2 = 2.2$, 4.0, 5.2, and 4.3 (GeV/c)^2, as a function of precession angle χ.

5 Some Results from E93-038

The purpose of this section is to indicate the quality of the data obtained and the simulation made in E93-038. We selected real quasielastic $^2H(\vec{e}, e'\vec{n})$ events using a restricted HMS momentum bite, the cut on the missing momentum, and a cut on HMS-NPOL coincidence time (see Fig. 25).

Typical time-of-flight spectra for the highest Q^2 [viz., Q^2 = 1.45 (GeV/c)^2] are shown in Fig. 26. The left panel is an HMS-NPOL coincidence time-of-flight spectrum. We compared the measured time-of-flight, cTOF, with the time-of-flight calculated from electron kinematics and offsets determined by a calibration procedure; the result is centered on zero with a FWHM of approximately 1.5 ns, and the reals-to-accidentals ratio is $\approx$ 12 at a beam current of $\approx$ 50 μA [see Fig. 29]. The right panel is the time-of-flight spectrum between a neutron event in the front array and an event in the top or bottom rear array. We compared this measured time-of-flight, ΔTOF, with the time-of-flight calculated for elastic np scattering. This result, normalized to the nominal 2.5 m flight path, has a peak at zero also. The tail on the slow side is due to scattering from

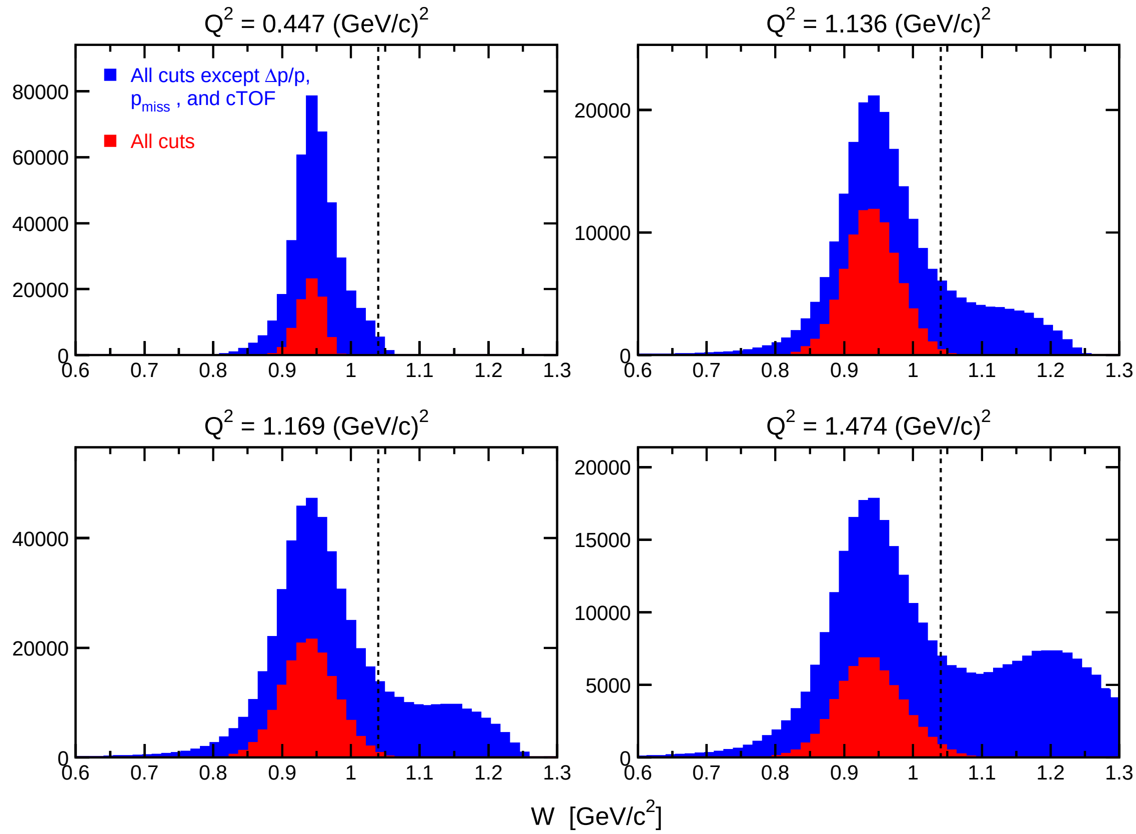

Figure 25: Invariant mass spectra before and after cuts on the scattered electron momentum, the missing momentum, and an HMS-NPOL coincidence time-of-flight.

carbon, and the secondary peak at ~ -2.5 ns is the result of π^0 production in the front array. To extract the physical scattering asymmetry, we calculated the cross ratio, r, which is defined to be the ratio of two geometric means, $(N_U^+ N_D^-)^{1/2}$ and $(N_U^- N_D^+)^{1/2}$, where $N_U^+(N_D^-)$ is the yield in the ΔTOF peak for neutrons scattered up(down) when the beam helicity was positive(negative); the yields, corrected for background, were obtained by peak fitting. The physical scattering asymmetry is then given by $(r-1)/(r+1)$. The merit of the cross ratio technique [Ohlsen (1973)] is that the neutron polarimeter results are independent of the luminosities for positive and negative helicities, and the efficiencies and acceptances of the top and bottom halves of the polarimeter. Beam charge asymmetries (of typically 0.1%) and detector threshold differences cancel in the cross ratio.

The result of an analysis of the asymmetries for each run at $Q^2 = 1.13$ (GeV/c)^2 and the error-bar weighted average for these data appear in Fig. 27; the sign of the asymmetries from runs with the $\lambda/2$-plate IN have been reversed. A histogram of the asymmetries (see Fig. 28) clearly demonstrates that the distribution of the asymmetries is of an appropriate Gaussian shape.

To estimate the reals-to-accidentals ratio r, we simulated the rate of inclusive electrons in the HMS with the MONQUEE code [Dytman (1987)], and we used single rates in NPOL simulated with the GEANT-based program of P. Degtyarenko (for details, see Section 4.4). Simulated accidental coincidence rates and r-values are shown in Fig. 29 together with ones measured in E93-038. The difference between the measured and calculated accidentals and the ratios of real-to-accidental coincidences at $Q^2 = 0.45$ (GeV/c)^2 is because the calculation doesn't take into account the larger radiation background in Hall C caused by multiple scattering of electrons at this lowest beam energy of 884 MeV.

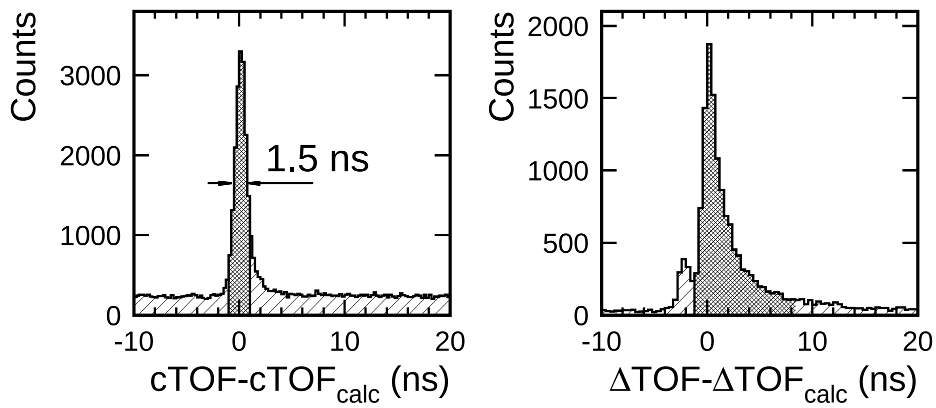

Figure 26: Typical time-of-flight spectra for $Q^2 = 1.45$ (GeV/c)^2. Selected portions are shaded.

We simulated the E93-038 neutron polarimeter efficiency, ϵ_n, (including the neutron transmission through the 10-cm lead curtain) using the FLUKA-2002 program, version 2.0 [Fasso et al. (2001)]. The "stand-alone" (not GEANT-based) FLUKA-2002 code is a general purpose Monte Carlo code for studying transport and interactions of particles in a material over a wide energy range. The program is best known for its hadron event generators; the used version of the code can also handle (with similar or better accuracy) muons, low-energy neutrons, and electromagnetic effects. Figure 30 (left panel) indicates good agreement of the results of the simulation with NPOL efficiencies extracted from the E93-038 data [Semenova et al. (2003)]. Both simulation and data analysis were made for the front (rear) array threshold of 8 (20) MeVee. Simulating the analyzing power (A_Y) for the E93-038 polarimeter, for elastic *n-p* and quasielastic scattering events in the front array, we determined (*in the rest frame of the target nucleon*) A_Y values from the partial-wave analysis embodied in the Scattering Analysis Interactive Dial-In (SAID) code [Arndt (1977, 2000)]. In our simplified approach, we supposed that $A_Y = 0$ for both inelastic reactions and multiple scattering events. Probably, this assumption leads to the disagreement between the simulated (and averaged over the NPOL acceptance) and the measured analyzing power at the low neutron energy of 239 MeV. Nevertheless, at higher neutron energies ($T_n = 608$ and 786 MeV), *the simulated and measured in E93-038 A_Y values are in very good agreement* (see right panel in Fig. 30).

The beam polarization measured in March 2001 is plotted in Fig. 31. The mean polarization during this two-weeks period was 82.2±0.1 (-81.0±0.2)% with the $\lambda/2$ wave plate "OUT" ("IN").

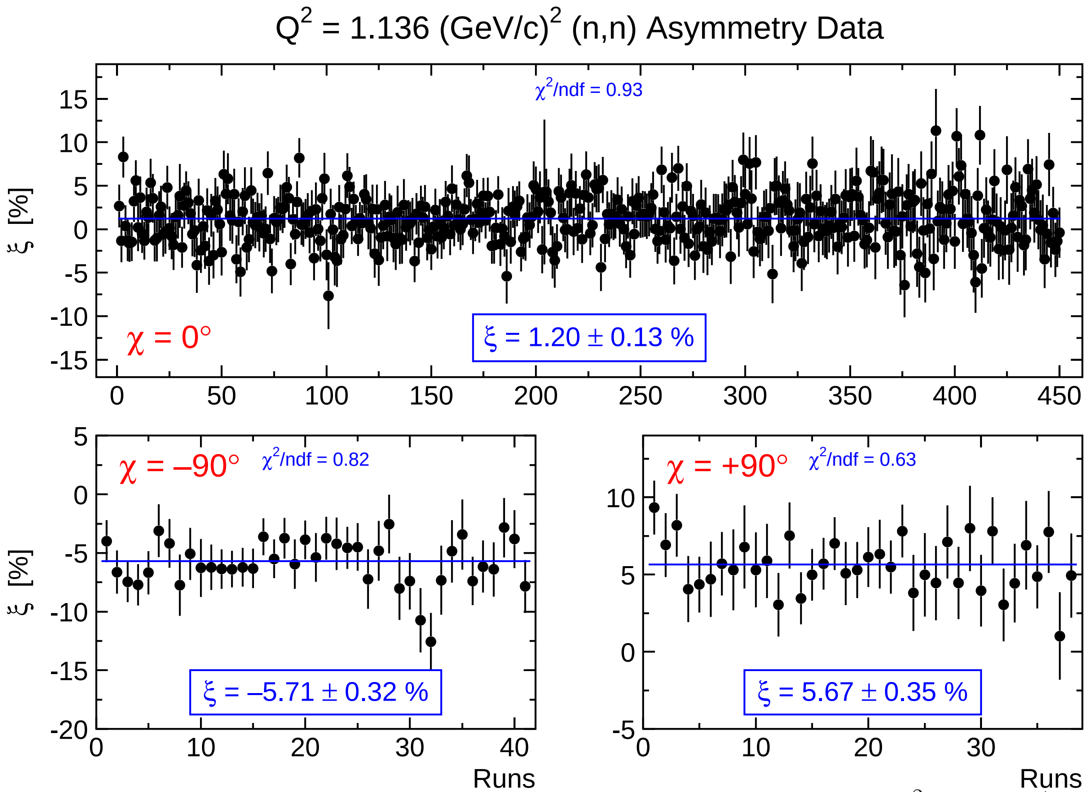

Figure 27: Asymmetries obtained from the analysis of E93-038 data at $Q^2 = 1.13$ (GeV/c)^2.

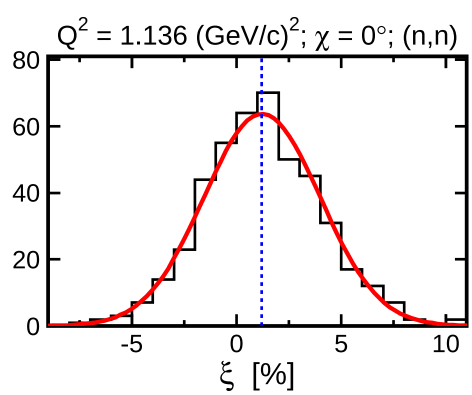

Figure 28: Histogram of E93-038 asymmetries at $Q^2 = 1.13$ (GeV/c)^2 ($\chi = 0^o$). The solid curve is a Gaussian fit, and the vertical dashed line is the mean value of the asymmetry from Fig. 27.

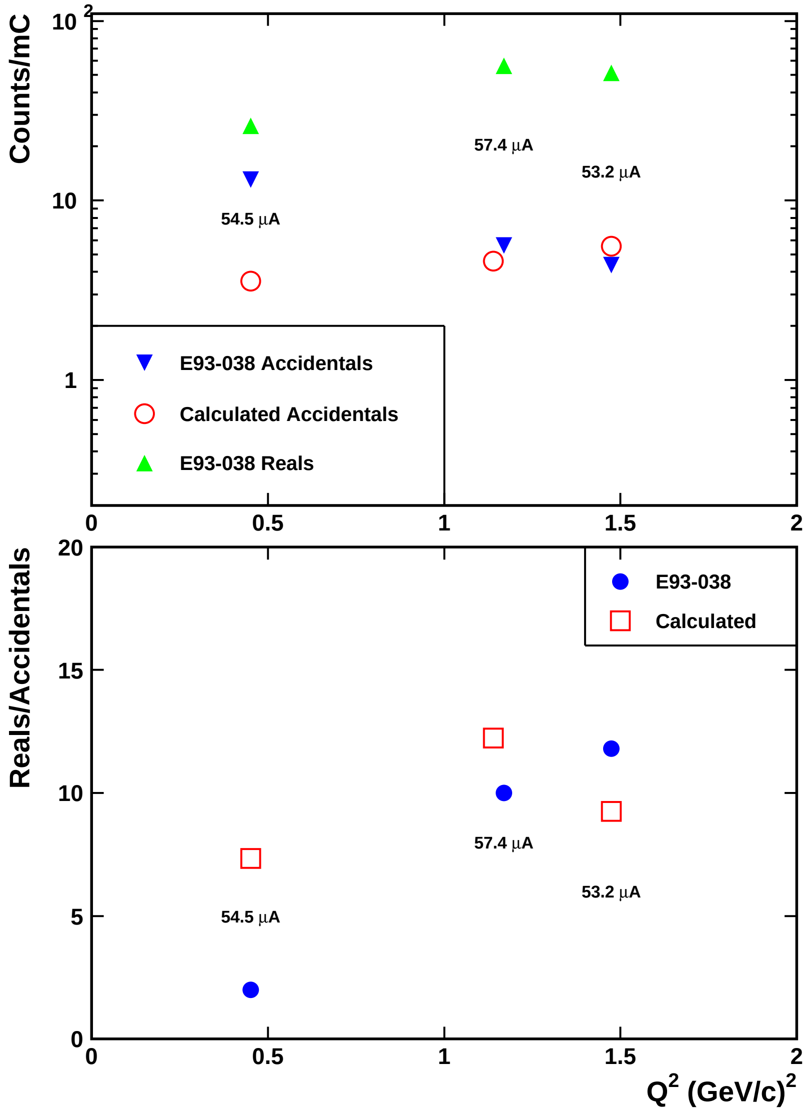

Figure 29: Real event rate, accidental coincidence rate, and the reals-to-accidentals ratio obtained from E93-038. The target-front array flight path was 7 m for NPOL at 46 degrees.

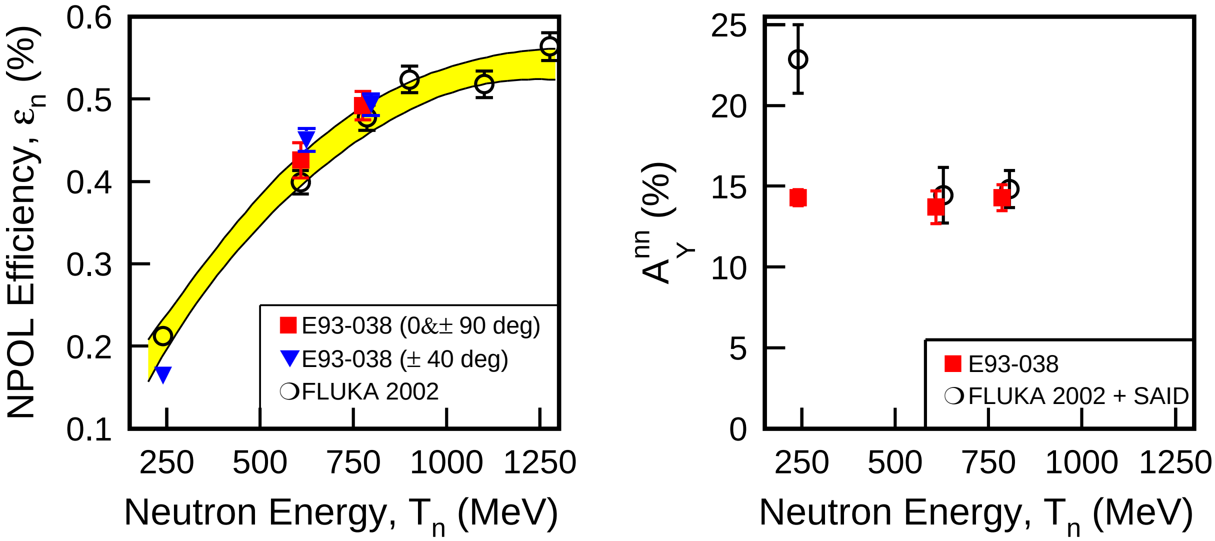

Figure 30: Comparison of the simulated neutron polarimeter parameters (viz., analyzing power, A_Y, and the neutron polarimeter efficiency, ϵ_n) with the results from E93-038. The shaded band in the left panel shows an uncertainty on the fit of the simulated efficiencies with a polynomial function.

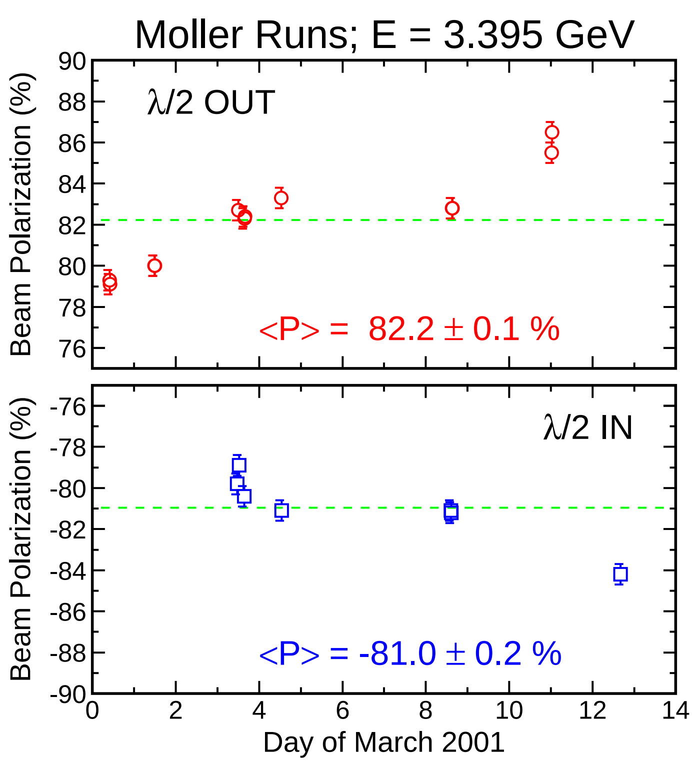

Figure 31: Electron beam polarization in March 2001.

6 Beam Time

Our beam-time request for measuring G_E^n at Q^2 = 2.2, 4.0, 5.2, and 6.9 (GeV/c)^2 is shown in Table 4. We estimate that a total data acquisition time of 66 days in Hall C will be needed to produce a statistical uncertainty ΔG_E^n in the vicinity of 0.002 at each of the Q^2 points. The projection was based on a calculation of the fraction of electron-neutron coincidence events corrupted from a background particle (charged or neutral) that appears during a coincidence time window of 20 ns. For an 80 μA beam, 40-cm LD_2 target, and 15-cm thickness of the Pb curtain, the corrupted fractions were about 18, 26, 31, and 36% at Q^2 = 2.2, 4.0, 5.2, 6.9 (GeV/c)^2, respectively (see Fig. 21). The estimated acquisition times for runs on a 15-cm LH_2 target will be needed to assess the false asymmetry or dilution from the two-step process d($\vec{e}$,e'$\vec{p}$)n + Pb($\vec{p}$,$\vec{n}$).

G_E^n physics measurements Q^2 [(GeV/c)^2]	2.2	4.0	5.2	6.9	Total
LD_2 target	5	10	15	30	60
LH_2 target	0.5	0.5	0.5	0.5	2
Dummy target	0.1	0.1	0.1	0.2	0.5
Beam polarization	0.2	0.3	0.5	1	2
Time calibrations [LD_2 target]	0.1	0.1	0.1	0.2	0.5
Overhead	0.1	0.1	0.3	0.5[(a)]	1
Total physics measurements	6	11.1	16.5	32.4	66

Table 4: Beam-time [days] for measuring G_E^n at Q^2 = 2.2, 4.0, 5.2, and 6.9 (GeV/c)^2 for an 80 μA, 80% polarized beam on a 40-cm LD_2 target.

(a) 40 changes in dipole current, 9 target changes, starting and stopping the DAQ system for runs that are typically 5 hours long.

Also needed will be seven days of commissioning time with beam to check out the spectrometer, the Moeller polarimeter, and the neutron polarimeter [NPOL] and electronics. NPOL checkout includes checking all detectors and detector thresholds, adjusting timing, adjusting the thickness of the Pb curtain and determining the optimal beam current, and checking room background with a shadow shield. Seven days will be required without beam for pulse-height calibrations and cosmic ray tests of the polarimeter detectors.

7 Collaboration

Most of the participants listed earlier contributed to the success of E93-038. The collaboration is a strong, experienced, and large team (currently about 100 scientists from 31 institutions). Graduate students and postdocs will be added after the proposed experiment is approved and scheduled. As in E93-038, Kent State University (KSU) will be responsible for the neutron polarimeter; MIT, for the neutron spin-precession dipole magnet; and JLab for the magnetic spectrometer [SHMS]. KSU provided the neutron detectors in the rear array and the polarimeter electronics; Hampton University provided ten of the neutron detectors in the front array, while JLab provided another ten. The University of Virginia provided the tagger detectors used in E93-038. Duke University took responsibility for the Analysis Engine and also for setting up the electronics and timing. Professor Bradley Plaster at the University of Kentucky will be responsible for modification of analysis programs and upgrading the simulation programs used in E93-038. Plaster is the lead author on the archival paper on E93-038 [Phys.Rev.C73, 025205 (2006)]. Dr. A.Yu. Semenov (University of Regina) functioned as the coordinator of the E93-038 analysis effort. T. Reichelt (Bonn), H. Fenker (JLab), and S. Danagoulian (NCAT) were the lead scientists in establishing the operating conditions for running the Moeller polarimeter at a beam energy below one GeV, and in setting up and running the Moeller polarimeter at the two higher energies. Professor Stanley Kowalski has reaffirmed his commitment to oversee that the Bates engineering lab will modify dipole magnet and he will be responsible for the field mapping.

8 Equipment Needs for Enhanced Polarimeter

Equipment needs and estimated costs for the enhanced polarimeter are shown in Table 5. The front array consists of five layers with 12 scintillators in each layer. The scintillators in the first three layers are 10 cm×10 cm×100 cm; those in the last layers are 10 cm×12.5 cm×100 cm with the 12.5 cm dimension in the direction of the central neutron momentum.

With respect to the rear array, we are planning to replace the 12 [20-in×40-in×4-in] detectors in the rear array with 24 [10-in×40-in×4-in] detectors. This is accomplished by using 8 existing 10 in wide detectors plus cutting 9 20-in wide detectors in half, machining new light pipes, and re-assembling them as 10-in wide detectors. At this time, the 9 detectors plus new light pipes have all been cut, machined, and polished and the detectors are being assembled. These detectors are expected to be all assembled by Spring 2009. With respect to the front array, a price quote from Saint-Gobain for scintillators with machined and polished light pipes on each end is $1400 for each 10 cm×10 cm×100 cm detector; the total cost for 6 such detectors would be $8,400. KSU will assemble and test the detectors. For the front array, we estimate the need for 20 replacement PMT's [Hamamatsu R1828-01, 2-in diam] for those worn out in the front three layers; 12 new PMT's for the 6 new 10-cm×10-cm×100-cm scintillators; and another 56 of these 2-in diam PMT's for the front vetos. For the rear arrays, we need 40 more [Hamamatsu, 2-in diam] PMTs for the 20 veto detectors. The total number of 2-in diam PMT's needed is 128 at a cost of $128,000. For the rear arrays, we need a total of 44 (Hamamatsu, 5-in diam) PMT's at a cost of $84,000; the 44 consists of 24 for the 10 new 10-in×40-in×4-in scintillators and 20 replacements for worn out PMT's. We need a total of 112 magnetic shields for 2-in diam PMT's, which we plan to borrow and buy a total of 24 magnetic shields for 5-in diam PMT's at a cost of $6,000. New electronics needs for the enhanced polarimeter include 6 quad constant fraction discriminators at a cost of $18,000, 36 (400 ns) delay lines, an additional control box, and 152 PMT bases and preamps for the front array; 40 additional PMT bases and preamps for the rear veto detectors; and 24 PMT bases and preamps for the 12 new 10-in wide detectors in the rear array. We are requesting JLab to provide the quad constant-fraction discriminators, and the delay lines; KSU would provide the preamps, the control box, and the PMT bases. The quad constant fraction (CFD's) will be provided by existing KSU units, borrowing units from Tel Aviv and MSU, and purchasing 6 new units. In the enhanced polarimeter, we plan to use multi-hit TDC's, which we understand are available now at JLab.

Equipment items that need to be purchased are summarized in Table 5. Funds will be sought from DOE and NSF by the participating institutions. B. Plaster at the University of Kentucky has made a commitment to seek funds for the front veto detectors, and M. Elaasar (Southern University at New Orleans) has made a commitment to seek funds for the rear veto detectors.

The University of Regina and Argonne National Lab. groups can seek funds also because there may not be enough from the other two or one or both may not succeed.

		Cost
1.	**Front Array**	
1.1	6 [10 cm × 10 cm × 100 cm] Scintillator & Light Pipes	$8,400
1.2	28 [1 cm × 10 cm × 106 cm] Veto Scintillator & Light Pipes	$27,000
1.3	88 Photomultiplies Tubes (2-in diam)	$88,000
1.4	72 Magnetic Shields (for 2-in diam PMT) [Borrow]	0
1.5	68 Additional Preamplifiers [To be provided by KSU]	0
	Subtotal Front Array	**$123,400**
2.	**Rear Array**	
2.1	20 [1 cm × 25 cm × 106 cm] Veto Scintillator & Adiabatic Light Pipes	$40,000
2.2	44 Photomultiplier Tubes (5-in diam)	$110,000
2.3	40 Photomultiplier Tubes (2-in diam)	$40,000
2.4	24 Magnetic Shields (for 5-in diam PMT)	$6,000
2.5	40 Magnetic Shields (for 2-in diam PMT) [Borrow]	0
2.6	40 Preamplifiers [to be provided by KSU]	0
	Subtotal Rear Array	**$196,000**
3.	**Electronic Modules**	
3.1	6 Quad Discriminators [to be provided by JLab]	$18,000
	Subtotal Electronic Modules	**$18,000**
	Total	**$337,400**

Table 5: NPOL equipment items to be purchased.

References

[Alexandrou 2006] C. Alexandrou, G. Koutsou, J.W. Negele, and A. Tsapalis, Phys. Rev. **D74**, 034508 (2006).

[Arenhoevel 1987] H. Arenhoevel, Phys. Lett. **B199**, 13 (1987).

[Arenhoevel 1988] H. Arenhoevel *et al.*, Z. Phys. **A331**, 123 (1988).

[Arenhoevel 2002] H. Arenhoevel, private communication (2002).

[Arndt 1977] R.A. Arndt, R.H. Hackman, and L.D. Roper, Phys. Rev. **C15** 1002 (1977).

[Arndt 2000] R. A. Arndt, L. D. Roper *et al.*, Scattering Analysis Interactive Dial-In (SAID) Program. Virginia Polytechnic Institute and State University, Unpublished. The Virginia Tech Partial-Wave Analysis Facility is still available from the original web site *http://said.phys.vt.edu/*. This facility is available on-line at *http://www.gwdac.phys.gwu.edu/* from the CNS Data Analysis Center at The George Washington University.

[Arrington 2007] J. Arrington and I. Sick, Phys. Rev. **C76**, 035201 (2007).

[Azhgirei 2005] L.S. Azhgirei et al., Nucl. Instrum. Meth. **A538**, 431 (2005).

[Aznaurian 1993] I.G. Aznaurian, Phys. Lett. **B316**, 391 (1993).

[Beck 1992] G. Beck and H. Arenhoevel, Few Body Systems **13**, 165 (1992).

[Bermuth 2003] J. Bermuth et al., Phys. Lett. **B564**, 199 (2003) updates D. Rohe *et al.*, Phys. Rev. Lett. **83**, 4257 (1999).

[Bijker 2004] R. Bijker and F. Iachello, nucl-th/0405026, accepted for publication in Phys. Rev. C (2004).

[Bodek 2008] A. Bodek et al., Eur. Phys. J. C **53**, 349 (2008).

[Boffi 2002] S. Boffi, L. Ya. Glozman, W. Klink, W. Plessas, M. Radici, and R. F. Wagenbrunn, Eur. Phys. J. A **14**, 17 (2002); W. Plessas, S. Boffi, L. Ya. Glozman, W. Klink, M. Radici, and R. F. Wagenbrunn, Nucl. Phys. A **699**, 312c (2002); R. F. Wagenbrunn, S. Boffi, W. Klink, W. Plessas, and M. Radici, Phys. Lett. B **511**, 33 (2001).

[Brun 1993] R. Brun et al. *GEANT Detector Description and Simulation Tool.* CERN Program Library Long Writeup W5013, September, 1993.

[Cardarelli 2000] F. Cardarelli, S. Simula, Phys. Rev. **C62**, 065201 (2000); S. Simula (private communication).

[Cecil 1979] R. Cecil, B.D. Anderson, R. Madey. Nucl. Instrum. Meth. **161**, 439 (1979).

[Chung 1991] P.L. Chung and F. Coester, Phys. Rev. **D44**, 229 (1991).

[Cloet 2008] I.C. Cloet et al., arXiv:nucl-th/0812.0416 (2008).

[Degtyarenko 1992] P.V. Degtyarenko, M.V. Kossov. *Monte Carlo Program for Nuclear Fragmentation*. Preprint ITEF 11-92, Moskow (1992).

[Degtyarenko 2000] P.V. Degtyarenko, M.V. Kossov, and H.-P. Wellisch. *Chiral invariant phase space event generator*. Eur. Phys. J. A **8**, 217-222 (2000); A **9**, 411-420 (2000); A **9**, 421-424 (2000).

[Dong 1998] S.J. Dong, K.F. Liu, and A.G. Williams, Phys. Rev. **D58**, 074504 (1998).

[Drechsel 1989] D. Drechsel and M.M. Giannini, Rep. Prog. Phys. **52**, 1083 (1989).

[Dytman 1987] S. Dytman, private communication (1987).

[Eden 1994] T. Eden *et al.*, Phys. Rev. **C50**, R1749 (1994).

[Edwards 2006] R.G. Edwards *et al.*, Phys. Lett. **96**, 052001 (2006).

[Fasso 2001] A. Fasso, A. Ferrari, P.R. Sala, Electron-Photon Transport in FLUKA: Status, Proceedings of the Monte Carlo 2000 Conference, Lisbon, October 23-26, 2000, A. Kling, F. Barao, M. Nakagawa, L. Tavora, P. Vaz eds., Springer-Verlag Berlin, pp. 159-164 (2001).

[Fasso 2001a] A. Fasso, A. Ferrari, J. Ranft, P.R. Sala, FLUKA: Status and Perspective for Hadronic Applications, Proceedings of the Monte Carlo 2000 Conference, Lisbon, October 23-26, 2000, A. Kling, F. Barao, M. Nakagawa, L. Tavora, P. Vaz eds., Springer-Verlag Berlin, pp. 955-960 (2001).

[Feshbach 1967] H. Feshbach and E. Lomon, Rev. Mod. Phys. **39**, 611 (1967).

[Frank 1996] M.R. Frank, B.K. Jennings, and G.A. Miller, Phys. Rev. **C54**, 920 (1996).

[Friar 1990] J.L. Friar, Phys. Rev. **C42**, 2310 (1990).

[Gari 1985] M.F. Gari and W. Krumpelmann, Z. Phys. **A322**, 689 (1985).

[Gari 1992] M.F. Gari and W. Krumpelmann, Phys. Lett. **B274**, 159 (1992).

[Galster 1971] S. Galster, H. Klein, J. Moritz, K.H. Schmidt, D. Wegener, and J. Bleckwenn, Nucl. Phys. **B32**, 221 (1971).

[Gayou 2002] O. Gayou *et al.*, Phys. Rev. Lett. **88**, 092301 (2002).

[Glazier 2005] D.I. Glazier *et al.*, Eur. Phys. J. **A24**, 101 (2005).

[Golack 2001] J. Golak, G. Ziemer, H. Kamada, H. Witala, and W. Glöckle, Phys. Rev. C **63**, 034006 (2001) applies FSI corrections to J. Becker *et al.*, Eur. Phys. J. A **6**, 329 (1999).

[Hagler 2007] Ph. Hagler *et al.*, arXiv:0705.4295 [hep-lat] (2007).

[Herberg 1999] C. Herberg *et al.*, Eur. Phys. J. **A5**, 131 (1999) applies FSI corrections to M. Ostrick *et al.*, Phys. Rev. Lett. **83**, 276 (1999).

[Holzwarth 2002] G. Holzwarth, hep-ph/020138; Z. Phys. **A356**, 339 (1996).

[Iachello 1973] F. Iachello, A.D. Jackson, and A. Lande, Phys. Lett. **43B**, 191 (1973).

[Iachello 2003] F. Iachello, Proceedings of 4th Int. Conference on Perspectives in Hadronic Physics, Trieste, Italy (2003). To be published in Eur. Phys. J.

[Isgur 1998] N. Isgur, Phys. Rev. Lett. **83**, 272 (1999).

[Isgur 2000] N. Isgur and J.W. Negele, Nuclear Theory with Lattice QCD, a proposal to DOE, PI's (2000).

[Ji 1991] X. Ji, Phys. Lett. **B254**, 456 (1991).

[Jones 2000] M. Jones *et al.*, Phys. Rev. Lett. **84**, 1398 (2000).

[Kaskulov (2003)] M.M. Kaskulov and P. Grabmayr, Phys. Rev. C **67**, 042201(R) (2003); nucl-th/0308105; M.M. Kaskulov (private communication).

[Kelly 2000] J.J. Kelly, GENGEN: Event Generator for Gen Using the d(e,e'n)p Reaction, JLab E93-038 internal report (2000),
URL: *http://www.jlab.org/ semenov/reports/gengen2.5.ps*

[Kelly 2001a] J.J. Kelly, Time Calibration Procedures for E93-038 Polarimeter: Version 2.2, JLab E93-038 internal report (2001),
URL: *http://www.physics.umd.edu/enp/e93038/time_calibration.ps*

[Kelly 2003] J.J. Kelly, private communication (2003).

[Klein 1997a] F. Klein and H. Schmieden, Nucl. Phys. **A623**, 323c (1997).

[Klein 1997b] F. Klein, Proc. of the 14th Int. Conf. on Particles and Nuclei, ed. by C.E. Carlson and J.J. Domingo, World Scientific 1997, p.121.

[Kopecky 1997] S. Kopecky *et al.*, Phys. Rev. C **56**, 2229 (1997); Phys. Rev. Lett. **74**, 2427 (1995).

[Kroll 1992] P. Kroll, M. Schurmann, and W. Schweiger, Z. Phys. **A342**, 429 (1992).

[Laget 1990] J.M. Laget, Phys. Lett. **B273**, 367 (1990).

[Liu 2001] K.F. Liu, Private Communication (2001).

[Lomon 2002] E. L. Lomon, Phys. Rev. C **66**, 045501 (2002); Phys. Rev. C **64**, 035204 (2001).

[Lu 1998] D.H. Lu, A.W. Thomas, and A.G. Williams, Phys. Rev. **C57**, 2628 (1998).

[Lung 1993] A. Lung *et al.*, Phys. Rev. Lett. **70**, 718 (1993).

[Ma 2002] B.-Q. Ma, D. Qing, and I. Schmidt, Phys. Rev. C **65**, 035205 (2002).

[Madey 1995] R. Madey, A. Lai, and T. Eden, Polarization Phenomena in Nuclear Physics, edited by E.J. Stephenson S.E. Vigdor, AIP Proceedings No. 339, 47-54 (1995).

[Madey 2003] R. Madey *et al.*, Phys. Rev. Lett. **91**, 122002 (2003).

[Mergell 1996] P. Mergell, U.G. Meissner, D. Drechsel , Nucl. Phys. **A596**, 367 (1996).

[Meyerhoff 1994] M. Meyerhoff *et al.*, Phys. Lett. **B327**, 201 (1994).

[Milbrath 1998] B. D. Milbrath *et al.*, Phys. Rev. Lett. **80**, 452 (1998); Phys. Rev. Lett. **82**, 2221(E) (1999).

[Miller 2002] G. A. Miller, Phys. Rev. C **66**, 032201(R) (2002); nucl-th/0206027; G. A. Miller and M. R. Frank, Phys. Rev. C **65**, 065205 (2002); M. R. Frank, B. K. Jennings, and G. A. Miller, Phys. Rev. C **54**, 920 (1996); G. A. Miller, private communication (2003).

[Mosconi 1991] B. Mosconi, J. Pauchenwein, and P. Ricci, Proceedings of the XIII European Conference on Few-Body Problems in Physics, Marciana Marina (Elba), Italy (September 1991).

[Ohlsen 1973] G.G. Ohlsen and P.W. Keaton, Jr., Nucl. Instr. Meth. **109**, 41 (1973).

[Pace 2000] E. Pace, G. Salme, F. Cardarelli, and S. Simula, Nucl. Phys. **A666**, 33 (2000).

[Passchier 1999] I. Passchier *et al.*, Phys. Rev. Lett. **82**, 4988 (1999).

[Plaster 2006] B. Plaster *et al.* , Phys. Rev. **C73**, 025205 (2006).

[Platchkov 1990] S. Platchkov *et al.*, Nucl. Phys. **A508**, 343c (1990).

[Pospischil 2001] Th. Pospischil *et al.*, Eur. Phys. J. A **12**, 125 (2001).

[Radyushkin 1984] A.V. Radyushkin, Acta Phys. Polon. **B15**, 403 (1984).

[Rekalo 1989] M.P. Rekalo, G.I. Gakh, and A.P. Rekalo, J. Phys. **G15**, 1223 (1989).

[Rock 1992] S. Rock *et al.*, Phys. Rev. D **46**, 24 (1992).

[De Sanctis 2000] M. De Sanctis, M.M. Giannini, L. Repetto, and E. Santopinto, Phys. Rev. **C62**, 025208 (2000).

[Schiavilla 2001] R. Schiavilla and I. Sick, Phys. Rev. **C64**, 041002 (2001).

[Schmieden 1996] H. Schmieden, Proc. of the 12th Int. Symposium on High-Energy Spin Physics, Amsterdam (1996), ed. by C.W. de Jager et al., World Scientific 1997, p.538.

[Semenova 2002] I.A. Semenova, R. Madey, and A.Yu. Semenov, Gain in Figure-of-Merit of the E93-038 Neutron Polarimeter with Passive Converters, JLab E93-038 internal report (2002),
URL: *http://www.jlab.org/∼semenov/reports/irina-effConv.ps*

[Semenova 2003] I.A. Semenova, A.Yu. Semenov, and R. Madey, Simulation of the Efficiency of the E93-038 Neutron Polarimeter with the FLUKA code, JLab E93-038 internal report (2003).

[Ulmer 1991] P.E. Ulmer, MCEEP – Monte Carlo for Electro-Nuclear Coincidence Experiments, CEBAF–TN–91–101 (1991).

[Warren 2004] G. Warren *et al.*, Phys. Rev. Lett. **92**, 042301 (2004).

[Zeitnitz 1994] C. Zeitnitz and T.A. Gabriel, Nucl. Instrum. Meth. **A349**, 106 (1994).

[Zhu 2001] H. Zhu *et al.*, Phys. Rev. Lett. **87**, 081801 (2001).

Appendix A: Suppression of Inelastic Events

1 Results from E93-038

Extraction of a reliable result for G_E^n from the quasielastic $d(\vec{e}, e'\vec{n})p$ reaction requires the suppression of inelastic events associated with pion production. To illustrate, correlation plots of the missing momentum, $p_{\rm miss}$, plotted versus the invariant mass, W, are shown for the E93-038 acceptance of the two highest Q^2 points: 1.136 and 1.474 (GeV/c)^2. As can clearly be seen there, quasielastic events were associated with missing momenta in the range < 150 MeV/c. Larger values of $p_{\rm miss}$ were, of course, seen to correspond to inelastic events, with the $\Delta(1232)$ resonance prominent at large missing momenta in the $Q^2 = 1.474$ (GeV/c)^2 spectrum.

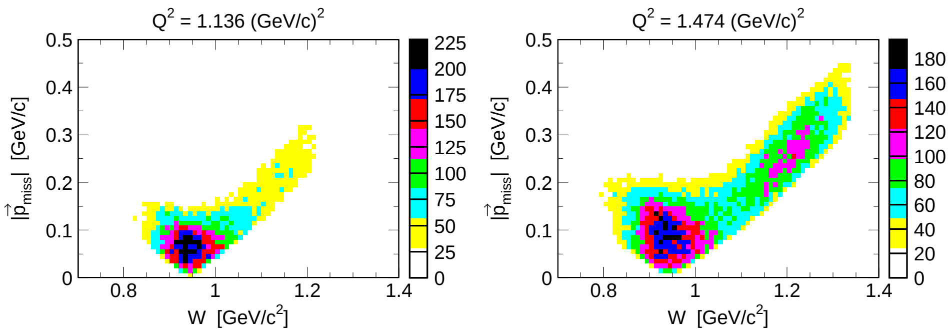

Figure 32: Correlation plot of $p_{\rm miss}$ versus W for the E93-038 acceptance at $Q^2 = 1.136$ and 1.474 (GeV/c)^2.

In E93-038, these inelastic events were suppressed with tight cuts on $\Delta p/p$ ($-3/+5\%$), $p_{\rm miss}$ (< 100 MeV/c), and cTOF ($\in [-1, 1]$ ns). As evidence these cuts suppressed inelastic events, invariant mass spectra obtained before and after these cuts are shown in Fig. 33 for these two Q^2 points. It is quite clear that after all cuts, the distributions converged to fairly narrow peaks centered on the neutron mass.

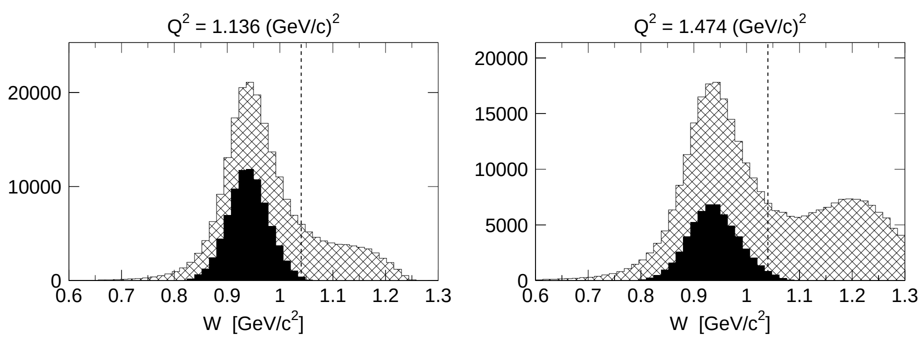

Figure 33: Distributions from E93-038 of the invariant mass W before (cross-hatched) and after (solid) all cuts except for those on $\Delta p/p$, $p_{\rm miss}$, and cTOF at $Q^2 = 1.136$ and 1.474 (GeV/c)^2. The vertical dashed lines denote the final E93-038 $W < 1.04$ GeV/c^2 cut.

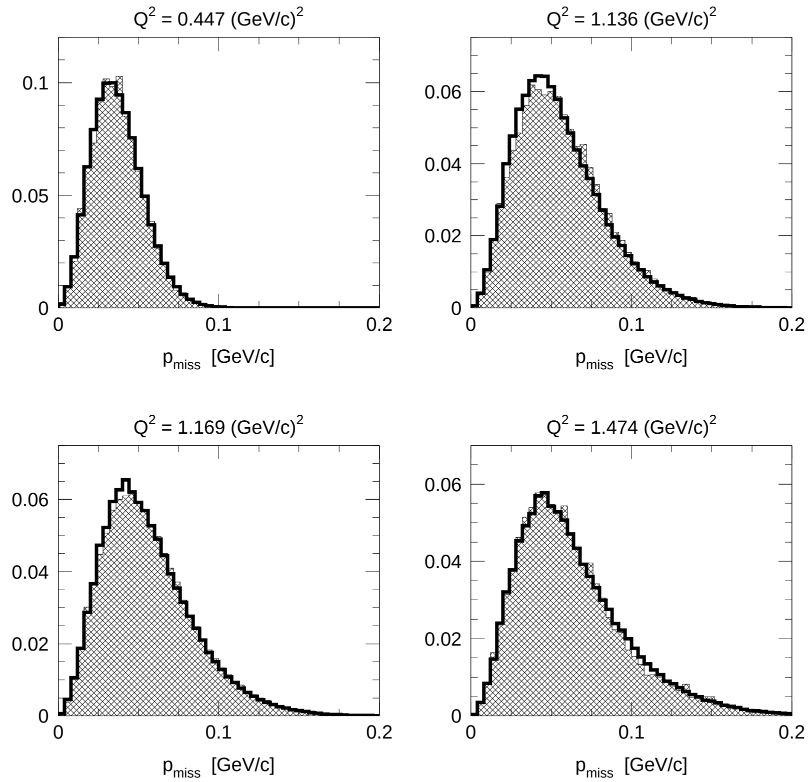

Figure 34: Comparison of `GENGEN` simulated (unfilled histograms with thick solid line borders) and experimental (cross-hatched filled histograms) distributions of p_{miss} for the four central E93-038 Q^2 points. Identical cuts were applied to both the simulated and experimental data.

2 Simulation results for kinematics similar to this proposal

To demonstrate the efficiency of the suppression of inelastic events for kinematics similar to this proposal, the `GENGEN` simulation code [1] was used to generate invariant mass spectra for quasielastic $d(e, e'n)p$ and inelastic $d(e, e'n\pi)$ events. This simulation code was developed to perform the kinematic acceptance-averaging and calculation of the FSI, MEC, and IC corrections for E93-038. The simulation includes an event generator for quasielastic and pion-production reactions, a model for the acceptance of a magnetic spectrometer, spin transport through the Charybdis dipole field, and a detailed model of the NPOL acceptance and interactions (including the front-to-rear array nucleon-nucleon scattering). Good agreement with experimental distributions was achieved, as shown in Fig. 34 where `GENGEN` simulated and experimental distributions of p_{miss} are compared for the four E93-038 central Q^2 points.

Note that quasielastic and inelastic events were not simulated simultaneously, because of the difficulty of developing such an event generator for a two-particle coincidence experiment.* Thus, to understand the efficiency of the suppression of inelastic events (relative to the selection of quasielastic events), it was necessary to normalize the separately simulated quasielastic and

*Simultaneous simulation of the quaisfree $d(e, e'n)p$ knockout (from a moving nucleon) and inelastic pion production (upon a moving nucleon) reactions is complicated by the fact that the knockout reaction is 5-fold differential, whereas that for pion production is 6-fold differential (in the presence of an undetected particle). Thus, simultaneous simulation of these reactions in a realistic, and efficient, manner is a non-trivial problem [2].

Data	Q^2 [(GeV/c)^2]	E_e [GeV]	$E_{e'}$ [GeV]	$\theta_{e'}$ [deg]	θ_n [deg]	T_n [GeV]
NE-11	4.00	5.507	3.377	26.8°	31.4°	2.130
E133	7.11	17.307	13.523	10.0°	30.5°	3.784

Table 6: Simulated SLAC NE-11 and E133 kinematics.

inelastic spectra to experimental results for W spectra. Simulations were performed for the kinematics of two experiments with Q^2 values similar to those in this proposal: SLAC NE-11 [3], reporting results for G_E^n from $Q^2 = 1.75$ to 4.00 (GeV/c)^2; and SLAC E133 [4], reporting results for the elastic electron-neutron cross section from $Q^2 = 2.5$ to 10.0 (GeV/c)^2. Both experiments reported measurements of W spectra for $d(e, e')$ scattering near the quasielastic peak and into the inelastic region. Simulations were performed for a subset of the kinematics from these experiments; results are shown below for the kinematics listed in Table 6.

Results from simulations of the SLAC NE-11 $Q^2 = 4.00$ (GeV/c)^2 kinematics are shown in Fig. 35. The top panel shows the simulated invariant mass spectra normalized to the experimental data, whereas the bottom panel shows the spectra after application of the nominal cuts for this proposal: $\Delta p/p = -3/+15\%$, $|\text{cTOF}| < 1$ ns, and $p_{\text{miss}} < 100$ MeV/c. With these cuts, the contamination from inelastic events is estimated to be small, $\sim 1\%$, for a proposed invariant mass cut of $W < 1.1$ GeV/c^2. After all cuts, the quasielastic event yield, relative to the original simulated quasielastic distributions prior to cuts, was calculated to be 57%. With a less stringent cut of $p_{\text{miss}} < 250$ MeV/c, the inelastic contamination increases to $\sim 6\%$ (shown in Fig. 36) for $W < 1.1$ GeV/c^2, while the quasielastic yield increases only slightly to 69%.

Results from simulations of the SLAC E133 $Q^2 = 7.11$ (GeV/c)^2 kinematics are shown in Fig. 37. Here, even though the ratio of the initial inelastic to quasielastic event population is greater (with a broader quasielastic peak), the inelastic contamination is still small, $\sim 3\%$, for $p_{\text{miss}} < 100$ MeV/c and $W < 1.1$ GeV/c^2. The quasielastic event yield was calculated to be 47%. The simulations indicate that loosening the p_{miss} cut to 250 MeV/c would increase the inelastic contamination to $\sim 8\%$ (see Fig. 38), while only increasing the quasielastic yield slightly from 47% to 59%. To summarize, simulations of the measurement proposed here in which a magnetic spectrometer is employed for detection of the scattered electron indicate that contamination from inelastic events will be small with a tight cut on p_{miss}. The simulations also indicate that the quasielastic event yield will also be (relatively) high, even with a tight p_{miss} cut.

3 Simulation results for calorimeter energy resolution

Quasielastic event yields and inelastic suppression efficiencies were also extracted from simulations of a degraded energy resolution for the detection of the scattered electron. The results of these simulations are relevant for a comparison between the measurement proposed here and the proposed measurement of G_E^n utilizing a polarized ^{3}He target and a calorimeter for the measurement of the scattered electron's energy [5].

The model for the calorimeter implemented in the `GENGEN` simulation code consisted of a "black box" acceptance, with an angular acceptance similar to that of the BigCal calorimeter (assumed to be positioned 10 m from the target) and an energy resolution (assumed to be purely Gaussian) of $\sigma_E = 5\%/\sqrt{E}$. Invariant mass spectra were generated for both the SLAC NE-11 $Q^2 = 4.00$ (GeV/c)^2 kinematics, and also the SLAC E133 $Q^2 = 7.11$ (GeV/c)^2 kinematics.

In the analysis of the data from the calorimeter simulations, the relative quasielastic/inelastic normalizations from the spectrometer simulations were retained (as the normalizations relate the relative underlying quasielastic/inelastic distributions, which are then folded with the acceptance and resolution).

Note that the SLAC NE-11 $Q^2 = 4.00$ (GeV/c)^2 kinematics are quite similar to those for the proposed polarized ^{3}He target / calorimeter measurement at $Q^2 = 5.00$ (GeV/c)^2, in which $E_e = 5.85$ GeV, $E_{e'} = 3.19$ GeV, and $\theta_{e'} = 30.0°$ [5]. Results from the calorimeter simulation for the SLAC NE-11 $Q^2 = 4.00$ (GeV/c)^2 kinematics are shown in the top panel of Fig. 39. As would be expected, these spectra are significantly broader than those shown for the magnetic spectrometer simulation. Despite these broader shapes, the inelastic contamination, shown in the bottom panel of Fig. 39, is still small for a tight $p_{\rm miss} < 100$ MeV/c cut, with the contamination estimated to be $\sim 1\%$. However, the quasielastic yield for this $p_{\rm miss}$ cut is only 33%. With a less stringent $p_{\rm miss} < 250$ MeV/c cut (see Fig. 40), the inelastic contamination increases to $\sim 4\%$, while the quasielastic yield increases to 55%. These results can be understood by comparing the $p_{\rm miss}$ distributions from the magnetic spectrometer and calorimeter simulations. As shown in Fig. 41, the degraded energy resolution of the calorimeter distorts the $p_{\rm miss}$ distributions, by "stretching" the spectra to larger values of $p_{\rm miss}$ away from $p_{\rm miss} = 0$.

Finally, results from the calorimeter simulation for the SLAC E133 $Q^2 = 7.11$ (GeV/c)^2 kinematics are shown in the top panel of Fig. 42. Again, these spectra are significantly broader than those from the magnetic spectrometer simulation. The inelastic contamination with a tight $p_{\rm miss} < 100$ MeV/c cut is estimated to be (very) small, $\sim 0.1\%$; however, the quasielastic yield is calculated to be small, $\sim 20\%$. With a looser $p_{\rm miss} < 250$ MeV/c cut (see Fig. 43), the inelastic contamination increases to $\sim 2\%$, and the quasielastic yield increases to $\sim 39\%$. Distributions of $p_{\rm miss}$ from the magnetic spectrometer and calorimeter simulations for these kinematics are shown in Fig. 44.

4 Summary

In summary, the simulations suggest that the relative inelastic contamination for both types of experiments, either with a magnetic spectrometer or a calorimeter for the measurement of the scattered electron's energy, can be reduced to a small level with a tight cut on the missing momentum; however, the simulations do suggest that the degraded energy resolution of the calorimeter will result in a significantly reduced quasielastic yield, as compared to the quasielastic yields in the magnetic spectrometer simulations.

It should be noted that the response of the calorimeter implemented in these simulations was highly simplistic, in that the energy resolution was assumed to be purely Gaussian with $\sigma_E = 5\%/\sqrt{E}$. A broader resolution, or the presence of a tail, would almost certainly lead to a greater distortion of the missing momentum distribution, resulting in an even smaller quasielastic yield.

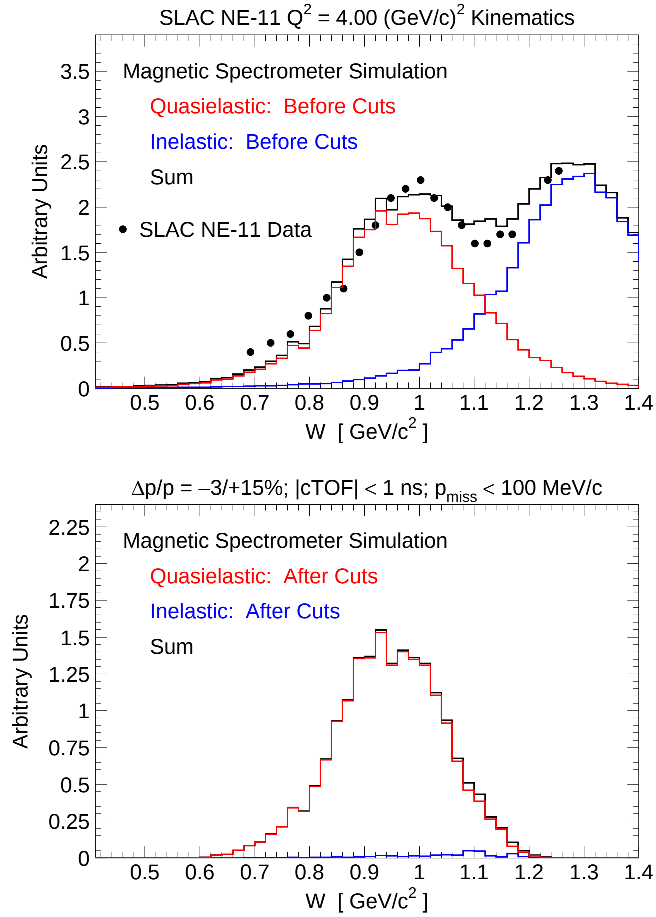

Figure 35: (Top panel) Results from simulations of quasielastic and inelastic invariant mass spectra for the $Q^2 = 4.00$ (GeV/c)^2 kinematics of SLAC NE-11. (Bottom panel) Invariant mass spectra after application of cuts. The inelastic contamination is estimated to be $\sim 1\%$ for $W < 1.1$ GeV/c^2.

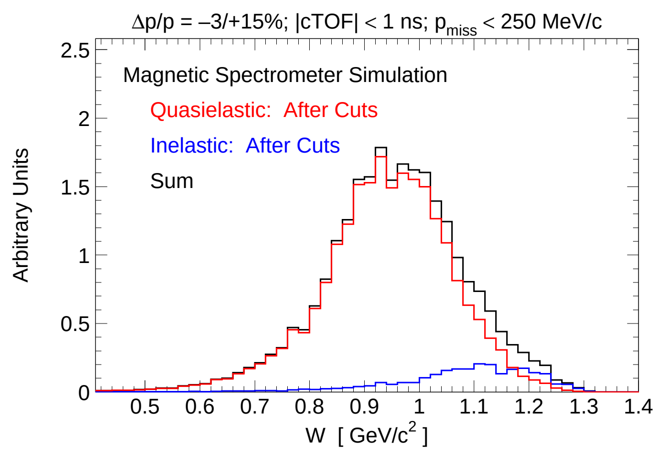

Figure 36: Invariant mass spectra after application of a less stringent $p_{\rm miss} < 250$ MeV/c cut. The inelastic contamination is estimated to be $\sim 6\%$ for $W < 1.1$ GeV/c^2.

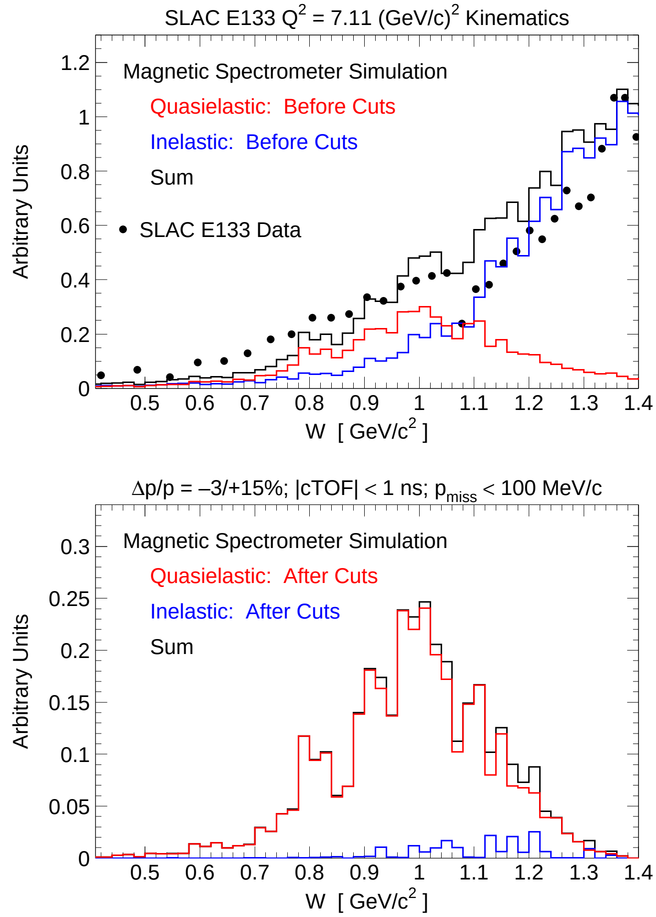

Figure 37: (Top panel) Results from simulations of quasielastic and inelastic invariant mass spectra for the $Q^2 = 7.11$ (GeV$/c)^2$ kinematics of SLAC E133. (Bottom panel) Invariant mass spectra after application of cuts. The inelastic contamination is estimated to be $\sim 3\%$ for $W < 1.1$ GeV$/c^2$.

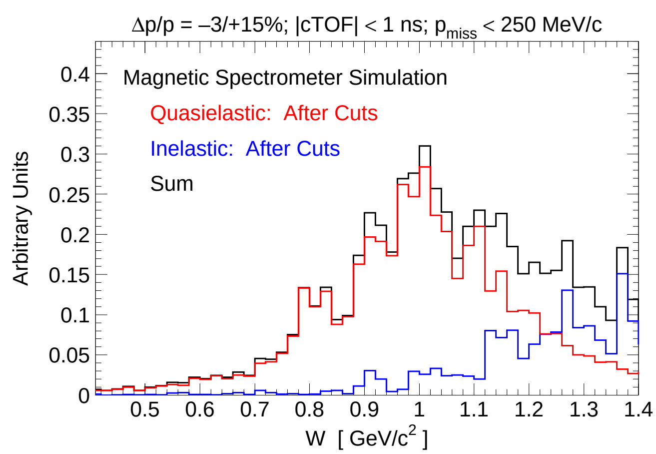

Figure 38: Invariant mass spectra at $Q^2 = 4.00$ (GeV$/c)^2$ after application of a less stringent $p_{\rm miss} < 250$ MeV$/c$ cut. The inelastic contamination is estimated to be $\sim 8\%$ for $W < 1.1$ GeV$/c^2$.

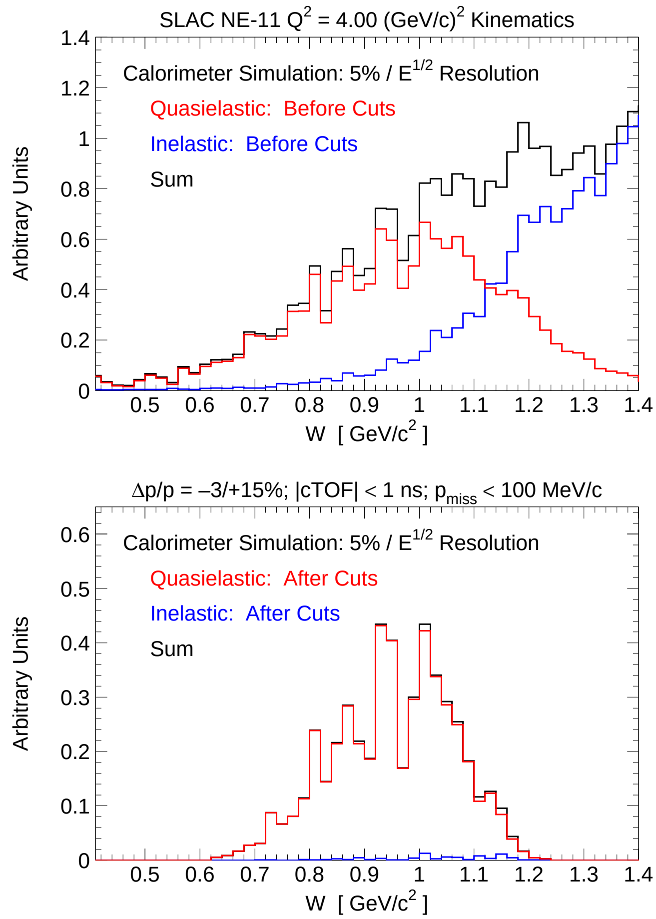

Figure 39: (Top panel) Results from simulations of quasielastic and inelastic invariant mass spectra for the $Q^2 = 4.00$ (GeV/c)^2 kinematics of SLAC NE-11, assuming a calorimeter measurement of the scattered electron energy with an energy resolution of $\sigma_E = 5\%/\sqrt{E}$. Top panel: spectra before application of cuts. (Bottom panel) Invariant mass spectra after application of cuts. The inelastic contamination is estimated to be $\sim 1\%$ for $W < 1.1$ GeV/c^2.

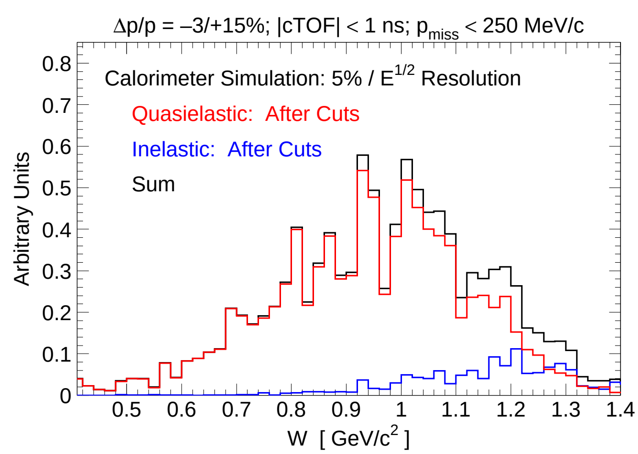

Figure 40: Invariant mass spectra at $Q^2 = 4.00$ (GeV/c)^2 after application of a less stringent $p_{\rm miss} < 250$ MeV/c cut. The inelastic contamination is estimated to be $\sim 4\%$ for $W < 1.1$ GeV/c^2.

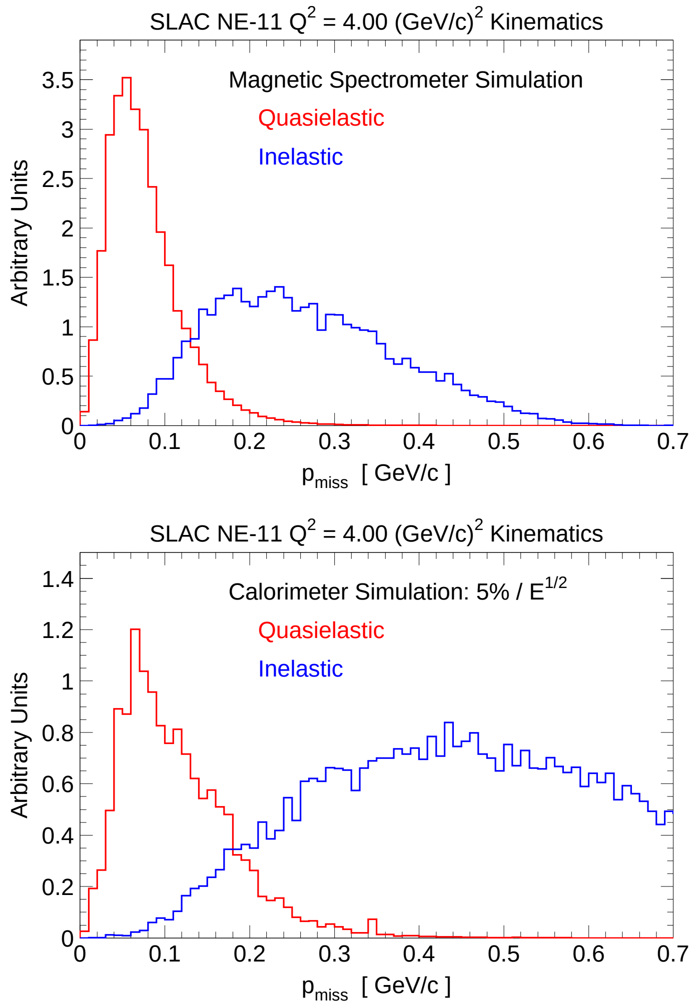

Figure 41: Missing momentum distributions for quasielastic and inelastic events from magnetic spectrometer (top panel) and calorimeter (bottom panel) simulations for the SLAC NE-11 $Q^2 = 4.00\ (\mathrm{GeV}/c)^2$ kinematics.

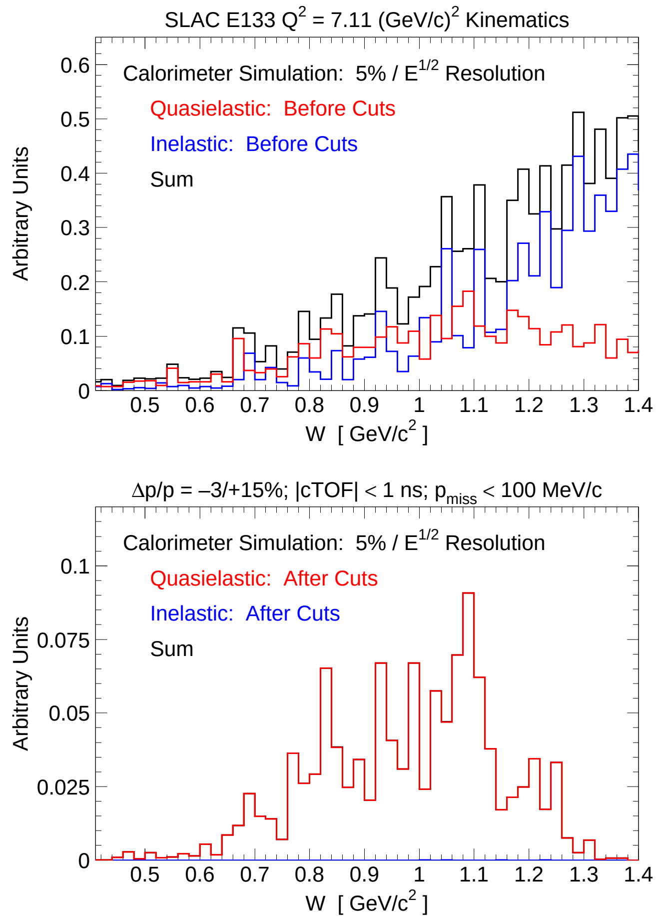

Figure 42: (Top panel) Results from simulations of quasielastic and inelastic invariant mass spectra for the $Q^2 = 7.11$ (GeV$/c)^2$ kinematics of SLAC E133, assuming a calorimeter measurement of the scattered electron energy with an energy resolution of $\sigma_E = 5\%/\sqrt{E}$. Top panel: spectra before application of cuts. (Bottom panel) Invariant mass spectra after application of cuts. The inelastic contamination is estimated to be $\sim 0.1\%$ for $W < 1.1$ GeV$/c^2$.

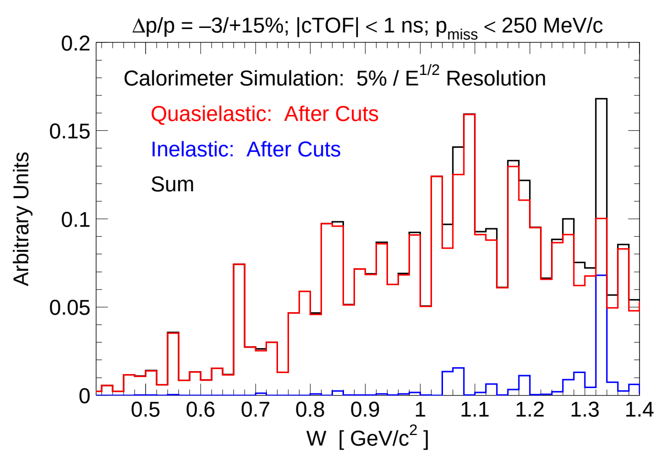

Figure 43: Invariant mass spectra at $Q^2 = 7.11$ (GeV$/c)^2$ after application of a less stringent $p_{\rm miss} < 250$ MeV$/c$ cut. The inelastic contamination is estimated to be $\sim 2\%$ for $W < 1.1$ GeV$/c^2$.

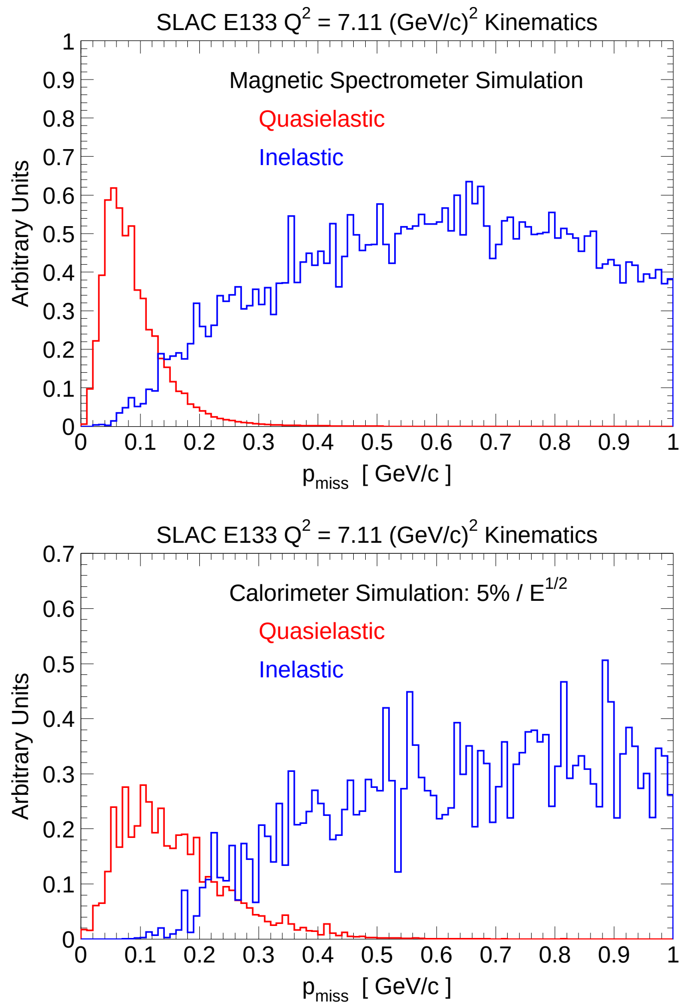

Figure 44: Missing momentum distributions for quasielastic and inelastic events from magnetic spectrometer (top panel) and calorimeter (bottom panel) simulations for the SLAC E133 $Q^2 = 7.11\ (\mathrm{GeV}/c)^2$ kinematics.

References

[1] B. Plaster *et al.*, Phys. Rev. C **73**, 025205 (2006).

[2] J. J. Kelly, private communication (2003).

[3] A. Lung *et al.*, Phys. Rev. Lett. **70**, 718 (1993).

[4] S. Rock *et al.*, Phys. Rev. D **46**, 24 (1992).

[5] G. Cates, Talk at the Second Super BigBite Workshop, September 5, 2008, `hallaweb.jlab.org/12GeV/SuperBigBite/meetings/02/agenda.html`

Appendix B

PHYSICAL REVIEW C **73**, 025205 (2006)

Measurements of the neutron electric to magnetic form factor ratio G_{En}/G_{Mn} via the $^2\mathrm{H}(\vec{e}, e'\vec{n})^1\mathrm{H}$ reaction to $Q^2 = 1.45$ (GeV/c)^2

B. Plaster,[1,2,*] A. Yu. Semenov,[3,4,†] A. Aghalaryan,[5] E. Crouse,[6] G. MacLachlan,[7] S. Tajima,[8] W. Tireman,[3,9] A. Ahmidouch,[10] B. D. Anderson,[3] H. Arenhövel,[11] R. Asaturyan,[5] O. K. Baker,[12] A. R. Baldwin,[3] D. Barkhuff,[1,‡] H. Breuer,[13] R. Carlini,[14] E. Christy,[12] S. Churchwell,[8,§] L. Cole,[12] S. Danagoulian,[10,14] D. Day,[15] T. Eden,[3,12,∥] M. Elaasar,[16] R. Ent,[14] M. Farkhondeh,[1] H. Fenker,[14] J. M. Finn,[6] L. Gan,[12] A. Gasparian,[10,12] K. Garrow,[14] P. Gueye,[12] C. R. Howell,[8] B. Hu,[12] M. K. Jones,[14] J. J. Kelly,[13] C. Keppel,[12] M. Khandaker,[17] W.-Y. Kim,[18] S. Kowalski,[1] A. Lung,[14] D. Mack,[14] R. Madey,[3,6,14] D. M. Manley,[3] P. Markowitz,[19] J. Mitchell,[14] H. Mkrtchyan,[5] A. K. Opper,[7] C. Perdrisat,[6] V. Punjabi,[17] B. Raue,[19] T. Reichelt,[20] J. Reinhold,[19] J. Roche,[6] Y. Sato,[12] N. Savvinov,[13] I. A. Semenova,[3,4] W. Seo,[18] N. Simicevic,[21] G. Smith,[14] S. Stepanyan,[5] V. Tadevosyan,[5] L. Tang,[12] S. Taylor,[1] P. E. Ulmer,[22] W. Vulcan,[14] J. W. Watson,[3] S. Wells,[21] F. Wesselmann,[15] S. Wood,[14] Chen Yan,[14] Chenyu Yan,[3] S. Yang,[18] L. Yuan,[12] W.-M. Zhang,[3] H. Zhu,[15] and X. Zhu[12]

(Jefferson Laboratory E93-038 Collaboration)

[1] *Massachusetts Institute of Technology, Cambridge, Massachusetts 02139, USA*
[2] *California Institute of Technology, Pasadena, California 91125, USA*
[3] *Kent State University, Kent, Ohio 44242, USA*
[4] *Joint Institute for Nuclear Research, Dubna RU-141980, Russia*
[5] *Yerevan Physics Institute, Yerevan 375036, Armenia*
[6] *The College of William and Mary, Williamsburg, Virginia 23187, USA*
[7] *Ohio University, Athens, Ohio 45701, USA*
[8] *Duke University and TUNL, Durham, North Carolina 27708, USA*
[9] *Northern Michigan University, Marquette, Michigan 49855, USA*
[10] *North Carolina A&T State University, Greensboro, North Carolina 27411, USA*
[11] *Johannes Gutenberg-Universität, D-55099 Mainz, Germany*
[12] *Hampton University, Hampton, Virginia 23668, USA*
[13] *University of Maryland, College Park, Maryland 20742, USA*
[14] *Thomas Jefferson National Accelerator Facility, Newport News, Virginia 23606, USA*
[15] *University of Virginia, Charlottesville, Virginia 22904, USA*
[16] *Southern University at New Orleans, New Orleans, Louisiana 70126, USA*
[17] *Norfolk State University, Norfolk, Virginia 23504, USA*
[18] *Kyungpook National University, Taegu 702-701, Korea*
[19] *Florida International University, Miami, Florida 33199, USA*
[20] *Rheinische Friedrich-Wilhelms-Universität, D-53115 Bonn, Germany*
[21] *Louisiana Tech University, Ruston, Louisiana 71272, USA*
[22] *Old Dominion University, Norfolk, Virginia 23508, USA*

(Received 13 November 2005; published 27 February 2006)

We report values for the neutron electric to magnetic form factor ratio, G_{En}/G_{Mn}, deduced from measurements of the neutron's recoil polarization in the quasielastic $^2\mathrm{H}(\vec{e}, e'\vec{n})^1\mathrm{H}$ reaction, at three Q^2 values of 0.45, 1.13, and 1.45 (GeV/c)^2. The data at $Q^2 = 1.13$ and 1.45 (GeV/c)^2 are the first direct experimental measurements of G_{En} employing polarization degrees of freedom in the $Q^2 > 1$ (GeV/c)^2 region and stand as the most precise determinations of G_{En} for all values of Q^2.

DOI: 10.1103/PhysRevC.73.025205 PACS number(s): 14.20.Dh, 13.40.Gp, 25.30.Bf, 24.70.+s

I. INTRODUCTION

The nucleon electromagnetic form factors are fundamental quantities needed for an understanding of the nucleon's electromagnetic structure. The Sachs electric, G_E, and magnetic, G_M, form factors [1], defined in terms of linear combinations of the Dirac and Pauli form factors, are of particular physical interest, as their evolution with Q^2, the square of the four-momentum transfer, is related to the spatial distribution of charge and current within the nucleon. As such, precise measurements of these form factors over a wide range of Q^2 are needed for a quantitative understanding of the electromagnetic structure not only of the nucleon but also of nuclei (e.g., Refs. [2–4]). Further, in the low-energy regime of the nucleon ground state, the underlying theory of the strong interaction, quantum chromodynamics (QCD), cannot be solved perturbatively. A proper description of even the static properties of the nucleon, the lowest stable mass excitation of

*Electronic address: plaster@caltech.edu
†Electronic address: semenov@jlab.org
‡Now at Renaissance Technologies, East Setauket, New York 11733, USA.
§Now at University of Canterbury, Christchurch 8020, New Zealand.
∥Now at National Center for Atmospheric Research, Boulder, Colorado 80307, USA.

the QCD vacuum, in terms of the QCD quark and gluon degrees of freedom still stands as one of the outstanding challenges of hadronic physics. Indeed, one of the most stringent tests to which nonperturbative QCD (as formulated on the lattice or in a model of confinement) can be subjected is the requirement that the theory reproduce experimental data on the nucleon form factors (e.g., Refs. [5–7]).

Because of the lack of a free neutron target, the neutron form factors are known with less precision than are the proton form factors, and measurements have been restricted to smaller ranges of Q^2. A precise measurement of the neutron electric form factor, G_{En}, has proven to be especially elusive as the neutron's net charge is zero. Prior to the realization of experimental techniques utilizing polarization degrees of freedom, values for G_{En} were extracted from measurements of the unpolarized quasielastic ${}^2\mathrm{H}(e,e'n)^1\mathrm{H}$ cross section and the deuteron elastic structure function $A(Q^2)$. Those results for G_{En} deduced from measurements of the quasielastic ${}^2\mathrm{H}(e,e'n)^1\mathrm{H}$ cross section provided little information on G_{En}, as all results were consistent with zero over all ranges of Q^2 accessed, $0 < Q^2 < 4$ (GeV/c)^2 (e.g., Ref. [8]). Similarly, results for G_{En} deduced from measurements of $A(Q^2)$, although establishing $G_{En} > 0$ for $0 < Q^2 < 0.7$ (GeV/c)^2, were plagued with large theoretical uncertainties ($\sim\pm40\%$) related to the choice of an appropriate *NN*-potential for the deuteron wave function (e.g., Ref. [9]).

With the advent of high duty-factor polarized electron beam facilities and state-of-the-art polarized nuclear targets and recoil nucleon polarimeters, experimental efforts over the past 15 years have now yielded the first precise determinations of G_{En}. In addition, recent theoretical efforts [10] have permitted an extraction of G_{En} from existing data on the deuteron quadrupole form factor with small theoretical uncertainties. Our experiment [11] was designed to extract the neutron electric to magnetic form factor ratio, G_{En}/G_{Mn}, from measurements of the neutron's recoil polarization in quasielastic ${}^2\mathrm{H}(\vec{e},e'\vec{n})^1\mathrm{H}$ kinematics at three Q^2 values of 0.45, 1.13, and 1.45 (GeV/c)^2. These results were published rapidly by Madey *et al.* [12]; here we provide a more detailed report of the experiment and analysis procedures.

The remainder of this article is organized as follows. We begin, in Sec. II, with a brief overview of the experimental techniques utilizing polarization degrees of freedom that have been employed for measurements of the neutron form factors. We continue with an overview of our experiment in Sec. III and then discuss our neutron polarimeter in Sec. IV. Details of the analysis procedure are discussed in Sec. V. Our final results are then presented in Sec. VI and compared with selected theoretical model calculations of the nucleon form factors. Finally, we conclude with a brief summary in Sec. VII. A more detailed account of the discussion that follows may be found in Ref. [13].

II. NEUTRON FORM FACTORS

A. Electron kinematics

We will use the following notation for the electron kinematics: $(E_e, \mathbf{p}_e)$ will denote the four-momentum of the initial electron, $(E_{e'}, \mathbf{p}_{e'})$ will denote the four-momentum of the scattered electron, $\theta_{e'}$ will denote the electron scattering angle, $\omega = E_e - E_{e'}$ will denote the energy transfer, $\mathbf{q} = \mathbf{p}_e - \mathbf{p}_{e'}$ will denote the three-momentum transfer, and $Q^2 = \mathbf{q}^2 - \omega^2 = 4E_eE_{e'}\sin^2(\theta_{e'}/2)$ will denote the square of the spacelike four-momentum transfer in the high-energy limit of massless electrons. The electron scattering plane is defined by $\mathbf{p}_e$ and $\mathbf{p}_{e'}$.

B. Measurements via polarized electron beams and recoil nucleon polarimetry

1. Elastic $N(\vec{e},e'\vec{N})$ scattering

The polarization of the recoil nucleon, $\mathbf{P}$, in elastic polarized-electron, unpolarized-nucleon scattering is well-known to be of the form [14–17]

$$\frac{d\sigma}{d\Omega_{e'}}(\mathbf{P}) = \sigma_0(\mathbf{P}^{(0)} + h\mathbf{P}^{(h)}), \tag{1}$$

where σ_0 denotes the unpolarized cross section, $\mathbf{P}^{(0)}$ denotes the helicity-independent recoil polarization, $\mathbf{P}^{(h)}$ denotes the helicity-dependent recoil polarization, and $h = \pm1$ denotes the electron helicity. The polarization is customarily projected onto a $(\hat{t}, \hat{n}, \hat{\ell})$ unit vector basis, with the longitudinal component, $\hat{\ell}$, along the recoil nucleon's momentum; the normal component, $\hat{n}$, perpendicular to the electron scattering plane; and the transverse component, $\hat{t}$, perpendicular to the $\hat{\ell}$ component in the scattering plane. In the one-photon exchange approximation, $\mathbf{P}^{(0)} = \mathbf{0}$, and $\mathbf{P}^{(h)}$ is confined to the scattering plane (i.e., $P_n^{(h)} = 0$). The transverse, $P_t^{(h)}$, and longitudinal, $P_\ell^{(h)}$, components are expressed in terms of kinematics and nucleon form factors as [14–17]

$$P_t^{(h)} = P_e \frac{-2G_EG_M\sqrt{\tau(1+\tau)}\tan\frac{\theta_{e'}}{2}}{G_E^2 + \left[\tau + 2\tau(1+\tau)\tan^2\frac{\theta_{e'}}{2}\right]G_M^2}, \tag{2a}$$

$$P_\ell^{(h)} = P_e \frac{2G_M^2\tau\sqrt{(1+\tau) + (1+\tau)^2\tan^2\frac{\theta_{e'}}{2}}\tan\frac{\theta_{e'}}{2}}{G_E^2 + \left[\tau + 2\tau(1+\tau)\tan^2\frac{\theta_{e'}}{2}\right]G_M^2}, \tag{2b}$$

where P_e denotes the electron beam polarization, $\tau = Q^2/4m^2$, and m denotes the nucleon mass.

Access to both $P_t^{(h)} \propto G_EG_M$ and $P_\ell^{(h)} \propto G_M^2$ via a secondary analyzing reaction in a polarimeter is highly advantageous, as the analyzing power of the polarimeter, denoted A_y, and P_e cancel in the $P_t^{(h)}/P_\ell^{(h)}$ ratio, yielding a measurement of G_E/G_M that is relatively insensitive to systematic uncertainties associated with these quantities. For the case of the neutron form factor ratio, as suggested by Arnold, Carlson, and Gross [17] and first implemented experimentally by Ostrick *et al.* [18], a vertical dipole field located ahead of a polarimeter configured to measure an up-down scattering asymmetry sensitive to the projection of the recoil polarization on the $\hat{t}$-axis permits access to both $P_t^{(h)}$ and $P_\ell^{(h)}$. During transport through the magnetic field, the recoil polarization vector will precess through some spin precession angle χ in the $\hat{t}$-$\hat{\ell}$ plane, leading to a scattering asymmetry, $\xi(\chi)$, which is sensitive to a mixing of $P_t^{(h)}$ and $P_\ell^{(h)}$,

$$\begin{aligned}\xi(\chi) &= A_y\left(P_t^{(h)}\cos\chi + P_\ell^{(h)}\sin\chi\right)\\ &= A_y|\mathbf{P}^{(h)}|\sin(\chi+\delta).\end{aligned} \tag{3}$$

In the above, $|\mathbf{P}^{(h)}| = [(P_t^{(h)})^2 + (P_\ell^{(h)})^2]^{1/2}$, and we define the phase-shift parameter δ according to

$$\tan\delta = \frac{P_t^{(h)}}{P_\ell^{(h)}} = -\frac{G_E}{G_M}\frac{\cos\dfrac{\theta_{e'}}{2}}{\sqrt{\tau + \tau^2\sin^2\dfrac{\theta_{e'}}{2}}}. \tag{4}$$

2. Quasielastic ^{2}H($\vec{e}, e'\vec{n}$)^{1}H scattering

The above formalism is directly applicable to an extraction of the proton form factor ratio, G_{Ep}/G_{Mp}, from measurements of the proton's recoil polarization in elastic ^{1}H($\vec{e}, e'\vec{p}$) scattering. An extraction of the neutron form factor ratio, G_{En}/G_{Mn}, from measurements of the neutron's recoil polarization in quasielastic ^{2}H($\vec{e}, e'\vec{n}$)^{1}H scattering is, however, complicated by nuclear physics effects, such as final-state interactions (FSI), meson exchange currents (MEC), isobar configurations (IC), and the structure of the deuteron. The pioneering study of the sensitivity of the quasielastic ^{2}H($\vec{e}, e'\vec{n}$)^{1}H reaction to the neutron form factors, reported by Arenhövel [19], revealed that for perfect quasifree emission of the neutron (i.e., neutron emission along the three-momentum transfer **q**), $P_t^{(h)}$ is proportional to G_{En}, but is relatively insensitive to FSI, MEC, IC, and the choice of the *NN* potential for the deuteron wave function. A more detailed study of the ^{2}H($\vec{e}, e'\vec{n}$)^{1}H reaction reported by Arenhövel, Leidemann, and Tomusiak [20] found that these results also apply to $P_\ell^{(h)}$. Similar findings were subsequently reported by Refs. [21,22].

These theoretical investigations [20,22] indicated that in quasifree kinematics the influence of these nuclear physics effects on the neutron's recoil polarization are sizable for Q^2 values below 0.2 (GeV/c)^2, but become small for $Q^2 \gtrsim 0.3$ (GeV/c)^2 and decrease with increasing Q^2. Indeed, in one recent ^{2}H($\vec{e}, e'\vec{n}$)^{1}H experiment [18,23], the corrections for FSI resulted in a 65 and 8% increase to the value of G_{En} at $Q^2 = 0.15$ and 0.34 (GeV/c)^2, respectively. As will be seen later, the corrections for nuclear physics effects at our three Q^2 points were on the order of a few percentages and decreased with each increment in Q^2.

In Appendix A, we present a detailed discussion of the formalism for the kinematics and recoil polarization observables for the quasielastic ^{2}H($\vec{e}, e'\vec{n}$)^{1}H reaction. In particular, we provide there a definition for $\Theta_{np}^{\text{c.m.}}$, the polar angle between the proton momentum and **q** in the recoiling neutron-proton center-of-mass frame (hereafter, n-p c.m. frame), a variable to which we refer frequently throughout this article. (Perfect quasifree emission of the neutron is defined by $\Theta_{np}^{\text{c.m.}} = 180^\circ$.) We follow this, in Appendix B, with a discussion of the sensitivity of the recoil polarization components to FSI, MEC, IC, and the choice of the *NN* potential for the deuteron wave function at and away from perfect quasifree emission.

C. Measurements via polarized electron beams and polarized targets

1. Elastic $\vec{N}$($\vec{e}, e'N$) scattering

The cross section in the one-photon exchange approximation for elastic polarized-electron, polarized-nucleon scattering is well known to be of the form [14–16,24]

$$\frac{d\sigma}{d\Omega_{e'}} = \sigma_0[1 + hA_{eN}(\theta^*, \phi^*)]. \tag{5}$$

Here, θ^* and ϕ^* denote, respectively, the polar and azimuthal angle between the target nucleon polarization vector and **q**, and $A_{eN}(\theta^*, \phi^*)$ denotes the polarized-electron, polarized-nucleon beam-target asymmetry, which is a function of kinematics and the nucleon form factors. The sensitivity of A_{eN} to the form factors is enhanced if the target polarization is oriented in the electron scattering plane either parallel or perpendicular to **q**; in the former (latter) case, the expression for A_{eN} is identical to that for $-P_\ell^{(h)}$ ($P_t^{(h)}$) and will be denoted $A_\parallel$ ($A_\perp$). Similar to the recoil polarization technique, measurements of both $A_\perp$ and $A_\parallel$ are desirable as the target polarization (analog to the analyzing power) and beam polarization cancel in the $A_\perp/A_\parallel$ ratio, again yielding a measurement of G_E/G_M that is relatively free of systematic uncertainties.

2. Quasielastic $^2\vec{\text{H}}$($\vec{e}, e'n$)^{1}H and $^3\vec{\text{He}}$($\vec{e}, e'n$) scattering

The above formalism is directly applicable to a measurement of G_{Ep}/G_{Mp} via the elastic $^1\vec{\text{H}}$($\vec{e}, e'p$) reaction, but an extraction of G_{En}/G_{Mn} from either the quasielastic $^2\vec{\text{H}}$($\vec{e}, e'n$)^{1}H reaction or the quasielastic $^3\vec{\text{He}}$($\vec{e}, e'n$) reaction is again complicated by nuclear physics effects. For the case of the $^2\vec{\text{H}}$($\vec{e}, e'n$)^{1}H reaction, Cheung and Woloshyn [25] were the first to show that the polarized-electron, vector-polarized-deuterium beam-target asymmetry, A_{ed}^V, is sensitive to G_{En}. More complete calculations of A_{ed}^V that accounted for nuclear physics effects were later reported by Tomusiak and Arenhövel [26] and others [20,22,27,28]. These calculations demonstrated that for quasifree neutron kinematics, A_{ed}^V is strongly sensitive to G_{En} but is relatively insensitive to FSI, MEC, IC, and the choice of the *NN* potential for the deuteron wave function.

For the case of quasielastic scattering from polarized ^{3}He, Blankleider and Woloshyn [29] were the first to study the sensitivity of the inclusive $^3\vec{\text{He}}$($\vec{e}, e'$) asymmetry to G_{En}. More detailed studies of the inclusive asymmetry carried out by others [30,31] suggested that a clean extraction of G_{En} from the inclusive asymmetry would be extremely difficult because of proton contamination of the inclusive asymmetry. Such difficulties for an extraction of G_{En} are, however, mitigated in a $^3\vec{\text{He}}$($\vec{e}, e'n$) coincidence experiment; as further motivation, Laget [22] demonstrated that the exclusive $^3\vec{\text{He}}$($\vec{e}, e'n$) asymmetry is relatively insensitive to the effects of FSI and MEC for $Q^2 \gtrsim 0.3$ (GeV/c)^2.

D. Analysis of the deuteron quadrupole form factor

The unpolarized elastic electron-deuteron cross section is generally expressed in terms of the elastic structure functions, $A(Q^2)$ and $B(Q^2)$. These are, in turn, functions of the deuteron's charge, G_C, quadrupole, G_Q, and magnetic, G_M, form factors. G_C and G_Q are of particular interest for an extraction of G_{En} as they are both proportional to ($G_{Ep} + G_{En}$).

An unambiguous extraction of G_C, G_Q, and G_M from a Rosenbluth separation of $A(Q^2)$ and $B(Q^2)$ requires some

TABLE I. Chronological summary of published data on the neutron form factors from experiments employing polarization degrees of freedom and a recent analysis combining data on the deuteron quadrupole form factor, G_Q, with data on t_{20} and T_{20}.

Reference	Facility	Published	Type	Q^2 [(GeV/c)^2]	Quantities	Note(s)
Jones-Woodward *et al.* [32]	MIT-Bates	1991	$^3\vec{\mathrm{He}}(\vec{e}, e')$	0.16	$A_\perp \to G_{En}$	a,b
Thompson *et al.* [33]	MIT-Bates	1992	$^3\vec{\mathrm{He}}(\vec{e}, e')$	0.2	$A_\perp, A_\parallel \to G_{En}$	a,b
Eden *et al.* [34]	MIT-Bates	1994	$^2\mathrm{H}(\vec{e}, e'\vec{n})$	0.255	$P_t^{(h)} \to G_{En}$	c,d
Gao *et al.* [36]	MIT-Bates	1994	$^3\vec{\mathrm{He}}(\vec{e}, e')$	0.19	$A_\parallel \to G_{Mn}$	a,e
Meyerhoff *et al.* [38]	MAMI	1994	$^3\vec{\mathrm{He}}(\vec{e}, e'n)$	0.31	$A_\perp, A_\parallel \to G_{En}$	a,b
Becker *et al.* [39]	MAMI	1999	$^3\vec{\mathrm{He}}(\vec{e}, e'n)$	0.40	$A_\perp, A_\parallel \to G_{En}$	b,f
Ostrick *et al.* [18], Herberg *et al.* [23]	MAMI	1999	$^2\mathrm{H}(\vec{e}, e'\vec{n})$	0.15, 0.34	$P_t^{(h)}, P_\ell^{(h)} \to G_{En}$	b,c
Passchier *et al.* [41]	NIKHEF	1999	$^2\vec{\mathrm{H}}(\vec{e}, e'n)$	0.21	$A_{ed}^V \to G_{En}$	b,c
Rohe *et al.* [42], Bermuth *et al.* [43]	MAMI	1999/2003	$^3\vec{\mathrm{He}}(\vec{e}, e'n)$	0.67	$A_\perp, A_\parallel \to G_{En}$	g,h
Xu *et al.* [46]	JLab	2000/2003	$^3\vec{\mathrm{He}}(\vec{e}, e')$	0.1–0.6	$A_\parallel \to G_{Mn}$	a,i
Schiavilla and Sick [10]	—	2001	Analysis	0.00–1.65	$G_Q \to G_{En}$	j
Zhu *et al.* [48]	JLab	2001	$^2\vec{\mathrm{H}}(\vec{e}, e'n)$	0.495	$A_{ed}^V \to G_{En}$	b,c
Madey *et al.* [12], this article	JLab	2003	$^2\mathrm{H}(\vec{e}, e'\vec{n})$	0.45, 1.13, 1.45	$P_t^{(h)}, P_\ell^{(h)} \to G_{En}$	c,k
Warren *et al.* [50]	JLab	2004	$^2\vec{\mathrm{H}}(\vec{e}, e'n)$	0.5, 1.0	$A_{ed}^V \to G_{En}$	c,g
Glazier *et al.* [51]	MAMI	2005	$^2\mathrm{H}(\vec{e}, e'\vec{n})$	0.30, 0.59, 0.79	$P_t^{(h)}, P_\ell^{(h)} \to G_{En}$	c,l

[a]Uncorrected for nuclear physics effects (i.e., for FSI, MEC, or IC).
[b]Used the dipole parametrization for G_{Mn}.
[c]Applied corrections for FSI, MEC, and IC by averaging calculations of Arenhövel *et al.* [19,20,26–28] over the acceptance.
[d]Used the value for G_{Mn} at $Q^2 = 0.255$ (GeV/c)^2 as measured by Markowitz *et al.* [35].
[e]Used the Galster parametrization [37] for G_{En}.
[f]Corrections for FSI and MEC calculated by Golak *et al.* [40].
[g]Used values for G_{Mn} taken from the parametrization of Kubon *et al.* [44].
[h]Estimated corrections for FSI by scaling calculations of Golak *et al.* [45] at $Q^2 = 0.37$ (GeV/c)^2 to $Q^2 = 0.67$ (GeV/c)^2.
[i]Used values for G_{En} taken from the parametrization of Höhler *et al.* [47].
[j]Theoretical analysis of data on the deuteron quadrupole form factor, G_Q, tensor moment, t_{20}, and tensor analyzing power, T_{20}.
[k]Used values for G_{Mn} taken from the parametrization of Kelly [49].
[l]Used values for G_{Mn} taken from the parametrization of Friedrich and Walcher [52].

third observable. The tensor moments, t_{2j} $(j = 0, 1, 2)$, extracted from recoil polarization measurements in elastic unpolarized-electron, unpolarized-deuteron scattering, and the tensor analyzing powers, T_{2j} $(j = 0, 1, 2)$, as measured in elastic unpolarized-electron, tensor polarized-deuteron scattering, are of particular interest as they are functions of G_C, G_Q, and G_M [17,24]. Indeed, after G_C, G_Q, and G_M have been separated from $A(Q^2)$, $B(Q^2)$, and the polarization-dependent observables, a value for G_{En} can be extracted from either G_C or G_Q; however, as was shown by Schiavilla and Sick [10], an extraction of G_{En} from data on G_Q is particularly advantageous as the contributions of theoretical uncertainties associated with short-range two-body exchange operators to G_Q are small.

E. Summary of results

In Table I, we have compiled a complete chronological summary of all published data on the neutron form factors from experiments employing polarization degrees of freedom and a recent analysis combining data on the deuteron quadrupole form factor with the polarization-dependent observables t_{20} and T_{20}. The current status of these results for G_{En} is shown in Fig. 1. We have omitted the results of Jones-Woodward *et al.* [32], Thompson *et al.* [33], and Meyerhoff *et al.* [38] from this plot as these results were not corrected for nuclear physics effects. It should be noted that the results of Herberg *et al.* [23] and Bermuth *et al.* [43] supersede those of Ostrick *et al.* [18] and Rohe *et al.* [42], respectively, as the former set reported the final results (corrected for nuclear physics effects) for their respective experiments.

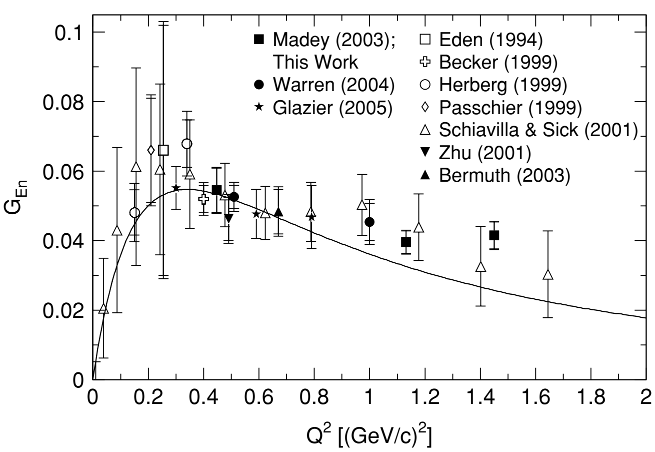

FIG. 1. Current status of results for G_{En} ([10,12,23,34,39,41,43,48,50,51] and this work). The Galster parametrization [37] is shown as the solid curve. See Table I for the reaction types for the individual data points.

The Q^2 range of G_{En} is much more limited than those of the other three nucleon electromagnetic form factors, with only two results, those of Madey *et al.* [12] and the analysis results of Schiavilla and Sick [10], extending into the $Q^2 > 1\,(\mathrm{GeV}/c)^2$ region. The agreement between these modern data and the Galster parametrization [37] with its original fitted parameters can be judged only as fortuitous.

III. EXPERIMENT

A. Overview of experiment

Our experiment [11], E93-038, was conducted in Hall C of the Jefferson Laboratory (JLab) during a run period lasting from September 2000 to April 2001. Longitudinally polarized electrons extracted from the JLab electron accelerator [53] scattered from a liquid deuterium target mounted on the Hall C beamline. The scattered electrons were detected and momentum analyzed by the Hall C High Momentum Spectrometer (HMS) in coincidence with the recoil neutrons. A stand-alone neutron polarimeter (NPOL) [54], designed and installed in Hall C specifically for this experiment, was used to measure the up-down scattering asymmetry arising from the projection of the recoil neutrons' polarization on an axis perpendicular to their momentum and parallel to the floor of Hall C. A vertical dipole field located ahead of NPOL was used to precess the recoil neutrons' polarization vectors through some chosen spin precession angle to measure this up-down scattering asymmetry from different projections of the recoil polarization vector on the polarimeter's sensitive axis. This vertical dipole field also served as a sweeping field for the background flux of recoil protons from the deuteron target.

Data were taken at four central Q^2 values of 0.447, 1.136, 1.169, and 1.474 $(\mathrm{GeV}/c)^2$ with associated electron beam energies of 0.884, 2.326, 2.415, and 3.395 GeV, respectively. The nominal (central) values of the quasielastic electron and neutron kinematics and the neutron spin precession angles, χ, for each of these central Q^2 points are summarized in Table II. We note that the data acquired at the separate central Q^2 values of 1.136 and 1.169 $(\mathrm{GeV}/c)^2$ were combined in our final analysis. Beam polarizations of 70%–80% at currents of 20–70 μA were typical throughout the duration of the experiment. The central axis of the neutron polarimeter was fixed at a scattering angle of 46.0° relative to the incident electron beamline for the duration of the experiment. The scattering asymmetries measured in our polarimeter were on the order of a few percentages.

TABLE II. Nominal (central) values of the quasielastic electron and neutron kinematics and neutron spin precession angles for each Q^2 setting in the experiment. The data from the central Q^2 values of 1.136 and 1.169 $(\mathrm{GeV}/c)^2$ were combined in our final analysis.

Q^2 $[(\mathrm{GeV}/c)^2]$	E_e (GeV)	$E_{e'}$ (GeV)	$\theta_{e'}$	T_n (MeV)	Precession angles χ
0.447	0.884	0.643	52.65°	239	±40°
1.136	2.326	1.718	30.93°	606	0°, ±90°
1.169	2.415	1.789	30.15°	624	±40°
1.474	3.395	2.606	23.55°	786	0°, ±40°, ±90°

B. Polarized electron source

Polarized electrons were produced at the accelerator source via optical illumination of a strained GaAs photocathode (GaAs on GaAsP [55]) with circularly polarized laser light from a ∼500 mW Ti-sapphire laser [55,56]; the linearly polarized light from the laser was circularly polarized with a Pockels cell. The helicity of the circularly polarized light emerging from the Pockels cell was flipped at a frequency of 30 Hz (by switching the polarity of the high voltage applied to the Pockels cell) according to a pseudorandom scheme in which the helicity of one 33.3-ms window was randomly chosen, and the helicity of the following 33.3-ms window required to be that of the opposite helicity (i.e., a sequence of such "helicity pairs" could have been $+-$, $-+$, $-+$, $+-$, etc.). A $\lambda/2$ plate was intermittently placed in the optics path upstream of the Pockels cell. This $\lambda/2$ plate reversed the helicity of the electron beam that would otherwise have been induced by the Pockels cell, thereby providing the means for important systematic checks of any possible helicity-correlated differences.

C. Hall C beamline

Beam of the desired energy was extracted from the accelerator and then transported along the Hall C arc (series of steering/bending magnets) and beamline. A number of superharps [57] were used to monitor the beam profile, and four beam position monitors (cavities with four antennas oriented at angles of ±45° relative to the horizontal and vertical directions) provided absolute determinations of the beam position. The beam current was monitored with two monitors (cylindrical wave guides with wire loop antennas coupling to resonant modes of the beam cavity, yielding signals proportional to the current).

D. Beam polarization measurements

The beam polarization was measured periodically with a Møller polarimeter [58] located along the Hall C beamline approximately 30 m upstream of the cryotarget. We measured the beam polarization approximately every 1 to 2 days during stable accelerator operations. Measurements were also typically conducted following the insertion or removal of the $\lambda/2$ plate at the polarized source or other major accelerator changes. A statistical precision of <1% was typically achieved after ∼15–20 min of data taking. Details of the results of our beam polarization measurements are discussed later, where it will be seen that the details of the analysis are relatively insensitive to the exact values of the beam polarization. Instead, the beam polarization information was primarily used to assess systematic uncertainties associated with temporal fluctuations in the polarization.

It should be noted that although our production scattering asymmetry data were taken with beam currents as high as 70 μA, the Møller polarimeter was designed only for currents up to ∼8 μA (because of the heating and subsequent depolarization of the iron target foil); therefore, it was necessary to assume that our beam polarization measurements conducted at currents of 1–2 μA were valid for the higher beam currents of our production running. The validity of this assumption has been verified for operations in Hall A at JLab where the results from beam polarization measurements conducted at low currents (Møller polarimeter) and high currents (Compton polarimeter) were found to agree to $\sim$3% [59].

E. Scattering chamber and cryotargets

The scattering chamber consisted of a vertically standing cylindrical aluminum chamber vacuum coupled to the incoming beamline. Two exit windows (made of beryllium) faced the HMS and NPOL, whereas an exit port faced the downstream beamline leading to the beam dump. During our experiment, the scattering chamber housed only one target ladder divided into a cryogenic target section and a solid target section. The cryogenic target section consisted of three cryogenic target "loops." Each of these loops consisted of 4- and 15-cm long aluminum target "cans," heat exchangers (heat loads from the electron beam were typically several hundred watts), high- and low-power heaters (used to maintain the cryotargets at their specified temperatures and to correct for fluctuations in the beam current), and various sensors. Liquid deuterium and liquid hydrogen, maintained at (nominal) operating temperatures of 22 and 19 K, respectively, circulated through two of these loops; the third loop was filled with gaseous helium. Solid (carbon) targets and 4- and 15-cm long "dummy targets," composed of two aluminum foils spaced 4 and 15 cm apart, were mounted on the solid target section of the target ladder. As discussed in more detail later, data were taken with the dummy targets to assess the level of contamination because of scattering from the target cell windows. The thicknesses of the liquid deuterium and liquid hydrogen target cell windows were on the order of 4–6 mils, whereas those of the dummy targets were much thicker and on the order of 36–37 mils.

To mitigate the effects of local boiling, the beam was rastered over a 2×2 mm^2 spot on the cryotargets using a fast raster system [60] located $\sim$21 m upstream of the cryotargets. Target conditions (e.g., temperatures, heater power levels, etc.) were monitored continuously throughout the duration of the experiment using the standard Hall C cryotarget control system.

F. High momentum spectrometer

Scattered electrons were detected in the HMS, a three-quadrupole, single-dipole (QQQD) spectrometer (all magnets are superconducting) with a solid angle acceptance of 6 msr (defined by an octogonally shaped flared collimator), a maximum central momentum of 7.5 GeV/c, a $\pm$18% momentum acceptance, and a $\sim$27 m flight path from the target to the detector package.

1. Magnets

The three quadrupole magnets and the dipole magnet are mounted on a common carriage that rotates on a rail system about the target. The quadrupoles are 1.50 T maximum 20-ton (first, Q_1) and 1.56 T maximum 30-ton (second, Q_2, and third, Q_3) superconducting coils with magnetic lengths of 1.89 and 2.10 m, respectively. Q_1 and Q_3 are used for focusing in the dispersive direction, whereas Q_2 provides transverse focusing. The dipole is a 1.66 T maximum 470-ton superconducting magnet with a magnetic length of 5.26 m, a bend angle of 25°, and a bend radius of 12.06 m.

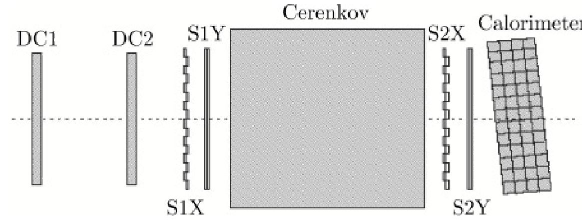

FIG. 2. Schematic diagram of the ordering of the HMS detector package elements. Shown are the two drift chambers (DC1 and DC2), the two x-y hodoscopes (S1X/S1Y and S2X/S2Y), the gas Cerenkov counter, and the lead-glass calorimeter.

The magnets were operated in their standard point-to-point tune in both the dispersive and nondispersive directions. For our central Q^2 points of 0.447, 1.136, 1.169, and 1.474 (GeV/c)^2, the nominal field strengths of Q_1 were 0.11, 0.31, 0.32, and 0.46 T; those of Q_2 were 0.13, 0.37, 0.38, and 0.55 T; those of Q_3 were 0.06, 0.17, 0.18, and 0.26 T; and, finally, those of the dipole were 0.18, 0.47, 0.49, and 0.71 T.

2. Detector package

The detector package is enclosed within a concrete shielding hut and includes two drift chambers, two sets of hodoscopes, a gas Cerenkov counter, and a lead-glass calorimeter. A schematic diagram depicting the ordering of the detector package elements is shown in Fig. 2.

a. Drift chambers. The two multiwire drift chambers [61], used for tracking, each consist of six wire planes: (1) the X and X' planes, which provide position information on the x coordinate (dispersive direction); (2) the Y and Y' planes, which provide position information on the y coordinate (nondispersive direction); and (3) the U and V planes, which are inclined at $\pm15°$ angles relative to the orientation of the X and X' planes. As seen by incoming particles, the ordering of these planes is $XYUVY'X'$. The active area of each plane is 113 (x) $\times$ 52 (y) cm^2 with an alternating sequence of anode wires (25 μm gold-plated tungsten) and cathode wires (150 μm gold-plated copper-beryllium) spaced $\sim$1 cm apart. The individual wire planes are separated by 1.8 cm, and the two drift chambers are separated by 81.2 cm. The chambers were filled with equal mixtures (by weight) of argon and ethane and maintained at a pressure slightly above atmospheric pressure. The signals from the anodes were read out in groups of 16 by multihit time-to-digital convertors (TDCs). The fast branch of the signals from the hodoscope TDCs (to be described shortly) defined the TDC start for the electron arm trigger, whereas the delayed signals from the drift chamber TDCs formed the TDC stop.

b. Hodoscopes. The x (y) planes of the two hodoscopes, denoted S1X/S2X (S1Y/S2Y), consist of 16 (10) 75.5-cm (120.5-cm) long Bicron BC404 plastic scintillator bars with a thickness of 1.0 cm and a width of 8.0 cm. UVT lucite light guides and Philips XP2282B photomultiplier tubes (PMTs) are coupled to both ends of each scintillator bar. The S1X/S1Y and S2X/S2Y planes are separated by $\sim$2.2 m. The fast branch of the PMT signals was routed to leading-edge discriminators. The discriminated signals were then split, with one set of outputs directed to logic delay modules, TDCs, and scalers, and the other set directed to a logic module. The overall logic signaling a hit in any one of the hodoscope planes required a signal above threshold in at least one of the 16 (10) PMTs mounted on the $x > 0$ ($y > 0$) side of the bars and at least one of the 16 (10) PMTs mounted on the opposite $x < 0$ ($y < 0$) side. The slow branch of the PMT signals was directed to analog-to-digital convertors (ADCs).

c. Cerenkov detector. The Cerenkov detector is a cylindrical tank (165-cm length and 150-cm inner diameter) filled with Perfluorobutane (C_4F_{10}, index of refraction $n = 1.00143$ at STP). The pressure and temperature in the tank were monitored on an (approximately) daily basis and were observed to be highly stable. Pressures were typically $\sim$0.401–0.415 atm (indices of refraction $\sim$1.00057–1.00059), translating into energy thresholds of $\sim$21 MeV ($\sim$5.6 GeV) for pions (electrons). The tank is viewed by two mirrors, located at the rear of the tank, which focus the resulting Cerenkov light into two Burle 8854 PMTs. The signals from these PMTs were directed to ADCs. During this experiment, information from the Cerenkov detector was used only for electron-hadron discrimination and not for HMS trigger logic purposes.

d. Lead-glass calorimeter. The calorimeter consists of 52 TF1 lead-glass blocks stacked into four vertical layers of 13 blocks each. Each block has dimensions of $70 \times 10 \times 10$ cm^3, corresponding to $\sim$16 radiation lengths for the total four-layer-thickness of 40 cm. As is indicated in Fig. 2, the four layers of the calorimeter are tilted at an angle of 5° relative to the central axis of the detector package to eliminate losses in the gaps between the individual blocks. Philips XP3462B PMTs are coupled to one end of each block, and the signals from these PMTs were routed to ADCs. Again, information from the lead-glass calorimeter was not used for HMS trigger logic purposes during this experiment.

IV. NEUTRON POLARIMETER

A. Overview

A schematic diagram of the experimental arrangement with an isometric view of the neutron polarimeter is shown in Fig. 3. The first element in the NPOL flight path was a dipole magnet (Charybdis) with a vertically oriented field that was used to precess the neutrons' spins through an angle χ in a horizontal plane. As a by-product, protons and other charged particles were swept from the acceptance during asymmetry measurements conducted with the field energized. The next item in the flight path was a 10.16-cm-thick lead curtain, located directly in front of a steel collimator (not shown in this figure). The lead curtain served to attenuate the flux of electromagnetic radiation and to degrade in energy the flux of charged particles incident on the polarimeter's detectors.

The polarimeter consisted of 70 plastic scintillation detectors enclosed within a steel-and-concrete shielding hut. The front array of the polarimeter functioned as the polarization analyzer (via spin-dependent scattering from unpolarized

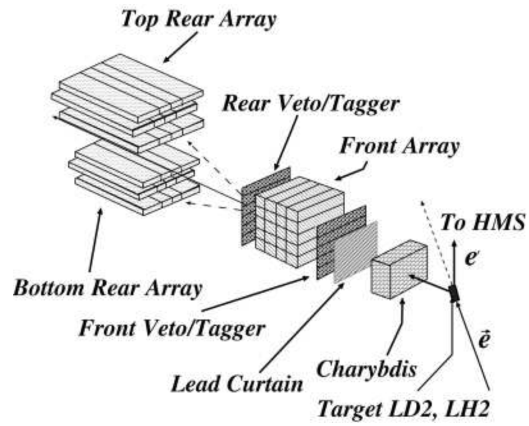

FIG. 3. Isometric view of the NPOL flight path showing the Charybdis dipole magnet, the lead curtain, the front veto/tagger array, the front array, the rear veto/tagger array, and the top and bottom rear arrays.

protons in hydrogen and carbon nuclei), whereas the top and bottom rear arrays, shielded by the collimator from a direct line-of-sight to the target, were configured for sensitivity to an up-down scattering asymmetry proportional to the projection of the recoil polarization on a horizontally oriented "sideways" axis (see next subsection). Double layers of thin-width "veto/tagger" detectors located directly ahead of and behind the front array tagged incoming and scattered charged particles. The flight path from the center of the target to the center of the front array was 7.0 m, and the distance from the center of the front array to the center of the rear array (along the polarimeter's central axis) was $\sim$2.5 m.

B. Polarimetry

1. Coordinate systems

Here we establish some necessary notation for a number of different coordinate systems to which we refer throughout the remainder of this article.

First, calculations of recoil polarization for the quasielastic $^2\mathrm{H}(\vec{e}, e'\vec{n})^1\mathrm{H}$ reaction are usually referred to a $(\hat{t}, \hat{n}, \hat{\ell})$ *reaction basis*, defined on an *event-by-event basis* in the n-p c.m. frame according to

$$\hat{\ell} \| \mathbf{p}_n^{\mathrm{c.m.}}, \quad \hat{n} \| \mathbf{q}^{\mathrm{c.m.}} \times \mathbf{p}_n^{\mathrm{c.m.}}, \quad \hat{t} = \hat{n} \times \hat{\ell}, \tag{6}$$

where $\mathbf{p}_n^{\mathrm{c.m.}}$ and $\mathbf{q}^{\mathrm{c.m.}}$ denote, respectively, the incident neutron's momentum and the momentum transfer in the n-p c.m. frame. The reaction basis can best be visualized by referring to the schematic diagram of the kinematics in the n-p c.m. frame shown in Fig. 30 of Appendix A.

Second, we define a *polarimeter basis*, ($\hat{x}_{\mathrm{NPOL}}$, $\hat{y}_{\mathrm{NPOL}}$, $\hat{z}_{\mathrm{NPOL}}$), *fixed for all events*, defined in the laboratory frame according to

$$\hat{z}_{\mathrm{NPOL}} \parallel \text{NPOL central axis}, \tag{7a}$$

$$\hat{y}_{\mathrm{NPOL}} \perp \text{Hall C floor}, \tag{7b}$$

$$\hat{x}_{\mathrm{NPOL}} = \hat{y}_{\mathrm{NPOL}} \times \hat{z}_{\mathrm{NPOL}}, \tag{7c}$$

with the center of the target defined to be the origin of this coordinate system.

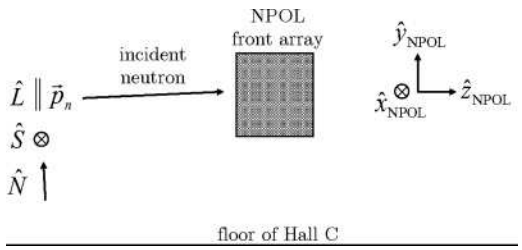

FIG. 4. Schematic diagram of the ($\hat{x}_{\rm NPOL}$, $\hat{y}_{\rm NPOL}$, $\hat{z}_{\rm NPOL}$) polarimeter basis (fixed for all events) and the ($\hat{S}$, $\hat{N}$, $\hat{L}$) polarimeter momentum basis (defined on an event-by-event basis). Note that as $\mathbf{p}_n$ is not, in general, restricted to the $\hat{y}_{\rm NPOL}$-$\hat{z}_{\rm NPOL}$ plane, $\hat{S}$ is not, in general, parallel to $\hat{x}_{\rm NPOL}$.

Third, the symmetric geometric configuration of the polarimeter's top/bottom rear arrays suggests the introduction of a *polarimeter momentum basis*, ($\hat{S}$, $\hat{N}$, $\hat{L}$), which we again define on an *event-by-event basis* in the laboratory frame according to

$$\hat{L} \parallel \hat{p}_n, \quad \hat{S} \parallel \hat{y}_{\rm NPOL} \times \hat{p}_n, \quad \hat{N} = \hat{L} \times \hat{S}, \tag{8}$$

where $\hat{p}_n$ denotes a unit vector along the incident neutron's momentum in the laboratory frame. We will henceforth refer to the $\hat{S}$ and $\hat{L}$ axes as the polarimeter's "sideways" and "longitudinal" axes of sensitivity, respectively. We express the recoil polarization in terms of the polarimeter momentum basis as $\mathbf{P} = P_S\hat{S} + P_N\hat{N} + P_L\hat{L}$.

A schematic diagram showing the orientation of the polarimeter basis and polarimeter momentum basis coordinate systems is shown in Fig. 4.

2. *Detected scattering asymmetry*

We define NPOL polar and azimuthal scattering angles, denoted $\theta_{\rm scat}$ and $\phi_{\rm scat}$, according to

$$\sin\theta_{\rm scat} = |\hat{p}_n \times \hat{p}'_n|, \tag{9a}$$

$$\cos\phi_{\rm scat} = \hat{S}\cdot\hat{u}, \tag{9b}$$

where $\hat{p}'_n$ is a unit vector along the scattered neutron's three-momentum, and the unit vector $\hat{u}$ is defined according to $\hat{u} = (\hat{p}_n \times \hat{p}'_n)/|\hat{p}_n \times \hat{p}'_n|$.

The cross section for elastic polarized-nucleon, unpolarized-nucleon scattering, denoted $\sigma(\theta_{\rm scat}, \phi_{\rm scat})$ for short, is of the form [62]

$$\begin{aligned}\sigma(\theta_{\rm scat}, \phi_{\rm scat}) &= \sigma_0(\theta_{\rm scat})[1 + A_y(\theta_{\rm scat})\mathbf{P}\cdot\hat{u}] \\ &\approx \sigma_0(\theta_{\rm scat})[1 + A_y(\theta_{\rm scat})P_S\cos\phi_{\rm scat}],\end{aligned} \tag{10}$$

where $\sigma_0(\theta_{\rm scat})$ and $A_y(\theta_{\rm scat})$ denote the unpolarized cross section and the analyzing power, respectively. The above approximation is valid in the limit that P_N is small. It is then clear that the asymmetry, $\xi(\theta_{\rm scat}, \phi_{\rm scat})$, between scattering "up" ($\hat{S}\cdot\hat{u} < 0 \Rightarrow \cos\phi_{\rm scat} < 0$) and scattering "down" ($\hat{S}\cdot\hat{u} > 0 \Rightarrow \cos\phi_{\rm scat} > 0$) into infinitesimal solid angles ($\theta_{\rm scat}, \phi_{\rm scat}$) and ($\theta_{\rm scat}, \phi_{\rm scat} + \pi$), respectively, for a particular value of P_S is

$$\begin{aligned}\xi(\theta_{\rm scat}, \phi_{\rm scat}) &= \frac{\sigma(\theta_{\rm scat}, \phi_{\rm scat}) - \sigma(\theta_{\rm scat}, \phi_{\rm scat} + \pi)}{\sigma(\theta_{\rm scat}, \phi_{\rm scat}) + \sigma(\theta_{\rm scat}, \phi_{\rm scat} + \pi)} \\ &= A_y(\theta_{\rm scat})P_S\cos\phi_{\rm scat}.\end{aligned} \tag{11}$$

A single value of P_S is not, of course, presented to the polarimeter. Also, the top and the bottom rear arrays have a finite geometry; therefore, if the polarimeter is geometrically symmetric in $\phi_{\rm scat}$ (i.e., geometrically symmetric top and bottom rear arrays), the detected scattering asymmetry (i.e., averaged over kinematics and the top/bottom finite geometry), $\langle\xi\rangle$, is

$$\langle\xi\rangle = \langle P_S\rangle A_y^{\rm eff}, \tag{12}$$

where $\langle P_S\rangle$ and $A_y^{\rm eff}$ denote, respectively, the acceptance-averaged value of the sideways component of the polarization and the polarimeter's effective analyzing power averaged over its geometric acceptance (i.e., over $\cos\phi_{\rm scat}$). Henceforth, when we refer to the analyzing power A_y, it should be understood that we are referring to $A_y^{\rm eff}$.

C. Charybdis dipole magnet and spin precession

The Charybdis magnet was a water-cooled, 38-ton, 1.5-m-tall, 2.3-m-wide, and 1.7-m-long iron dipole magnet installed in Hall C specifically for this experiment. The magnet was configured such that the gap between the pole pieces was 8.25 inches, and the geometric center of the magnet was located a distance of 2.107 m from the center of the target. The two poles were wired in parallel and powered with a 160-V 1000-A power supply. Two-inch-thick iron field clamps with apertures machined to match the 8.25-inch pole gap were placed at the entrance and exit apertures, resulting in an effective magnetic length of ~1.7 m.

Calculations of the Charybdis field profile were performed with the TOSCA program [63] for various currents, and values for the field integral, $\int|\mathbf{B}|d\ell$, along the central axis were derived from these calculations. The currents were tuned for the various spin precession angles, χ, according to the relation

$$\chi = \frac{\mu_N g}{\beta_n}\int|\mathbf{B}|d\ell, \tag{13}$$

where μ_N is the nuclear magneton, $g/2 = -1.913$ for the neutron, and β_n denotes the neutron's velocity in units of c. The field integrals for the precession angles at each of our Q^2 points are tabulated in Table III.

The field along the central axis was mapped [64] at the conclusion of the experiment. We found that the values for the field integrals derived from our mapping results and the TOSCA calculations agreed to better than 0.76% for

TABLE III. Summary of the nominal values of the field integrals (along the central axis) for the spin precession angles at each Q^2 setting. β_n denotes the neutron velocity in units of c for the nominal (central) kinematics.

Central Q^2 [(GeV/c)^2]	β_n	Precession angle χ	$\int|\mathbf{B}|d\ell$ (T-m)
0.447	0.604	$\pm40^\circ$	0.6884
1.136	0.794	$\pm90^\circ$	2.0394
1.169	0.799	$\pm40^\circ$	0.9123
1.474	0.839	$\pm40^\circ$	0.9576
1.474	0.839	$\pm90^\circ$	2.1547

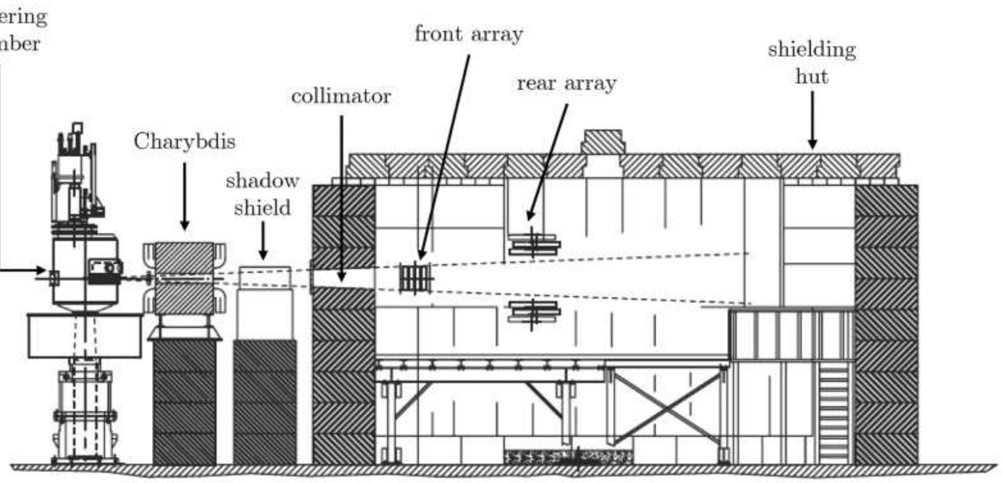

FIG. 5. Schematic diagram (side view) of the NPOL shielding hut. The physical acceptance of the polarimeter, as defined by the collimator, is indicated by the dashed lines originating in the target. The rear array detectors were shielded from a direct line-of-sight to the target. The shadow shield, when inserted, was used to assess the room background rates.

$\chi = \pm 40^\circ$ precession at $Q^2 = 0.447$ (GeV/c)^2, 0.21% for $\chi = +40^\circ$ precession at $Q^2 = 1.169$ (GeV/c)^2, and 0.35% for $\chi = +40^\circ$ precession at $Q^2 = 1.474$ (GeV/c)^2. Small differences in the measured field integrals for the two magnet polarities (corresponding to a $\pm 0.3^\circ$ spread) were observed for $\chi = \pm 40^\circ$ precession at $Q^2 = 0.447$ (GeV/c)^2. Although we did not conduct field measurements for both polarities at the other Q^2 points, it is reasonable to assume that the magnet behaved similarly for other current settings.

D. Neutron polarimeter physical acceptance

The physical acceptance of the polarimeter was defined by a steel collimator with entrance and exit apertures located 483.92 and 616.00 cm, respectively, from the center of the target. The collimator was tapered, with the entrance (exit) port spanning a width of 72.6 cm (92.4 cm) and a height of 37.3 cm (47.5 cm). The 10.16-cm-thick lead curtain was located immediately upstream of the collimator's entrance port.

A schematic diagram of the polarimeter's shielding hut showing the shielding of the rear array detectors by the collimator from a direct line-of-sight to the target appears in Fig. 5.

E. Neutron polarimeter detectors

The polarimeter consisted of a total of 70 mean-timed BICRON-400 plastic scintillation detectors subdivided into a front veto/tagger array, a front array, a rear veto/tagger array, and symmetric top and bottom rear arrays. The front wall of the polarimeter's shielding hut was composed of 132.08-cm-thick steel blocks; the only opening in this wall was the lead-shielded collimator. A schematic diagram of the polarimeter's detector configuration is shown in Fig. 6.

1. Front veto/tagger array

The function of the first series of detectors in the neutron flight path, the front veto/tagger array, was to identify charged

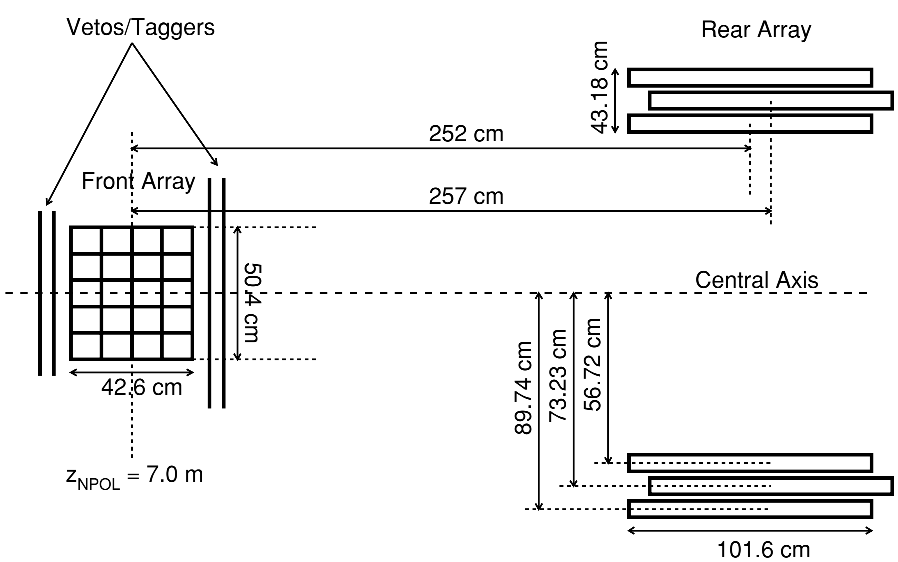

FIG. 6. Schematic diagram (side view) of the NPOL detector configuration showing the top and bottom rear subarrays for measurement of an up-down scattering asymmetry.

particles incident on the polarimeter. This veto array consisted of two vertically stacked layers of five $160.0 \times 11.0 \times 0.635$ cm^3 scintillators stacked with their long (160.0 cm) axes oriented horizontally and perpendicular to the central flight path and the thin (0.635 cm) dimension oriented along the flight path. The vertical spacing between the detectors in each layer was ~1 mm; therefore, to eliminate charged particle leakage, the two layers were offset from each other in the vertical direction by ~1 cm. Each scintillator bar was coupled to two Philips XP2262 2-inch PMTs via Plexiglas light guides.

2. Front array

The front array was segmented into 20 $100 \times 10 \times 10$ cm^3 scintillators; segmentation of the front array permitted us to run with luminosities as high as 3×10^{38} cm^{-2} s^{-1} (70 μA current on a 15-cm liquid deuterium target). The long (100 cm) axes of these detectors were oriented horizontally and perpendicular to the central flight path and were stacked vertically into four layers of five detectors. The long ends of each scintillator were coupled via Plexiglas light guides to 2-inch Hamamatsu R1828-01 PMTs powered by bases designed specifically for this experiment for purposes of high gain and highly linear output under conditions of high rate [65].

3. Rear veto/tagger array

Similar to the front veto/tagger array, the purpose of the rear veto/tagger array was to identify charged particles (e.g., recoil protons from *np* interactions in the front array) exiting the front array. The detectors in this array were identical to those in the front veto/tagger array and were vertically stacked in a similar fashion into two layers of eight detectors each. [We note that only one layer of eight detectors existed for the early part of the experiment during our $Q^2 = 1.136$ (GeV/c)^2 run.] As in the front veto/tagger array, each scintillator was coupled to two 2-inch Philips XP2262 PMTs.

4. Rear array

The top and bottom rear arrays each consisted of 12 detectors stacked into 3 layers of 4 detectors each. Each layer contained two "10-inch" $25.4 \times 10.16 \times 101.6$ cm^3 detectors sandwiched in between two larger "20-inch" $50.8 \times 10.16 \times 101.6$ cm^3 detectors. These detectors were oriented with their long (101.6 cm) axes parallel to the central flight path and their 50.8 or 25.4 cm dimensions oriented horizontally. The centers of the inner, middle, and outer layers were located a vertical distance of 56.72, 73.23, and 89.74 cm, respectively, above or below the central axis of the polarimeter and a horizontal distance of 2.52, 2.57, and 2.52 m, respectively, from the front-array geometric center (see Fig. 6). The long ends of each scintillator were coupled via Plexiglas light guides to 5-inch Hamamatsu R1250 PMTs powered by the same bases built for the front array.

The vertical positions of the top and bottom arrays relative to the polarimeter's central axis were optimized for front-to-rear scattering angles near the peak of the analyzing power for *np* scattering (~15°–20° for our range of neutron energies). This configuration with scattering angles in the vicinity of ~15°–20° also guaranteed, for our kinematics, that only one of the nucleons (for elastic *np* interactions in the front array and assuming straight-line trajectories for the recoil proton through the front array) scattered into either the top or bottom array. We also note that the horizontal position of the middle detector plane was staggered relative to those of the inner and outer layers so that the majority of the front-to-rear tracks passed through at least two of the three horizontal planes, reducing the dependence of the rear array detection efficiency on the scattering angle.

F. Electronics, event logic, and data acquisition

1. Electronics

The signals from the 140 NPOL PMTs were processed with electronics sited in two locations: (1) one set, located inside the shielding hut, was used to form the timing logic signal for each PMT (past experience with neutron time-of-flight and polarimetry experiments [66] revealed that locating the discriminators as close to the PMTs as practical yielded the best timing resolution); and (2) another set, located in the counting house, was used to define the logic for the various event types.

A schematic diagram of the configuration of the electronics in the shielding hut for each scintillator bar in the front and rear arrays is shown in Fig. 7. High voltage was applied to each PMT remotely by an EPICS-controlled 64-channel high-voltage CAEN mainframe crate located in the counting house. Modest levels of high voltage were applied to the PMTs for the front array detectors, as deterioration in the performance of these PMTs was of concern because of the high count rates in these scintillators; however, no deterioriation in their performance was observed during the experiment (instead, gains were stable to within ~10%). To compensate for the resulting lower levels of gain obtained directly from these PMTs, the anode signals were preamplified by fast preamplifiers with a gain of eight, custom-designed and assembled for this experiment. The anode signals from the PMTs in the rear array and the front and rear veto/tagger arrays were not preamplified.

The anode signals from the front and rear arrays were then directed to an LED driver and pulse height monitor. When desired, this device was used to assess the response of each PMT to a flashing blue LED mounted on its light guide. The centroid channels of the LED spectra were monitored periodically, and any necessary changes to the high voltage levels were performed remotely. The gains of the front and rear veto/tagger array PMTs were not monitored with this system.

The anode signals from all four detector arrays were then split. The signals in the fast branch (for the event trigger and timing measurements) were directed to either constant-fraction discriminators (front and rear arrays) or leading-edge discriminators (front and rear veto/tagger arrays) located inside the shielding hut and then sent to the electronics in the counting house. We did not employ constant-fraction discrimination for the veto/tagger array detectors for the following reasons: (1) the dynamic range of energy deposition in these detectors was small for those events of interest, so the time-walk was tolerable; and (2) the timing measurements from these detectors were not used for energy determinations,

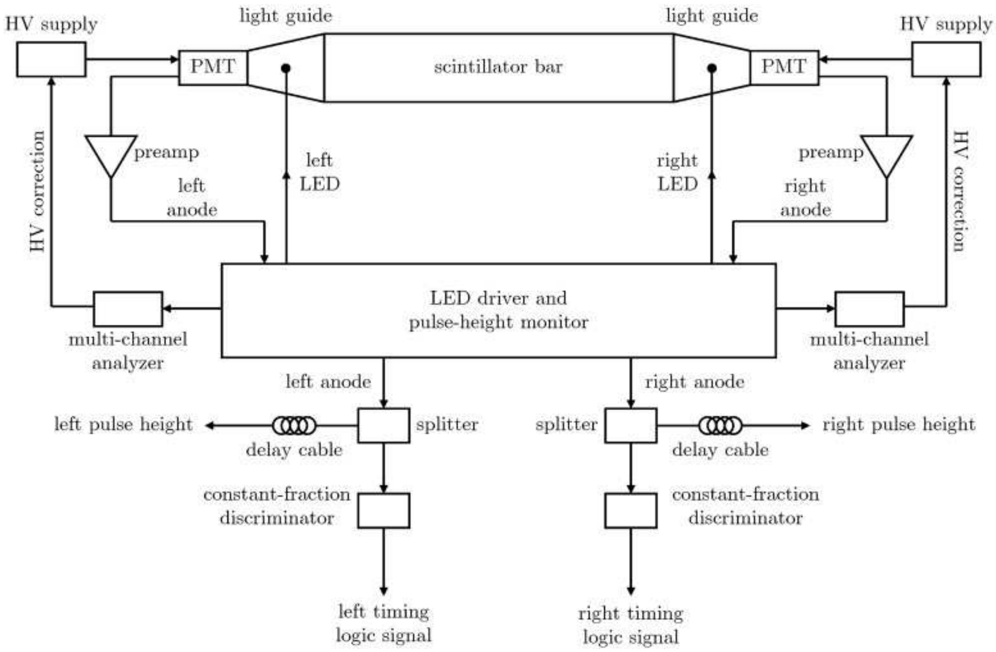

FIG. 7. Schematic diagram of the configuration of the electronics in the shielding hut for the front and rear array detectors. Note that the anode signals from the rear array detectors were not preamplified.

so resolutions of a few ns were sufficient for charged particle tagging. Those signals diverted to the slow branch were routed through delays located inside the shielding hut and then sent to the counting house.

Upon arrival in the counting house, both the analog and timing signals were directed through filters/transformers designed to eliminate low-frequency noise. The analog signals were then sent directly to ADCs, whereas the timing signals were first sent to discriminators and then routed to two branches of a timing circuit. In one branch, the output from these discriminators were directed through level translators, delays, discriminators, and then further split and directed to TDCs and scalers. In the other branch of this timing circuit (used to form the event triggers), the timing signals from the PMTs on all of the detectors, except those in the rear veto/tagger array, were first sent to logic modules that were used to generate logic signals for coincidences between the timing signals for the two PMTs on each detector. Logical ORs were generated for each of the 20 front array detector two-PMT coincidences. These signals were then sent to a fan-in with one set of outputs directed to scalers and the other through a discriminator; the output from this discriminator was then directed to the trigger circuit. The logical ORs for the rear array detectors and the front veto/tagger-array detectors were routed through a fan-in and then directed to the trigger circuit. The timing signals from the rear veto/tagger-array detectors were not used for trigger purposes.

2. *Event logic and triggers*

All event trigger logic was performed by two LeCroy 8LM 2365 Octal Logic Matrix modules. Pretrigger logic signals from the HMS (coincident hits in at least three of the four hodoscope planes), the NPOL front array, the NPOL rear array, and the NPOL front veto/tagger array were routed to the 8LM modules. In addition to these logic signals, triggers from the polarized electron source were also input to these modules. As previously discussed, the helicity of the electron beam was flipped pseudorandomly at 30 Hz. Electronics at the polarized source generated a logic signal for readout of helicity-gated scalers for each 33.3-ms helicity window. Further, these modules also generated a helicity-transition logic signal that was used to veto otherwise valid data triggers that occured during transitions at the polarized source from one helicity state to another. The duration of this helicity-transition logic pulse was $\sim$600 μs, resulting in an effective data-taking helicity window of $\sim$32.7 ms.

An electronic module known as the trigger supervisor (TS) functioned as the interface between the 8LM logic modules and the data acquisition system (DAQ). The TS generated a logic signal indicating the status of the DAQ (e.g., busy or not busy) that was input to the logic modules. The logic modules then determined whether the logic for any of the eight possible physics triggers (e.g., electron singles, electron/front array coincidences, electron/front array/rear array coincidences, etc.) was satisfied. If the logic for any particular trigger was satisfied, the TS generated an accept signal leading to generation of the appropriate ADC gate and TDC common signals. The ADCs, TDCs, and scalers were then read out with real-time UNIX-based processors.

The event triggers of interest were threefold coincidences between hits in the electron arm, the front array, and the rear array. These events constituted $\sim$80–85% of the event triggers, as the higher rate events, such as electron singles or twofold coincidences between the electron arm and the front array, were prescaled.

3. Data acquisition

The DAQ was controlled by the CEBAF Online Data Acquisition System (CODA) [67]. CODA includes an event-builder subsystem programed to assemble the individual ADC channel, TDC channel, and scaler read-out data fragments into an event. The data for the events were then written to disk in CODA format by another subsystem.

Typical data acquisition rates were one million events in ∼1.0 (∼0.5) hr with the Charybdis dipole field energized (deenergized).

V. DATA ANALYSIS

A. Electron reconstruction and tracking

1. Overview of analysis code

The raw ADC, TDC, and scaler data written to disk and encoded by the DAQ in CODA format were decoded with a modified version of the standard Hall C ENGINE analysis code (see, e.g., Ref. [68] for a discussion of the standard version) employed for the analysis of nearly all experiments conducted in Hall C. Modifications to the standard version were necessary to accommodate the raw data stream from the 70 NPOL detectors; hereafter, whenever we refer to the ENGINE analysis code, it should be assumed that we are referring to our modified version of this code.

For each event, the scattered electron's track through the HMS was reconstructed, and various kinematic quantities (e.g., momentum, energy, focal plane distributions, etc.) were computed. ENGINE was not configured to reconstruct the track of the nucleon through the polarimeter; instead, the NPOL detector data were simply written to new data files for later processing by other analysis tools.

2. Extraction of electron information

a. Tracking. The overall strategy of the tracking algorithm [68] was to use the hit information from the drift chambers and reference start times provided by TDC information from the scintillators in the hodoscope planes to reconstruct the trajectory of the particle through the drift chambers. TDC information from those scintillators in the hodoscope planes recording hits was used to establish reference start times. This information, coupled with TDC information from the drift chambers, was then used to determine the location of the hit in the drift chamber planes. "Left-right ambiguities" in the drift chambers (i.e., whether a particle passed to the left or right of any given wire) were resolved by fitting a (straight-line) track to each left-right hit combination in the six planes of each drift chamber. The full track through both drift chambers with the overall smallest track reconstruction χ^2 was defined to be the final reconstructed track through the drift chamber planes.

b. Transport. Engine then attempted to relate the positions and angles at the focal plane (determined from the track through the drift chambers) to target quantities. In standard coordinate notation for transport through a spectrometer, $\hat{z}_{\rm fp}$ is taken to point along the central ray of the spectrometer, $\hat{x}_{\rm fp}$ in the dispersive direction (by convention, taken to point "downwards"), and $\hat{y}_{\rm fp} = \hat{z}_{\rm fp} \times \hat{x}_{\rm fp}$. It should be noted that HMS focal-plane variables are traditionally referred to the detector focal plane, defined to be perpendicular to the central ray (i.e., parallel to the drift chamber planes) with the origin of the $x_{\rm fp}$-$y_{\rm fp}$ plane defined to be that point in space where the central ray of the spectrometer intersects the true (magnetic) focal plane. In addition to the dispersive and nondispersive variables, two other standard transport variables, $x'_{\rm fp}$ and $y'_{\rm fp}$, are defined to be the slopes of the rays at the focal plane, $x'_{\rm fp} \equiv dx_{\rm fp}/dz$ and $y'_{\rm fp} \equiv dy_{\rm fp}/dz$, respectively. The focal plane variables $x_{\rm fp}$, $y_{\rm fp}$, $x'_{\rm fp}$, and $y'_{\rm fp}$ were converted to target quantities $x'_{\rm tar} \equiv dx_{\rm tar}/dz$, $y_{\rm tar}$, $y'_{\rm tar} \equiv dy_{\rm tar}/dz$, and $\delta \equiv (|\mathbf{p}_{e'}| - |\overline{\mathbf{p}_{e'}}|)/|\overline{\mathbf{p}_{e'}}|$, where $|\overline{\mathbf{p}_{e'}}|$ denotes the central momentum setting, via computation of transport matrix elements derived from optics studies. For this choice of target coordinates, $x_{\rm tar}$ was not reconstructed but was, instead, defined to be $x_{\rm tar} = 0$ for all events.

3. Sample electron reconstruction results

Sample histograms of the reconstructed δ distribution, hereafter referred to as the "$\Delta p/p$ distribution," at our lowest and highest Q^2 points are shown in Fig. 8. The quasielastic peak is clearly visible in both spectra, but a large accompanying background of inelastic events associated with pion production in the target is present in the $Q^2 = 1.474$ (GeV/c)^2 spectrum. Inelastic peaks were also clearly visible in the $Q^2 = 1.136$ and 1.169 (GeV/c)^2 spectra but are not shown here. A sample two-dimensional histogram of $\Delta p/p$ plotted versus the

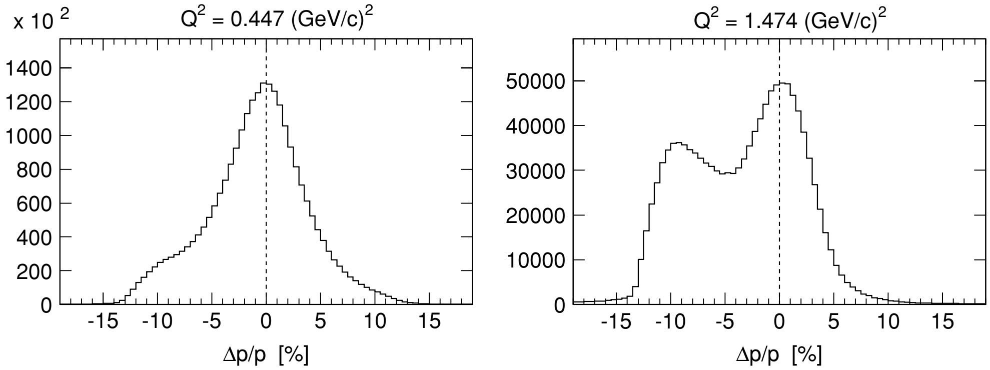

FIG. 8. Distributions of $\Delta p/p$ for the full HMS acceptance at $Q^2 = 0.447$ and 1.474 (GeV/c)^2.

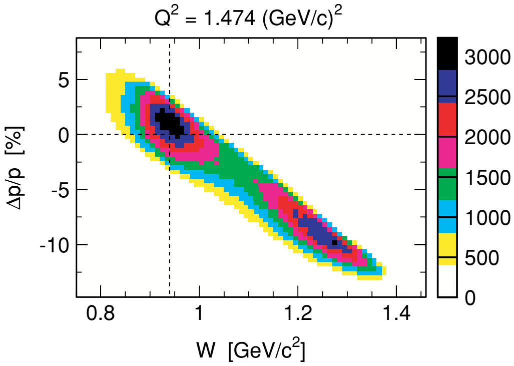

FIG. 9. (Color online) Correlation plot of $\Delta p/p$ versus W for the full HMS acceptance at $Q^2 = 1.474$ (GeV/c)^2.

invariant mass, W, calculated from the electron kinematics according to

$$W = \sqrt{(\omega + m_N)^2 - |\mathbf{q}|^2}, \tag{14}$$

where m_N is the nucleon mass, is shown in Fig. 9 for our $Q^2 = 1.474$ (GeV/c)^2 point. The $\Delta(1232)$ resonance is prominent in this distribution.

Hadrons in the HMS were identified via examination of the Cerenkov photoelectron spectrum. As expected, a hadron peak was not visible in the $Q^2 = 0.447$ (GeV/c)^2 spectrum; however, prominent hadron peaks (at zero photoelectrons) were observed at the three higher Q^2 settings. An example of such a photoelectron spectrum from our $Q^2 = 1.474$ (GeV/c)^2 data is shown in Fig. 10. Cuts on the number of photoelectrons, coupled with cuts on the energy deposition in the calorimeter, were sufficient for electron-hadron discrimination.

B. Neutron polarimeter energy calibration

The (charge-integrating) ADCs for the front and rear array detector PMTs were calibrated with the Compton spectra from a ^{228}Th source (2.61 MeV γ rays); the front and rear veto/tagger array detectors were not calibrated as ADC information was not used for charged particle tagging. These calibrations were parametrized in terms of an equivalent electron energy (denoted "eVee"), where the relation between

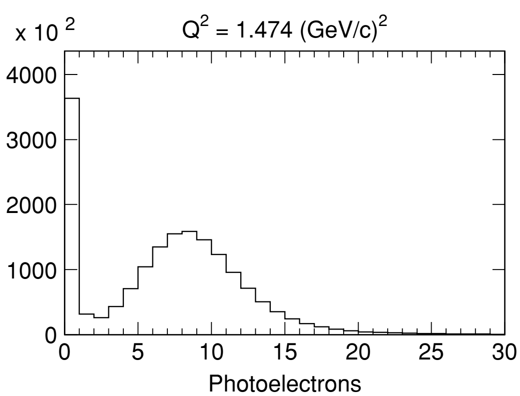

FIG. 10. Cerenkov photoelectron spectrum for the full HMS acceptance at $Q^2 = 1.474$ (GeV/c)^2. A prominent hadron peak appears at zero photoelectrons.

the light output of recoil protons and Compton-scattered electrons in organic scintillator was found by Madey *et al.* [69] to be well described by the parametrization

$$T_e = a_1[1 - \exp(-a_2(T_p)^{a_3}] + a_4 T_p. \tag{15}$$

Here, T_p denotes the energy deposition of a recoil proton, T_e denotes the energy deposition of an electron that yields the equivalent light output, and the a_i are empirically determined parameters.

Unfortunately, the range of electron energies (2.38 MeV Compton edge) was not sufficient, as typical energy depositions for the recoil protons were estimated to be approximately greater than several MeV [13]; further, the hardware thresholds for the front- (rear-) array detectors were set at 4 (10) MeVee. To remedy these shortcomings, a custom-designed linear amplifier with a gain of 10 was placed in the timing circuit during calibration runs. The resulting ADC spectra were fitted to the sum of the Klein-Nishina distribution (smeared by a Gaussian resolution function) and an exponential background tail. Pulse-height calibrations were performed at three different times during the experiment (roughly at the start, middle, and conclusion); minor differences ($\sim$10%) in the extracted calibration parameters were observed but were deemed to be relatively unimportant as the selection of quasielastic ^{2}H$(e, e'n)^1$H events did not rely heavily on pulse height information.

C. Neutron polarimeter timing calibration

To optimize track reconstruction and background rejection in the neutron polarimeter, the relative timing relationships between the NPOL detectors and the HMS were carefully calibrated with a series of algorithms designed to (1) generate position calibrations for each detector, (2) generate relative timing calibrations for each detector in the front array and discern the relationship between the mean time for each front array detector and the trigger mean time, (3) calibrate the timing between the HMS and the front array (yielding a coincidence time-of-flight), (4) generate relative timing calibrations for each detector in the rear array and calibrate the time-of-flight between the front array and the rear array, and (5) generate position and timing calibrations for the front and rear veto/tagger detectors.

1. Front- and rear-array position calibrations

The position calibration algorithm for the front- and rear-array detectors employed data acquired with the Charybdis magnet deenergized, such that charged particles illuminated the front array almost uniformly. The relationship between the hit position and the difference (in channels) between the TDCs from the PMTs mounted on the two ends of each scintillator was parametrized in a linear form with an unknown slope and offset. Histograms of these TDC channel differences were accumulated for each detector and then boxcar smoothed. The algorithm identified the channel of maximum content and then scanned away in both directions until channels with 10% of the maximum content were identified. Slope and offset parameters were then chosen such that these 10%-content channels were aligned with the physical edges of each detector; the resulting calibrated position spectra displayed sharp edges near the physical detector edges.

2. Front-array timing and trigger calibrations

The first goal of the front-array timing calibration was to align the mean times of all the detectors in the front array using events with a single hit in the front array. Data acquired with the Charybdis magnet energized (for suppression of background processes) were employed for this step of the timing calibration, and events with >0 (>1) hits in the front veto/tagger array (front array) were discarded. An offset was chosen for each detector such that the mean value of its mean-time spectrum was aligned on zero.

The second goal of the front array timing calibration was to construct a variable that could be used to identify which hit generated the trigger (for events with multiple front array hits), as the trigger circuit did not identify the triggering hit. Proper identification of the triggering hit via examination of the correlation between the TDC channels for the two PMTs on each detector and the position dependence of the mean times yielded self-timing spectra with FWHM of $\sim$0.4 ns.

3. Coincidence time-of-flight calibrations

To maximize our signal-to-noise ratio, we constructed a coincidence time-of-flight variable that accounted for the quasielastic $^2\mathrm{H}(e,e'n)^1\mathrm{H}$ kinematics, path-length variations through the HMS and NPOL, and variations in the delay between an interaction in a detector and the arrival of its timing signal at the TDC. For this step of the calibration, a minimal set of cuts were applied to the data for purposes of (loose) quasielastic event selection (e.g., cuts on the calorimeter energy deposition, $\Delta p/p$, etc.). Again, front array single-hit events (with no hits in the front veto/tagger array) acquired with the Charybdis magnet energized were used for this step of the calibration.

The algorithm first predicted the neutron time-of-flight from the target to the front array using only position information (i.e., the reconstructed vertex information for the primary scattering event in the target cell and the position of the front array hit) and electron kinematics. For a three-body final state (i.e., no pion production), four-momentum conservation demands

$$m_d + \omega = \sqrt{|\mathbf{p}_n|^2 + m_n^2} + \sqrt{|\mathbf{p}_p|^2 + m_p^2}, \tag{16a}$$

$$\mathbf{q} = \mathbf{p}_n + \mathbf{p}_p. \tag{16b}$$

From this, it follows that a value for $|\mathbf{p}_n|$ (and, then, the predicted neutron time-of-flight) can be derived from the solution to the quadratic equation $A|\mathbf{p}_n|^2 + B|\mathbf{p}_n| + C = 0$, where

$$A = (m_d + \omega)^2 - (\mathbf{q}\cdot\hat{p}_n)^2, \tag{17a}$$

$$B = -2(\mathbf{q}\cdot\hat{p}_n)D, \tag{17b}$$

$$C = m_n^2(m_d + \omega)^2 - D^2, \tag{17c}$$

$$2D = m_d^2 + m_n^2 - m_p^2 - Q^2 + 2m_d\omega. \tag{17d}$$

A value for the actual measured time-of-flight was then extracted from information in the signal output of a TDC started by a signal generated by the NPOL trigger and stopped by the HMS trigger, a correction for path-length variations and delays between interactions and signals in the HMS computed by ENGINE, and the mean time of the front-array detector recording the hit. This measured time-of-flight was then compared with the predicted time-of-flight, and the resulting difference, the coincidence time-of-flight (hereafter, referred to as cTOF), was computed for each event. The resulting cTOF spectra were fairly narrow with FWHM of $\sim$1.25 ns and signal-to-noise ratios of $\sim$6:1–10:1. Sample cTOF spectra are shown later in this article.

4. Rear-array timing calibrations

The algorithm for the rear-array timing calibration selected single-hit events (with no hits in both the front and rear veto/tagger arrays) acquired with the Charybdis magnet energized and then filtered these hits according to a set of cuts designed to select quasielastic events. In addition, a $|\mathrm{cTOF}| \leqslant 2$ ns cut was enforced.

In the first step, the algorithm aligned the mean time spectra of the rear array detectors relative to each other. As for the front array, histograms of mean times were accumulated for each detector. The channel of maximum content was identified, and an offset parameter for each detector was then chosen such that the peak channel was aligned on zero.

In the second step, the algorithm performed an absolute timing calibration of the rear-array detectors relative to the front-array detectors via a front-to-rear velocity calibration. The scattering angle for the front-to-rear track was computed using the incident neutron's three-momentum and the position information for the hits in the front and rear array. The algorithm then predicted the front-to-rear velocity for elastic *np* scattering in the front array via computation of the scattered neutron's kinetic energy, T_{np}, where

$$T_{np} = \frac{2T_n\cos^2\theta_{\mathrm{scat}}}{(\gamma_n+1) - (\gamma_n-1)\cos^2\theta_{\mathrm{scat}}}. \tag{18}$$

Here, T_n denotes the incident neutron's kinetic energy, θ_{scat} denotes the neutron scattering angle in the polarimeter, γ_n is the usual Lorentz factor for the incident neutron, and the proton and neutron masses are assumed to be equal. Relative time-of-flight (hereafter, referred to as rTOF) histograms, defined to be the difference between the predicted and measured values of the front-to-rear time-of-flight, were accumulated, and offsets were then chosen for each detector such that the peak channel was aligned on zero. Again, sample rTOF spectra are shown later in this article.

5. Front and rear veto/tagger array calibrations

The position and timing calibration of the front and rear veto/tagger array detectors consisted of three steps. Data for charged particle tracks acquired with the Charybdis magnet deenergized were employed for this calibration; hits were required in each layer of the front veto/tagger array, the front array, and the rear veto/tagger array.

First, as leading-edge discrimination was employed for these detectors, the algorithm began by computing corrections for walk. The relationship between the observed TDC and ADC channels, $\mathrm{TDC_{obs}}$ and $\mathrm{ADC_{obs}}$, was parametrized as $\mathrm{TDC_{obs}} = \mathrm{TDC} + \gamma \log(\mathrm{ADC_{obs}}/\mathrm{ADC_{peak}})$, where TDC denotes the TDC channel in the absence of walk effects, γ is an empirical parameter, and $\mathrm{ADC_{peak}}$ denotes the peak ADC channel. A value for γ was then computed via the method of least squares.

Second, the veto/tagger array detectors were position calibrated using a different algorithm than that employed for the position calibration of the front and rear array detectors because of the facts that the collimator partly obscured the edges of the front veto/tagger array detectors and that the outer rear veto/tagger array detectors did not receive adequate illumination from front-to-rear charged tracks. (The front and rear veto/tagger arrays were designed to provide more than adequate coverage of target-to-front and front-to-rear charged tracks.) As such, position calibration parameters for these detectors were deduced via a comparison of the recorded hit position with the nearest hit position in the front array, and offset parameters were determined via a χ^2 minimization of the difference between the predicted and recorded hit positions. To improve the statistics for the outer rear array veto/tagger detectors, the algorithm searched for (n, p) charge-exchange events in the front array. Tracks from these events were used to predict hit locations in the rear veto/tagger array detectors, and position calibration parameters were then deduced from another χ^2 minimization of the difference between the predicted and recorded hit positions. The resulting calibrated position spectra were well aligned about the physical center of each detector with somewhat more rounded spectra than observed in the front and rear array spectra because of the use of leading-edge discrimination.

Last, the mean times were aligned relative to each other via the same procedure employed for the mean-time calibration of all the other detectors.

D. Nucleon reconstruction and tracking

1. Overview of analysis code

The algorithm we developed for reconstruction and tracking in the neutron polarimeter began by translating the raw NPOL detector data decoded by ENGINE into hit positions and times. The code then attempted to determine which hit in the front array generated the trigger. All hits were then filtered according to a number of different selection criteria, with the surviving hits grouped into recognizable patterns. The code then attempted to determine the primary hits in the front and rear arrays and the charges of the incident particle and the particle detected in the rear array. Finally, kinematic quantities and time-of-flight variables were then computed for those events satisfying all tracking criteria.

2. Trigger selection and hit filtering

The algorithm assigned the location of the triggering front array hit to the detector with the smallest absolute self-timing value. All hits were then filtered according to a number of selection criteria designed to discard hits with unphysical reconstructed detector positions or mean times falling outside of specified windows. These mean-time windows were chosen sufficiently wide for purposes of quasielastic event selection, elastic/quasielastic scattering in the front array, and charged particle tagging in the veto/tagger arrays. In particular, the mean-time windows for both the front and rear veto/tagger arrays safely bracketed the entire peak regions with the borders extending into the regions of flat background.

3. Pattern grouping and track reconstruction

a. Incomplete and simple events. The algorithm began by identifying incomplete and simple events. First, events with either no surviving hits in the front and/or rear array or events with hits in both the top and bottom rear array were discarded. Second, simple events with exactly one hit in the front array, one hit in the rear array, and no hits in both the front and rear veto/tagger arrays were identified. For these events, the incident particle and the particle detected in the rear array were, obviously, designated neutral particles, and reconstruction of the track was deemed complete.

b. Multiple hit events. The majority of the events were more complicated than these simple events because of propagation of the recoil protons through adjacent scintillator bars or multiple scattering of the neutron. For these more complicated events, the code began by identifying which layer in the front array (i.e., first, second, third, or fourth) was hit first; henceforth, we refer to the hit(s) in this layer as the "first cluster." If the first cluster contained more than one hit, the (vertically) highest and lowest hits were identified; such hit patterns were assumed to be the result of an *np* or *pp* interaction in one detector followed by the penetration of the recoil proton into a vertically adjacent detector. Accordingly, if the hits occurred in noncontiguous detectors within the same vertical layer (i.e., existence of a vertical "gap"), the event was discarded.

The code then searched for evidence of one or more "missing layers" in the front array (e.g., an event with hits in the first layer and the fourth layer); a missing layer was taken to be evidence for multiple scattering of the incident neutron. If such a "second cluster" of hits was not found, the location of the front array scattering vertex was assigned to the highest (lowest) hit in the first cluster if the top (bottom) rear array recorded one or more hits. If, instead, a second cluster of hits was found, the code determined whether the second cluster contained a gap; again, events with gaps in the second cluster were discarded. The algorithm then attempted to discern whether the second cluster was located above or below the first cluster; if the second cluster was above (below) the first cluster, the location of the first cluster scattering vertex was assigned to the highest (lowest) hit in the first cluster. Then, if the top (bottom) rear array was hit, the location of the second cluster scattering vertex was assigned to the highest (lowest) hit in the second cluster. Finally, if more than one hit was recorded in either the top or bottom rear array, the rear array scattering vertex was assigned to that hit closest in distance to the final front array scattering vertex.

Illustrative examples of two possible types of reconstructed tracks are shown in Fig. 11. We note here, and discuss later in Sec. VE2, that events with a "second cluster" were reconstructed but were not used in our extraction of scattering asymmetries.

4. Charge identification

After the track through the front and rear arrays was reconstructed, the code then checked for hits in the veto/tagger

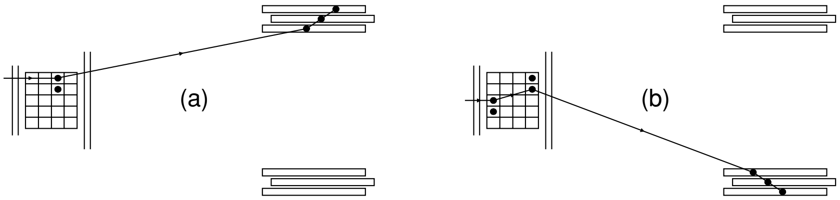

FIG. 11. Examples of reconstructed tracks for (a) an event with a single cluster in the front array, no missing layers, and multiple hits in the top rear array and (b) an event with two clusters in the front array (separated by two missing layers) and multiple hits in the bottom rear array.

arrays. The charge of the incident particle was determined via the following algorithm. (1) If there were no hits in any of the front veto/tagger detectors, the particle was designated a neutral particle. (2) If there were hits in the front veto/tagger detectors, the radial distance between the location of the veto/tagger hit and the location of the first scattering vertex was computed according to $d = \sqrt{(x_{\mathrm{vt}} - x_{\mathrm{fr}})^2 + (y_{\mathrm{vt}} - y_{\mathrm{fr}})^2}$, where the coordinates refer to the polarimeter basis, defined in Eq. (7). If at least one hit in each veto/tagger layer satisfied $d \leqslant 30$ cm, the incident particle was designated a charged particle. If no hits in either veto/tagger layer satisfied $d \leqslant 30$ cm, the incident particle was designated a neutral particle. Finally, if a hit in one of the front/veto tagger layers satisfied this distance requirement but no hits in the other layer satisfied this condition, the charge of the incident particle was declared to be ambiguous.

The algorithm for the determination of the charge of the particle detected in the rear array was essentially identical to that described above. The only difference was that the code predicted where the hits in the rear veto/tagger arrays should have occurred assuming a straight-line trajectory from the final front-array scattering vertex to the rear-array scattering vertex. The computed value of the radial distance between the location of the actual hit and the predicted hit was then used, in an identical manner, for rear-array neutral/charged tagging.

The choice of the 30-cm radial track-distance threshold was based on an examination of track-distance spectra for the front and rear veto/tagger arrays. The spectra for the front veto/tagger array were found to be relatively narrow with an abrupt change in slope around 30 cm, believed to be related to these scintillators' position resolution. The spectra for the rear veto/tagger array did not contain such a feature as the recoil protons arising from interactions in the front array were widely distributed in angle; nevertheless, the same 30-cm condition was employed as the position resolutions for these detectors were similar to those in the front veto/tagger array.

5. *Kinematic distributions and time-of-flight variables*

Following reconstruction of the track through the polarimeter, kinematic and time-of-flight quantities were computed for fully reconstructed events. First, the incident particle's momentum was computed using only position information for the reconstructed target vertex, position information for the first scattering vertex in the front array, and the four-momentum transfer $(\omega, \mathbf{q})$, via solution of the quadratic equation for $|\mathbf{p}_n|$ given previously in Eq. (17). The momentum was then used to predict the target-to-front array time-of-flight; the difference between the predicted and measured time-of-flight was then stored as the cTOF variable. Laboratory frame polar and azimuthal neutron scattering angles with respect to $\mathbf{q}$, θ_{nq} and ϕ_{nq}, were computed from information on $\mathbf{q}$ and $\mathbf{p}_n$. Second, front-to-rear polar and azimuthal scattering angles, θ_{scat} and ϕ_{scat}, were computed using information on $\mathbf{p}_n$ and the scattering vertices in the front and rear arrays. This information was used to compute a value for T_{np}, Eq. (18), which was then used to predict the front-to-rear time-of-flight; the difference between the predicted and measured time-of-flight was then stored as the rTOF variable. Finally, the missing momentum, $\mathbf{p}_{\mathrm{miss}}$, missing energy, E_{miss}, and missing mass, m_{miss}, were computed according to

$$\mathbf{p}_{\mathrm{miss}} = \mathbf{q} - \mathbf{p}_n, \tag{19a}$$

$$E_{\mathrm{miss}} = (m_d + \omega) - (T_n + m_n), \tag{19b}$$

$$m_{\mathrm{miss}} = \sqrt{E_{\mathrm{miss}}^2 - |\mathbf{p}_{\mathrm{miss}}|^2}. \tag{19c}$$

6. *Sample nucleon reconstruction results*

To illustrate the full range of the polarimeter's acceptance, sample two-dimensional histograms of $|\mathbf{p}_{\mathrm{miss}}|$ plotted versus the invariant mass W at our $Q^2 = 1.136$ and 1.474 (GeV/c)^2 points are shown in Fig. 12. A minimal set of cuts designed to eliminate scattering from the target cell walls, hadrons

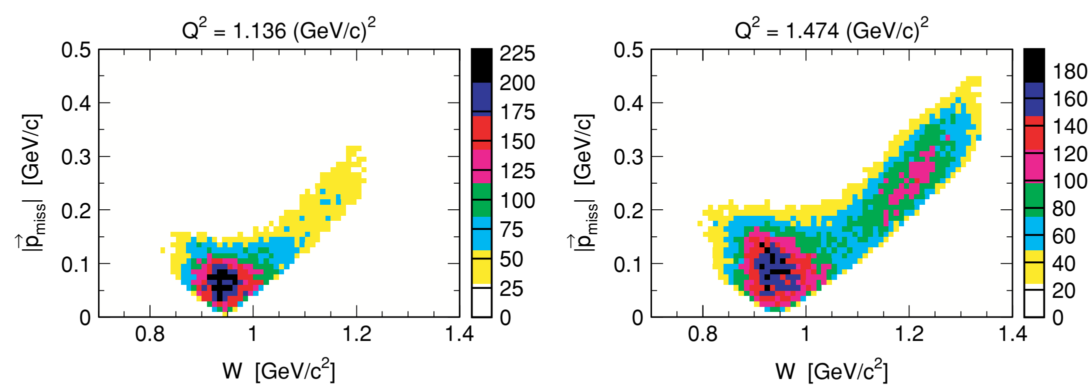

FIG. 12. (Color online) Correlation plot of $|\mathbf{p}_{\mathrm{miss}}|$ versus W for the full NPOL acceptance at $Q^2 = 1.136$ and 1.474 (GeV/c)^2.

in the HMS, and protons incident on NPOL were applied to these spectra. Our acceptance was sensitive to missing momenta ranging up to $\sim$450 MeV/c at our highest Q^2 point. As can clearly be seen in these correlation plots, quasielastic events were associated with missing momenta in the range $\lesssim$150 MeV/c. Larger values of $|\mathbf{p}_{\rm miss}|$ are, of course, seen to correspond to inelastic events, with the $\Delta(1232)$ resonance prominent at large missing momenta in the $Q^2 = 1.474$ (GeV/c)^2 spectrum. The correlation plot for $Q^2 = 1.169$ (GeV/c)^2 was essentially identical to that at $Q^2 = 1.136$ (GeV/c)^2, whereas the $Q^2 = 0.447$ (GeV/c)^2 distribution was restricted to considerably smaller ranges of $|\mathbf{p}_{\rm miss}|$ ($\lesssim$100 MeV/c).

E. Data selection criteria, data sets, and cuts

1. Data selection criteria and data sets

Only those data runs satisfying the following criteria were employed for the final production data analysis: (1) no problems with the HMS equipment (e.g., magnet trips, detector failures, etc.), (2) no problems with delivery of the electron beam (e.g., unstable beam parameters), (3) no problems with the DAQ, (4) no problems with the cryogenic target (e.g., large temperature fluctuations, monitoring system failures, etc.), and (5) no problems with the Charybdis magnet or the NPOL detectors (e.g., fluctuations in the magnet current, detector high-voltage trips, etc.). We note that additional problems may have resulted in the designation of a run as unsuitable for the production analysis.

The quantity of data satisfying the above selection criteria is summarized in Table IV. There, we list the accumulated charge for each of the individual Q^2 points and neutron spin precession angles.

2. Cuts for extraction of time-of-flight spectra

A summary of the final set of cuts applied to the production data sets for extraction of the cTOF and rTOF time-of-flight spectra is as follows.

TABLE IV. Quantity of data (accumulated charge) employed for the final production analysis. A total of 194 Coulombs of charge was delivered to the experiment for production running with the deuterium target.

Central Q^2 [(GeV/c)^2]	Precession angle χ	Charge (Coulombs)
0.447	-40°	25.122
0.447	$+40^\circ$	14.569
1.136	0°	27.587
1.136	-90°	4.701
1.136	$+90^\circ$	4.158
1.169	-40°	7.006
1.169	$+40^\circ$	6.321
1.474	0°	26.239
1.474	-90°	4.097
1.474	$+90^\circ$	4.098
1.474	-40°	20.803
1.474	$+40^\circ$	16.762
Total		161.463

(a) Target variables. Scattering from the target cell windows was suppresed via the requirement that the reconstructed target vertex lie within $\pm$7 cm of the center of the target (for the 15-cm target) along the incident beamline. Further, events with unreasonable reconstructed values for $x'_{\rm tar}$ and $y'_{\rm tar}$ were discarded.

(b) HMS variables. The reconstructed electron track was required to fall within the the collimator acceptance, and events with unreasonably large track reconstruction χ^2 values were discarded. Hadrons in the HMS were suppressed via cuts on the number of Cerenkov photoelectrons and the energy deposition in the calorimeter. Events away from the quasielastic peak were suppressed via a tight $\Delta p/p \in [-3\%, +5\%]$ cut.

(c) NPOL variables. Software thresholds of 8 (20) MeVee designed to suppress low-energy backgrounds were applied to the front- (rear-) array pulse height distributions. Also, to suppress lower-energy neutrons originating from charge-exchange Pb(p, n) reactions in the lead curtain (discussed in more detail later), the mean times for front array hits were required to lie within a $[-5, 5]$ ns window, because of the expected degradation in the energy of the incident protons prior to the charge-exchange reaction. Events with more than one scattering vertex in the front array (i.e., existence of a second cluster) were discarded to eliminate the effects of depolarization following the first interaction in the front array.

The front-to-rear polarimeter scattering angle, $\theta_{\rm scat}$, was required to satisfy $\theta_{\rm scat} \in [5^\circ, 35^\circ]$ at $Q^2 = 0.447$ (GeV/c)^2 and $\in [5^\circ, 30^\circ]$ for the other Q^2 points. The lower cut of 5° eliminated unreasonably small scattering angles, whereas the upper cut of 30° or 35° was used to suppress zero (or negative) values of the analyzing power at larger scattering angles (as predicted by SAID [70]).

(d) $^2H(e, e'n)^1H$ reaction variables. Pion-production events were suppressed via tight cuts on the missing momentum and invariant mass of $|\mathbf{p}_{\rm miss}| \leqslant 100$ MeV/c and $W \leqslant 1.04$ GeV/c^2.

F. Extraction of time-of-flight spectra and scattering asymmetries

1. Polarimeter event types

An analysis code developed to extract the physical scattering asymmetries subjected each event to the cuts discussed previously. In addition, each event was also subjected to a more stringent test for the determination of the incident particle's charge. As we used single-hit TDCs, an early accidental hit in a front veto/tagger detector falling outside the mean-time window for the front veto/tagger array would have prevented that TDC from recording any later (on-time) hits, leading to the incorrect tagging of a charged particle as a neutral particle.

Histograms of cTOF were accumulated for two types of front-array scattering events, (n, n) and (n, p) events, corresponding (for a neutral particle incident on the polarimeter) to the detection of a neutral and charged particle, respectively, in the rear array. We identified (n, n) events with the scattering of the neutron from the front array to the rear array, whereas we identified (n, p) events with forward scattering of the recoil proton with sufficient energy for penetration of the front array. It should be noted that for the incident neutron kinetic energies

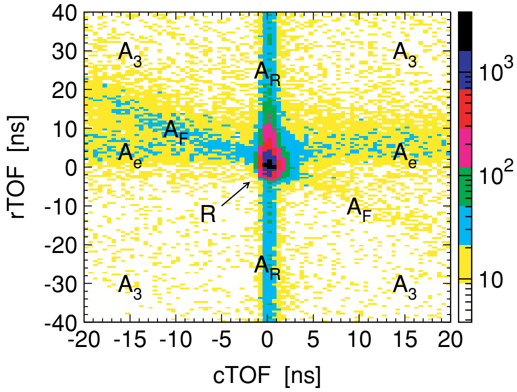

FIG. 13. (Color online) Correlation between cTOF and rTOF at $Q^2 = 1.474$ (GeV/c)^2 with the various event types (see text) identified.

of interest, the analyzing power for elastic np scattering becomes negative for neutron scattering angles greater than $\sim 40^\circ$; therefore, the signs of the detected asymmetries for (n, n) and (n, p) events were the same. Events with charges deemed ambiguous in either the front or rear array were rejected.

Histograms of rTOF summed over all front-to-rear tracks were accumulated for those events falling within a prescribed cTOF window. To compensate for variations in the flight path between the front array and the rear array, the rTOF values were normalized to a nominal 250-cm flight path. The accumulated rTOF spectra were decomposed into the following event types: (1) "RU events" (positive beam helicity and scattering from the front array to the top rear array), (2) "LU events" (negative beam helicity, top rear array), (3) "RD events" (positive beam helicity, bottom rear array), and (4) "LD events" (negative beam helicity, bottom rear array). The scattering asymmetries were then extracted from the yields in these four spectra.

2. HMS-NPOL coincidence event types

A two-dimensional histogram of the correlation between cTOF and rTOF summed over (n, n) and (n, p) events at $Q^2 = 1.474$ (GeV/c)^2 is shown in Fig. 13.

Five different event types can readily be identified in this correlation plot. (1) Real threefold HMS/front-array/rear-array coincidence events are denoted with R and form the peak centered at cTOF = rTOF = 0 ns. (2) Threefold accidental coincidences, denoted with A_3, require a random electron in the HMS, a random neutral particle in the front array, and a random particle in the rear array, and are distributed uniformly over the entire plot area. (3) Real twofold front-array/rear-array coincidences with an accidental electron are denoted with A_e and are associated with the "horizontal band" defined by rTOF = 0 ns. (4) Real twofold electron/front-array coincidences with an accidental rear array particle are denoted with A_R and are identified with the "vertical band" defined by cTOF = 0 ns. (5) Real twofold electron/rear-array coincidences with an accidental front-array particle are denoted with A_F. These events are located along a diagonal band defined (approximately) by cTOF = −rTOF. Such events are attributed to the corruption of an otherwise R-type event by an accidental front array hit occuring some time Δt_A before or after the true interaction. The values of cTOF and rTOF extracted from the data will then be $\mathrm{cTOF} = \mathrm{cTOF}_{\mathrm{uncorr}} - \Delta t_A$ and $\mathrm{rTOF} = \mathrm{rTOF}_{\mathrm{uncorr}} + \Delta t_A$, where the subscript "uncorr" denotes the (true) uncorrupted values. For uncorrupted values centered on zero, it then follows that cTOF = −rTOF, in accordance with the observed result.

3. Quasielastic event selection

Real R-type coincidence events were selected via tight $\mathrm{cTOF} \in [-1, 1]$ ns and $\mathrm{rTOF} \in [-1, 8]$ ns cuts. As evidence our cuts selected quasielastic $^2\mathrm{H}(e, e'n)^1\mathrm{H}$ events, comparisons of invariant mass spectra, W, obtained before and after cuts on $\Delta p/p$, $|\mathbf{p}_{\mathrm{miss}}|$, and cTOF are shown in Fig. 14 for our $Q^2 = 1.136$ and 1.474 (GeV/c)^2 points. After all cuts (except for the additional cut on $W < 1.04$ GeV/c^2 itself), these distributions converged to fairly narrow peaks centered on the neutron mass.

4. Extraction of asymmetries from time-of-flight spectra

One-dimensional projections of cTOF are shown in Fig. 15 for our lowest and highest Q^2 points. Histograms of rTOF were accumulated for those events falling within the [−1, 1] ns peak cTOF window. In addition, histograms of rTOF

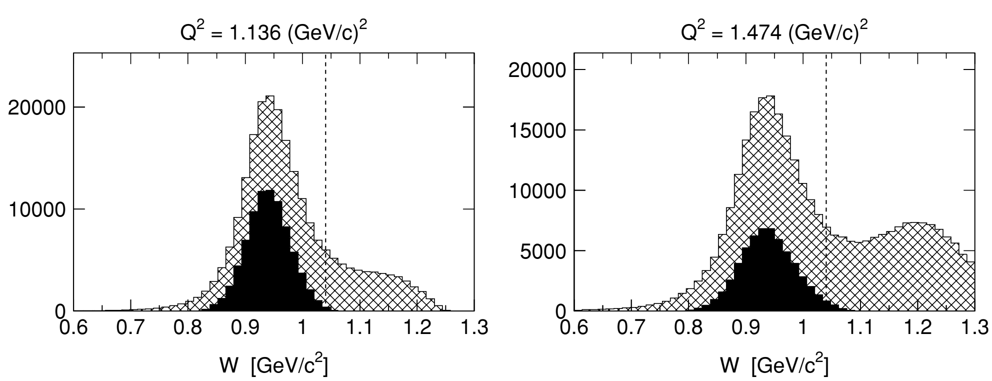

FIG. 14. Distributions of the invariant mass W before (cross-hatched) and after (solid) all cuts except for those on $\Delta p/p$, $|\mathbf{p}_{\mathrm{miss}}|$, and cTOF at $Q^2 = 1.136$ and 1.474 (GeV/c)^2. The vertical dashed lines denote the final $W < 1.04$ GeV/c^2 cut.

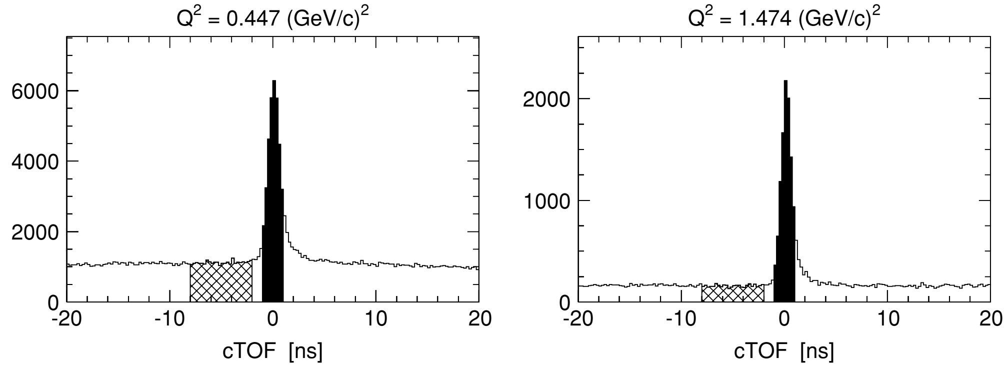

FIG. 15. Distributions of cTOF after application of the final set of cuts at $Q^2 = 0.447$ and 1.474 (GeV/c)^2. The dark shaded regions indicate the selected peak window, whereas the cross-hatched regions indicate the sampled background region.

were accumulated also for a sampled background region of $[-8, -2]$ ns in the cTOF spectrum. The signal-to-noise ratios were independent of the state of the Charybdis magnet at each of our Q^2 points.

Sample rTOF spectra summed over all RU, LU, RD, and LD events for cTOF peak events at our lowest and highest Q^2 points are shown in Fig. 16. The asymmetric tails on the slow sides are because of scattering from protons bound in carbon nuclei and other nuclear reactions, and the small satellite peak observed in the $Q^2 = 1.474$ (GeV/c)^2 spectrum on the fast side at ~ -2.5 ns is attributed to quasifree π^0 production in the scintillators, followed by decay and detection of a photon in the rear array. Indeed, front-to-rear velocity spectra for these events are centered on c. This π^0-production peak was observed in the $Q^2 = 1.136$, 1.169, and 1.474 (GeV/c)^2 rTOF spectra but was absent in the $Q^2 = 0.447$ (GeV/c)^2 spectrum, as the energies of those neutrons were below threshold.

The yields for those events falling within the $[-1, 8]$ ns rTOF window were obtained via peak fitting, with contributions from the π^0-production peak and the flat background excluded. These yields were then further corrected for the contents of the rTOF spectra accumulated for the sampled cTOF background region. The desired quantities, the physical scattering asymmetries, ξ, were extracted from the final background-subtracted yields in the four decomposed rTOF spectra via the cross-ratio technique [71]. In obvious notation, the cross ratio, r, is defined to be the ratio of two geometric means,

$$r = \sqrt{\frac{N_{RU}N_{LD}}{N_{RD}N_{LU}}}, \tag{20}$$

and is related to the asymmetry ξ via

$$\xi = \frac{r-1}{r+1} = \frac{\sqrt{N_{RU}N_{LD}} - \sqrt{N_{RD}N_{LU}}}{\sqrt{N_{RU}N_{LD}} + \sqrt{N_{RD}N_{LU}}}. \tag{21}$$

The merit of the cross-ratio technique is that ξ is insensitive to [71] (1) the number of particles incident on the polarimeter (i.e., target luminosities) for the two beam helicity states and (2) the relative efficiencies and acceptances of the polarimeter's top and bottom rear arrays.

G. Asymmetry results

1. Electron beam polarization normalization

Unlike recoil polarization measurements in which both polarization components, $P_t^{(h)}$ and $P_\ell^{(h)}$, can be extracted simultaneously from the data (e.g., recoil polarization experiments with focal-plane polarimeters), our polarimeter was sensitive to only one of these components (or a combination thereof). As such, it was necessary to normalize our run-by-run

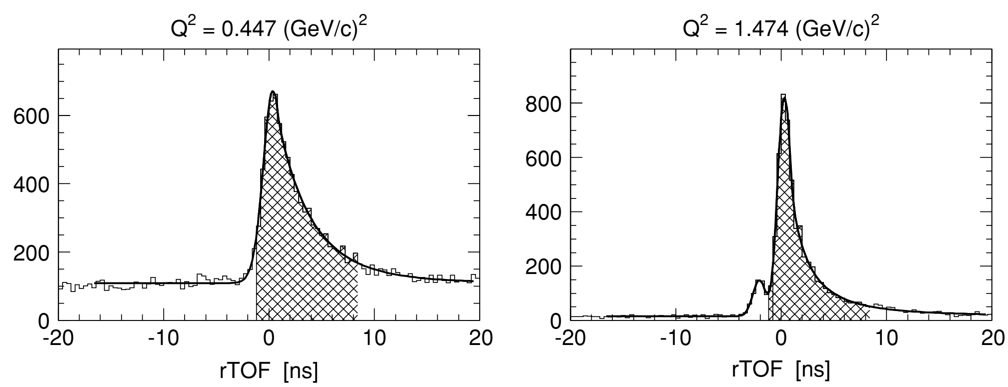

FIG. 16. Distributions of rTOF for cTOF peak events at $Q^2 = 0.447$ and 1.474 (GeV/c)^2. The cross-hatched regions indicate the accepted window. The solid curves are the results of our fits to these spectra.

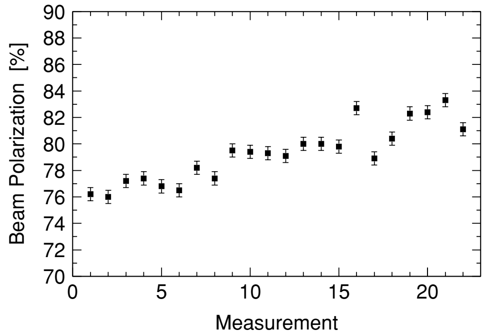

FIG. 17. Results of 23 successive Møller beam-polarization measurements conducted during the $Q^2 = 1.474\ (\mathrm{GeV}/c)^2$ $\chi = \pm 40^\circ$ running period spanning the days of February 20, 2001, through March 5, 2001. The errors shown are statistical.

scattering asymmetries to some common value of the beam polarization.

Our normalization procedure was as follows. As the beam polarization was measured only periodically with the Møller polarimeter, we defined the beam polarization for a run to be the result of the most recent prior Møller measurement (if the accelerator parameters were unchanged in the interim). All of our run-by-run scattering asymmetries and their statistical errors were then normalized to a common value of 80%.

We found that the beam polarization was fairly stable, with small (few percentages) fluctuations observed in successive measurements during periods of continuous beam delivery to our experiment. To illustrate, the results of 23 successive Møller measurements conducted during our $Q^2 = 1.474\ (\mathrm{GeV}/c)^2$ $\chi = \pm 40^\circ$ running period spanning the days of February 20, 2001, through March 5, 2001, are shown in Fig. 17.

2. Corrections for charge-exchange in the lead curtain

Contamination from the two-step $^2\mathrm{H}(\vec{e}, e'\vec{p})$+$\mathrm{Pb}(\vec{p}, \vec{n})$ charge-exchange reaction in the lead curtain could either dilute the "real" $^2\mathrm{H}(\vec{e}, e'\vec{n})$ asymmetry or contribute to a false asymmetry if the flux of charge-exchange neutrons was unpolarized or polarized, respectively. A significant advantage of our neutron flight path setup in which the lead curtain was located downstream of the Charybdis dipole field was that the majority of the quasielastic protons were swept from the front face of the lead curtain.

Accounting for such nuclear reactions, the measured asymmetry, ξ_M, can be parametrized as

$$\xi_M = f_R \xi_R + f_B \xi_B, \tag{22}$$

where f_B denotes the contamination level from the two-step charge-exchange process, ξ_B denotes the asymmetry for charge-exchange neutrons, $f_R = 1 - f_B$ denotes the fraction of $^2\mathrm{H}(\vec{e}, e'\vec{n})$ neutrons, and ξ_R denotes the asymmetry for the $^2\mathrm{H}(\vec{e}, e'\vec{n})$ reaction. The asymmetry for the background process can further be written as

$$\xi_B = \left(P_S^p \cos\chi_p + P_L^p \sin\chi_p\right) D_{SS}^{\mathrm{Pb}} A_y, \tag{23}$$

where P_S^p and P_L^p denote, respectively, the projections of the $^2\mathrm{H}(\vec{e}, e'\vec{p})$ recoil proton's polarization on the polarimeter momentum basis $\hat{S}$ and $\hat{L}$ axis; χ_p is the proton spin precession angle in the Charybdis field; and D_{SS}^{Pb} denotes the polarization transfer coefficient for the $\mathrm{Pb}(\vec{p}, \vec{n})$ reaction. It then follows that if f_B, P_S^p, P_L^p, χ_p, D_{SS}^{Pb}, and A_y are all known or measured, ξ_R can be determined.

To estimate the contamination levels, f_B, we took data with a liquid hydrogen target. The rates for (n, n) and (n, p) events extracted from these data were compared with those extracted from our liquid deuterium data and corrected for differences in the two targets' densities and atomic numbers. We found that the contamination levels were negligible ($\lesssim 0.3\%$) at all of our Q^2 points when the Charybdis field was energized for $\chi = \pm 40^\circ$ and $\pm 90^\circ$ precession and also when the field was deenergized at $Q^2 = 1.136\ (\mathrm{GeV}/c)^2$ for $\chi = 0^\circ$ precession; therefore, we did not apply corrections to any of these asymmetries. Nonnegligible event rates were observed when the Charybdis field was deenergized for $\chi = 0^\circ$ precession at $Q^2 = 1.474\ (\mathrm{GeV}/c)^2$, with observed contamination levels of $\sim$2.2% and $\sim$4.2% for (n, n) and (n, p) events, respectively. Corrections were applied to these asymmetries assuming $D_{SS}^{\mathrm{Pb}} = 0$ for our kinematics of $T_p \sim 786$ MeV. D_{SS}^{Pb} was measured at $T_p = 795$ MeV and found to be consistent with zero (0.014 ± 0.013) [72].

3. Summary of asymmetry results

Our final asymmetry data for (n, n) and (n, p) events at each of our Q^2 points and precession angles are tabulated in Table V. To illustrate the quality of our asymmetry data, a histogram of the (n, n) asymmetries for the $Q^2 = 1.136\ (\mathrm{GeV}/c)^2$ $\chi = 0^\circ$ data set is shown in Fig. 18; the distribution is of an appropriate Gaussian shape.

H. Extraction of uncorrected values for G_{En}/G_{Mn}

We extracted values for G_{En}/G_{Mn} from our asymmetry data assuming elastic scattering from a free neutron and infinitesimal pointlike HMS and NPOL acceptances and

TABLE V. Final (n, n) and (n, p) asymmetry data normalized to a beam polarization of 80%. The $Q^2 = 1.474\ (\mathrm{GeV}/c)^2$ $\chi = 0^\circ$ asymmetries were corrected for contamination from charge-exchange in the lead curtain.

Central Q^2 $[(\mathrm{GeV}/c)^2]$	Precession angle χ	(n, n) ξ [%]	(n, p) ξ [%]
0.447	-40°	-4.51 ± 0.22	-2.97 ± 0.19
0.447	$+40^\circ$	6.38 ± 0.28	4.98 ± 0.29
1.136	0°	1.20 ± 0.13	0.57 ± 0.10
1.136	-90°	-5.71 ± 0.32	-3.11 ± 0.25
1.136	$+90^\circ$	5.67 ± 0.35	3.18 ± 0.25
1.169	-40°	-2.92 ± 0.29	-1.42 ± 0.22
1.169	$+40^\circ$	4.75 ± 0.31	2.76 ± 0.25
1.474	0°	1.29 ± 0.19	0.64 ± 0.17
1.474	-40°	-2.26 ± 0.20	-0.88 ± 0.18
1.474	$+40^\circ$	4.03 ± 0.24	2.11 ± 0.21
1.474	-90°	-4.64 ± 0.47	-2.92 ± 0.50
1.474	$+90^\circ$	5.07 ± 0.49	2.14 ± 0.43

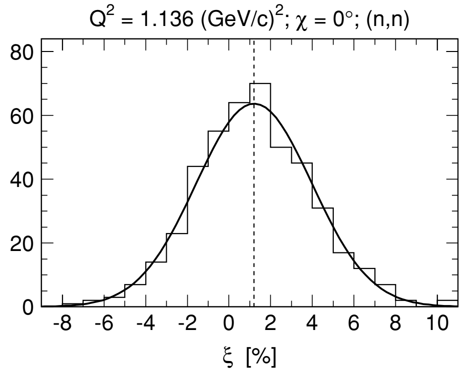

FIG. 18. Histogram of the $Q^2 = 1.136$ (GeV/c)^2 $\chi = 0^\circ$ (n, n) asymmetries. The solid curve is a Gaussian fit, and the vertical dashed line denotes the mean value for the asymmetry given in Table V.

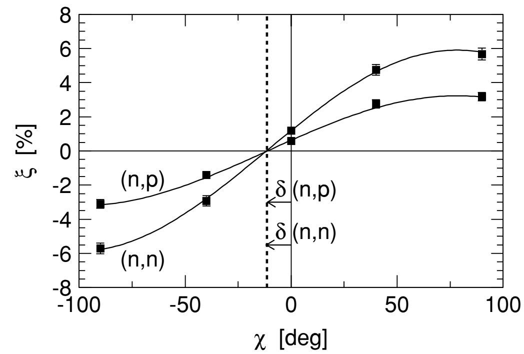

FIG. 19. Sinusoidal fits of the $Q^2 = 1.136/1.169$ (GeV/c)^2 (n, n) and (n, p) asymmetries as a function of the precession angle.

neglecting nuclear physics corrections for FSI, MEC, and IC. To do so, we fitted the asymmetries as a function of the precession angle to the functional form $\xi(\chi) \propto \sin(\chi + \delta)$, where the phase-shift parameter $\delta = \tan^{-1}(P_t^{(h)}/P_\ell^{(h)})$ was defined in terms of form factors and kinematics in Eq. (4). To illustrate the quality of these fits, our $Q^2 = 1.136/1.169$ (GeV/c)^2 (n, n) and (n, p) asymmetry data are plotted as a function of the precession angle in Fig. 19. These data are fitted well by sinusoids with excellent agreement seen between the independent fits to the (n, n) and (n, p) asymmetry data. We could not fit the $Q^2 = 0.447$ (GeV/c)^2 asymmetries to a sinusoid as asymmetry data were taken only at two precession angles.

The values for G_{En}/G_{Mn} we derived from our values for δ using the nominal (central) values for the kinematics listed in Table II are summarized in Table VI.

I. Simulation programs

We developed two independent simulation programs, GENGEN and the ACCEPTANCE program, to extract acceptance-averaged and nuclear physics-corrected values for G_{En}/G_{Mn} from our measured experimental asymmetries. The GENGEN simulation program, a pure Monte Carlo simulation program, included realistic models for the primary $^2\mathrm{H}(\vec{e}, e'\vec{n})^1\mathrm{H}$ reaction in the target, the HMS acceptance, neutron spin precession in the Charybdis dipole field, spin-dependent neutron scattering in the lead curtain, elastic and quasielastic np scattering in the front and rear arrays of NPOL, tracking of the incident neutron and recoil proton from the front array to the rear array, and the detector response of the polarimeter to np interactions in the front and rear array. The ACCEPTANCE program was not a Monte Carlo simulation program, but was, instead, designed to extract the corrections for the finite experimental acceptance and nuclear physics effects directly from our experimental data.

1. GENGEN simulation program

a. Event sampling technique. A uniform sampling scheme was employed in which events were generated uniformly over the available kinematic phase space, with an event weight computed according to a model cross section. The vertex position for the primary $^2\mathrm{H}(\vec{e}, e'\vec{n})^1\mathrm{H}$ interaction in the extended target was sampled uniformly within the raster pattern, and the scattered electron's kinematics were sampled uniformly over specified ranges. The physical acceptance of the HMS was enforced via inclusion of an HMS transport model taken from the SIMC simulation code [73]. In-plane and out-of-plane scattering angles for the recoil neutron were sampled uniformly over specified ranges, permitting computation of the magnitude of the neutron's momentum according to Eq. (17). Complete specification of the electron and neutron kinematics permitted computation of those variables of particular interest for the quasielastic $^2\mathrm{H}(e, e'n)^1\mathrm{H}$ reaction, such as $\Theta_{np}^{\mathrm{c.m.}}$, $\mathbf{p}_{\mathrm{miss}}$, and so on.

b. Cross section and recoil polarization. We employed the Arenhövel formalism [19,20] for computation of the $^2\mathrm{H}(\vec{e}, e'\vec{n})^1\mathrm{H}$ differential cross section and recoil polarization. These calculations modeled the deuteron as a nonrelativistic n-p system and employed the Bonn R-space NN potential [74] for the deuteron wave function and the inclusion of FSI; further, leading-order relativistic contributions (RC) to the

TABLE VI. Values of $\delta = \tan^{-1}(P_t^{(h)}/P_\ell^{(h)})$ and the uncorrected results for G_{En}/G_{Mn} at each of the Q^2 points.

Central Q^2 [(GeV/c)^2]	δ [deg] (n, n)	δ [deg] (n, p)	G_{En}/G_{Mn} (n, n)	G_{En}/G_{Mn} (n, p)	G_{En}/G_{Mn} combined[a]
0.447	8.2 ± 1.5	12.0 ± 1.9	-0.0580 ± 0.0106	-0.0854 ± 0.0138	-0.0681 ± 0.0084
1.136/1.169[b]	11.7 ± 1.2	11.2 ± 1.7	-0.124 ± 0.013	-0.118 ± 0.019	-0.122 ± 0.011
1.474	14.0 ± 1.6	16.9 ± 2.9	-0.166 ± 0.020	-0.203 ± 0.037	-0.174 ± 0.017

[a]Weighted average of G_{En}/G_{Mn} from (n, n) and (n, p) events.
[b]Result obtained via averaging of the nominal (central) electron kinematics for the two Q^2 points.

wave functions and one-body current were added via inclusion of the most important kinematic part of the wave function boost. In the current operator, explicit MEC contributions beyond the Siegert operators (essentially from π and ρ exchange) and IC were included. The treatment of IC permitted consideration of kinematic regions away from the quasielastic ridge and excitations up to the Δ region.

Acceptance-averaging of those calculations performed within the Born approximation (hereafter, termed the PWBA model) permitted extraction of the corrections for the finite experimental acceptance (over the pointlike results discussed in Sec. VH), whereas averaging of the full calculations that included FSI, MEC, IC, and RC (hereafter, termed the FSI+MEC+IC+RC model) permitted application of corrections for nuclear physics effects. To implement the Arenhövel formalism within GENGEN, lookup tables for the structure functions for the $^2\mathrm{H}(\vec{e}, e'\vec{n})^1\mathrm{H}$ reaction were constructed over a sufficiently dense kinematic grid indexed by $(E_{e'}, \theta_{e'}, \Theta_{np}^{\mathrm{c.m.}})$, and tricubic spline interpolation among the grid elements was used to compute the cross section and recoil polarization for the kinematics of each simulated event according to the formalism outlined in Appendix A.

c. Nucleon form factors. All of the structure function calculations assumed the dipole parametrization for G_{Mn}, G_{Ep}, and G_{Mp}. For the form factor of interest, G_{En}, the structure function calculations were first performed for various multiplicative factors of the standard Galster parametrization, $G_{En} = -S\mu_n\tau G_D/(1 + 5.6\tau)$, where the scale factor $S \in \{0.50, 0.75, 1.00, 1.25, 1.50\}$. To investigate the influence of a different Q^2 dependence for G_{En}, structure function calculations were performed also for multiplicative factors of a modified Galster parametrization, $G_{En} = -Sa\mu_n\tau G_D/(1 + b\tau)$, with $a = 0.894$, $b = 3.55$ (which choice will be explained later), and the same set of S factors.

d. Charybdis field transport. The recoil polarization was transported point by point through a grid of the Charybdis field, with the time derivative of the spin vector computed at each grid point according to standard relativistic electrodynamics. The precession angle was computed from information on the initial and final spatial orientations of the spin vector.

e. Lead curtain interactions. Neutron interactions in the lead curtain were simulated with a spin-dependent multiple-scattering algorithm that employed quasifree scattering from a lead nucleus modeled as a Fermi gas, with the Fermi momentum for $^{208}\mathrm{Pb}$ taken to be 265 MeV/c [2]. The probability for an interaction of the neutron with a lead nucleus was determined via interpolation (or extrapolation) of existing data on total $n + \mathrm{Pb}$ cross sections [75]. A polar scattering angle was sampled from cumulative probability distributions for the polar scattering angle as a function of neutron energy, and an azimuthal scattering angle was chosen via an acceptance-rejection algorithm for the spatial scattering asymmetry resulting from nonzero analyzing power. Pauli blocking was enforced. For those neutrons suffering an interaction, the scattered neutron's and recoil nucleon's polarization components were constructed via computation of the depolarization and polarization-transfer tensors for *NN* scattering using helicity amplitude routines obtained from SAID [70].

f. Polarimeter interactions. Finally, following (successful) transport of the neutron through the steel collimator into the front array, interactions in NPOL were simulated. A scattering vertex was chosen randomly assuming a fixed value for the mean free path of neutrons in the plastic scintillator, and both the elastic (scattering from free protons) and quasielastic (scattering from protons bound in carbon nuclei) channels were simulated. The scattering angles in the polarimeter were determined using the same algorithms employed for *NN* scattering in the lead curtain. We employed a rather simple model for the propagation of the recoil proton, with the energy deposition and range (assuming a straight-line trajectory) computed according to the Cecil, Anderson, and Madey [76] range-energy formulas for protons in the hydrocarbon scintillator.

2. GENGEN *performance*

A rigorous and reliable extraction of the corrections for the finite experimental acceptance and nuclear physics effects from simulated data is feasible if the simulated acceptance reasonably matches the experimental acceptance; therefore, we now document the performance of GENGEN by comparing (1) simulated distributions of important kinematic quantities with those derived from experimental data and (2) the behavior of the acceptance-averaged simulated polarizations and the experimental asymmetries as a function of the cut on some kinematic variable (here, taken to be the invariant mass W).

a. Kinematic distributions. Sample comparisons of experimental and simulated kinematic distributions of two important kinematic variables, W and $|\mathbf{p}_{\mathrm{miss}}|$, are shown in Figs. 20 and 21. Reasonable agreement is seen between the GENGEN distributions and those extracted from experimental data. Although not shown here, reasonable agreement was also obtained between simulated and experimental distributions of variables related to *np* scattering in NPOL (e.g., scattering angles, velocity spectra, etc.).

b. Experimental asymmetries and simulated polarizations. A sample comparison of the behavior of the experimental asymmetries and acceptance-averaged simulated polarizations following transport through the Charybdis dipole field is shown in Fig. 22. There, we plot the ratio of the experimental asymmetries to the simulated polarizations as a function of the upper cut on W for (n, p) events and $\chi = -40^\circ$ precession at our $Q^2 = 1.169$ (GeV/c)^2 point. Within statistical errors, the experimental asymmetries and simulated polarizations are seen to scale similarly with the cut on W. Similar results were observed for our other Q^2 points and precession angles.

It should be noted that in this figure the simulated acceptance-averaged polarizations were computed assuming some certain parametrization for G_{En} (here, the Galster parametrization); therefore, the ratios of the asymmetries to the simulated polarizations shown in this figure are not equivalent to the polarimeter's analyzing power.

3. ACCEPTANCE *program*

The ACCEPTANCE program was developed as an alternative to the GENGEN Monte Carlo simulation program. This program used the kinematics of the reconstructed quasielastic events from the actual experimental data to compute, on an

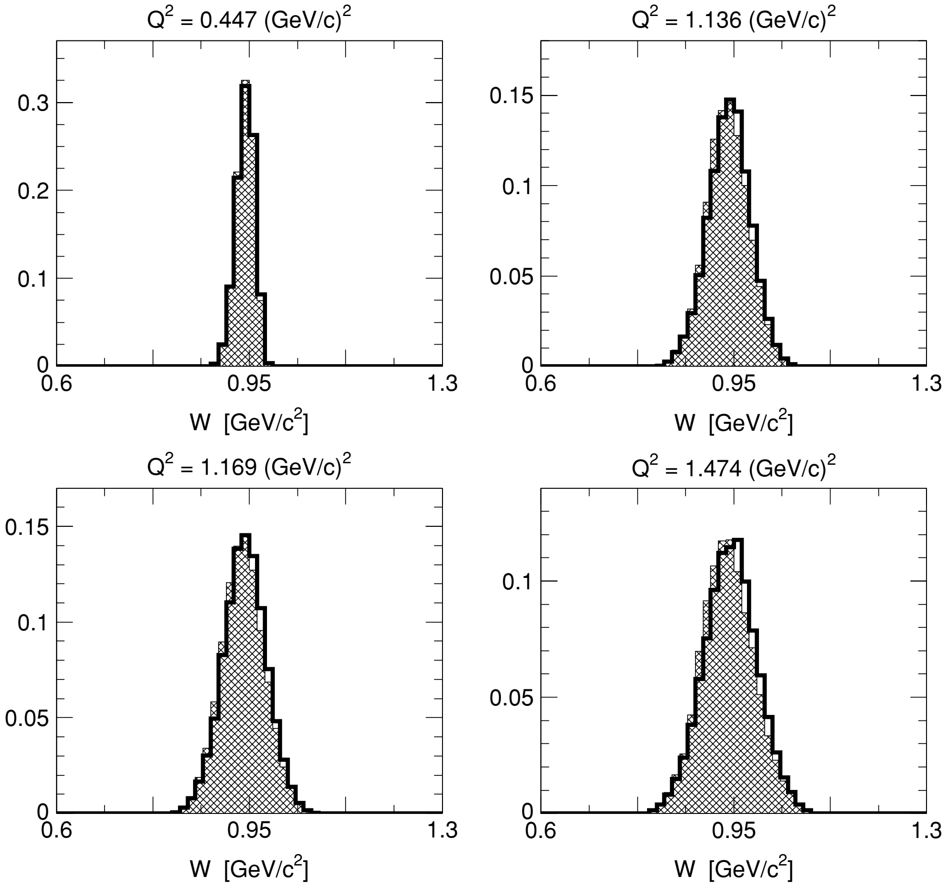

FIG. 20. Comparison of GENGEN simulated (unfilled histograms with thick solid line borders) and experimental (cross-hatched filled histograms) distributions of W for the four central Q^2 points. Identical cuts were applied to both the simulated and experimental data. The simulated results shown here employed the FSI+MEC+IC+RC model and the Galster parametrization for G_{En}.

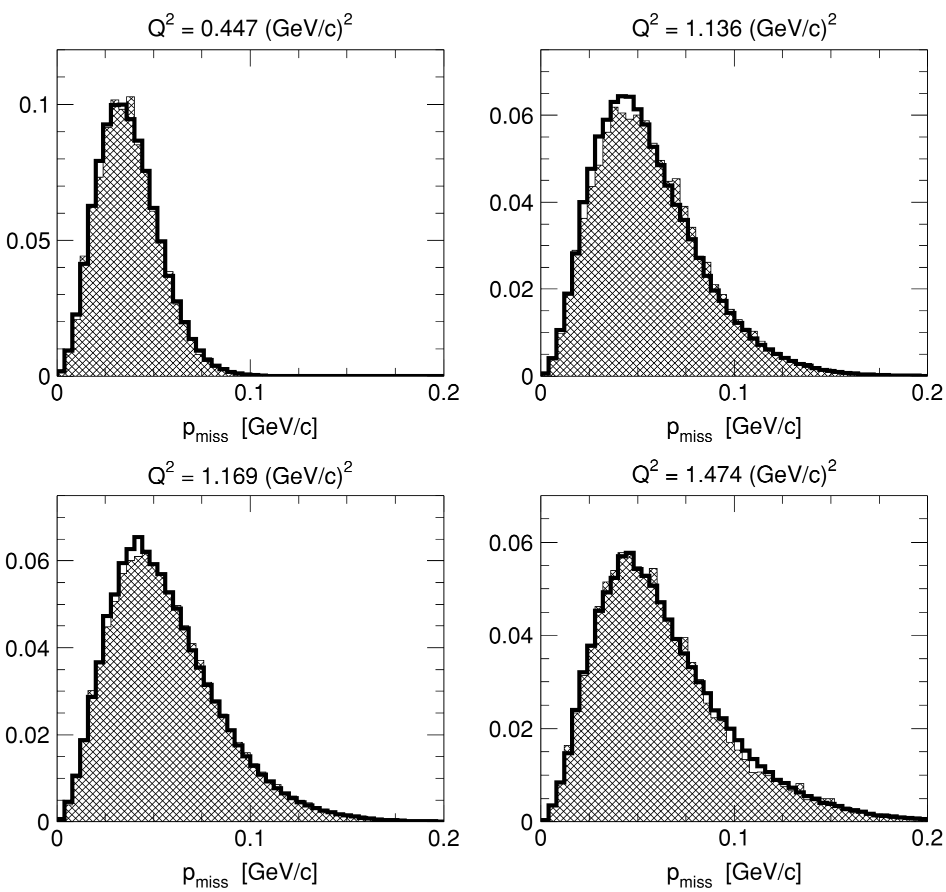

FIG. 21. Comparison of GENGEN simulated (unfilled histograms with thick solid line borders) and experimental (cross-hatched filled histograms) distributions of $|\mathbf{p}_{\text{miss}}|$ for the four central Q^2 points. Identical cuts were applied to both the simulated and experimental data. The simulated results shown here employed the FSI+MEC+IC+RC model and the Galster parametrization for G_{En}.

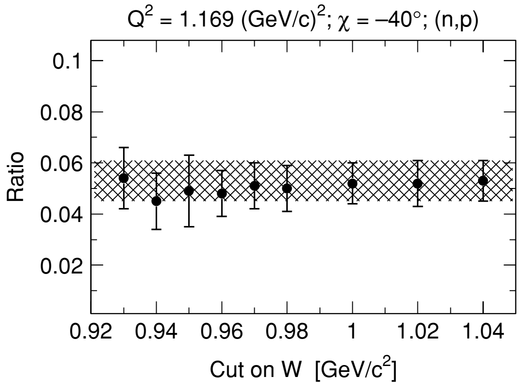

FIG. 22. Ratio of the asymmetries extracted from the experimental data to the GENGEN simulated polarizations as a function of the cut on W for (n, p) events and $\chi = -40^\circ$ precession at our $Q^2 = 1.169\,(\mathrm{GeV}/c)^2$ point. The shaded band indicates the statistical error on the ratio for the nominal cut on W of <1.04 GeV/c^2. The simulated results shown here employed the FSI+MEC+IC+RC model and the Galster parametrization for G_{En}.

event-by-event basis, the recoil polarization presented to the polarimeter for each event employed in our final data analysis (i.e., for those events satisfying all final analysis cuts). The ACCEPTANCE program used the same $^2\mathrm{H}(\vec{e}, e'\vec{n})^1\mathrm{H}$ interpolation and Charybdis spin transport algorithms developed for GENGEN. Although the ACCEPTANCE program was, technically, not a true Monte Carlo simulation, a significant advantage of this method was that it did not require a model for the experimental acceptance; however, the disadvantage of this method was that the reconstruction of the event-by-event kinematics is, of course, subject to measurement uncertainties, leading to uncertainties in the computation of the recoil polarization.

VI. FINAL RESULTS FOR G_{En}/G_{Mn} AND G_{En}

A. Distributions of $\Theta_{np}^{\mathrm{c.m.}}$

Distributions of $\Theta_{np}^{\mathrm{c.m.}}$ for those events surviving all analysis cuts at our lowest Q^2 point are shown in Fig. 23. The majority of the accepted events are seen to fall within $\sim$10–15° of perfect quasifree emission. The distributions of $\Theta_{np}^{\mathrm{c.m.}}$ at our other Q^2 points are similar but are restricted to somewhat smaller ranges, $170^\circ < \Theta_{np}^{\mathrm{c.m.}} < 180^\circ$.

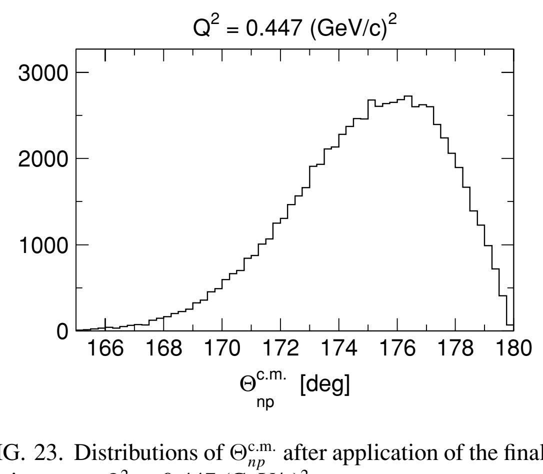

FIG. 23. Distributions of $\Theta_{np}^{\mathrm{c.m.}}$ after application of the final set of analysis cuts at $Q^2 = 0.447\,(\mathrm{GeV}/c)^2$.

Even for perfect quasifree emission, $\Theta_{np}^{\mathrm{c.m.}} = 180^\circ$, the PWBA and FSI+MEC+IC+RC calculations of the $P_t^{(h)}/P_\ell^{(h)}$ polarization ratio differ by 4.2% for the central kinematics of our lowest $Q^2 = 0.447\,(\mathrm{GeV}/c)^2$ point and 1.6% at our highest $Q^2 = 1.474\,(\mathrm{GeV}/c)^2$ point. As the differences between the PWBA and FSI+MEC+IC+RC calculations increase away from $\Theta_{np}^{\mathrm{c.m.}} = 180^\circ$, these numbers provide essentially lower bounds for the expected magnitude of corrections for nuclear physics effects.

B. Extraction of acceptance-averaged and nuclear physics-corrected values for G_{En}/G_{Mn}

1. Overview of acceptance-averaging analysis procedure

The recoil polarization component we were interested in was the projection of the polarization vector on the polarimeter momentum basis $\hat{S}$ axis following transport through the Charybdis field and the lead curtain. We denote this polarization component as P_S', where the prime denotes transport through the dipole field and lead curtain. Acceptance-averaged and nuclear physics-corrected values for G_{En}/G_{Mn} were extracted from our experimental asymmetries and simulations at each Q^2 point via the following procedure:

(i) Acceptance-averaged polarizations $\langle P_S' \rangle$ computed according to the PWBA and FSI+MEC+IC+RC models were extracted from simulated data for each precession angle at each Q^2 point and for each scale factor S of the Galster parametrization (see Sec. VI1).

(ii) In our "pairwise analysis method," for each S factor, we compared the ratio of the experimental asymmetries to the ratio of the simulated polarizations for the different precession angle combinations (i.e., $\chi = 0^\circ, \pm 90^\circ$ and $\chi = \pm 40^\circ$) and then computed a χ^2 value for each precession angle combination and each event type [i.e., (n, n) or (n, p) events] according to

$$\chi^2 = \frac{(\eta_{\mathrm{sim}} - \eta_{\mathrm{exp}})^2}{(\Delta\eta_{\mathrm{sim}})^2 + (\Delta\eta_{\mathrm{exp}})^2}, \tag{24}$$

where $\eta_{\mathrm{sim}} = \langle P_S'(0^\circ)\rangle / \langle P_S'(\pm 90^\circ)\rangle$ for the $\chi = 0^\circ$, $\pm 90^\circ$ precession angle combination and $\langle P_S'(-40^\circ)\rangle / \langle P_S'(+40^\circ)\rangle$ for the $\chi = \pm 40^\circ$ precession angle combination. The expressions for η_{exp} are identical, with the acceptance-averaged polarizations replaced by the experimental asymmetries. $\Delta\eta_{\mathrm{sim}}$ and $\Delta\eta_{\mathrm{exp}}$ denote the statistical errors. The resulting χ^2 values were fitted as a function of the scale factor S to a parabolic function, with the optimal value of S defined by the zero of the parabolic fitting function.

(iii) In our "global analysis method," we compared the experimental asymmetries with the simulated polarizations via minimization of a global χ^2 value computed according to

$$\chi^2\left(A_y^{(n,n)}, A_y^{(n,p)}\right) = \sum \frac{\left(\xi - A_y^{(n,n),(n,p)}\langle P_S'\rangle\right)^2}{(\Delta\xi)^2 + (\Delta\langle P_S'\rangle)^2}. \tag{25}$$

Here, the sum runs over all 10 asymmetries, ξ, and simulated polarizations, $\langle P'_S \rangle$, for each Q^2 point [i.e., five different precession angles, and (n, n) and (n, p) events], and $A_y^{(n,n)}$ and $A_y^{(n,p)}$ denote the polarimeter's analyzing power for (n, n) and (n, p) events. $\Delta\xi$ and $\Delta\langle P'_S \rangle$ denote the statistical errors. In this analysis, the analyzing powers and scale factor S were treated as free parameters, with the optimal values extracted from the minimal χ^2 value.

We note that the simulation statistical errors were generally an order of magnitude smaller than the experimental statistical errors.

2. Acceptance-averaged values of Q^2

The acceptance-averaged values of Q^2, denoted $\langle Q^2 \rangle$, were determined to be $\langle Q^2 \rangle = 0.447$, 1.126, 1.158, and 1.450 (GeV/c)^2 for the central $Q^2 = 0.447$, 1.136, 1.169, and 1.474 (GeV/c)^2 points, respectively. The distribution of Q^2 values for the $\langle Q^2 \rangle = 0.447$ (GeV/c)^2 point was sharply peaked around the central value of 0.447 (GeV/c)^2, whereas the distributions of Q^2 values for the $\langle Q^2 \rangle = 1.126/1.158$ and 1.450 (GeV/c)^2 points were integrated from $\sim$1.0 to $\sim$1.3 (GeV/c)^2 and from $\sim$1.2 to $\sim$1.7 (GeV/c)^2, respectively.

Henceforth, we use $\langle Q^2 \rangle = 1.132$ (GeV/c)^2 to denote the sample-size weighted average of the $\langle Q^2 \rangle = 1.126$ and 1.158 (GeV/c)^2 data sets.

3. Acceptance-averaging analysis iterations

We performed two iterations of the above-described analysis procedure with both the ACCEPTANCE and GENGEN simulation programs.

In the first iteration, the simulations were conducted with the PWBA and FSI+MEC+IC+RC calculations that assumed different multiplicative factors of the standard Galster parametrization for the Q^2 dependence of G_{En}. The optimal values for the scale factors S were then used to compute the optimal values for G_{En}/G_{Mn} according to $G_{En}/G_{Mn} = -S_{\text{optimal}} \times \langle\tau\rangle/(1 + 5.6\langle\tau\rangle)$, where $\langle\tau\rangle = \langle Q^2 \rangle/4m_n^2$. Values for G_{En} were then extracted from our optimal values for G_{En}/G_{Mn} using the best-fit values for G_{Mn} taken from the parametrization of Kelly [49]. Then we fitted our first-iteration results for G_{En} together with the then-available world data on G_{En} (as of early 2003) to the modified Galster parametrization described previously in Sec. VI1; the best-fit parameters we found at that time were $a = 0.894 \pm 0.023$ and $b = 3.55 \pm 0.37$. This fit included the then-available data on G_{En} extracted from measurements using polarization degrees of freedom [23,34,39,41,43,48] and an analysis of the deuteron quadrupole form factor [10], and also data on the slope of G_{En} as measured via low-energy neutron scattering from electrons in heavy atoms [77]. Since the conclusion of this analysis, new data on G_{En} have been published [50,51], and a new modified Galster parametrization has been published [78].

In our second analysis iteration, a second set of the PWBA and FSI+MEC+IC+RC calculations were performed that assumed this modified Galster parametrization for the Q^2 dependence of G_{En}. The ACCEPTANCE and GENGEN simulations were both repeated using these new calculations, and the procedure for the extraction of the optimal G_{En}/G_{Mn} values was identical to that of the first iteration.

TABLE VII. Analyzing powers for (n, n) and (n, p) events at each of our Q^2 points. The errors are statistical.

Event type	$\langle Q^2 \rangle$ [(GeV/c)^2]		
	0.447	1.132	1.450
(n, n)	0.141 ± 0.004	0.137 ± 0.010	0.144 ± 0.013
(n, p)	0.103 ± 0.005	0.075 ± 0.007	0.071 ± 0.011

The differences between the first and second analysis iterations were negligible. This result is not surprising, because (1) both parametrizations have small second derivatives in the vicinity of our Q^2 points and (2) the acceptance was fairly symmetric about the acceptance-averaged values of Q^2.

4. Acceptance-averaging analysis results

The pairwise analysis method was employed for the extraction of our G_{En}/G_{Mn} values at $\langle Q^2 \rangle = 0.447$ (GeV/c)^2 (only two precession angles), whereas the global analysis method was employed for the analysis of our $\langle Q^2 \rangle = 1.132$ and 1.450 (GeV/c)^2 data sets. The final acceptance-averaged and nuclear physics-corrected values for G_{En}/G_{Mn} we obtained with the ACCEPTANCE program and GENGEN agreed to better than 1% at $\langle Q^2 \rangle = 0.447$ and 1.132 (GeV/c)^2 and 2% at $\langle Q^2 \rangle = 1.450$ (GeV/c)^2, well within the statistical errors; therefore, the values for G_{En}/G_{Mn} we report later in Table IX are the average of the central values obtained with our two simulation programs. The analyzing powers we extracted from our acceptance-averaging analysis procedures are summarized in Table VII.

C. Systematic uncertainties

An itemized summary of estimates for the magnitudes of our relative systematic uncertainties in G_{En}/G_{Mn} appears in Table VIII. Our final values for the total relative systematic uncertainties, 2–3%, are much smaller than our relative statistical uncertainties. Brief discussions of each itemized systematic uncertainty (and others deemed negligibly small) appear below.

TABLE VIII. Compilation of our estimated relative systematic uncertainties in G_{En}/G_{Mn} [%]. The total systematic error that is quoted for each Q^2 point and precession angle combination is the quadrature sum of the itemized systematic uncertainties.

Source	$\langle Q^2 \rangle$ [(GeV/c)^2]				
	0.447[a]	1.132[a]	1.132[b]	1.450[a]	1.450[b]
Beam polarization	1.6	0.7	0.4	1.2	0.3
Charge-exchange	<0.1	<0.1	0.1	<0.1	0.2
Depolarization	<0.1	0.1	<0.1	<0.1	0.6
Positioning/traceback	0.2	0.3	0.3	0.4	0.4
Precession angle	1.1	0.3	0.1	0.5	0.1
Radiative corrections	0.7	0.1	0.1	0.1	0.1
Timing calibration	2.0	2.0	2.0	2.0	2.0
Total	2.9	2.2	2.1	2.4	2.2

[a] $\chi = \pm 40^\circ$ precession.
[b] $\chi = 0^\circ, \pm 90^\circ$ precession.

1. Beam polarization

The beam polarization cancels in the form factor ratio only if it does not vary during sequential measurements of the scattering asymmetries. Consequently, fluctuations in the beam polarization measurements introduce a systematic uncertainty. We estimated the temporal uncertainty in the beam polarization via the following procedure. First, polarization measurements conducted under similar conditions at the polarized source were grouped into clusters. Second, the mean value of the polarization for each cluster was computed and then recentered about the nominal 80% polarization. Next, the statistical error for the entire data set (i.e., all identified clusters) was computed, and the overall uncertainty was then increased by the square root of χ^2 (to account for the observed fluctuations). Finally, our total estimated uncertainty in the polarization was propagated through the expression for the form factor ratio, Eq. (4).

2. Charge-exchange in the lead curtain

Estimates of the contamination levels from the two-step $^2\mathrm{H}(\vec{e}, e'\vec{p}) + \mathrm{Pb}(\vec{p}, \vec{n})$ charge-exchange reaction were given previously in Sec. VG2. To estimate the systematic uncertainty in G_{En}/G_{Mn} because of contamination from this background process, we computed values for the recoil proton's polarization using values for G_{Ep} and G_{Mp} taken from the parametrization of Ref. [79]. These polarization components were then transported through the Charybdis dipole field using estimates for the proton spin precession angles. As there are very few data on the lead polarization transfer coefficient, D_{SS}^{Pb}, we calculated the correction to the asymmetries (using information on the analyzing powers extracted from our acceptance-averaging analysis and the values for, and the uncertainties in, the charge-exchange contamination levels) for various (reasonable) choices of D_{SS}^{Pb}. Spreads in the resulting values of G_{En}/G_{Mn} were then defined to be the systematic uncertainties.

3. Neutron depolarization in the lead curtain

The total n+Pb cross section is fairly flat at ∼3 barns over the range of neutron kinetic energies in our experiment (slow rise with energy) [75]. For our 10.16-cm-thick lead curtain, our GENGEN simulations indicated a 30.8%, 42.5%, 43.0%, and 46.7% interaction probability for the neutron energies at our $\langle Q^2\rangle = 0.447$, 1.126, 1.158, and 1.450 (GeV/c)^2 points, respectively. We found that the contamination levels within our [−1, 1] ns cTOF window from neutrons suffering one or more interactions in the lead curtain were 0.04%, 3.8%, 4.2%, and 9.3% at $\langle Q^2\rangle = 0.447$, 1.126, 1.158, and 1.450 (GeV/c)^2, respectively. The fact that our simulations predicted a much more rapid increase in the contamination levels with energy as compared to the interaction probabilities is because the angular distributions for nn and np scattering peak at large (small) scattering angles for the neutron kinetic energies at our lowest (highest) Q^2 point (as computed by SAID [70]). Further, our simulations suggested that interactions in the lead curtain may have been partly responsible for the small tail observed on the slow side of our experimental cTOF distributions at our highest Q^2 point (see Fig. 15).

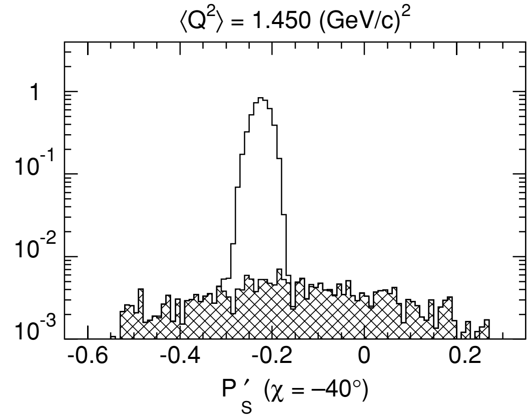

FIG. 24. Sample GENGEN simulated $\langle P_S'\rangle$ spectrum for $\chi = -40^\circ$ precession at $\langle Q^2\rangle = 1.450$ (GeV/c)^2. The unfilled histogram is summed over all simulated events, whereas the cross-hatched histogram is summed over those events suffering one or more interactions in the lead curtain. The units of the ordinate are arbitrary.

The quantity of interest was the spectrum of the polarization presented to the polarimeter front array for neutrons that did and did not interact with the lead curtain. A sample result comparing polarization spectra for these two types of events for $\chi = -40^\circ$ precession at $\langle Q^2\rangle = 1.450$ (GeV/c)^2 is shown in Fig. 24. Our simulations indicated that the distribution of polarizations for neutrons suffering an interaction in the lead curtain is a broad continuum, yielding a depolarization of the neutron flux presented to the polarimeter. Similar results were observed at our other Q^2 points. We found, though, that the effects of depolarization in the lead curtain tend to cancel in the polarization ratio, leading to small systematic uncertainties in the G_{En}/G_{Mn} ratio. The magnitudes of the residual noncancellations were taken to be the uncertainties listed in Table VIII.

4. Positioning and traceback

Two contributions to an uncertainty in the electron scattering angle were considered: positioning (offset in the scattering angle from the nominal value) and traceback (reconstruction from the focal plane to the target). For the purposes of this analysis, we assumed the uncertainties in the electron scattering angle, $\Delta\theta_{e'}$, were $\Delta\theta_{e'} = 1.2$ and 1.3 mrad for the positioning and traceback uncertainties, respectively; these values were derived from a systematic analysis of kinematic data taken during this experiment. The systematic uncertainties in G_{En}/G_{Mn} were obtained via propagation of these values for $\Delta\theta_{e'}$ through Eq. (4) for the form factor ratio.

5. Precession angle

Uncertainties in the neutron spin precession angle were estimated [64] via a calculational scheme that employed the reconstructed kinematics from the experimental data as the source of the neutron momentum vectors incident on the Charybdis dipole field. Spin vectors were transported through the field using the same magnetic spin transport algorithms developed for our two simulation programs. This technique

TABLE IX. Summary of our final results for G_{En}/G_{Mn} and G_{En}. The first (second) set of errors is statistical (systematic). The results reported here are the weighted average of (n, n) and (n, p) events in the polarimeter.

Analysis	Quantity	$\langle Q^2\rangle$ [(GeV/c)^2] 0.447	1.132	1.450
$n(\vec{e}, e'\vec{n})$	G_{En}/G_{Mn}	$-0.0681 \pm 0.0084 \pm 0.0020$	$-0.122 \pm 0.011 \pm 0.003$	$-0.174 \pm 0.017 \pm 0.004$
^{2}H$(\vec{e}, e'\vec{n})^1$H PWBA	G_{En}/G_{Mn}	$-0.0713 \pm 0.0086 \pm 0.0021$	$-0.126 \pm 0.010 \pm 0.003$	$-0.183 \pm 0.018 \pm 0.004$
^{2}H$(\vec{e}, e'\vec{n})^1$H FSI+MEC+IC+RC	G_{En}/G_{Mn}	$-0.0755 \pm 0.0089 \pm 0.0022$	$-0.131 \pm 0.011 \pm 0.003$	$-0.189 \pm 0.018 \pm 0.004$
Values from Ref. [78]	$G_{Mn}/\mu_n G_D$	1.003 ± 0.005	1.067 ± 0.012	1.064 ± 0.016
$n(\vec{e}, e'\vec{n})$	G_{En}	$0.0492 \pm 0.0061 \pm 0.0015$	$0.0370 \pm 0.0032 \pm 0.0009$	$0.0383 \pm 0.0038 \pm 0.0011$
^{2}H$(\vec{e}, e'\vec{n})^1$H PWBA	G_{En}	$0.0515 \pm 0.0062 \pm 0.0015$	$0.0381 \pm 0.0032 \pm 0.0009$	$0.0403 \pm 0.0039 \pm 0.0011$
^{2}H$(\vec{e}, e'\vec{n})^1$H FSI+MEC+IC+RC	G_{En}	$0.0545 \pm 0.0064 \pm 0.0016$	$0.0396 \pm 0.0032 \pm 0.0010$	$0.0415 \pm 0.0039 \pm 0.0011$

provided a measure of the sensitivity of the precession angle to details of the field map. The uncertainties in the mean values of the precession angles derived from these studies (at the level of $\pm 0.2^\circ$) were combined in quadrature with two other sources of uncertainty. First, as discussed in Sec. IV C, we observed small differences between the measured field integrals for opposite magnet polarities and also between the field integrals derived from our measured maps and the calculated TOSCA maps. These uncertainties were estimated to be on the level of $\pm 0.3^\circ$. Second, as also discussed in Sec. IV C, the field was mapped only along the central axis; therefore, we assigned further uncertainties (at the level of $\pm 0.2^\circ$) for incomplete knowledge of the field beyond the central axis. Our best estimates of the total uncertainties in the precession angle were then propagated through the form factor ratio, Eq. (4).

6. Radiative corrections

Radiative corrections were calculated specifically for the kinematics of this experiment by Afanasev *et al*. [80]. The primary effect of radiative corrections on the recoil polarization components $P_t^{(h)}$ and $P_\ell^{(h)}$ was found to be depolarization of the electron such that both components of the recoil polarization should be increased by ~1.9% ~3.7%, and ~4.4% at $\langle Q^2\rangle = 0.447$, 1.132, and 1.450 (GeV/$c$)^2, respectively; however, these corrections nearly cancel in the form factor ratio such that the net effect is small at $\langle Q^2\rangle = 0.447$ (GeV/c)^2 and negligible at the two higher Q^2 points. The residual noncancellations of the corrections in the form factor ratio were taken to be the systematic uncertainties we quote in Table VIII.

7. Timing calibration of the polarimeter

The timing calibrations we deemed suitable for certain running conditions (e.g., periods in between changes to the high-voltages for the PMTs) were obtained using a subset of the data for that particular running period. To assess the dependence of our results for the scattering asymmetries on the choice of the subset of data employed for the timing calibration, various calibrations were generated from different subsets of the available data. Excellent agreement was always found between the results for the scattering asymmetries obtained from analyses using these different calibrations; however, we did find a ~2% sensitivity of our results to the choice of the subset of data employed for the timing calibration.

8. Other uncertainties

We deemed two other possible sources of systematic uncertainties to be negligible. First, we demonstrated quantitatively that our scattering asymmetries were insensitive (within statistical errors) to a possible geometric asymmetry in the polarimeter (i.e., a spin-averaged "top-bottom" asymmetry) by varying our software energy thresholds on the top (bottom) rear array while maintaining a constant threshold on the bottom (top) rear array. Second, analysis of our data taken with the "dummy targets" (see Sec. IIIE) showed that the level of contamination within our $[-1, 1]$ ns cTOF window from scattering in the target cell windows was negligible (<0.05%).

D. Summary of final G_{En}/G_{Mn} and G_{En} results

Our final results for G_{En}/G_{Mn} and G_{En} extracted from three different analyses are tabulated in Table IX and compared in Fig. 25. The three analyses are for: (1) elastic $n(\vec{e}, e'\vec{n})$ scattering and infinitesimal HMS and NPOL point

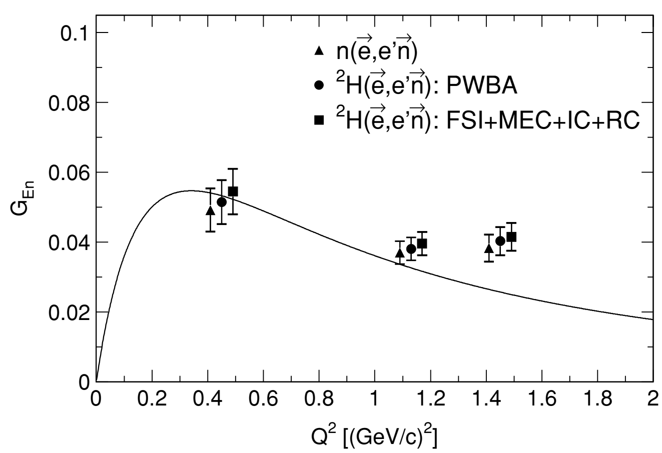

FIG. 25. Comparison of our results for G_{En} at $\langle Q^2\rangle = 0.447$, 1.132, and 1.450 (GeV/$c$)^2 extracted from the various analyses summarized in Table IX. The data points shown for the three analyses at each $\langle Q^2\rangle$ point have been slightly displaced about the actual $\langle Q^2\rangle$ value for clarity. The solid curve is the Galster parametrization [37].

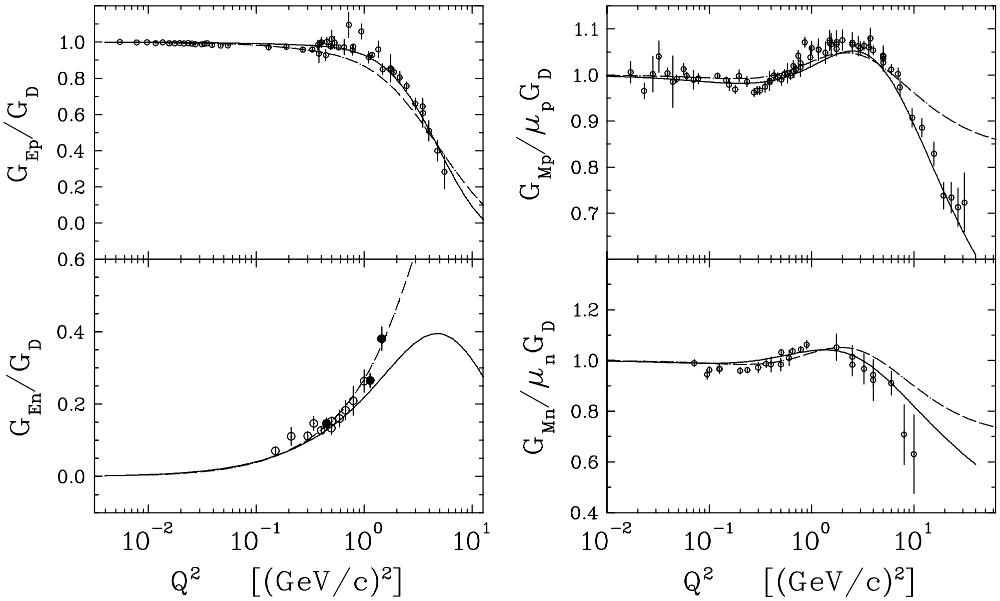

FIG. 26. Comparison of representative VMD models with nucleon form factor data (G_{Ep} from Refs. [81,82]; G_{Ep}/G_{Mp} from Refs. [83–86]; G_{Mp} from Refs. [47,79]; G_{En} from Refs. [23,39,41,43,48,50,51]; G_{Mn} from Refs. [8,44,46,87,88]). (Dashed curve) Bijker and Iachello [92]; (solid curve) version GKex(02S) of Lomon [94].

acceptances; (2) quasielastic $^2\mathrm{H}(\vec{e}, e'\vec{n})^1\mathrm{H}$ scattering and acceptance-averaging of the PWBA model; and (3) quasielastic $^2\mathrm{H}(\vec{e}, e'\vec{n})^1\mathrm{H}$ scattering and acceptance-averaging of the FSI+MEC+IC+RC model.

We note that in our first publication [12] we used values for G_{Mn} taken from Ref. [49]; here we use slightly different values for G_{Mn} taken from Ref. [78]. The total systematic errors we quote for G_{En} are the quadrature sum of the experimental sytematic errors and the relative uncertainties in G_{Mn}.

E. Comparison of nucleon form factor data with selected theoretical model calculations

The availability of precise new data on nucleon form factors has stimulated much more theoretical work in the last few years than we can review here; our selection of models is not intended to be complete. Although the present experiment is limited to G_{En}, we believe that comparison with models must consider all four Sachs form factors. In this section, we compare representative models with selected data. The data from this experiment are shown as filled circles in Figs. 26–29, whereas data from other experiments are shown as open circles. We selected [81,82] for G_{Ep}, [83–86] for G_{Ep}/G_{Mp}, [47,79] for G_{Mp}, [23,39,41,43,48,50,51] for G_{En}, and [8,44, 46,87,88] for G_{Mn}.

1. Models based on vector meson dominance

Models based on vector meson dominance (VMD) postulate that the virtual photon couples either directly to an intrinsic nucleon core or through the mediation of a neutral vector meson, initially limited to the lowest ω, ρ, and ϕ mesons. The earliest versions assumed that the core is a structureless Dirac particle. Iachello *et al.* [89] assigned the core a form factor and employed a model of the ρ width. Gari and Krümpelmann [90,91] then permitted different Dirac and Pauli intrinsic form factors and introduced modifications that ensured consistency with pQCD scaling at large Q^2 and logarithmic running of the strong coupling constant. Bijker and Iachello [92] adopted the Gari and Krümpelmann (GK) pQCD prescriptions and refit their model to modern data, still using a common intrinsic form factor. This fit, using a total of six free parameters, is compared with the data in Fig. 26. Finally, Lomon [93,94] produced a more flexible set of fits using a model described as "GK extended"; the GKex(02S) version is also shown in Fig. 26. The Lomon model uses two intrinsic form factors, the GK prescription for the pQCD limit, and includes $\rho'(1450)$ and $\omega'(1419)$ couplings in addition to the customary ρ, ω, and ϕ couplings. The ρ width is included but the ρ' and ω' structures are not. The fit achieved by this extended model, with 13 free parameters, is clearly superior, especially at large Q^2. The Bijker and Iachello model describes the qualitative behavior of G_{Ep}, but its transition between $G_{Ep}/G_D \approx 1$ at low Q^2 and the nearly linear decrease for $1 < Q^2 < 6$ (GeV/c)^2 is too gradual. Nor does it reproduce the slope in $G_{Mp}/\mu_p G_D$ for $Q^2 > 10$ (GeV/c)^2. Both of these features are fit well by the Lomon model. Unfortunately, the neutron data do not discriminate between these models very strongly. The Bijker and Iachello model provides a slightly better fit to the present G_{En} data, but the Lomon fit was performed before these data became available; it is likely that only a slight parameter adjustment would be needed to achieve a comparable fit without sacrificing the fits to the other form factors. It will be interesting to see whether the rather large values for G_{En}/G_D for $Q^2 > 2$ (GeV/c)^2 predicted by the Bijker and Iachello model are confirmed by upcoming experiments [95,96] that will probe G_{En} to $Q^2 = 4.3$ (GeV/c)^2. Note, however, that the Bijker and Iachello fit is systematically above the G_{Mn} data for the same kinematics, $Q^2 > 2$ (GeV/c)^2.

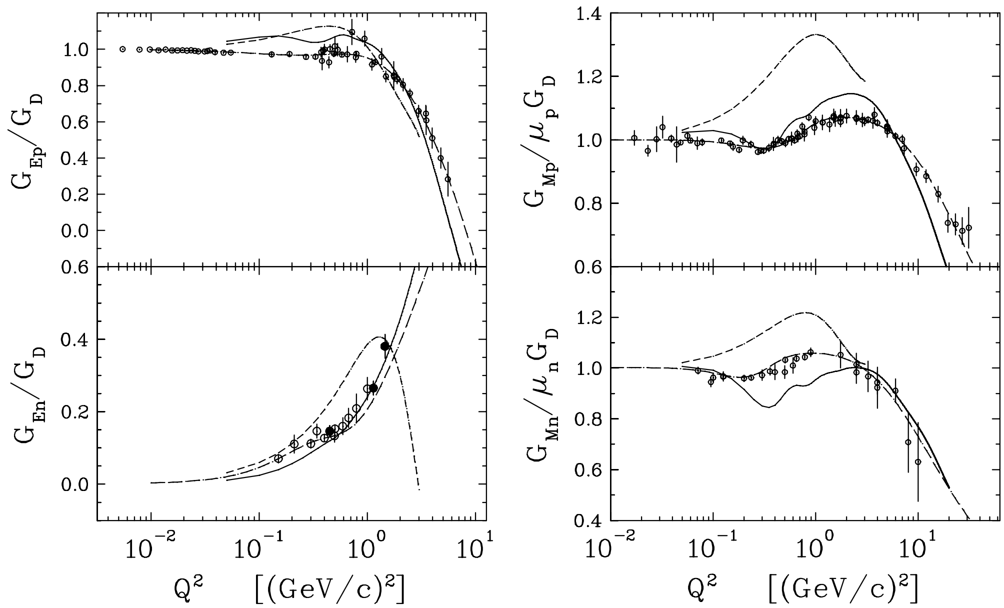

FIG. 27. Comparison of representative pion cloud models with nucleon form factor data (G_{Ep} from Refs. [81,82]; G_{Ep}/G_{Mp} from Refs. [83–86]; G_{Mp} from Refs. [47,79]; G_{En} from Refs. [23,39,41,43,48,50,51]; G_{Mn} from Refs. [8,44,46,87,88]). (Short-dashed curve) QMC model [97]; (solid curve) LFCBM [103]; (long-dashed curve) Friedrich and Walcher parametrization [52].

2. *Models emphasizing the pion cloud*

The role of the pion in mediation of the long-range nucleon-nucleon interaction clearly demonstrates its importance in understanding form factors for low Q^2. Typical pion cloud models describe nucleon form factors using diagrams in which the virtual photon couples to either a bare nucleon core or to the nucleon or the pion loop in a single-pion loop. Some models also permit excitation of the intermediate state and include additional contact terms. A relatively simple example is the Adelaide version [97] of the cloudy bag model (CBM) in which the core is based on the bag model, intermediate excitation is neglected, and relativistic corrections are made using a simple ansatz for Lorentz contraction [98]. Predictions from Lu *et al.* [97] using a bag radius of 0.8 fm are compared with the data in Fig. 27. Although density-dependent extensions of this model, described as the quark-meson coupling (QMC) model, have been used to study the sensitivity of recoil polarization in nucleon electromagnetic knockout to medium modifications of the nucleon form factors [99–102], its description of free form factors is rather poor and one must hope that the density dependence of G_E/G_M ratios is more accurate.

Alternatively, the light front cloudy bag model (LFCBM) of Miller [103] maintains Poincaré invariance by formulating wave functions using the light-front approach. This version should then be applicable to higher Q^2. There are only four adjustable parameters and the results for Set 1 are compared with data in Fig. 27. A previous version of this model [104] provided one of the earliest predictions of the sharp slope in G_{Ep}/G_{Mp} for $Q^2 > 1$ (GeV/c)^2, but the agreement with recent recoil-polarization data is only qualitative. The LFCBM calculation for G_{Mp}/G_D also decreases too rapidly at large Q^2. Calculations using this model agree relatively well with the G_{En} data for $Q^2 \gtrsim 1$ (GeV/c)^2 but are too small at lower Q^2. Interestingly, this model predicts much stronger values for G_{En}/G_D at large Q^2 than the Lomon parametrization. However, the LFCBM calculations for three of the four form factors show complicated and rather implausible shapes for $Q^2 < 1$ (GeV/c)^2 that disagree strongly with data.

Chiral effective field theory [105,106] provides a more systematic procedure that includes intermediate excitation and can be extended to two pion loops [107]. Alternatively, two-loop contributions can be evaluated in dispersion theory [108]. Recently it has become possible also to include both pion loops and vector meson diagrams in a consistent manner [109]; however, we do not show curves here because this approach remains limited to $Q^2 \lesssim 0.4$ (GeV/c)^2.

Friedrich and Walcher [52] performed a phenomenological analysis of the nucleon electromagnetic form factors using a parametrization motivated by pion cloud models. The core form factor is represented by two dipole form factors with different ranges, whereas the pion cloud contribution, represented as a "bump" at low Q^2, is described by two Gaussians. These fits, with five free parameters for G_{En} and six for each of the other form factors, are also compared with data in Fig. 27. The quality of these fits is generally satisfactory, but it is not clear that the postulated oscillation in G_{En}/G_D is warranted by the available data; considerably better experimental precision at $Q^2 \sim 0.3$ (GeV/c)^2 would be needed to justify such a structure.

A closer look at the G_{En} data is given in Fig. 28. The original Friedrich and Walcher fit (short-dashed curve) used a very preliminary version of the data from the present experiment and falls systematically below the final data for this and other more recent experiments for $Q^2 > 0.5$ (GeV/c)^2. A reanalysis using final data for this experiment plus new data [43,50,51] was made by Glazier *et al.* [51] and is shown as the long-dashed curve featuring a bump for $Q^2 \sim 0.3$ (GeV/c)^2 superimposed upon a much flatter core form factor. With five parameters

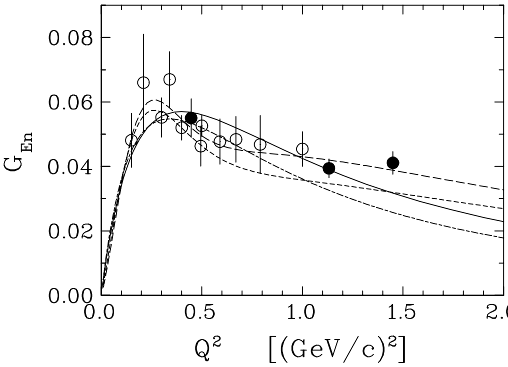

FIG. 28. Closer look at comparison of representative pion cloud models with data on G_{En} (data from Refs. [23,39,41,43,48,50,51]). (Solid curve) A fit based on the pion cloud model of Kaskulov and Grabmayr [110]. (Short-dashed curve) Parametrization of Friedrich and Walcher [52]. (Long-dashed curve) Reanalysis by Glazier *et al*. [51] using the Friedrich and Walcher model. The dash-dotted curve is the original Galster parametrization [37].

it is obviously possible to fit the data very well, perhaps too well—the simple two-parameter fit of Kelly [78] based on the Galster parametrization already provides $\chi^2_\nu = 0.8$ without distinguishing between soft and hard structures. The data presently available do not require this complication. Data at higher Q^2 should test whether such a hard core is needed but significantly more precise data for low Q^2 would be needed to establish the soft pion cloud contribution to G_{En}.

Finally, Kaskulov and Grabmayr [110] used a chiral quark model (χQM) to derive a relationship

$$G_{En} = \bar{S}(1 - F_\pi)G_C, \tag{26}$$

between G_{En}, the pion form factor F_π, and the core form factor G_C for the three-quark component of the nucleon. The coefficient $\bar{S}$ is a weighted average over spectroscopic factors for N and Δ intermediate states in the one-pion loop contribution to the self-energy but is treated as an adjustable parameter. If one stipulates a monopole for $F_\pi = (1 + Q^2/\Lambda_\pi^2)^{-1}$ and a dipole for $G_C = (1 + Q^2/\Lambda_C^2)^{-2}$, the neutron electric form factor

$$G_{En} = \bar{S}\frac{b\tau}{1 + b\tau}G_C, \tag{27}$$

with $b = 4m_N^2/\Lambda_\pi^2$ reduces to a Galster-like form with up to three free parameters ($\bar{S}$, Λ_π, Λ_C); however, $\bar{S}$ is largely determined by the neutron radius

$$\langle r^2 \rangle_n = -6\left(\frac{\partial G_{En}}{\partial Q^2}\right)_{Q^2\to 0} = -\frac{3\bar{S}b}{2m_N^2}. \tag{28}$$

If we further assume that Λ_π within a loop is the same as that for pion electroproduction, only Λ_C remains to be fit to data for G_{En}. Thus, using fixed parameters $\bar{S} = 0.26$ and $b = 6.65$ suggested by Kaskulov and Grabmayr, we fit $\Lambda_C^2 = 1.00 \pm 0.03$ (GeV/c)^2 to the current G_{En} data. The value given in Ref. [110] for Λ_C is slightly smaller because they used the same preliminary data as [52] that are smaller than the final results. Our fit is shown in Fig. 28 and is practically indistinguishable from the two-parameter Galster fit given in Ref. [78]. The Kaskulov and Grabmayr model has the same physical basis as that of Friedrich and Walcher, but is much more constrained; nevertheless, it fits the G_{En} data quite well. This result suggests that the radius of the $3q$ nucleon core is

$$\langle r^2 \rangle_{3q}^{1/2} = \frac{\sqrt{12}}{\Lambda_C} = (0.68 \pm 0.01)\ \text{fm}. \tag{29}$$

3. Quark models

The predictions of several recent relativistic constituent quark models are compared with the data in Fig. 29. All

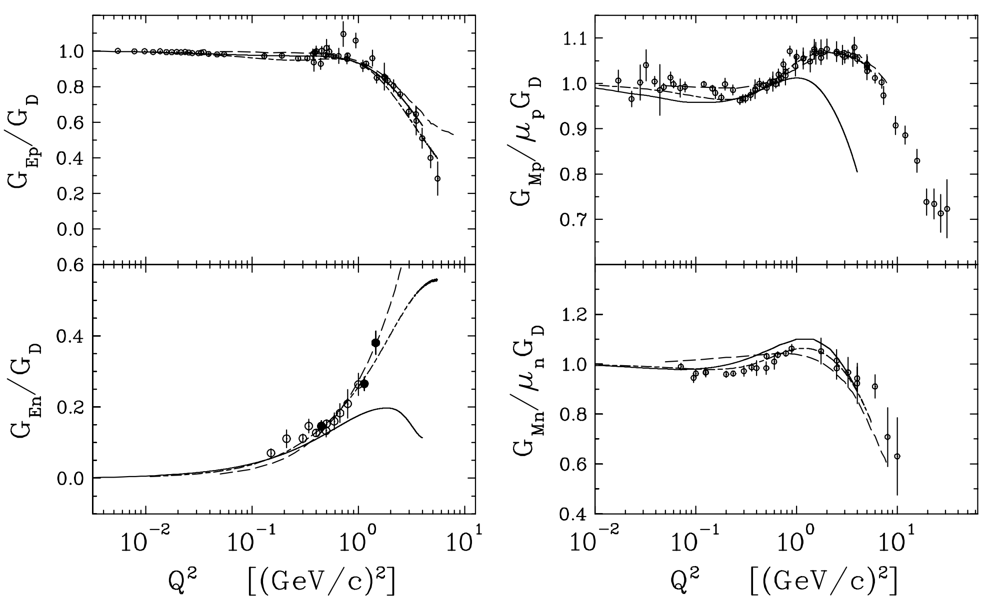

FIG. 29. Comparison of representative quark models with nucleon form factor data (G_{Ep} from Refs. [81,82]; G_{Ep}/G_{Mp} from Refs. [83–86]; G_{Mp} from Refs. [47,79]; G_{En} from Refs. [23,39,41,43,48,50,51]; G_{Mn} from Refs. [8,44,46,87,88]). (Solid curve) PFSA using pointlike constituents [111]. (Long-dashed curve) Light-front using OGE interaction and constituent-quark form factors [112,113]. (Dash-dotted curve) hCQM with constituent-quark form factors [114].

employ a linear confining potential. The solid curves show calculations of the Pavia-Graz collaboration [111] that used the point-form spectator approximation (PFSA) for pointlike constituent quarks and a Goldstone boson exchange interaction fitted to spectroscopic data. No additional parameters were adjusted to fit the form factors. The data for G_{Ep}/G_D are reproduced very well and the data for magnetic form factors are also described relatively well for $Q^2 \lesssim 1$ (GeV/c)^2, but the calculated value of $G_{Mp}/\mu_p G_D$ decreases too rapidly for larger Q^2. The prediction for G_{En}/G_D lies well below the data for $Q^2 > 1$ (GeV/c)^2. The long-dashed curves show calculations of Simula [112], based on the model of Cardarelli *et al.* [113], that used the light-front approach and the one-gluon exchange (OGE) interaction. Here, constituent-quark form factors were fitted to data for $Q^2 < 1$ (GeV/c)^2 and the calculations were extrapolated to larger Q^2. This approach provides good fits up to about 4 (GeV/c)^2. Finally, the dash-dotted curves show the results for a semirelativistic hypercentral constituent quark model (hCQM) [114] where the constituent-quark form factors, chosen as linear combinations of monopole and dipole forms, were also fitted to recent data. Of the selected quark model calculations, their results clearly achieve the best overall agreement with the data.

Finally, the most recent lattice QCD calculations of nucleon form factors were reported by the QCDSF collaboration [115] using nonperturbatively improved Wilson fermions in the quenched approximation. Unfortunately, straightforward chiral extrapolation [116] does not provide adequate agreement with data for $Q^2 < 1.5$ (GeV/c)^2. Matevosyan *et al.* [117] proposed a model-dependent extrapolation procedure based on the LFCBM. This extrapolation is quite severe because the lattice calculations remain limited to quark masses that correspond to $m_\pi \geqslant 0.5$ GeV, lattice spacings with $a \geqslant 0.05$ fm, and volumes that might not fully contain the pion cloud; therefore, comparison with data is probably premature.

VII. SUMMARY AND CONCLUSIONS

We reported values for the neutron electric to magnetic form factor ratio, G_{En}/G_{Mn}, deduced from measurements of the neutron's recoil polarization in quasielastic $^2\mathrm{H}(\vec{e}, e'\vec{n})^1\mathrm{H}$ kinematics at three acceptance-averaged Q^2 values of 0.45, 1.13, and 1.45 (GeV/c)^2. In the one-photon exchange approximation for elastic scattering from a free neutron, the polarization vector of the recoil neutron is confined to the scattering plane and consists of a longitudinal component, $P_\ell^{(h)} \propto G_{Mn}^2$, and a transverse component, $P_t^{(h)} \propto G_{En}G_{Mn}$. The use of a deuteron target to access the neutron form factor ratio via the quasielastic $^2\mathrm{H}(\vec{e}, e'\vec{n})^1\mathrm{H}$ reaction has the advantage, as established by Arenhövel *et al.* [19,20], that both $P_t^{(h)}$ and $P_\ell^{(h)}$ are relatively insensitive to final-state interactions (FSI), meson-exchange currents (MEC), isobar configurations (IC), and theoretical models of deuteron structure.

A high-luminosity neutron polarimeter designed specifically for our experiment, Jefferson Laboratory E93-038, was used to measure neutron polarization-dependent scattering asymmetries proportional to the projection of the polarization vector on the transverse axis. A dipole magnet located upstream of the polarimeter was used to precess the neutron polarization vector in the transverse-longitudinal plane, thereby permitting access to the ratio $P_t^{(h)}/P_\ell^{(h)} \propto G_{En}/G_{Mn}$. Values for the scattering asymmetries were extracted from neutron time-of-flight measurements in our polarimeter via the cross ratio technique. The merit of the cross ratio technique is that the scattering asymmetries are independent of the luminosities for the two electron beam helicity states and independent of the efficiencies and acceptances of the top and bottom halves of the polarimeter. Systematic uncertainties in our results are minimal as the analyzing power of the polarimeter and the polarization of the electron beam cancel in the form factor ratio. Further, other sources of uncertainty, such as radiative corrections and neutron depolarization by lead shielding, are small as they nearly cancel in the ratio.

To account for the finite experimental acceptance and nuclear physics effects (i.e., FSI, MEC, and IC), we used two independent simulation programs to average theoretical $^2\mathrm{H}(\vec{e}, e'\vec{n})^1\mathrm{H}$ recoil polarization calculations computed according to the model of Arenhövel *et al.* [19,20] over the acceptance. The results from these two simulation programs agreed to better than 1% at our two lower Q^2 points and 2% at our highest Q^2 point. Further, by averaging two different sets of theoretical calculations assuming different parametrizations for G_{En}, our acceptance-averaged and nuclear physics-corrected values for G_{En} were found to be insensitive to the choice of the Q^2 dependence of G_{En}.

Our results for G_{En} and data on the nucleon form factors were compared with selected theoretical model calculations. All of the model calculations based on vector meson dominance and those emphasizing the pion cloud presented here provide qualitative agreement with some of the four nucleon form factors, but no model achieves simultaneous agreement with all four form factors. The predictions of several recent relativistic quark models also achieve qualitative agreement with the data, with the most successful models utilizing form factors for the constituents; the results from a chosen model assuming pointlike constituents are not as successful. Although a comparison between data and the results of lattice QCD calculations is probably premature, the recent precise data obtained from experiments employing polarization degrees of freedom will no doubt serve as a future challenging test of QCD as formulated on the lattice.

In conclusion, our results at $Q^2 = 1.13$ and 1.45 (GeV/c)^2 are the first direct measurements of G_{En} using polarization degrees of freedom in the $Q^2 > 1$ (GeV/c)^2 region and are the most precise determinations of G_{En} over all ranges of Q^2. The achievement of relative statistical uncertainties in the form factor ratio G_{En}/G_{Mn} of 8.4% and 9.5%, respectively, at these two Q^2 points, together with relative systematic uncertainties on the level of 2%, was a triumph for our high figure-of-merit and high luminosity neutron polarimeter.

ACKNOWLEDGMENTS

This work was supported in part by grants from the U.S. National Science Foundation, the U.S. Department of Energy, and the Deutsche Forschungsgemeinschaft. Two of us (R.M. and T.E.) acknowledge support during the planning phase of E93-038 from the Nuclear and High Energy Physics Center at Hampton University. The Southeastern Universities Research Association operates the Thomas Jefferson National Accelerator Facility under the U.S. Department of Energy contract no. DE-AC05-84ER40150. We thank the Jefferson Laboratory accelerator division staff for delivering the high-quality polarized electron beam to our experiment. Finally, we thank the Jefferson Laboratory Hall C engineering and technical staff for their skillful assistance during our experiment.

APPENDIX A: FORMALISM FOR THE QUASIELASTIC $^2\mathrm{H}(\vec{e}, e'\vec{n})^1\mathrm{H}$ REACTION

Our notation for the kinematics and nucleon recoil polarization for the quasielastic $^2\mathrm{H}(\vec{e}, e'\vec{n})^1\mathrm{H}$ reaction follows that of Arenhövel *et al.* (e.g., [118]). For ease of notation, all kinematic quantities in the center-of-mass (c.m.) frame of the recoiling neutron-proton (n-p) system will carry a superscript c.m.; however, kinematic quantities referred to the laboratory frame will not be adorned with a superscript lab.

1. Kinematic notation

A schematic diagram of the kinematics for the electrodisintegration of the deuteron in the one-photon exchange approximation is shown in Fig. 30. Our notation for the electron kinematics is as usual, and we assume the electron scatters from a deuteron with initial four-momentum $(m_d, \mathbf{0})$. Following the breakup of the deuteron, the proton and neutron exit with three-momenta $\mathbf{p}_p$ and $\mathbf{p}_n$, respectively. As is customary, we use θ_{pq} (θ_{nq}) to denote the polar angle between $\mathbf{p}_p$ ($\mathbf{p}_n$) and $\mathbf{q}$ in the laboratory frame, and a reaction plane is defined by any two of $\mathbf{q}$, $\mathbf{p}_p$, and $\mathbf{p}_n$. As is shown in Fig. 30, the reaction plane is tilted at a dihedral angle ϕ with respect to the scattering plane. It should be noted that in the n-p c.m. frame, this dihedral angle, $\phi_{np}^{\text{c.m.}}$, is, obviously, just equal to ϕ.

The n-p c.m. frame is reached via a boost along $\mathbf{q}$. In the laboratory frame, the n-p final state has an invariant mass, W_{np}, of $W_{np} = \sqrt{E_{np}^2 - \mathbf{q}^2}$, where the relative n-p energy in the laboratory frame, E_{np}, is $E_{np} = \omega + m_d$. With these definitions, it is clear that the Lorentz factor for the boost from

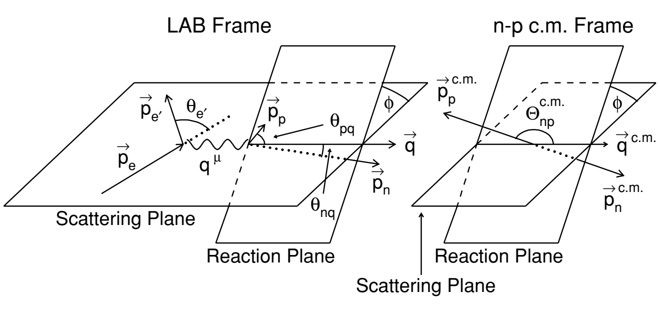

FIG. 30. Schematic diagram of the kinematics for the electrodisintegration of the deuteron in the one-photon exchange approximation as viewed from the laboratory frame and the recoiling n-p c.m. frame.

the laboratory frame to the n-p c.m. frame is

$$\gamma = \frac{E_{np}}{W_{np}} = \frac{\omega + m_d}{\sqrt{(\omega + m_d)^2 - \mathbf{q}^2}}. \tag{A1}$$

We denote the polar angle between the relative n-p motion in the c.m. frame, $\mathbf{p}_{np}^{\text{c.m.}} = \frac{1}{2}(\mathbf{p}_p^{\text{c.m.}} - \mathbf{p}_n^{\text{c.m.}}) = \mathbf{p}_p^{\text{c.m.}}$ (assuming equal nucleon masses), and $\mathbf{q}^{\text{c.m.}}$ as $\Theta_{np}^{\text{c.m.}}$. As can be shown easily, this angle can be written solely in terms of the laboratory frame observables $E_n = \sqrt{\mathbf{p}_n^2 + m_n^2}$, $|\mathbf{p}_n|$, θ_{nq}, and ω as

$$\cos\Theta_{np}^{\text{c.m.}} = -\frac{|\mathbf{p}_n|\cos\theta_{nq} - |\mathbf{q}|E_n/E_{np}}{\sqrt{A+B}}, \tag{A2}$$

where

$$A = \mathbf{p}_n^2 \sin^2\theta_{nq}\left(1 - \frac{\mathbf{q}^2}{E_{np}^2}\right), \tag{A3a}$$

$$B = \left(|\mathbf{p}_n|\cos\theta_{nq} - \frac{|\mathbf{q}|E_n}{E_{np}}\right)^2. \tag{A3b}$$

Clearly, $\Theta_{np}^{\text{c.m.}} = 0^\circ$ (180°) corresponds to perfect quasifree emission of the proton (neutron); however, it should be noted that there is vanishing phase space for perfect quasifree emission.

2. Recoil polarization

The fivefold differential coincidence cross section for the electrodisintegration of the deuteron in polarized-electron, unpolarized-deuteron scattering is of the simple form [20]

$$\sigma(h,0,0) \equiv \frac{d^5\sigma}{dE_{e'}d\Omega_{e'}d\Omega_{np}^{\text{c.m.}}} = \sigma_0\left(1 + hP_eA_e\right), \tag{A4}$$

as the electron asymmetry, A_e, is the only polarized contribution to the cross section. As usual, σ_0 denotes the unpolarized cross section. The above expression for the cross section can also be written in terms of structure functions as [20]

$$\begin{aligned}\sigma(h,0,0) = C\big(&\rho_L f_L + \rho_T f_T + \rho_{LT} f_{LT}\cos\phi_{np}^{\text{c.m.}} \\ &+ \rho_{TT} f_{TT}\cos 2\phi_{np}^{\text{c.m.}} + hP_e\rho'_{LT} f'_{LT}\sin\phi_{np}^{\text{c.m.}}\big),\end{aligned} \tag{A5}$$

where the f_i structure functions are evaluated in the n-p c.m. frame, the ρ_i are elements of the virtual photon density matrix and functions of kinematics, and C is a function of kinematics. It should be noted that the above expression for the cross section is differential in $E_{e'}$, $\Omega_{e'}$, and $\Omega_{np}^{\text{c.m.}}$. The Jacobian, $\mathcal{J} = \partial\Omega_{np}^{\text{c.m.}}/\partial\Omega_n$, which transforms $\Omega_{np}^{\text{c.m.}} \to \Omega_n$ is given by [118]

$$\mathcal{J} = \frac{1}{\gamma}\left(\frac{\beta_n\gamma_n}{\beta_n^{\text{c.m.}}\gamma_n^{\text{c.m.}}}\right)^3\left[1 + \frac{\beta}{\beta_n^{\text{c.m.}}}\cos\left(\pi - \Theta_{np}^{\text{c.m.}}\right)\right]^{-1}. \tag{A6}$$

Here, γ is as given in Eq. (A1), $\gamma_n^{\text{c.m.}}$ is the Lorentz factor for the boost that takes the neutron from its rest frame to the n-p CM frame,

$$\gamma_n^{\text{c.m.}} = \frac{W_{np}}{2m_n}, \tag{A7}$$

and γ_n is the Lorentz factor for the boost that takes the neutron from its rest frame to the laboratory frame,

$$\gamma_n = \gamma\gamma_n^{\text{c.m.}}\left[1 + \beta\beta_n^{\text{c.m.}}\cos\left(\pi - \Theta_{np}^{\text{c.m.}}\right)\right], \qquad \text{(A8)}$$

where β, $\beta_n^{\text{c.m.}}$, and β_n are the velocities (in units of c) associated with γ, $\gamma_n^{\text{c.m.}}$, and γ_n, respectively.

The nucleon recoil polarization in the n-p c.m. frame, $\mathbf{P}^{\text{c.m.}}$, is of the form [20]

$$\frac{d^5\sigma}{dE_{e'}d\Omega_{e'}d\Omega_{np}^{\text{c.m.}}}(\mathbf{P}^{\text{c.m.}}) = \sigma_0[(\mathbf{P}^{(0)})^{\text{c.m.}} + hP_e(\mathbf{P}^{(h)})^{\text{c.m.}}], \quad \text{(A9)}$$

where $\mathbf{P}^{(0)}$ and $\mathbf{P}^{(h)}$ denote, respectively, the helicity-independent and helicity-dependent recoil polarization. Written in terms of $g_i^{t,n,\ell}$ structure functions, the helicity-independent polarization components are as follows:

$$\left(P_t^{(0)}\right)^{\text{c.m.}} = \frac{C}{\sigma_0}\left(\rho_{LT}g_{LT}^t \sin\phi_{np}^{\text{c.m.}} + \rho_{TT}g_{TT}^t \sin\phi_{np}^{\text{c.m.}}\right), \qquad \text{(A10a)}$$

$$\left(P_n^{(0)}\right)^{\text{c.m.}} = \frac{C}{\sigma_0}\left(\rho_L g_L^n + \rho_T g_T^n + \rho_{LT}g_{LT}^n \cos\phi_{np}^{\text{c.m.}} + \rho_{TT}g_{TT}^n \cos 2\phi_{np}^{\text{c.m.}}\right), \qquad \text{(A10b)}$$

$$\left(P_\ell^{(0)}\right)^{\text{c.m.}} = \frac{C}{\sigma_0}\left(\rho_{LT}g_{LT}^\ell \sin\phi_{np}^{\text{c.m.}} + \rho_{TT}g_{TT}^\ell \sin 2\phi_{np}^{\text{c.m.}}\right), \qquad \text{(A10c)}$$

and the helicity-dependent polarization components are as follows:

$$\left(P_t^{(h)}\right)^{\text{c.m.}} = \frac{C}{\sigma_0}\left(\rho'_{LT}g_{LT}^{\prime t}\cos\phi_{np}^{\text{c.m.}} + \rho'_T g_T^{\prime t}\right), \qquad \text{(A11a)}$$

$$\left(P_n^{(h)}\right)^{\text{c.m.}} = \frac{C}{\sigma_0}\rho'_{LT}g_{LT}^{\prime n}\sin\phi_{np}^{\text{c.m.}}, \qquad \text{(A11b)}$$

$$\left(P_\ell^{(h)}\right)^{\text{c.m.}} = \frac{C}{\sigma_0}\left(\rho'_{LT}g_{LT}^{\prime \ell}\cos\phi_{np}^{\text{c.m.}} + \rho'_T g_T^{\prime \ell}\right). \qquad \text{(A11c)}$$

The boost from the laboratory frame to the n-p c.m. frame is along $\mathbf{q}$, which is not, in general, parallel to either nucleon's momentum vector; therefore, the recoil polarization components in the laboratory frame are related to the recoil polarization components in the n-p c.m. frame via a relativistic Wigner spin rotation. As the nucleons' momenta span the $\hat{t}$-$\hat{\ell}$ plane, the $\hat{n}$ component is unchanged, whereas the $\hat{t}$- and $\hat{\ell}$-components mix according to the following:

$$P_i = \mathcal{R}_{ij}\left(\theta_n^W\right)P_j^{\text{c.m.}}, \qquad \text{(A12)}$$

where $i, j \in \{t, n, \ell\}$, $\mathcal{R}_{ij}(\theta_n^W)$ denotes a matrix element of the Wigner rotation matrix,

$$\mathcal{R}\left(\theta_n^W\right) = \begin{pmatrix} \cos\theta_n^W & 0 & \sin\theta_n^W \\ 0 & 1 & 0 \\ -\sin\theta_n^W & 0 & \cos\theta_n^W \end{pmatrix}, \qquad \text{(A13)}$$

and θ_n^W, the Wigner rotation angle for the neutron, is expressed in terms of kinematics as [118,119]

$$\theta_n^W = \sin^{-1}\left[\frac{1+\gamma}{\gamma_n^{\text{c.m.}} + \gamma_n}\sin\left(\theta_n^{\text{c.m.}} - \theta_n\right)\right]. \qquad \text{(A14)}$$

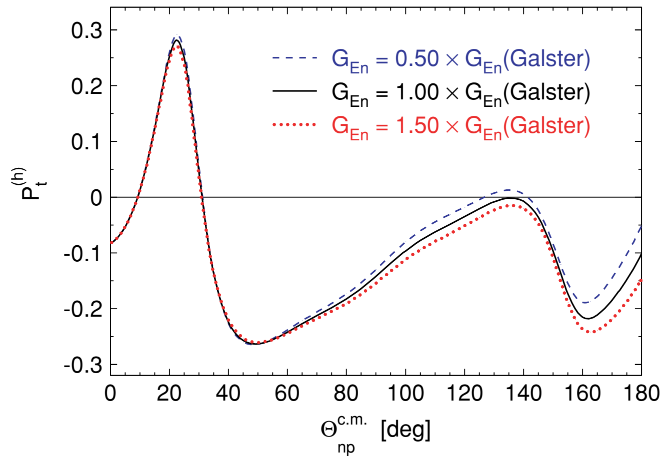

FIG. 31. (Color online) Sensitivity of FSI+MEC+IC+RC calculations of $P_t^{(h)}$ to the value of G_{En} for the central kinematics of our $Q^2 = 1.136\,(\text{GeV}/c)^2$ point. The results shown are for $\phi_{np}^{\text{c.m.}} = 0°$ and the Bonn potential.

Here, $\theta_n^{\text{c.m.}} (= \pi - \Theta_{np}^{\text{c.m.}})$ and θ_n denote, respectively, the polar angle of the neutron's momentum vector relative to $\mathbf{q}$ in the n-p c.m. frame and the laboratory frame. For nonrelativistic

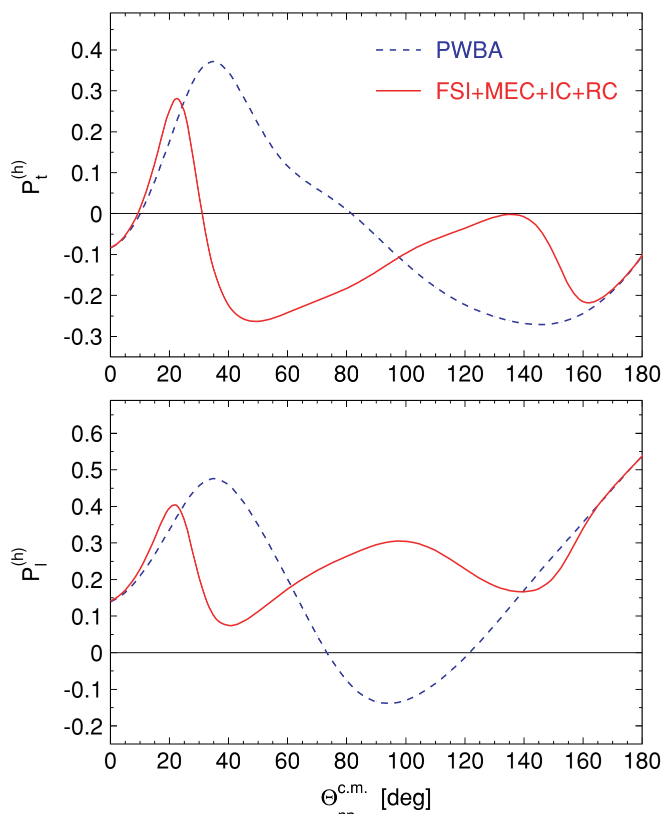

FIG. 32. (Color online) Comparison of PWBA and FSI+MEC+IC+RC calculations of $P_t^{(h)}$ (top panel) and $P_\ell^{(h)}$ (bottom panel) for the central kinematics of our $Q^2 = 1.136\,(\text{GeV}/c)^2$ point. The results shown are for $\phi_{np}^{\text{c.m.}} = 0°$ and the Bonn potential.

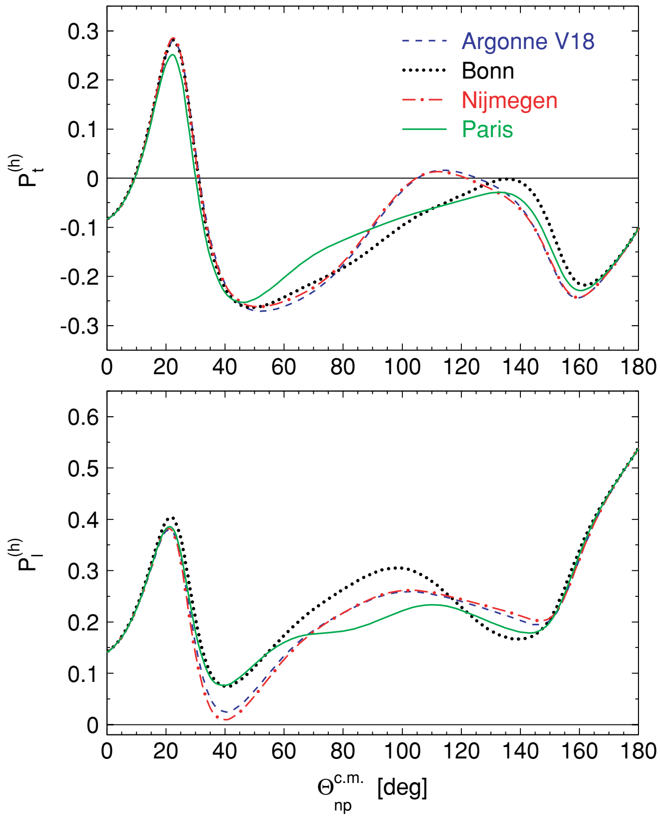

FIG. 33. (Color online) Comparison of FSI+MEC+IC+RC calculations of $P_t^{(h)}$ (top panel) and $P_\ell^{(h)}$ (bottom panel) for the Argonne V18, Bonn, Nijmegen, and Paris potentials. The results shown are for the central kinematics of our $Q^2 = 1.136$ (GeV/c)^2 point and $\phi_{np}^{\text{c.m.}} = 0^\circ$.

boosts (i.e., γ, $\gamma_n^{\text{c.m.}}$, and γ_n all $\sim$1), it is clear that we recover the nonrelativistic result, $\theta_n^W \to \theta_n^{\text{c.m.}} - \theta_n$. Also, it is obvious that for perfect quasifree emission (i.e., $\Theta_{np}^{\text{c.m.}} = 0$ or π), the recoil polarization components in the n-p c.m. frame are identical to those in the laboratory frame.

APPENDIX B: SENSITIVITY TO NUCLEAR PHYSICS EFFECTS AND DEUTERON STRUCTURE

To demonstrate the sensitivity of $P_t^{(h)}$ to the value of G_{En} and the insensitivity of $P_t^{(h)}$ and $P_\ell^{(h)}$ to FSI, MEC, IC, and the choice of the *NN* potential, we present several examples of $^2\text{H}(\vec{e}, e'\vec{n})^1\text{H}$ recoil polarization calculations performed within the PWBA and FSI+MEC+IC+RC models of Arenhövel *et al.* [19,20,120] in Figs. 31, 32, and 33. We have (arbitrarily) chosen to show examples of these calculations for the central kinematics of our $Q^2 = 1.136$ (GeV/c)^2 point (i.e., $E_e = 2.326$ GeV, $E_{e'} = 1.718$ GeV, $\theta_{e'} = 30.93^\circ$).

First, FSI+MEC+IC+RC calculations of $P_t^{(h)}$ are shown in Fig. 31 as a function of $\Theta_{np}^{\text{c.m.}}$ for three values of G_{En} scaled by the Galster parametrization: 0.5, 1.0, and 1.5. A strong (nearly linear) sensitivity of $P_t^{(h)}$ to the value of G_{En} is seen at and near quasifree emission. Second, the insensitivity of $P_t^{(h)}$ and $P_\ell^{(h)}$ to FSI, MEC, and IC for quasifree emission is shown in Fig. 32, where little difference between the PWBA and FSI+MEC+IC+RC calculations is observed at and near quasifree emission. Finally, we compare FSI+MEC+IC+RC calculations of $P_t^{(h)}$ and $P_\ell^{(h)}$ for the Argonne V18 [121], Bonn [74], Nijmegen [122], and Paris [123] NN potentials in Fig. 33. Again, at and near quasifree emission, there is little model dependence.

[1] D. R. Yennie, M. M. Lévy, and D. G. Ravenhall, Rev. Mod. Phys. **29**, 144 (1957); F. J. Ernst, R. G. Sachs, and K. C. Wali, Phys. Rev. **119**, 1105 (1960); R. G. Sachs, *ibid.* **126**, 2256 (1962); L. N. Hand, D. G. Miller, and R. Wilson, Rev. Mod. Phys. **35**, 335 (1963).
[2] S. Frullani and J. Mougey, Adv. Nucl. Phys. **14**, 1 (1984).
[3] D. Drechsel and M. M. Giannini, Rep. Prog. Phys. **52**, 1083 (1989).
[4] I. Sick, Prog. Part. Nucl. Phys. **47**, 245 (2001).
[5] A. W. Thomas and W. Weise, *The Structure of the Nucleon* (Wiley-VCH, Berlin, 2001).
[6] H. Gao, Int. J. Mod. Phys. E **12**, 1 (2003); **12**, 567 (2003).
[7] C. E. Hyde-Wright and K. de Jager, Annu. Rev. Nucl. Part. Sci. **54**, 217 (2004).
[8] A. Lung *et al.*, Phys. Rev. Lett. **70**, 718 (1993).
[9] S. Platchkov *et al.*, Nucl. Phys. **A510**, 740 (1990).
[10] R. Schiavilla and I. Sick, Phys. Rev. C **64**, 041002(R) (2001).
[11] R. Madey and T. Eden, Fizika B (Zagreb) **8**, 35 (1999); Jefferson Laboratory experiment 93-038, R. Madey and S. Kowalski, spokespersons.
[12] R. Madey *et al.*, Phys. Rev. Lett. **91**, 122002 (2003).
[13] B. Plaster, Ph.D. thesis, Massachusetts Institute of Technology (2003); S. Tajima, Ph.D. thesis, Duke University (2003); W. Tireman, Ph.D. thesis, Kent State University (2003); G. MacLachlan, Ph.D. thesis, Ohio University (2004); A. Aghalaryan, Ph.D. thesis, Yerevan Physics Institute (in preparation); E. Crouse, Ph.D. thesis, The College of William and Mary (in preparation).
[14] A. I. Akhiezer, L. N. Rozentsveig, and I. M. Shmushkevich, Sov. Phys. JETP **6**, 588 (1958).
[15] N. Dombey, Rev. Mod. Phys. **41**, 236 (1969).
[16] A. I. Akhiezer and M. P. Rekalo, Sov. J. Part. Nuclei **4**, 277 (1974).
[17] R. G. Arnold, C. E. Carlson, and F. Gross, Phys. Rev. C **23**, 363 (1981).
[18] M. Ostrick *et al.*, Phys. Rev. Lett. **83**, 276 (1999).
[19] H. Arenhövel, Phys. Lett. **B199**, 13 (1987).
[20] H. Arenhövel, W. Leidemann, and E. L. Tomusiak, Z. Phys. A **331**, 123 (1988); **334**, 363 (1989).
[21] M. P. Rekalo, G. I. Gakh, and A. P. Rekalo, J. Phys. G **15**, 1223 (1989).
[22] J. M. Laget, Phys. Lett. **B273**, 367 (1991).
[23] C. Herberg *et al.*, Eur. Phys. J. A **5**, 131 (1999).
[24] T. W. Donnelly and A. S. Raskin, Ann. Phys. **169**, 247 (1986); A. S. Raskin and T. W. Donnelly, *ibid.* **191**, 78 (1989).
[25] C. Y. Cheung and R. M. Woloshyn, Phys. Lett. **B127**, 147 (1983).
[26] E. L. Tomusiak and H. Arenhövel, Phys. Lett. **B206**, 187 (1988).

[27] H. Arenhövel, W. Leidemann, and E. L. Tomusiak, Phys. Rev. C **46**, 455 (1992); **52**, 1232 (1995).
[28] W. Leidemann, E. L. Tomusiak, and H. Arenhövel, Phys. Rev. C **43**, 1022 (1991).
[29] B. Blankleider and R. M. Woloshyn, Phys. Rev. C **29**, 538 (1984).
[30] C. Ciofi degli Atti, E. Pace, and G. Salmè, Phys. Rev. C **46**, R1591 (1992).
[31] R.-W. Schulze and P. U. Sauer, Phys. Rev. C **48**, 38 (1993).
[32] C. E. Jones-Woodward *et al*., Phys. Rev. C **44**, R571 (1991).
[33] A. K. Thompson *et al*., Phys. Rev. Lett. **68**, 2901 (1992).
[34] T. Eden *et al*., Phys. Rev. C **50**, R1749 (1994).
[35] P. Markowitz *et al*., Phys. Rev. C **48**, R5 (1993).
[36] H. Gao *et al*., Phys. Rev. C **50**, R546 (1994); H. Gao, Nucl. Phys. **A631**, 170c (1998).
[37] S. Galster *et al*., Nucl. Phys. **B32**, 221 (1971).
[38] M. Meyerhoff *et al*., Phys. Lett. **B327**, 201 (1994).
[39] J. Becker *et al*., Eur. Phys. J. A **6**, 329 (1999).
[40] J. Golak, G. Ziemer, H. Kamada, H. Witala, W. Glockle, Phys. Rev. C **63**, 034006 (2001).
[41] I. Passchier *et al*., Phys. Rev. Lett. **82**, 4988 (1999).
[42] D. Rohe *et al*., Phys. Rev. Lett. **83**, 4257 (1999).
[43] J. Bermuth *et al*., Phys. Lett. **B564**, 199 (2003).
[44] G. Kubon *et al*., Phys. Lett. **B524**, 26 (2002).
[45] J. Golak, W. Glockle, H. Kamada, H. Witala, R. Skibinski, A. Nogga, Phys. Rev. C **65**, 044002 (2002).
[46] W. Xu *et al*., Phys. Rev. Lett. **85**, 2900 (2000); W. Xu *et al*., Phys. Rev. C **67**, 012201(R) (2003).
[47] G. Höhler *et al*., Nucl. Phys. **B114**, 505 (1976).
[48] H. Zhu *et al*., Phys. Rev. Lett. **87**, 081801 (2001).
[49] J. J. Kelly, Phys. Rev. C **66**, 065203 (2002).
[50] G. Warren *et al*., Phys. Rev. Lett. **92**, 042301 (2004).
[51] D. I. Glazier *et al*., Eur. Phys. J. A **24**, 101 (2005).
[52] J. Friedrich and Th. Walcher, Eur. Phys. J. A **17**, 607 (2003).
[53] C. W. Leemann, D. R. Douglas, and G. A. Krafft, Annu. Rev. Nucl. Part. Sci. **51**, 413 (2001).
[54] R. Madey, A. Lai, and T. Eden, AIP Conf. Proc. **339**, 47 (1995); I. Niculescu *et al*., IEEE Trans. Nucl. Sci. **45**, 68 (1998); A. Yu. Semenov *et al*., Nucl. Instrum. Methods Phys. Res. A **557**, 585 (2006).
[55] M. Poelker *et al*., AIP Conf. Proc. **570**, 943 (2001).
[56] M. Poelker and J. Hansknecht, *Proceedings of the IEEE Particle Accelerator Conference (PAC 2001)*, 95 (2001).
[57] C. Yan *et al*., Nucl. Instrum. Methods Phys. Res. A **365**, 261 (1995).
[58] M. Hauger *et al*., Nucl. Instrum. Methods Phys. Res. A **462**, 382 (2001).
[59] J. Alcorn *et al*., Nucl. Instrum. Methods Phys. Res. A **522**, 294 (2004).
[60] C. Yan *et al*., Nucl. Instrum. Methods Phys. Res. A **365**, 46 (1995); R. Wojcik and C. Yan, *ibid*. **484**, 690 (2002).
[61] O. K. Baker *et al*., Nucl. Instrum. Methods Phys. Res. A **367**, 92 (1995).
[62] L. Wolfenstein, Phys. Rev. **75**, 1664 (1949); **85**, 947 (1952).
[63] J. Simkin and C. W. Trowbridge, Rutherford Laboratory Report 79-097 (unpublished).
[64] S. Taylor, E93-038 technical reports (unpublished): http://www.jlab.org/∼plaster/reports/charybdis1.ps; http:www.jlab.org/∼plaster/reports/charybdis2.ps; http:www.jlab.org/∼plaster/reports/charybdis3.ps.
[65] R. Madey *et al*., Nucl. Instrum. Methods Phys. Res. **214**, 401 (1983).
[66] J. W. Watson *et al*., Nucl. Instrum. Methods Phys. Res. A **272**, 750 (1988); R. Madey *et al*., IEEE Trans. Nucl. Sci. **36**, 231 (1989); T. Eden *et al*., Nucl. Instrum. Methods Phys. Res. A **338**, 432 (1994).
[67] http://coda.jlab.org
[68] J. Arrington, Ph.D. thesis, California Institute of Technology (1998).
[69] R. Madey *et al*., Nucl. Instrum. Methods Phys. Res. **151**, 445 (1978).
[70] R. A. Arndt, I. I. Strakovsky, and R. L. Workman, Int. J. Mod. Phys. A **18**, 449 (2003).
[71] G. G. Ohlsen and P. W. Keaton Jr., Nucl. Instrum. Methods Phys. Res. **109**, 41 (1973).
[72] D. L. Prout *et al*., Phys. Rev. C **63**, 014603 (2000).
[73] J. Arrington, SIMC computer code, http://www.jlab.org/∼johna/SIMC_documents/simc.ps.
[74] R. Machleidt, K. Holinde, and Ch. Elster, Phys. Rep. **149**, 1 (1987).
[75] R. W. Finlay, W. P. Abfalterer, G. Fink, E. Montei, T. Adami, P. W. Lisowski, G. L. Morgan, and R. C. Haight, Phys. Rev. C **47**, 237 (1993).
[76] R. A. Cecil, B. D. Anderson, and R. Madey, Nucl. Instrum. Methods Phys. Res. **161**, 439 (1979).
[77] S. Kopecky, P. Riehs, J. A. Harvey, and N. W. Hill, Phys. Rev. Lett. **74**, 2427 (1995); S. Kopecky, J. A. Harvey, N. W. Hill, M. Krenn, M. Pernicka, P. Riehs, and S. Steiner, Phys. Rev. C **56**, 2229 (1997).
[78] J. J. Kelly, Phys. Rev. C **70**, 068202 (2004).
[79] E. J. Brash, A. Kozlov, Sh. Li, and G. M. Huber, Phys. Rev. C **65**, 051001(R) (2002).
[80] A. Afanasev, I. Akushevich, and N. Merenkov, Phys. Rev. D **64**, 113009 (2001).
[81] G. G. Simon, C. Schmitt, F. Borkowski, and V. H. Walther, Nucl. Phys. **A333**, 381 (1980).
[82] L. E. Price *et al*., Phys. Rev. D **4**, 45 (1971).
[83] M. K. Jones *et al*., Phys. Rev. Lett. **84**, 1398 (2000); O. Gayou *et al*., Phys. Rev. C **64**, 038202 (2001); V. Punjabi *et al*., *ibid.* **71**, 055202 (2005).
[84] O. Gayou *et al*., Phys. Rev. Lett. **88**, 092301 (2002).
[85] T. Pospischil *et al*., Eur. Phys. J. A **12**, 125 (2001).
[86] B. D. Milbrath *et al*., Phys. Rev. Lett. **82**, 2221 (1999).
[87] H. Anklin *et al*., Phys. Lett. **B336**, 313 (1994).
[88] H. Anklin *et al*., Phys. Lett. **B428**, 248 (1998).
[89] F. Iachello, A. D. Jackson, and A. Lande, Phys. Lett. **B43**, 191 (1973).
[90] M. F. Gari and W. Krümpelmann, Z. Phys. A **322**, 689 (1985).
[91] M. F. Gari and W. Krümpelmann, Phys. Lett. **B274**, 159 (1992).
[92] R. Bijker and F. Iachello, Phys. Rev. C **69**, 068201 (2004).
[93] E. L. Lomon, Phys. Rev. C **64**, 035204 (2001).
[94] E. L. Lomon, Phys. Rev. C **66**, 045501 (2002).
[95] Jefferson Laboratory experiment 02-013, G. Cates, K. McCormick, B. Reitz, and B. Wojtsekhowski, spokespersons.
[96] Jefferson Laboratory experiment 04-110, B. Anderson, J. Kelly, S. Kowalski, R. Madey, and A. Semenov, spokespersons.
[97] D. H. Lu, A. W. Thomas, and A. G. Williams, Phys. Rev. C **57**, 2628 (1998).
[98] A. L. Licht and A. Pagnamenta, Phys. Rev. D **2**, 1150 (1970).
[99] D. H. Lu, K. Tsushima, A. W. Thomas, and A. G. Williams, Nucl. Phys. **A634**, 443 (1998).
[100] D. H. Lu, K. Tsushima, A. W. Thomas, A. G. Williams, and K. Saito, Phys. Rev. C **60**, 068201 (1999).

[101] S. Dieterich *et al.*, Phys. Lett. **B500**, 47 (2001).
[102] S. Strauch *et al.*, Phys. Rev. Lett. **91**, 052301 (2003).
[103] G. A. Miller and M. R. Frank, Phys. Rev. C **65**, 065205 (2002); G. A. Miller, *ibid.* **66**, 032201(R) (2002).
[104] M. R. Frank, B. K. Jennings, and G. A. Miller, Phys. Rev. C **54**, 920 (1996).
[105] B. Kubis and U.-G. Meissner, Nucl. Phys. **A679**, 698 (2001).
[106] T. Fuchs, J. Gegelia, and S. Scherer, J. Phys. G **30**, 1407 (2004).
[107] M. R. Schindler, J. Gegelia, and S. Scherer, Nucl. Phys. **B682**, 367 (2004).
[108] H.-W. Hammer, D. Drechsel, and U.-G. Meissner, Phys. Lett. **B586**, 291 (2004).
[109] M. R. Schindler, J. Gegelia, and S. Scherer, Eur. Phys. J. A **26**, 1 (2005).
[110] M. M. Kaskulov and P. Grabmayr, Phys. Rev. C **69**, 028201 (2004); Eur. Phys. J. A **19**, 157 (2004).
[111] R. F. Wagenbrunn, S. Boffi, W. Klink, W. Plessas, and M. Radici, Phys. Lett. **B511**, 33 (2001); S. Boffi, L. Ya. Glozman, W. Klink, W. Plessas, M. Radici, and R. F. Wagenbrunn, Eur. Phys. J. A **14**, 17 (2002).
[112] S. Simula, arXiv:nucl-th/0105024.
[113] F. Cardarelli, E. Pace, G. Salmè, and S. Simula, Phys. Lett. **B357**, 267 (1995).
[114] M. De Sanctis, M. M. Giannini, E. Santopinto, and A. Vassallo, arXiv:nucl-th/0506033.
[115] M. Göckeler, T. R. Hemmert, R. Horseley, D. Pleiter, P. E. L. Rakow, A. Schafer, and G. Schierholz, Phys. Rev. D **71**, 034508 (2005).
[116] J. D. Ashley, D. B. Leinweber, A. W. Thomas, and R. D. Young, Eur. Phys. J. A **19**, 9 (2004).
[117] H. H. Matevosyan, G. A. Miller, and A. W. Thomas, Phys. Rev. C **71**, 055204 (2005).
[118] H. Arenhövel, W. Leidemann, and E. L. Tomusiak, Eur. Phys. J. A **23**, 147 (2005).
[119] D. R. Giebink, Phys. Rev. C **32**, 502 (1985).
[120] H. Arenhövel, private communication (2001, 2002, 2003).
[121] R. B. Wiringa, V. G. J. Stoks, and R. Schiavilla, Phys. Rev. C **51**, 38 (1995).
[122] M. M. Nagels, T. A. Rijken, and J. J. de Swart, Phys. Rev. D **17**, 768 (1978).
[123] M. Lacombe *et al.*, Phys. Lett. **B101**, 139 (1981).